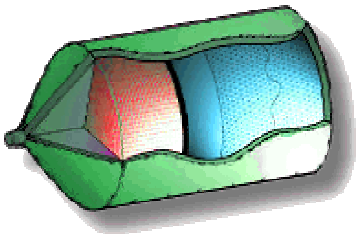

CENTER FOR SIMULATION OF DYNAMIC RESPONSE OF MATERIALS

A DOE ASCI / ASAP CENTER OF EXCELLENCE

TECHNICAL REPORT 033

The 1999 Center for Simulation of Dynamic Response in Materials
Annual Technical Report

ASCI Alliance Center for Simulation of Dynamic Response in Materials California Insitute of Technology FY 99 Annual Report

Michael Aivazis, Bill Goddard, Dan Meiron, Michael Ortiz, James C. T. Pool, Joe Shepherd

Principal Investigators

Contents

Chapter 1

Introduction and Overview

1.1 Introduction

This annual report describes research accomplishments for FY 99 of the Center for Simulation of Dynamic Response of Materials. The Center is constructing a virtual shock physics facility in which the full three dimensional response of a variety of target materials can be computed for a wide range of compressive, tensional, and shear loadings, including those produced by detonation of energetic materials. The goals are to facilitate computation of a variety of experiments in which strong shock and detonation waves are made to impinge on targets consisting of various combinations of materials, compute the subsequent dynamic response of the target materials, and validate these computations against experimental data.

An illustration of the simulations that are to be facilitated by the Center's Virtual Test Facility (VTF) are shown in Figure 1.1 The research is centered on the three primary stages required to conduct a virtual experiment in this facility: detonation of high explosives, interaction of shock waves with materials, and shock-induced compressible turbulence and mixing. The modeling requirements are addressed through five integrated research initiatives which form the basis of the simulation development road map to guide the key disciplinary activities:

1. Modeling and simulation of fundamental processes in detonation,
2. Modeling dynamic response of solids,
3. First principles computation of materials properties,
4. Compressible turbulence and mixing, and
5. Computational and computer science infrastructure.

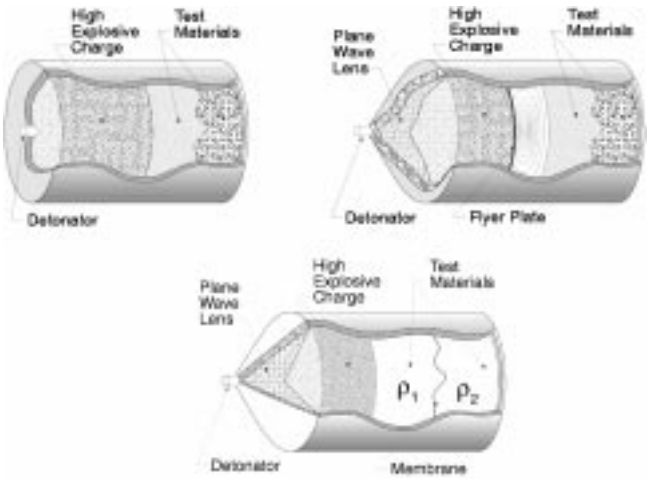

Figure 1.1: Illustrations of three key simulations performed using the Virtual Test Facility. Top left: High velocity impact generated by the interaction of a detonation wave with a set of solid test materials. Top right: High velocity impact generated by a flyer plate driven by a high explosive plane wave lens. Bottom: configuration used to examine compressible turbulent mixing

1.2 Administration of the Center

1.2.1 Personnel Overview

The center activities are guided by five principal investigators:

J. Shepherd	High Explosives
M. Ortiz	Solid Dynamics
W. A. Goddard	Materials Properties
D. Meiron	Compressible Turbulence
J. C. T. Pool	Computational Science
M. Aivazis	Computational Science and Software Integration

In FY 99 the center personnel numbered as follows:

- 17 Caltech faculty (including the center steering committee
- 9 external faculty affiliated with the center via subcontracts
- 17 Caltech graduate students
- 31 research staff and postdoctoral scholars
- 15 administrative staff (primarily part-time support from the Caltech Center for Advanced Computing Research (CACR)

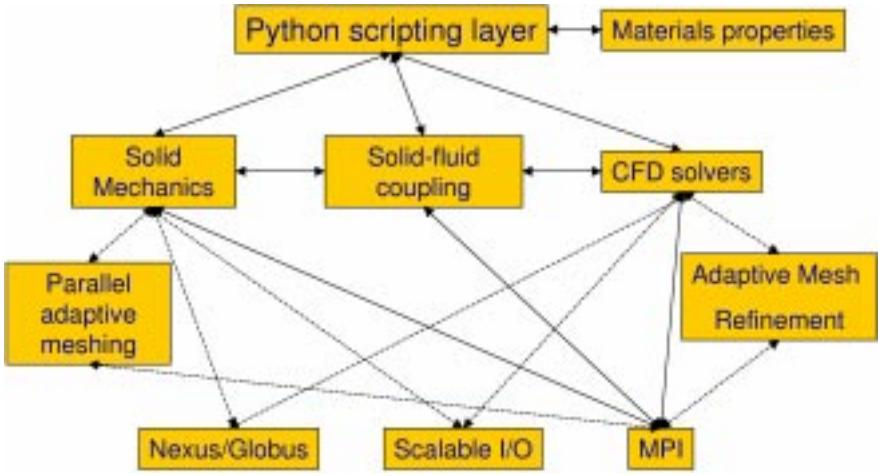

Figure 1.2: Diagrammatic representation of the VTF software architecture.

Detailed personnel listings are provided in the beginning of each chapter detailing the efforts of each disciplinary effort within the center.

1.2.2 Subcontracts

In addition to participants based at Caltech the Center has associated with it several sub-contractors who are providing additional support in a few key areas. In the table below we list the contractors, their institutional affiliation and their area of research:

R. Phillips	Brown University	Quasi-continuum methods for plasticity
R. Cohen	Carnegie Institute of Washington	High pressure equation of state of metals
G. Miller	U. C. Davis	Multi-phase Riemann solvers
R. Ward	Univ. Tennessee	Large scale eigenvalue algorithms
C. Kesselman	Univ. So. California, ISI	Metacomputing, Globus
D. Reed	Univ. Illinois	Scalable I/O
M. Parashar	Rutgers University	Parallel AMR

1.3 Overview of the integrated simulation capability

1.3.1 VTF software architecture

The VTF software architecture is illustrated in Figure 1.2. The top layer is a scripting interface written in the Python scripting language which sets up all aspects of the simulation and coordinates the interaction of the simulation with

the operating system and platform. Also associated with the scripting environment is a materials properties database. The database provides information to the solvers regarding equation of state, reaction rates, etc.

The next layer consists of the VTF computational engines. These engines are packaged as shared objects for which Python bindings are then generated. At present the VTF architecture supports two such engines, a 3-D parallel Eulerian CFD solver which is used for simulations of high explosive detonation and simulations of compressible turbulent mixing, and a 3-D Lagrangian solid dynamics solver. The solid dynamics solver is now fully parallel as of this writing.

At the next layer we have designated some of the lower level functionality of the engines. For example, the CFD solver ultimately will have the ability to perform 3-D simulations using patch based parallel AMR. Similarly the solid dynamics solver will ultimately also possess a capability to perform parallel adaptive meshing.

Finally at the lowest level are services used to facilitate various low level aspects of the simulations such as the ability to access distributed resources via metacomputing infrastructures such as Globus, and facilities for parallel communication and scalable disposition of the large date sets generated during the computation.

The philosophy of this software architecture is to enable a multi-pronged approach to the simulation of high velocity impact problems and the associated fluid-solid interaction. For example it is well known that such simulations can be performed using a purely Lagrangian approach, a purely Eulerian approach, or some mixture of the two (such as ALE). The objective of the VTF architecture is to provide a flexible environment in which such simulations can be performed and the results of the differing approaches can be assessed.

As of the end of FY99 we have completed a prototype implementation of the VTF. Fully coupled axisymmetric simulations of shock waves and detonations interacting with solid targets. The present prototype utilizes a parallel fluid mechanics solver and a serial solid mechanics solver. In addition a full implementation of the Python based problem solving environment has been completed. Details of the implementation can be found in Chapter 2.

1.4 Highlights of Research Accomplishments

Research accomplishments associated with the various disciplinary activities are detailed in Chapters 3 through 7. Below we list highlights of research accomplishments achieved in FY 99. Each chapter provides an overview of progress, a list of the relevant personnel as well as a brief synopsis of plans for the FY 00.

1.4.1 High Explosives

Material Properties and Chemical Reactions Classical force fields have been refined and used to compute equations of state for HMX, Kel-F, estane and PMMA. Quantum mechanical computations were used to determine potential energy surfaces and calculate reaction rate constants for the

initial steps in RDX and HMX decomposition. A detailed reaction mechanism for gas-phase combustion of RDX and HMX was assembled.

Engineering Models of Explosives The JTF model of high explosives was implemented into the Eulerian fluid solver for the VTF. Micromechanics of plastic-bonded granular explosives were investigated by determining the effect of pressure-stiffening on the visco-elastic response of binder layers.

Integrated Simulations A technique (ghost–fluid method) for coupling Lagrangian and Eulerian solvers was explored. A number of test cases was computed and a prototype for the VTF was developed. Computations were run on detonation and shock wave propagation interacting with deforming boundaries described by a model solid or a full FEM simulation of solid mechanics.

1.4.2 Solid Dynamics

Modeling of spall In FY99 we started to formulate a model of spall which contemplates three different scales. At the smallest scale, the model estimates the density of vacancies generated by the dragging of jogs formed as a result of dislocation intersections and double cross slip. The super-saturated distribution of vacancies eventually collapses to form voids. Following this nucleation phase, the voids grow by the accumulation of vacancies migrating by pipe diffusion. Once the void attains a size comparable to the mean distance between dislocations, growth occurs primarily by single-crystal plasticity. A finite element model of a single void cavitating in a plastically deforming crystal under the action of a high hydrostatic tensile pressure and at high strain rates is under development. This fundamental calculation will provide an irreversible equation of state which can be incorporated into the single-crystal plasticity models to predict ductile rupture.

Fracture and fragmentation This has been completed. Present capability includes finite-deformation irreversible cohesive elements to simulate fracture and fragmentation within a finite-element framework. The capability has been extensively verified and validated.

Mixed atomistic-continuum modeling in 2D We have completed calculations of defect-mediated material properties and unit processes, including dislocation junction strength; dislocation energies in fcc and bcc crystals as a function of orientation; and pipe diffusivities for vacancy migration. A 3D mixed continuum/atomistic capability has also been completed. The capability is presently being applied to problems of nanoindentation in ductile single crystals.

2D and 3D prototype of the integrated VTF We have completed prototypes of the fully lagrangian 2D and 3D VTF including engineering models of HE materials and metals. We have completed verification problems in 2D,

with validation runs to begin soon. We have completed preliminary test runs in 3D and further runs are in progress, including the use of mesh adaption. MPI versions of the explicit dynamics and the Taylor averaging polycrystal model have been developed and their scalability properties have been assessed. A main focal point of activity has been the parallelization of our 2D and 3D tetrahedral meshers. Parallel versions of both meshers are presently in existence. The good scalability of the 2D mesher on the ASCI platforms has been established. A similar effort to appraise the scalability properties of the 3D mesher is presently underway.

Other activities Other activities developed during the year which exceed the scope of the milestones include: the development and validation of a model of single crystal plasticity in Ta; the development of a mesh refinement/coarsening algorithm based on subdivision and edge collapse; models of subgrain dislocation structures in crystals.

1.4.3 Materials Properties

High Explosives We have studied extensively binder and grain interactions for Kel-F and Estane. We have further refined the equations of state for HMX and TATB. We have also made significant progress in computation of reaction dynamics and molecular processes for nitramines and have developed fairly complete reaction networks for RDX and HMX.

Solid Dynamics We have further refined the equations of state for Ta, Fe, Oxides, and Ceramics. We have also performed phase transition studies of Ta, Carbon, and Ceramics. We have developed constitutive equations describing:

1. Elastic properties of metals, alloys, and ceramics;
2. Thermodynamic properties;
3. Plasticity and behavior under large strain rates.

Software Integration We have completed the integration of MP code with the HE group. We have also completed a self-integration of MP code for further development of a materials properties database.

1.4.4 Compressible Turbulence

Simulation of 3-D Richtmyer-Meshkov instability We have performed several large runs of shock-contact interaction resulting in R-M instability including the effects of reshock. To date resolutions of $2048 \times 256 \times 256$ have been achieved on the LANL Blue Mountain platform. Scalability assessments have been performed and have shown that our unigrid CFD capability is very scalable. High resolution visualization of this data via the Responsive Workbench are currently in progress.

High resolution 3-D DNS of decaying turbulence This work is now complete. We have produced a database of highly accurate fully resolved decaying compressible turbulent flows for comparison with simulations utilizing SGS schemes. Achievements to date include the development of two parallel codes, one a fully compressible multi-species DNS code with full physical viscosity utilizing Padé-base methods and the other a high order incompressible spectral element solver. Both codes have been implemented on the ASCI platforms.

LES of compressible turbulence Two models have been developed and comparisons have been carried out with DNS simulations of decaying turbulence with encouraging results. The first is a model based on the stretched subgrid vortex model of Saffman and Pullin. The second is based on the nonlinear model of Kosovic.

Development of 3-D AMR solver We have successfully developed a 2-D solver for compressible flow utilizing adaptive mesh refinement under the GrACE computational framework. Extensions to 3-D are underway with the objective of high resolution simulations of Richtmyer-Meshkov simulations with reshock.

High resolution 3-D DNS of R-M and R-T flows To date we have developed two parallel codes, one a fully compressible multi-species DNS code with full physical viscosity utilizing Padé-base methods and the other a high order incompressible spectral element solver. Both codes have been implemented on the ASCI platforms.

1.4.5 Computational Science

Pyre problem solving environment We have defined the architecture of the overarching application and we have made significant progress towards the full implementation of our problem solving environment.

Scalability we have conducted extensive studies of the scalability properties of the codes that were used to achieve our goals for FY 99.

Visualization the primary focus of our visualization activities was the construction of custom modules for the IRIS Explorer visualization environment in order to support the current needs of the Center. In addition, we have identified a small set of candidate visualization engines for integration into Pyre.

Distributed computing We completed an investigation of the Globus facilities necessary for the various aspect of remote staging and remote data access. Prototype modules that employ them have been constructed and an effort is well underway for a complete integration of the relevant Globus facilities in Pyre.

Scalable I/O We have performed performance studies of the various layers of the Scalable I/O infrastructure that were made available to us during this year.

Chapter 2

Integrated Simulation Capability

2.1 Introduction

In this section we provide a detailed description of the Center's primary deliverable: the Virtual Test Facility. The VTF software is a set of computational engines driven by a script-based problem solving environment.

In Section 2.2 we describe the algorithmic approach to integrating the CFD and solid dynamics engines. In Section 2.3 a detailed overview of the CFD engine is presented. In Section 2.4 we present a description of the solid mechanics engine adlib. Further details on adlib's capabilities are provided in Chapter 4. Finally, in Section 2.5 we provide an overview of the problem solving environment designed for the VTF.

2.2 Algorithmic integration

The study of high explosives (HE) often involves experiments in which the explosive behavior is closely coupled to the deformation of the surrounding material. For example, in the cylinder-test experiment, Figure 2.1, an explosive is detonated in a metal cylinder or pipe [39]. The cylinder deforms, resulting in an expanding flow behind the detonation wave. This expansion causes the detonation front to be curved and decreases the propagation speed. In addition, the detonation has to be initiated at a finite distance from the measurement location using an explosive lens arrangement which can result in significant transient behavior that persists for some distance.

In order to interpret such an experiment, it is necessary to model both the high explosive and the surrounding material motion. One of the goals of our research project is to develop new methods for accurately computing such problems. The key issue that immediately arises is what sort of numerical methods

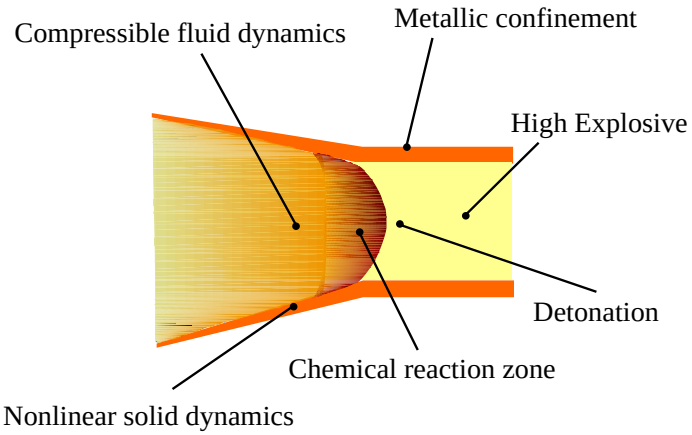

Figure 2.1: Cylinder test schematic illustrating key physical phenomena.

are appropriate. The standard approach for fluid mechanics and other problems in which very large deformations occur is to use an Eulerian (spatially stationary mesh) technique. The standard method used in mechanics is the Lagrangian (mesh moves with the material) technique. It is possible to use a multi-material algorithm to compute these problems but these methods are substantially more complex and less robust than single material algorithms. For example, using Eulerian methods with multiple materials requires ad hoc methods to treat cells that contain a mixture of materials or else complex interface tracking and reconstruction methods. Most of the Eulerian flow solvers are constructed to properly capture shock waves but in general do poorly in representing contact discontinuities. Lagrangian methods have difficulty with large material deformations or strong shock waves. There are techniques such as the Arbitrary Lagrangian Eulerian (ALE) method that use a hybrid of both methods. ALE codes allow a transition between an Eulerian and a Lagrangian formulation by incorporating an arbitrary, user-specified moving mesh.

We propose yet another approach in which different solvers and meshes are used in different materials. A reactive fluid solver based on an Eulerian method is used for the detonating HE and a conventional solid mechanics solver based on a Lagrangian method is used for the surrounding metallic confinement. The key issue is how to represent the moving boundary between fluid and solid and also devise a coupling technique that propagates information between the solvers for each material. Our treatment of the boundary is based on the Ghost Fluid Method (GFM) of Fedkiw *et al.* [28]. This technique is an extension of the standard concept of the ghost cell notion that is used to apply the boundary conditions at external stationary boundaries for solution methods based on finite-difference or finite-volume discretizations. The original GFM technique captured an interface or contact discontinuity between two fluids by defining a level set (signed distance function) that determined the interface location.

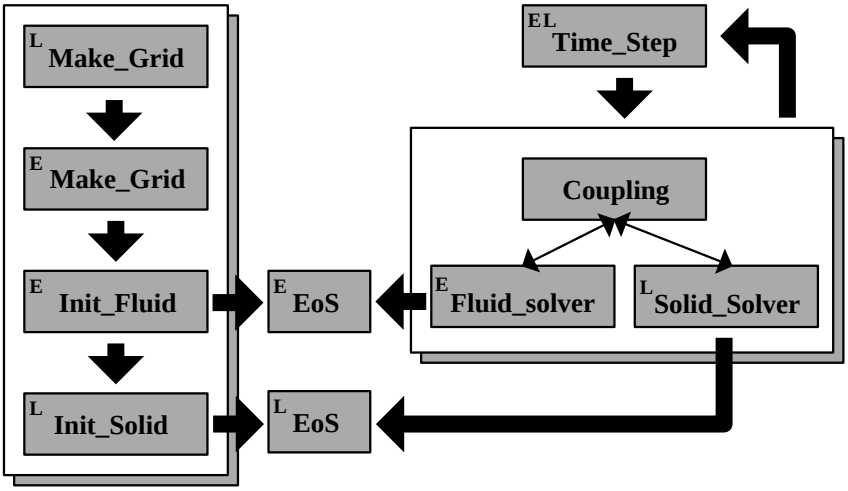

Figure 2.2: Modular architecture of VTF.

The level set was evolved as a function of time by solving a separate evolution equation. Ghost cell values on each side of the interface were populated with a prescription that combines actual and extrapolation values on both sides of the interface.

Our technique is a variation on this idea since we already have a representation of the interface location and we do not require the solution of an evolution equation to locate the boundary. Rather, we take advantage of the boundary representation inherent in the Lagrangian solution method. We still construct a level set since a signed distance function is needed in order to locate the neighborhood of the boundary and populate the ghost cells. When the location of the boundary is known, a ghost region, whose extent depends upon the fluid solver stencil, is constructed in order to enforce the boundary condition to the flow solution. The location of the boundary and the boundary velocity are supplied by the Lagrangian solver to the Eulerian solver. Simultaneously, the Eulerian solver supplies the pressure (normal component of boundary force) to the Lagrangian solver.

The coupling technique, described in Figure 2.2, is implemented in a modular fashion. It consists of the following modules: initialization (including the grid generation), equation of state, time-step, fluid solver, solid solver and coupling algorithm. The letter "E" in each box refers to the Eulerian solver while the letter "L" refers to the Lagrangian solver. Standardized interfaces were designed for each module so that various implementations of the solid and fluid solvers could be used interchangeably.

2.2.1 Equation Framework: Fluid Model

In general, the fluid model can be of any type that is solved on a fixed (Eulerian) mesh. The particular examples that we have explored are models of ideal gases or high explosives based on simplified one-fluid models which represent a mixture of products and reactants in equilibrium. The particular model equations for this case are the reactive Eulerian equations with a single composition variable:

$$\begin{aligned} \frac{\partial \rho}{\partial t} + \nabla \cdot (\rho \mathbf{u}) &= 0, \\ \frac{\partial}{\partial t}(\lambda \rho) + \nabla \cdot (\lambda \rho \mathbf{u}) &= \rho R, \\ \frac{\partial}{\partial t}(\rho \mathbf{u}) + \nabla \cdot (\rho \mathbf{u}\,\mathbf{u} + \mathbf{I}P) &= 0, \\ \frac{\partial}{\partial t}(\rho E) + \nabla \cdot \left[\rho \mathbf{u}\left(E + \frac{P}{\rho}\right)\right] &= 0. \end{aligned} \tag{2.1}$$

where ρ is the density of the fluid, λ the product mass fraction, R the reaction rate, $\mathbf{u}$ the velocity vector, P the pressure and e the specific internal energy. $E = e + 1/2\,\|\mathbf{u}\|^2$ is the specific total energy.

These equations are numerically solved in conservative form:

$$\mathbf{U}_t + \nabla \cdot \mathbf{F}(\mathbf{U}) = \Omega(\mathbf{U}), \tag{2.2}$$

where $\mathbf{U} = (\rho, \lambda\,\rho, \rho\mathbf{u}, \rho E)^T$ is the vector of the conservative variables. The reaction model used for the detonation simulations is based on a simple one-step irreversible reaction, as discussed in Section 3.4. The equations are closed with an appropriate choice of equation of state. Experiments were conducted using the perfect-gas model, the Mie-Grüneisen model of solids, and an engineering mixture model designed to represent high explosives, described in more detail in Section 3.4. In order to integrate equations (2.1), we use the standard time-splitting technique of Strang [114]. The time integration is split into two portions, one defined by the solution of the advection operation

$$\mathbf{U}_t + \nabla \cdot \mathbf{F}(\mathbf{U}) = \mathbf{0} \tag{2.3}$$

and the other by the system of ODE's associated with the chemical reaction:

$$\mathbf{U}_t = \Omega(\mathbf{U})\,. \tag{2.4}$$

If we denote the advection operator $\mathcal{L}_A$ and the "chemistry" ODE operator $\mathcal{L}_C$, then the operator sequence for time advancement can be written symbolically as:

$$\mathbf{U}^{(n+1)} = \mathcal{L}_C\left(\frac{\Delta t}{2}\right)\,\mathcal{L}_A\,(\Delta t)\,\mathcal{L}_C\left(\frac{\Delta t}{2}\right)\,\mathbf{U}^{(n)}\,. \tag{2.5}$$

We discretize equations (2.3) through either a finite-volume formulation or a finite-difference formulation on a Cartesian grid. The finite-difference approach is used for inert flows using the perfect-gas equation of state, while the finite-volume approach is used for HE models using the mixture equation of state.

The finite-difference approach is the Essentially-Non-Oscillatory Local Lax-Friedrichs (ENO-LLF) method. ENO was introduced by Shu and Osher in its conservative finite-difference form [109]. ENO schemes were designed in order to minimize spurious oscillations that appear in the solution where a flux computation is performed at an interface or near a steep gradient. The one-dimensional finite-difference discretization at node x_i is

$$\partial_t \mathbf{U}_i + \frac{\Phi_{i+1/2} - \Phi_{i-1/2}}{\Delta x} = 0, \tag{2.6}$$

where $\Phi_{i\pm1/2}$ are the values of the numerical flux at the midpoint. The evaluation of the numerical flux is achieved through a higher-order interpolation of the numerical flux by applying Newton divided differences to compute the higher-order terms in the interpolant. The one-dimensional scheme is extensible to multiple dimensions through a dimension-by-dimension technique where each component of the multi-dimensional flux is computed separately and then assembled to form the residual, *i.e.*, the divergence part of equations (2.2). The ENO-LLF variant is described in [86]. Time marching is achieved through a third-order TVD multi-step technique.

The finite-volume approach proceeds by discretization of the integral control volume relationship

$$\frac{\partial}{\partial t}\int_{\mathcal{C}_i} \mathbf{U}\,\mathrm{d}\mathbf{x} + \int_{\partial\mathcal{C}_i} \mathbf{F}(\mathbf{U})\cdot\mathbf{n}\,\mathrm{dl} = 0, \tag{2.7}$$

where $\mathcal{C}_i$ represents the control volume, $\partial\mathcal{C}_i$ its boundary, $\mathrm{d}\mathbf{x}$ the element of volume and $\mathbf{n}$ the outward normal unit vector to $\mathcal{C}_i$. The integration of the convective fluxes at a cell interface is achieved via Roe's upwind numerical flux, extended by Glaister [35] to general equations of state. We use Harten's entropy correction [38] on all waves and time marching is by explicit forward integration.

The reaction part (2.4) of the equations reduces to the integration of the following ordinary differential equation

$$\frac{d}{dt}\lambda = R(\lambda, P). \tag{2.8}$$

The time-splitting process consists first of integrating the equation above, by means of a Runge-Kutta time integrator. The result is then used to correct the advected value of λ obtained as a solution to (2.3).

2.2.2 Equation Framework: Solid Model

Mechanics models can all be cast into a general form that resembles Newton's second law of motion

$$\mathbf{M}\,\ddot{\mathbf{X}} + \mathbf{C}\,\dot{\mathbf{X}} + \mathbf{K}\,\mathbf{X} = \mathcal{F}, \tag{2.9}$$

where $\dot{(\cdot)} = d/dt(\cdot)$ is the time derivative operator, $\mathbf{X}$ is the vector of displacements, $\mathbf{M}$ is the mass-matrix, $\mathbf{C}$ is the damping-matrix, $\mathbf{K}$ is the stiffness-matrix and $\mathcal{F}$ is the sum of exterior forces applied to the system. Three models were used for simulating solid dynamics:

1. A spring-mass system: A one-dimensional spring-mass system is described by

$$m\ddot{x} = \Delta P - k\,(x - x_0)\,, \tag{2.10}$$

where x_0 is the equilibrium position of the spring, k the stiffness of the spring and $\Delta P = P - P_{ref}$ the pressure differential applied to the mass *per* unit area.

If we define the force to be $F = \Delta P + kx_0$, then equation (2.10) may be recast in the familiar form of a forced harmonic oscillator

$$\ddot{x} + \omega_0^2\, x = \frac{F}{m}\,, \tag{2.11}$$

where $\omega_0^2 = k/m$ is the natural frequency of the harmonic oscillator.

2. The Euler-Bernoulli beam: Considering a linear elastic, isotropic and homogeneous material sustaining infinitesimal strains, displacements and rotations, and no shear deformation (pure bending), the governing equation for the transverse motion of a beam is given by

$$\frac{\partial^2}{\partial x^2}\left(EI\,\frac{\partial^2 y}{\partial x^2}\right) + \rho A\,\frac{\partial^2 y}{\partial t^2} = q(x,t)\,. \tag{2.12}$$

It is possible to construct the various matrices of equation (2.9) by means of elementary displacements [131].

3. Adlib: A Lagrangian finite-element approach to solid dynamics which is described in Section 2.4.

All of these models require time integration of coupled equations with the characteristics of spring-mass-damper systems. A first-order (Euler) time integration scheme for the spring-mass-damper system is unstable and produces an exponentially growing error with time. A thorough analysis of various schemes (including second and fourth order Runge-Kutta, a third order TVD variant Runge-Kutta and Newmark) was performed for the spring-mass system and higher order integrators were implemented. High–order schemes result in an error that grows linearly with time; however, the growth rate is sufficiently small so that the solution is usable for the time of interest in the simulation.

2.2.3 Framework for Fluid-Solid Coupling

The fluid solver and the solid solver coupling shown in Figure 2.2 serves to establish the boundary conditions for each solver. It is therefore important to first consider the type of boundary conditions required by each solver and the information that is available from each solver at the boundary.

Foremost, the fluid solver requires the location of the boundary to establish the boundary conditions. Since, by construction, the solid solver has a clearly defined boundary, we choose to use it as the fluid-solver boundary.

For an impermeable boundary, there shall not be any mass transfer across the boundary. This means that the normal component of velocity at the boundary must be equal to the boundary normal velocity.

In an inviscid flow calculation, appropriate to the Euler model we use, the velocity is arbitrary for the flow tangential to the boundary. This is usually referred to as a "slip" boundary condition in contrast to the "no-slip" condition applied in viscous flow.

In addition to conditions on the velocity, additional conditions are needed on two thermodynamic variables in order to completely specify the boundary conditions. The choice and the conditions on the variables are not unique. The only requirements are that there are no mass or energy fluxes through the boundary. Several choices for these boundary conditions are presented below.

A Lagrangian-type solid solver requires information at the boundary information on either the forces or the displacements. Our formulation uses the force calculated from the pressure in the fluid and applied normally to the boundary. Depending on the solid model, this force may have to be interpolated onto the Lagrangian mesh.

Level set Method

We use a level set function in order to specify the boundary of the fluid domain as discussed in [28]. The original formulation used a signed distance function φ that was advected with the fluid velocity

$$\varphi_t + V \cdot \nabla\varphi = 0\,. \tag{2.13}$$

This requires the additional implementation of a numerical algorithm in order to convect φ. This is the logical approach to take when working with an interface between two fluids, neither of which has a natural boundary representation.

In our case, we already have a boundary in the form of the representation of the boundary elements of the finite element data structure used by the Lagrangian solid. This boundary is evolved as part of the solution to the Lagrangian mechanics. If we use a separate evolution equation for the distance function based on the fluid velocity at the boundary, then the two specifications of the boundary will differ at the end of the time step and will have to be reconciled. In order to avoid that, we simply construct the level set function anew at each time step of the algorithm. This is done by determining the distance of each point in the Eulerian domain to the closest point on the boundary. The sign of the distance function is determined by the winding number based on the number of crossings of the boundary from the current point to a known reference location. Once the raw distance function is formed by the closest-point algorithm, a smoothing operation is performed so that derivatives can be obtained by finite differences. The smooth level set is obtained by numerical solution of the following equation

$$\varphi_t + \mathrm{sign}(\varphi_0)\left(\sqrt{\varphi_{\mathrm{x}}^2 + \varphi_{\mathrm{y}}^2} - 1\right) = 0 \tag{2.14}$$

Coupling and Boundary Conditions

Implementation of boundary conditions in finite volume or finite difference methods relies on the construction of so-called ghost cells. Ghost cells lie outside the physical boundary and the value of the solution vector within the ghost cells is chosen so that the boundary conditions are enforced when the numerical flux is computed across a cell-interface. Three methods for doing this are discussed later.

In the case of a fixed (rigid, non-moving) boundary, it is simple to identify the ghost cell region. In the case of a moving boundary, the location of the boundary is provided by the level set function. As mentioned above, the level set function is a signed distance function, *i.e.*, the sign of φ determines whether the computational cell is in the real-fluid region ($\varphi < 0$) or in the ghost-fluid region ($0 \leq \varphi \leq \varphi_S$). The value of φ_S depends on the stencil of the numerical scheme used to model the fluxes. For example, a third-order accurate ENO scheme requires six nodes for computing the flux. The flux computed at the boundary interface thus requires three nodes in the real-fluid region and three nodes in the ghost-fluid region. Therefore, the extent of the ghost-region should be at least $\varphi_S = 3\Delta x$. In practice, we increase this buffer area to $\varphi_S = 5\Delta x$ to avoid possible problems at corners.

Having defined the ghost region, we now need to "populate" the ghost cells. This is achieved by a combination of extrapolating information from the real fluid region and substituting values obtained from the boundary region of the solid. The advected quantities will depend upon the type of boundary conditions we wish to implement.

In order to extrapolate information from the real fluid to the ghost cells, a mock advection process is used. Advection or extrapolation of the property I is achieved by marching in time the eikonal equation

$$I_t + \mathbf{n} \cdot \nabla I = 0, \tag{2.15}$$

where the normal vector to the level set isocontours is defined by

$$\mathbf{n} = (\varphi_x, \varphi_y) / \|\nabla \varphi\|. \tag{2.16}$$

The numerical discretization of (2.15) relies on a simple upwind space discretization and a first-order accurate time integration. The pseudo-time t at the end of the integration is made large enough to populate the ghost-region completely. In the following, advected/extrapolated quantities will be indexed with the letter E, *e.g.* $\mathbf{V}_E$ is the velocity vector advected in the ghost-region, while actual variables in the ghost-region will be indexed with the letter G (note that $\mathbf{V}_G$ is not necessarily equal to $\mathbf{V}_E$).

Modified Ghost-Fluid Method

In the original ghost-fluid technique, variables were divided into two categories, those that were continuous across the interface and those that were discontinuous. Continuous quantities are the normal component of the velocity and the

normal component of the traction force, i.e., the pressure. In our case, on one side of the interface, the traction is represented by the pressure of the fluid in the normal direction, while on the other side, the traction vector is the normal component of the stress at the solid surface. Discontinuous quantities are the tangential component of the velocity and thermodynamic properties such as entropy or density. These conditions are fairly general and only rely on the notion of a continuum and the conservation relations applied at an interface [116].

The original ghost-fluid approach involves the extrapolation of the continuous variables across the interface and then applied a correction or substitution based on the value of variables in the adjacent fluid at the ghost location in order to properly treat the discontinuous variables. In our implementation, a similar process is performed but we use information from the solid boundary in order to construct the appropriate values of the discontinuous variables. The velocity and density are advected into the ghost fluid region. The velocity is then modified with the boundary velocity to enforce the slip and no-penetration boundary conditions. The fluid pressure is then replaced by the normal component of the solid traction force at the closest point on the boundary.

In summary, this procedure results in a solution vector within the ghost region defined by

$$\begin{pmatrix} \rho \\ \mathbf{V} \\ P \end{pmatrix}_G = \begin{pmatrix} \rho_E \\ \mathbf{V}_E + (\mathbf{V}_w \cdot \mathbf{n} - \mathbf{V}_E \cdot \mathbf{n})\ \mathbf{n} \\ P_S \end{pmatrix}, \tag{2.17}$$

where P_S is the pressure on the solid boundary and $\mathbf{V}_w \cdot \mathbf{n}$ is the normal component of the solid boundary velocity.

Reflective Boundary Conditions

The standard approach for stationary rigid boundaries is to employ reflective or mirror BCs. This approach automatically enforces zero mass and energy flux across an interface. Operationally this is carried out by enforcing symmetry in the density and pressure profiles across the interface and anti-symmetry in the normal component of the velocity.

This idea can be extended to the case of a moving wall by modifying the velocity in the ghost fluid so that the slip and no-penetration boundary conditions are satisfied. A low-order approximation of strict mirroring is to simply advect the density and pressure from the real–fluid to the ghost–fluid region. The mirrored velocity is then corrected with the appropriate projections of the wall velocity. This results in a ghost fluid solution vector of

$$\begin{pmatrix} \rho \\ \mathbf{V} \\ P \end{pmatrix}_G = \begin{pmatrix} \rho_E \\ (2\,\mathbf{V}_w \cdot \mathbf{n} - \mathbf{V}_E \cdot \mathbf{n})\ \mathbf{n} + (\mathbf{V}_E \cdot \mathbf{t})\ \mathbf{t} \\ P_E \end{pmatrix}, \tag{2.18}$$

The pressure may be advantageously replaced in the formula above by the internal energy; the equation of state is then used to determine the pressure.

Inverse Riemann Problem

In general, an interface with arbitrary states on each side will evolve by producing a set of waves in each material on either side of the interface. This situation is similar to that of solving the Riemann problem for arbitrary adjacent states in a single fluid. Solutions to the Riemann problem in a single fluid predict the resulting fluid motion and fluxes of the conserved variables. A similar approach could be followed at an interface between a fluid and solid in motion. Given the equations of motion and state, simultaneous solution of the Riemann problem in each material will predict the change of velocity and pressure at the boundary.

This problem can now be inverted so that if the boundary motion is specified, a fictitious set of conditions (the ghost–fluid values) can be determined that are consistent with the given boundary motion. This is of particular interest if the interface is accelerating since we know that accelerations are created by pressure gradients in a material. So far, we have not used any information about accelerations in constructing our boundary conditions.

A first approach is simply to account for the effect of the boundary acceleration on the spatial distribution of pressure in the ghost fluid region. Consider the momentum equation in the fluid next to the interface

$$P_x(x_w(t),t) = -\rho(x_w(t),t) \quad \frac{du_w}{dt}(t) = -\rho(x_w(t),t)\,\ddot{x}_w(t), \tag{2.19}$$

where $\ddot{x}_w(t)$ represents the acceleration of the interface.

As depicted in Figure 2.3, the interface may not lie exactly at a cell interface. Assume for simplicity that the interface is located at a cell interface and perform a simple one-dimensional discretization of equation (2.19). This yields

$$P_G = P_R - \rho_w\,\ddot{x}_w\,\Delta x, \tag{2.20}$$

where the density ρ_w is assumed constant across the interface ($\rho_w = \rho_R = \rho_G$). A better approximation consists of using a Taylor expansion of the solution around its value at the interface and accounting for the "exact" location of the interface. The merits of various methods of determining the ghost–fluid values are still under investigation. The complexity of higher-order boundary conditions must be balanced against the recognition that the basic method is intrinsically low-order in locating the boundary.

2.2.4 One-Dimensional Tests

The ghost–fluid method was implemented in several research codes to examine the ability to handle different types of fluid-solid coupling situations. The solid was simulated by a spring-mass system and as a continuum hydrodynamic material (no strength). The spring-mass system was useful for quickly exploring concepts but suffers from the problem of how to define pressure in an incompressible solid. Results from these simulations are not shown here.

In order to examine coupling between Eulerian and Lagrangian methods, a one-dimensional finite-element (Lagrangian) gas dynamics solver with artificial

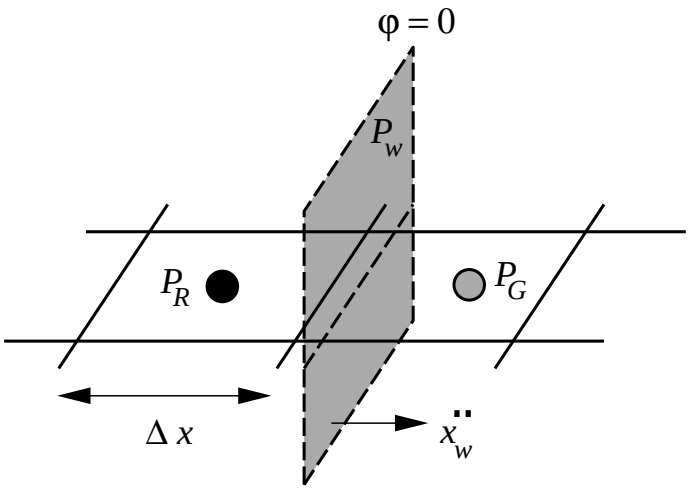

Figure 2.3: Schematic of accelerating interface and ghost nodes.

viscosity [124] was developed. The Lagrangian solver is coupled with the ghost-fluid method to an Eulerian gas dynamics solver. Various test problems are currently being examined with this tool. One class of problems is the transmission of a shock wave through an interface between two solution methods but with identical fluid properties in each domain. We refer to this as the *transparency* test.

An example of the results of one test are given in this section. A Mach number 1.5 shock propagates from left to right in a perfect gas. On the left-hand side of the interface, the Eulerian solver is employed, and on the right-hand side the Lagrangian solver is used. The vertical line at $x = 0.7$ is the initial position of the interface. An ENO solver (implemented in POOMA, to be described in a later section) is used for the Eulerian domain (Fig 2.4). The discrete points are the results from the simulations, where the solid line is the analytical shock profile. Figure 2.5 shows the same simulation at a later time after the shock wave passes through the Eulerian-Lagrangian interface. Note the thicker shock wave profile in the Lagrangian domain and the existence of a slight reflected wave propagating back into the Eulerian domain. The motion of the interface and the strength of the artifact waves is currently under examination.

2.2.5 Two-Dimensional Tests

The Euler-Lagrangian coupling algorithm was applied to several types of two-dimensional simulations. In these tests, various modules were used to simulate both fluid (Eulerian) and solid (Lagrangian) mechanics. Three examples are given here. The first two examples use simplified representations of a solid, and the last uses the full sophistication of a complex finite-element package.

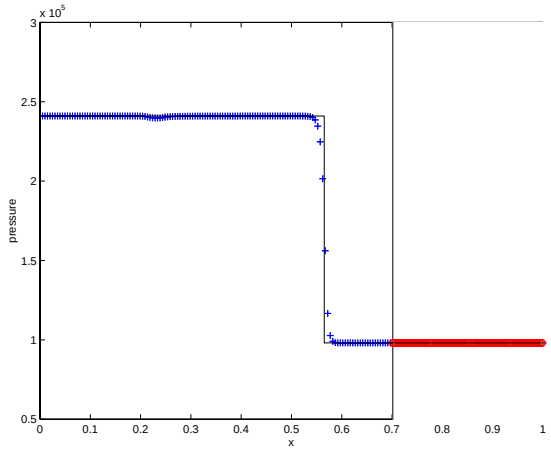

Figure 2.4: Transparency test. Pressure vs. distance prior to shock wave reaching the interface.

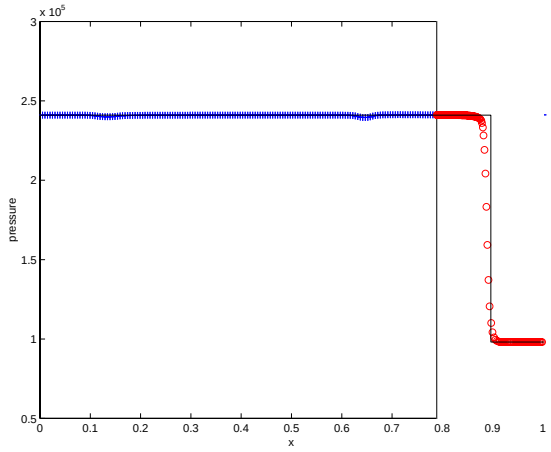

Figure 2.5: Transparency test. Pressure vs. distance after shock wave has passed through the interface.

Mock Solid Mechanics

These examples illustrate an M=3 shock wave in a perfect gas with γ=1.4 propagating between deformable metal plates. The geometry is planar. In the first case, Figure 2.6, the plates are simulated by a set of spring-mass elements with the springs perpendicular to the propagation direction of the shock wave. In the second case, Figure 2.7, the solid is represented by an Euler-Bernoulli beam. In the third case, Figure 2.8, the plates are represented by a full finite-element description (Adlib) with a neo-hookean material model. In all cases,

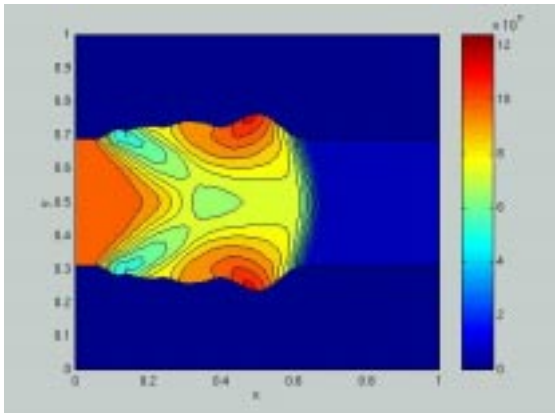

Figure 2.6: Example of two-dimensional simulation of shock wave propagation with deformable boundaries. Contours of pressure shown in fluid region. Fluid solution by ENO-LLF and solid simulation using spring-mass arrays.

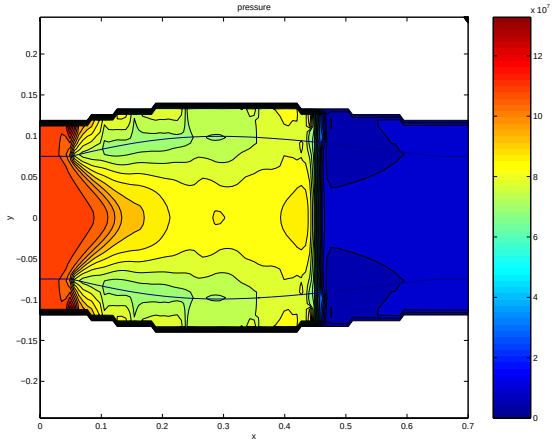

Figure 2.7: Example of two-dimensional simulation of shock wave propagation with deformable boundaries. Contours of pressure shown in fluid region. Fluid solution by ENO-LLF and solid simulation using Euler-Bernoulli Beam Elements

the Eulerian solver is based on the ENO-LLF method, the solution technique is second-order in space, and third-order in time.

Integration with Adlib

The culmination of the algorithmic integration efforts in FY99 was a cylinder test simulation performed with the VTF prototype utilizing the reflective boundary condition variation of the ghost–fluid method. The explosive was modeled

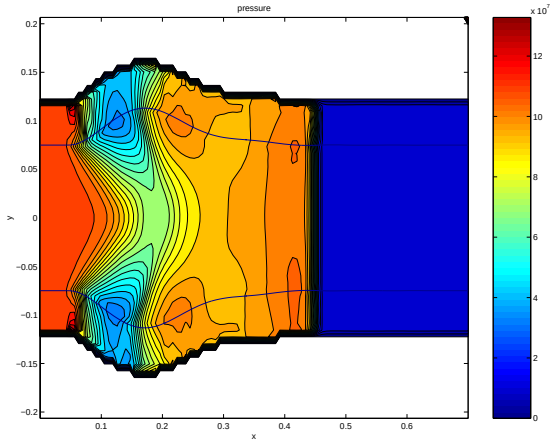

Figure 2.8: Example of two-dimensional simulation of shock wave propagation with deformable boundaries. Contours of pressure shown in fluid and ghost cell region. Fluid solution by ENO-LLF and solid simulation using Adlib (neo-hookean steel)

as HMX with the engineering detonation model described in Section 3.4 and the solution was obtained using an Eulerian simulation in cylindrical geometry. The cylinder deformation was computed using a neo-hookean (nonlinear elastic) model of steel with the Lagrangian-based Adlib package. A snapshot at one point in time is shown in Figure 2.9. The thickness of the steel cylinder was chosen to allow significant deformation.

Although the Eulerian grid is still rather coarse (251×251 grid points), the ZND profile of the detonation wave is clearly visible. Physically correct features of the flow can be observed. For example, note the curvature of the detonation front due to the deformation of the boundary. This curvature and the related reduction of detonation propagation speed is one of the key issues in accurate modeling of detonation waves. A system of stress waves is generated in the steel tube. Since the bulk sound speed in the metal is lower than the CJ velocity, the leading front of these waves forms a characteristic angle with respect to the axis of symmetry; reflections of these waves are visible at the inner and outer walls of the steel cylinder.

2.2.6 POOMA and the VTF

Several implementations of the VTF notion have been carried out in the last year. One novel approach is to use the POOMA environment developed by the Advanced Computing Lab (ACL) at Los Alamos National Laboratory (LANL). The following is an excerpt from the ACL web site.

> POOMA, which stands for Parallel Object-Oriented Methods and Applications, is an object-oriented framework for applications in

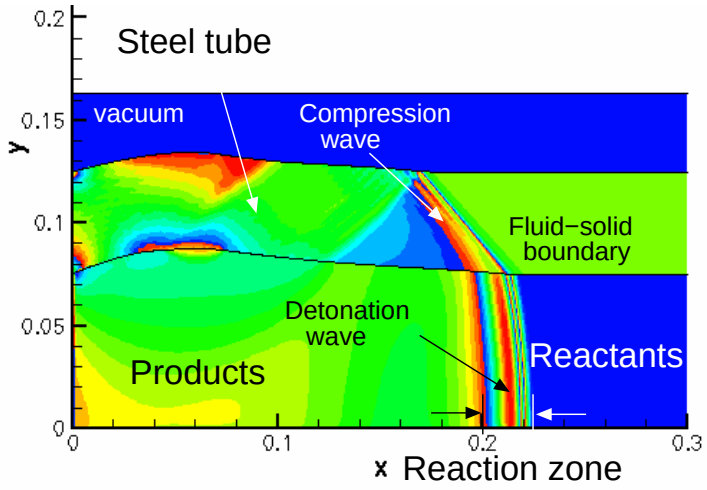

Figure 2.9: Cylinder test simulation with VTF prototype. Explosive modeled using HMX parameters and Eulerian solver. Confining cylinder modeled as neo-hookean steel using Adlib software package. Contours of pressure shown in explosive and one stress component shown in the steel.

computational science requiring high-performance parallel computers. It is a library of C++ classes designed to represent common abstractions in these applications.

An Eulerian solver and moving rigid solids (walls with prescribed motion, spheres and wedges) were implemented using POOMA. A number of test cases have been performed with this system and a few are described below.

Figure 2.10 shows on the left the density contours of a wedge (40°) moving through a stationary ideal gas at supersonic speeds (Mach 2). On the right is a simulation of a Mach 2 shock wave running up an incline (30°). These two cases are simple but nontrivial coupled Eulerian-Lagrangian problems that can be handled easily with our coupling framework.

2.3 Fluid dynamics algorithms

This section describes the parallel CFD engine, named "RM3d" in the VTF. We also briefly describe the parallel implementation of the fluid-solid coupling algorithm. This is followed by results for various test cases. Scalability results are discussed in Section 7.3.

2.3.1 RM3d: Parallel CFD Engine

RM3d solves the Euler equations, written below in strong conservation form, for inviscid compressible flow with a perfect gas equation of state.

$$\mathbf{U}_t + \mathcal{F}_x(\mathbf{U}) + \mathcal{G}_y(\mathbf{U}) + \mathcal{H}_z(\mathbf{U}) = 0 \tag{2.21}$$

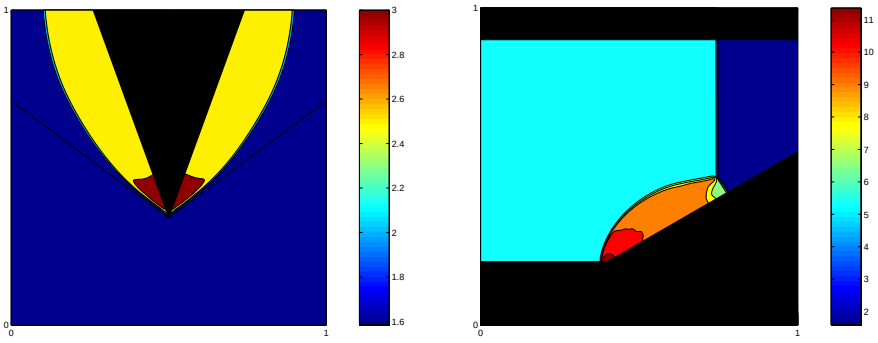

Figure 2.10: Left: Illustration of POOMA implementation of VTF concept. Density contours for supersonic wedge moving through an ideal gas. Right: Illustration of POOMA implementation of VTF concept. Density contours for shock wave propagation up an incline modeled as a stationary rigid body.

$$\mathbf{U} = \{\rho, \rho u, \rho v, \rho w, E, \rho\zeta\}^T \tag{2.22}$$

$$\mathcal{F}(\mathbf{U}) = \{\rho u, \rho u^2 + p, \rho uv, \rho uw, (E+p)u, \rho\zeta u\}^T \tag{2.23}$$

$$\mathcal{G}(\mathbf{U}) = \{\rho v, \rho uv, \rho v^2 + p, \rho vw, (E+p)v, \rho\zeta v\}^T \tag{2.24}$$

$$\mathcal{H}(\mathbf{U}) = \{\rho w, \rho uw, \rho vw, \rho w^2 + p, (E+p)w, \rho\zeta w\}^T \tag{2.25}$$

$$p = (\gamma - 1)(E - \frac{1}{2}\rho\mathbf{u}.\mathbf{u}) \tag{2.26}$$

The code operates in two and three dimensional Cartesian, and axisymmetric geometries. The time stepping is second order Runge-Kutta. The fluxes at the cell interfaces may be calculated either by the Equilibrium Flux Method (EFM) (a kinetic flux vector splitting scheme) [90], or the Godunov or Roe method (a flux difference splitting schemes). Second order accuracy is achieved via linear reconstruction with Van Leer type slope limiting applied to projections in characteristic state space. The code is flexible enough to allow for the advection of multiple species using level-sets (ζ) and a volume-of-fluid approach.

The two dimensional version of this CFD engine has been validated with shock-contact discontinuity experiments of Sturtevant and Haas (Caltech 1985). The two dimensional version of the CFD engine has also been used successfully for Richtmyer-Meshkov instability investigations [102, 104].

2.3.2 Fluid-Solid Coupling

In this subsection we describe the reflective boundary condition algorithm to achieve coupling between the CFD and the solid mechanics solvers. This algorithm is one of those discussed in section 2.2. We note that there are other alternatives for achieving the proper interfacial boundary conditions. Results to date indicate that the reflective boundary condition produces correct results for solid-fluid coupling.

The underlying assumption in the development of the algorithm is that the

coupling is *explicit*. The two solvers exchange information at the beginning of every time step. The genesis of this algorithm was in the ghost fluid method (GFM) [100]. The underlying idea of this coupling algorithm is that the zero mass flux boundary condition for the Euler equations at the interface between the fluid and the solid be strictly enforced. Consider Figure 2.11 which schematically depicts the reflecting boundary conditions at a solid. The Solution of the Riemann Problem at the interface gives zero contact velocity which in turn implies zero mass flux. The present work generalizes this idea of a ghost cell from standard Eulerian shock-capturing methods to an arbitrary solid boundary which may move with a prescribed velocity or in response to the fluid pressure forces (e.g. see Figure 2.12). The Eulerian domain Ω is decomposed as follows

$$\begin{aligned} \Omega &= \{\Omega_{nm} | n = 1 \cdots N, m = 1 \cdots M\} \\ \Omega_{nm} &= \{[x_{i,j}, x_{i+1,j}] \times [y_{i,j}, y_{i,j+1}]|, \quad i = 1 \cdots I_n, j = 1 \cdots J_m\} \end{aligned}$$

At the end of every time step, nearest neighbor communication is applied.

The Lagrangian boundary $\delta\Omega$ between the solid and the fluid is broadcast to all processors

$$\delta\Omega = \{C_p | p = 1 \cdots P\}, \quad C_p = \{[\bar{x}_{p,q}(t), \bar{x}_{p,q+1}(t)], q = 1 \cdots Q\} \tag{2.27}$$

Pressure and velocity at the Lagrangian boundary are defined as:

$$\bar{V}_s(\bar{x}_{p,q}(t)), \quad p_s(\bar{x}_{p,q}(t)) \tag{2.28}$$

A signed distance level-set function is defined as follows.

$$\begin{aligned} \phi(\bar{x}_{i,j}, t) &= C_s \quad \min[d(\bar{x}_{i,j}, \bar{x}_{p,q}), \quad p = 1 \cdots P, q = 1 \cdots Q] \\ C_s &= +1 \quad (Solid) \quad C_s = -1 \quad (Fluid) \end{aligned}$$

where C_s is determined by a parity rule and a fast recursive algorithm. The level set $\phi(\bar{x}_{i,j}, t) = 0$ defines $\delta\Omega$. Once the signed distance function has been calculated, we extrapolate two thermodynamic variables ($\psi \equiv (p, \rho)$) by advection in pseudo-time.

$$\psi_\tau + \hat{n} \cdot \nabla\psi = 0, \quad \hat{n}(\bar{x}_{i,j}, t) = \frac{\nabla\phi}{|\nabla\phi|} \tag{2.29}$$

where the advection velocity is $\hat{n}(\bar{x}_{i,j}, t)$, the normal to ϕ. Note that this advection equations is solved only where $\phi(\bar{x}_{i,j}, t) > 0$ so as to populate the ghost cells with extrapolated values of pressure and density. It is clear that nearest neighbor communication is required at the end of each pseudo-time step in the above extrapolation by advection.

We then follow the same extrapolation procedure for the velocity which is then reconstructed to reflect normal velocity component in a local frame attached to $\delta\Omega$. We choose $\psi \equiv (\bar{u}.\hat{i}, \bar{u}.\hat{j})$ and solve

$$\begin{aligned} \psi_\tau + \hat{n} \cdot \nabla\psi &= 0 \\ \bar{u}(\bar{x}_{i,j}, t) &= (-\bar{u}.\hat{n} + 2\bar{V}_s.\hat{n}, \bar{u}.\hat{s}) \end{aligned} \tag{2.30}$$

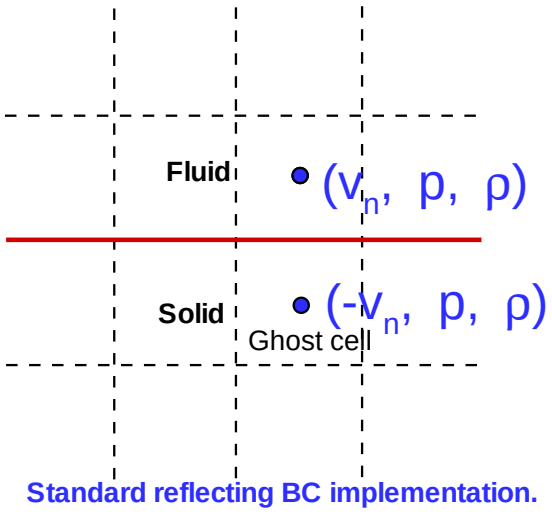

Figure 2.11: Schematic illustrating the use of reflecting boundary conditions at stationary walls.

where $\phi(\bar{x}_{i,j}, t) > 0$.

The final step is the bilinear interpolation of pressure $p(\bar{x}_{i,j}, t)$ to obtain the pressure $p_s(\bar{x}_{p,q}(t))$ on the Lagrangian boundary. This step, also involves communication between processors. Note that continuity of normal stress is thus satisfied by imposition.

Finally, we remark that the present code is implemented using Fortran 90 and uses MPI. It has Python bindings for ease of scripting. Wherever possible non-blocking communications, (MPI_IRECV, MPI_ISEND) were used. The code is implemented on a variety of platforms including SGI Workstations, SGI Origin 2000, Cray T3E, Intel Paragon and Intel PC's running Linux.

2.3.3 Results

In this subsection we examine a number of flows in order to verify and validate the use of our level set based approach to simulating flow with complex boundaries.

Validation Test: Static Rigid Solid

We begin by considering steady supersonic ($M_\infty = 2$) flow over a sphere. The steady solution to this is a bow shock in front of the sphere. We plot density contours in Figure 2.13 (left) and the centerline pressure in Figure 2.13 (right). The arrow indicates the experimental shock stand-off distance [1]. We note excellent agreement with the experimental results.

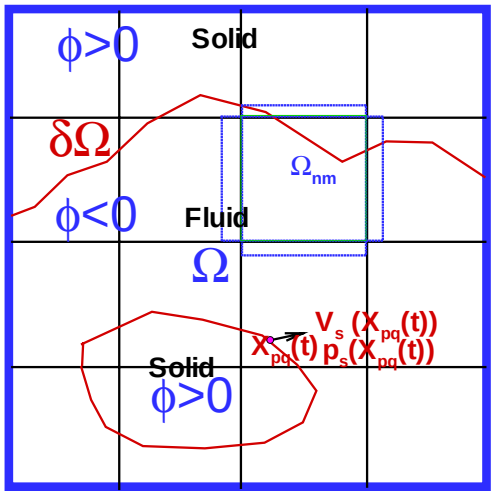

Figure 2.12: Schematic indicating the nature of the data distribution for the fluid-solid coupling. The blue denotes Eulerian data and is Blue distributed among all processors. The red is the Lagrangian data which is replicated and resides on all processors

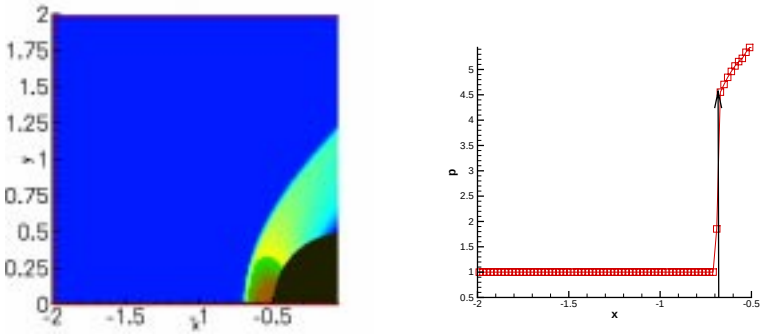

Figure 2.13: Validation of the Ghost Fluid Method. On the left is a plot of the density field for the steady supersonic flow over a sphere. On the right is a plot of the pressure along the center line. The arrow represents the experimental value of the shock standoff distance for this flow

Moving Piston Test

Another test flow for which an analytical solution is available in one dimension is the impulsively started piston. We measured the jump conditions across the

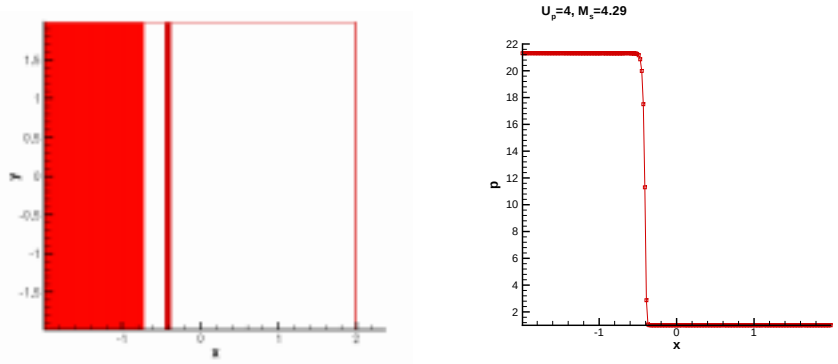

Figure 2.14: Verification test of the GFM. Shown on the left is a contour plot of the density field for an impulsively started piston. Shown on the right is the pressure for this solution. Overlaid on top of the computed pressure field (points) is the analytical pressure (solid). Note the excellent agreement.

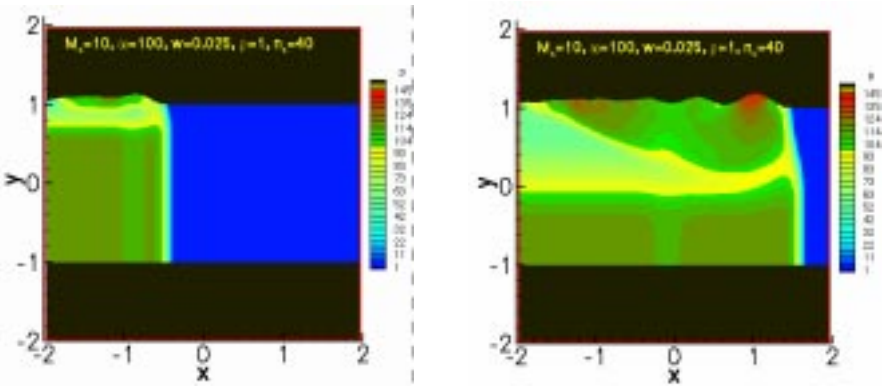

Figure 2.15: Pressure contours at two different times for a shock moving in a shock-tube whose top wall is composed of spring-masses.

shock which develops and found that these match the analytical result exactly. The results are displayed in Figure 2.14

Spring-Mass Pseudo-Solid Model

In this verification test the domain is a rectangular shock tube with the top wall of the shock tube modeled as a spring-mass system. A shock is initialized using Rankine-Hugoniot jump conditions and moves from left to right. In Figure 2.15, we see that the pressure loading behind the shock leads to damped oscillations of the springs. For an impulsive pressure loading on the springs one can derive

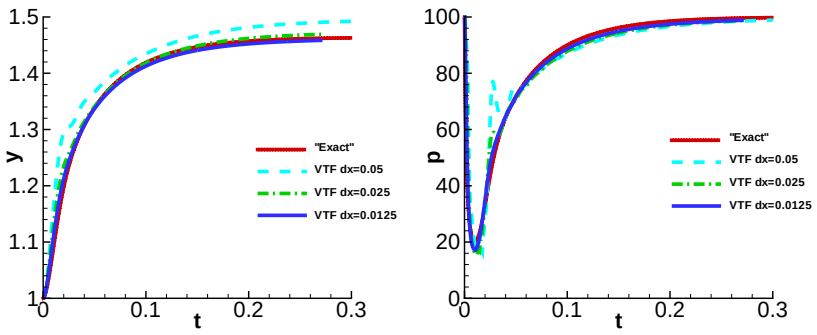

Figure 2.16: Comparison of impulsively loaded springs at different resolutions. The "exact" solution is obtained from solving the ODE.

an ordinary differential equation written below.

$$\ddot{y} + \omega^2 y \quad = \quad \frac{p_0 A \rho}{w \rho_0} \left(1 - \frac{\gamma - 1}{2} \frac{\dot{y}}{c_0} \right)^{\frac{2\gamma}{\gamma - 1}} \tag{2.31}$$

We solve this ODE "exactly" using a fourth order RK scheme and compare the results obtained at different resolutions from the VTF. In Figure 2.16 we observe that as the resolution increases the VTF solution converges to the solution of the ODE.

Verification Test: Euler-Bernoulli Beam Model

The physical problem solved is the same as that of a shock moving from left to right in a shock tube whose walls are now modeled using Euler-Bernoulli beam elements. The beam solver was provided by Patrick Hung. Because the signal speed is infinite in the beams, we observe a deflection of the beams ahead of the shock (see Figure 2.17). In Figure 2.18, we observe that the interface position between the fluid and the beam elements appears to converge as we refine the mesh.

In this test case, we also compare the solution obtained by using the Godunov method with an ENO solver (provided by M. Arienti) In a point-wise comparison, pressure contours from both solvers, presented in Figure 2.19, show good agreement.

Coupling with Lagrangian Solid Dynamics

In this section, we present results where the coupling is between the fluid solver and the finite element solid dynamics solver. The solid dynamics solver was provided by in the form of a library called Adlib by R. Radovitzky.

The test case investigated is that of a shock moving down a cylindrical shell and capped on one end by two test materials, and is depicted schematically in Figure 2.20. Two test cases, one with a relatively weak shock and one with a

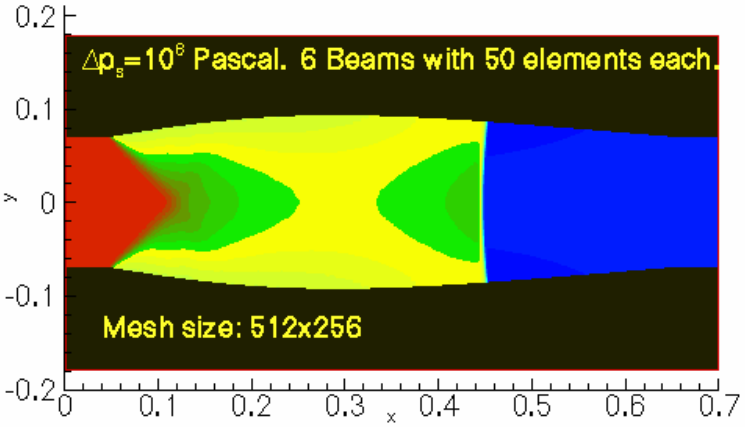

Figure 2.17: Pressure contours in a shocktube with walls composed of Euler-Bernoulli beam elements. The shock is moving from left to right.

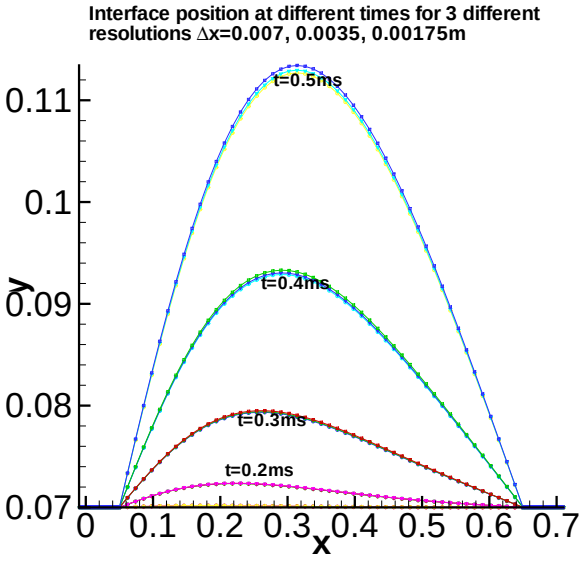

Figure 2.18: Convergence test of the interface position at various VTF resolutions. The solid is modeled by Euler-Bernoulli beam elements.

relatively strong shock are shown in Figures 2.21 and 2.22, respectively. In the weak shock case, observe that the test materials are stressed before the arrival of the incident shock due to the fact that the sound speed in the shell is larger than the incident shock. In the strong shock, case the transmitted shock now

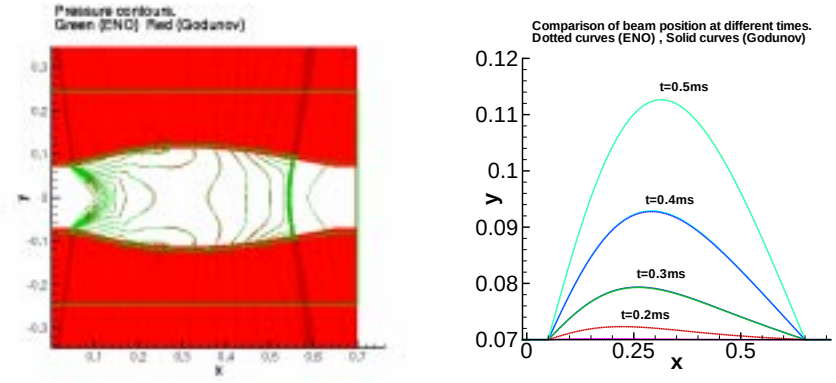

Figure 2.19: Left: Point wise comparison between the Godunov and the ENO method. Right: Comparison of the interface position at different times between the Godunov and ENO solvers.

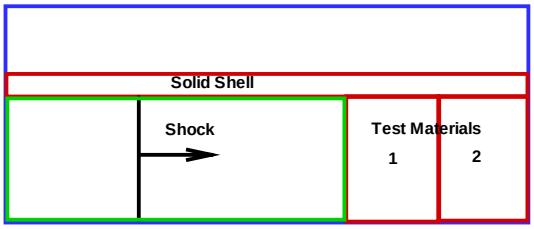

Figure 2.20: Schematic of the test case where the coupling is between the Eulerian fluid dynamics and the Lagrangian solid dynamics.

lags behind the incident shock. In this case, finite large deformations of the cylindrical shell are observed. Figure 2.23 is included to give the reader a flavor of the meshes and the coupling, and other features in the VTF.

2.3.4 Issues

In the present version of the VTF, we have not included acceleration effects in the fluid-solid coupling. It is clear that more validation and benchmark calculations are desirable. We have addressed the issue of convergence with respect to mesh refinement for a few gross quantities such as the interface position.

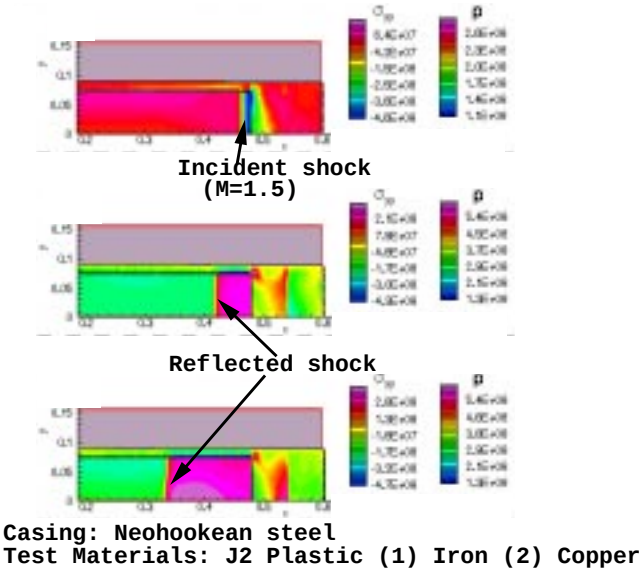

Figure 2.21: A relatively weak shock moving down a cylindrical tube. The tube is modeled using Lagrangian solid dynamics while the fluid inside is modeled by an Eulerian method.

However, it is known from previous work [103] that point-wise convergence may be an issue.

2.4 Solid Mechanics algorithms

In this section we describe the capabilities of the solid mechanics engine used to perform the integrated simulations.

During this fiscal year, the Center has directed a significant amount of effort towards the development and implementation of a method for the analysis and simulation of high-speed flows interacting with solids which undergo large dynamic deformations. The novel approach proposed originates in the level set method [108] and the ghost fluid method [29], and furnishes, in effect, a general method to couple grid-based Eulerian solvers with unstructured-mesh Lagrangian finite element solvers, Figure 2.24. The method is shown to be equally suitable for finite-difference and finite-volume based fluid solvers. It represents the gluing ingredient that enables the Center's Eulerian-Lagrangian Integrated Simulation Capability.

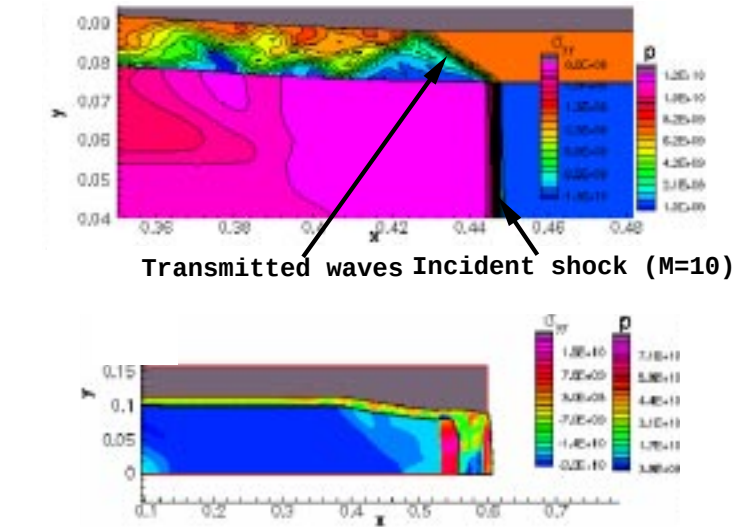

Figure 2.22: A relatively strong shock moving down a cylindrical tube.

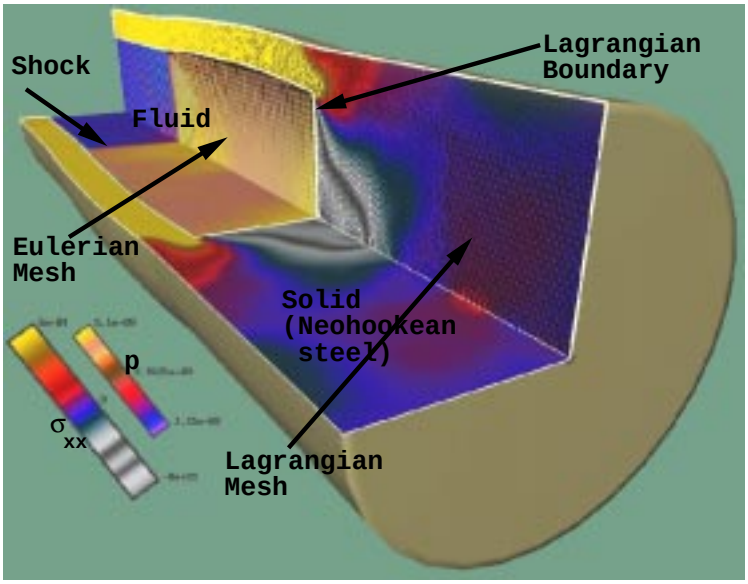

Figure 2.23: An example showing all the features of the VTF.

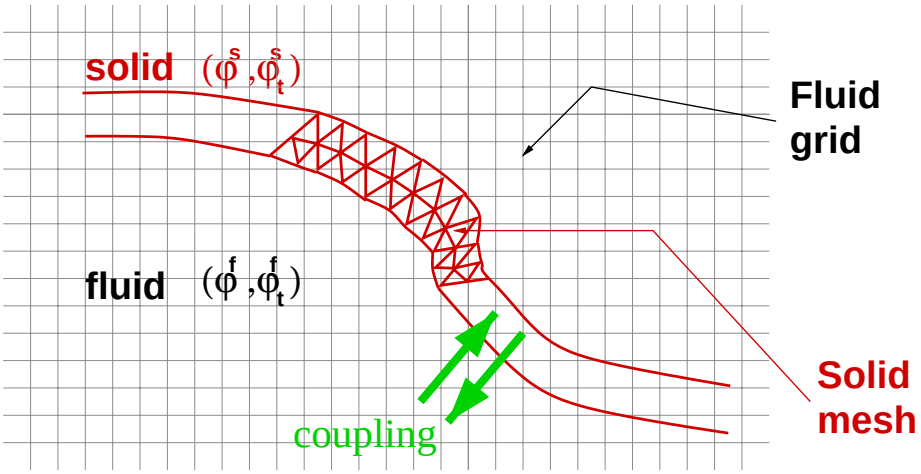

Figure 2.24: Schematic of fluid-solid coupling problem

At a high level of description, Figure 2.25, the method consists in an exchange of momentum and energy between the solid and the fluid and an enforcement of their kinematic compatibility, both of which are done at the beginning of the time step. This is accompanied by the negotiation of a common stable time step and a subsequent time integration step which occurs independently for the fluid and the solid.

The geometrical location of the boundary between the solid and the fluid, which is dictated by the Lagrangian finite element mesh boundary, is used to construct the level set function, which in turn is informed to the Eulerian solver grid. The Eulerian fluid solver uses the level set to define the fluid boundary and treats the exterior cells as "ghost". The particular way in which the fluid solver treats the "ghost cells" and incorporates the feedback from the solid in order to satisfy the relevant governing equations (kinematic compatibility, balance of momentum and energy) is explained in Section 2.2.

The transfer of momentum from the fluid to the solid is accomplished *via* a consistent integration of the fluid pressure as traction boundary conditions on the Lagrangian finite element mesh, Figure 2.26.

Special emphasis has been given to the implementation of a software interface in the Center's Lagrangian engine, *Adlib*, which endow the code with the proposed capability to interact with a generic Eulerian solver. The implementation takes advantage of the engine's built-in Boundary Representation of Solids by exploiting its topological information for the purposes of defining solid-fluid boundaries. This approach, in turn, renders the extension to three dimensions straightforward. The software interface consists of:

- a set of data structures which stores the fluid-solid boundaries.

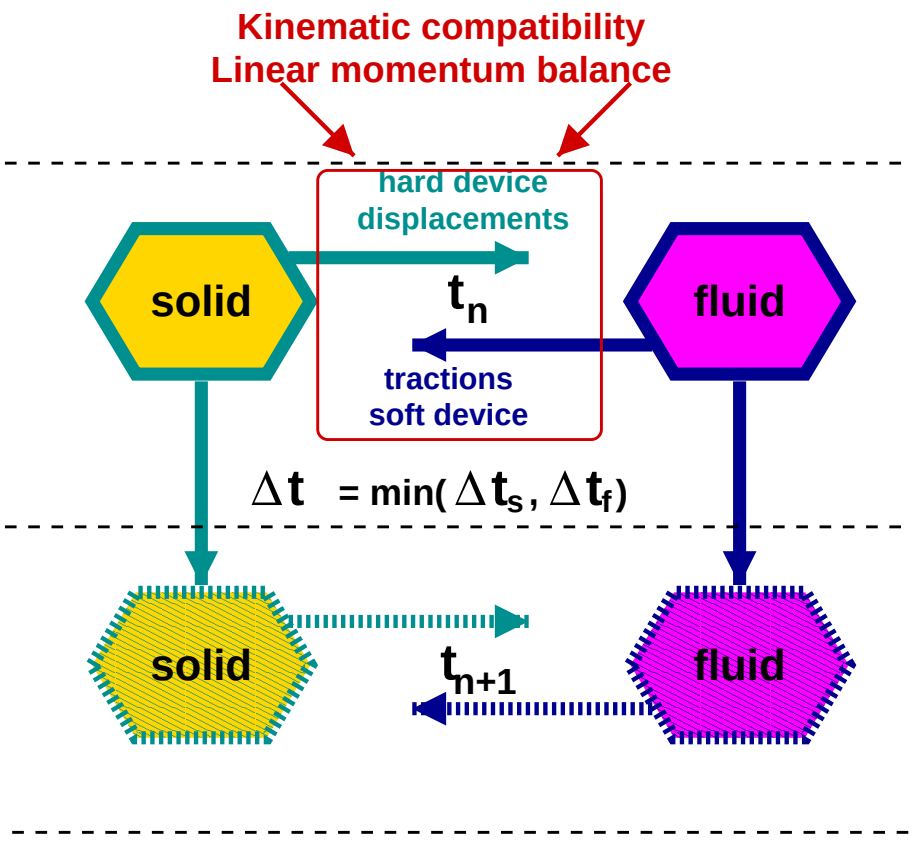

Figure 2.25: High level description of fluid-solid coupling approach

- a set of methods which provide the requisite functionality to:
  - define the problem boundaries.
  - exchange mechanical fields with the Eulerian solver.
  - dynamically evolve the boundary information.

The specific methods that need to be implemented for the proposed fluid-solid coupling algorithm are:

- initialization and set up of the fluid-solid boundaries from *Adlib*'s BRep.
- computation of the fluid-solid boundary location for the computation of the level set on the Eulerian grid points.
- computation of the pressure exerted by the fluid on the solid boundary for subsequent application of traction boundary conditions on solid. This is obtained from the Eulerian grid, Section 2.2.

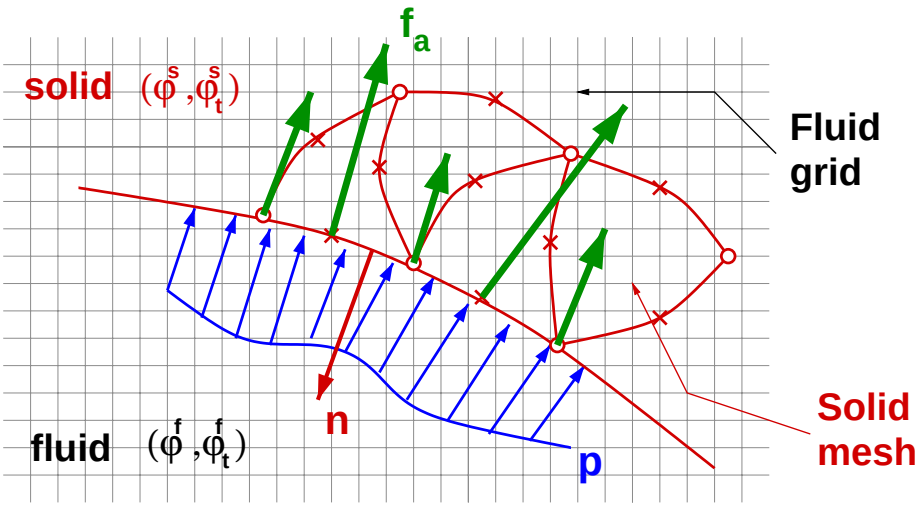

Figure 2.26: Application of fluid pressures as consistent traction boundary conditions on solid

- application of traction boundary conditions on solid from fluid pressure computed in previous item.
- computation of solid mechanical fields at solid boundary for subsequent application to the fluid.
- application of solid mechanical fields to fluid.
- boundary evolution update.

It bears emphasis that the implemented software interface has been used seamlessly for two different Eulerian codes, one based on finite differences and another one based on finite volumes.

Figure 2.27 illustrates the robustness and versatility of the proposed approach under the challenging conditions that correspond to an initially planar strong shock wave originated in a gas and which propagates through a highly-deformable tube that contains a test material at the end. The tube wall incurs large deformations as the shock front passes. When the shock front reaches the test material a wave is transmitted inside the solid and another one is reflected inside the fluid, significantly raising the fluid pressure, which in turn causes bulging of the tube walls.

The implementation has been integrated in the Problem Solving Environment, Section 2.5.

2.5 Software integration

In the previous sections we discussed the status of the computational engines that provide the building blocks for the overarching application. In this section we discuss the status of the integrated environment in which the users of the overarching application can specify parameters of a simulation and launch it.

2.5.1 The architecture of the VTF

One of the challenges in the construction of the overarching application is providing the user with a flexible way to interact with the diverse computational modules and facilities that are going to be available as part of the VTF.

Developers of sizeable applications have been faced with similar challenges for many years. As a result, a few architectural solutions have emerged as viable. One such solution is the construction of an interpretive environment in which the user interacts with the application by composing scripts that control the behavior of the major components of the application.

In case of the VTF, we chose not to write such an environment from scratch, but to leverage Python, a widely used, well maintained and open source interpretive environment. The user interacts with the Python interpreter's virtual machine by constructing scripts written in the Python language. The Python interpreter has been ported to a wide variety of machines, including massively parallel supercomputers such as those available through the ASCI program. The Python language provides a modern, object oriented programming environment and is well documented and easily extensible.

The resulting integration framework, an overview of which can be found in this section, was demonstrated during the October, 1999 site visit. In our opinion, the construction of a usable, flexible, feature-rich integration framework in less than a year is one of our major successes, and the decision to use Python as the problem solving environment has been the enabling factor in this success.

2.5.2 Pyre

It is our expectation that by the end of the project, our users will have at their disposal a wide variety of solvers, each with its own initialization requirements and set of tunable parameters. This is already the case in a smaller scale for the wide variety of constitutive models for materials that our center is currently capable of simulating. The complexity of this problem is going to increase as our simulation capabilities improve. In addition, the overarching application requirements of good performance when run on thousands of processors imply the need for leveraging of external efforts along these lines, most of which are in various stages of development and are evolving rapidly. Finally, the staging of a complicated simulations such as those performed by our applications will present a multitude of tunable parameters.

As a result, it appears necessary to construct a general purpose simulation framework that addresses all of these concerns in the most robust and reliable way possible. Leveraging Python in the construction of the enabling environ-

ment has been the primary source of success to this day.

At the end of FY1999, Pyre consisted of roughly 10,000 lines of Python and 3,000 lines of C++ in the form of bindings and infrastructure. The estimated size of the code that is being leveraged by the environment, both in the form of computational engines developed locally by Center participants and facilities provided by third parties, exceeds half a million lines of code. The resulting environment in a full featured, object oriented environment that is capable of handling all aspects of the specification and launching of a simulation. Considerable improvements are planned for FY2000, when much of the distributed infrastructure necessary for the successful completion of the overarching application will be integrated.

In order to perform a simulation, a user constructs the various components of the physical model by specifying their geometry. There is a variety of primitive planar and solid objects that are currently supported, as well as a variety of operators from combining them to form more complicated objects. The physical dimensions of the geometrical objects can be specified in any supported system of units and so the specifications are self-documenting. Boundary and initial conditions can be specified by providing a high-level geometrical description of the affected regions of space, e.g. the contact surface between the explosive and the first test material. This insulates the user from the particular representation of that region of space by any particular solver and allows the user transparent access to the underlying data structures. Materials and constitutive models are selected and attached to regions of space in a similar way and finally the user selects the solvers that are responsible for the simulation of the behavior of each component.

Finally, the user has complete control over the structure and implementation of the main simulation loop. A complete specification is available that governs the interaction between the simulation driver and the various engines that guarantees consistency, but the user is free to add arbitrary operations at any part of the time step. Activities such as restarts and visualization can be supported with minimal effort, assuming the corresponding facilities are accessible from the Python interpreter.

2.5.3 Writing parallel applications in Python

The stock distribution of Python interpreter has no native support for parallel programming and in fact can not even start up properly on multiple processors. Similarly, the language does not have any provisions for distributed data structures or message passing. When faced with this situation, one can either forgo expressing the required applications parallelism in Python or modify the interpreter and extend the language.

The first choice, has very unfortunate implications, especially given the fact that our choice of programming model is MPI. For example, launching the application requires that **mpirun** be given an executable binary image to spawn on the required number of processors. Having to interact with such an executable would imply that the user's choices as found in the Python script would

either have to be somehow encoded and passed to the executable or that the Python interpreter would have to be embedded into the executable so that it can re-interpret the processor specific parts of the user scripts. Both of these solutions are cumbersome to implement and hard to maintain.

In principle, the second alternative is also unattractive in spite of the enormous architectural simplifications it affords. One would prefer not to have to modify the source code of the stock distribution of the interpreter as this places the burden of constructing a parallel-enabled version of the interpreter on each target platform and could potentially make the process of upgrading to later versions of the interpreter problematic.

Both of these concerns have been addressed successfully by taking advantage of last year's configuration management effort. The existence of a source repository managed by **cvs** and our portable mechanism for building the center's code on all platforms of interest reduced the complexity of both of these tasks. Furthermore, there was an existing effort to produce an MPI aware version of Python by David Beazly, then at LANL, which has been used successfully by Pat Miller of the Kull group at LLNL to start the Python interpreter on more than 1000 processors.

Unfortunately, the modifications to the Python source that were required for this early attempt to work were somewhat extensive and specific to the version of the interpreter available then. This forced both the LLNL and the Caltech groups to conduct a thorough re-examination of the approach used by David Beazly. As a result of this interaction, an effort has emerged to define the standard Python parallel programming model in collaboration with Guido van Rossum, the author of Python, which will then be incorporated in the standard distribution of the language.

In the meantime, we have constructed a sufficiently capable version of the interpreter so that the development and testing of the overarching application can proceed uninhibited.

2.5.4 Composition and integration of diverse modules

One of the requirements for our problem solving environment is the ability to easily integrate diverse computational engines with minimal effort. This requirements imposes constraints on both the environment and the computational engines.

On the one hand, the environment must be constructed in a way that permits new facilities to be brought on-board without re-compilation or relinking of anything other than code that directly relates to the new computational module. This in turn implies the use of dynamic techniques for linking the code associated with the solvers, a model that is not only supported but is in fact the recommended way of constructing extensions to the Python interpreter.

On the other hand, there are architectural constraints on the solvers. The integration is particularly easy in the case of solvers that are constructed using modular techniques and observing the established guidelines for well designed software. Such solvers require little more than a set of very thin wrappers

that publish the entry points of the solver to Python and orchestrate the data exchange between the solver and the interpreter. These wrappers typically consist of a dozen lines of C and in many cases can be generated automatically from the underlying solver code by a variety of freely available tools.

Furthermore, error handling becomes an important aspect of the solver. The typical error handling practiced by authors of scientific software is exiting with an error message. This is not acceptable in a larger environment. Our problem solving environment ameliorates this by providing the general infrastructure for modular error handling.

In general, the modifications that may be required of computational engines before they can be integrated in the problem solving environment constitute upgrades and significant improvements. The PSE provides infrastructure that solves many of the problematic areas in the construction of scientific software.

2.5.5 Re-using existing solvers

The ease with which the interpreter can be extended has played a crucial role in the success of our integration efforts. For each computational facility that we wish to include in our simulation environment, we have to construct a thin wrapper that exports the entry points of the solver to the environment. A set of Python classes is then constructed to give the solver an object oriented veneer and facilitate its interaction with the rest of the environment. An excellent example of the leveraging of legacy code is the integration of adlib, the solid mechanics engine, into Pyre. For each component of adlib we have constructed a class that manages the initialization and access of the component. As a result, even stand-alone adlib simulation can now be performed in terms of Python scripts that give the user the illusion of an object oriented system with well-defined interaction mechanism and complete data encapsulation.

2.5.6 Incorporating third party facilities

The ability to easily incorporate facilities produced by third parties is another crucial aspect of the simulation environment. The timely delivery of the overarching applications depends on progress, delivery and integration of facilities such as those in development under the Scalable IO initiative and Globus. Furthermore, we currently employ commercial engines and libraries for tasks such as solid modeling and three dimensional visualization.

The extensibility of the Python interpreter is making it possible to integrate such third party facilities with ease. As an example, during the site visit we demonstrated the tight integration of ACIS, a commercial constructive solid geometry engine, which is employed by our PSE to dynamically generate user-specified models of the VTF configuration, visualize them and provide initial coarse surface meshes for our volume mesher.

We have had similar success with our early attempts to integrate rendering engines, such as OpenGL, and even more complicated and powerful visualization systems such as OpenInventor and VTK.

The integration of Globus facilities in our environment will be achieved

through the encapsulation of these facilities in Python classes and the direct use of these classes by the simulation staging scripts. We have completed a preliminary investigation of the Globus facilities necessary for the various aspect of remote staging and remote data access and prototype modules that employ them have been constructed. Globus related milestones for FY2000 have been constructed and are described in detail in the implementation plan for FY2000.

2.6 Future work

In FY200 we will continue to develop the VTF with the objective of performing full 3-D full system simulations. Our goals are outlined below:

- Eulerian CFD solver
  - Development of a parallel 3-D CFD solver with AMR capability utilizing the GrACE class library.
  - Development of a multi-species HE capability using the EOS models under development by the HE group
  - Integration of a full 3-D level set capability using an advanced fast algorithm
- Lagrangian solid mechanics solver
  - A full parallel meshing capability will be developed for the Lagrangian solver adlib using METIS
  - The Lagrangian solver will be able to perform fully scalable parallel mechanics
  - The adlib solver will be upgraded with a full 3-D interface to the level set capability
  - Work will begin on development of a parallel adaptive meshing capability
- Fluid-solid coupling
  - The fluid solid coupling algorithm will utilize a new fast 3-D algorithm to generate the distance function.
  - The fluid-solid coupling algorithm will be fully integrated into the problem solving environment so that it can be scripted.
  - The fluid and solid solvers will run in separate process spaces
  - The coupled approach will be evaluated for scalability on the ASCI platforms.

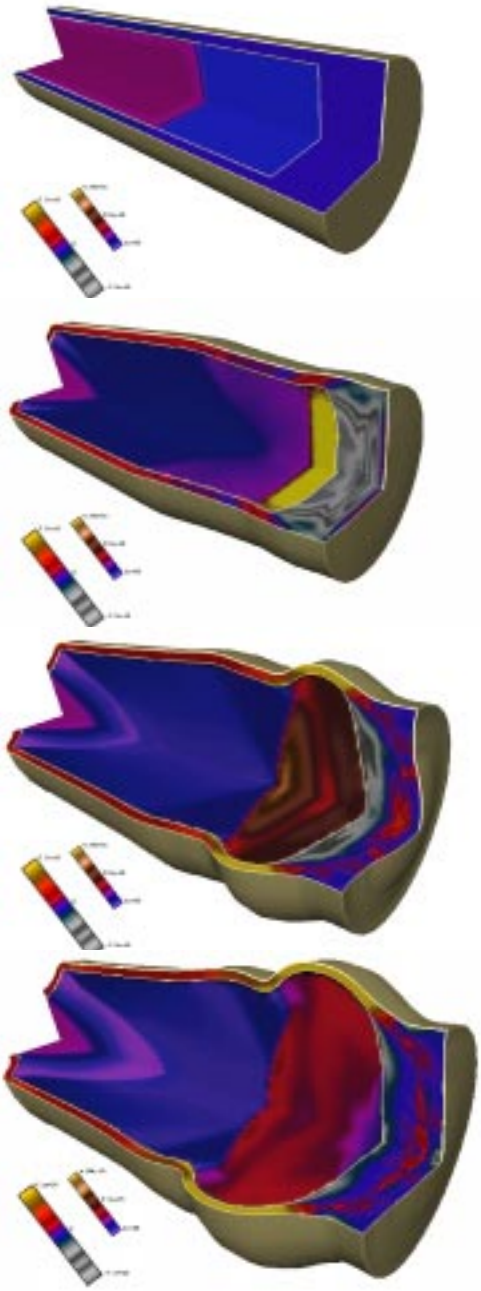

Figure 2.27: Simulation of initially planar strong shock wave propagating through a highly-deformable tube

Chapter 3

High Explosives

3.1 Overview of FY 99 Accomplishments

The principal accomplishments of the HE group in FY99 were in the following areas:

1. Material Properties and Chemical Reactions

   Classical force fields were refined and used to compute equations of state for HMX, Kel-F, estane and PMMA. Quantum mechanical computations were used to determine potential energy surfaces and calculate reaction rate constants for the initial steps in RDX and HMX decomposition. A detailed reaction mechanism for gas-phase combustion of RDX and HMX was assembled.

2. Engineering Models of Explosives

   The JTF model of high explosives was implemented into the Eulerian fluid solver for the VTF. Micromechanics of plastic-bonded granular explosives were investigated by determining the effect of pressure-stiffening on the visco-elastic response of binder layers.

3. Integrated Simulations

   A technique (ghost–fluid method) for coupling Lagrangian and Eulerian solvers was explored. A number of test cases was computed and a prototype for the VTF was developed. Computations were run on detonation and shock wave propagation interacting with deforming boundaries described by a model solid or a full FEM simulation of solid mechanics.

3.2 Personnel

The personnel in the High Explosives effort were drawn from many disciplines and organizations. The participants in FY99 were:

- CIT Material Properties Group (Goddard)
  - S. Dasgupta
  - R. Muller
  - D. Chakraborty
  - G. Caldwell
  - E. Pifarre
- CIT Solid Mechanics (Ortiz)
  - S. Sundaram
  - W. Knauss
  - A. Lew
  - R. Radovitzky
- CIT High Explosives (Shepherd)
  - M. Arienti
  - C. Eckett
  - P. Hung
  - E. Morano
  - R. Samtaney
- LANL
  - J. Cummings
  - P. Tang
- UCLA
  - R. Fedkiw

3.3 Material Properties and Chemical Reactions

The research on material properties is performed by members of the MSC in collaboration with the high explosives researchers. The details of the MSC research activities are given in Chapter 5.

Briefly, the activities were:

1. High Explosive Equation of State

   This work is based on classical molecular dynamics simulations of crystalline high explosives using force fields that are derived from optimized electronic structure computations. The resulting $P(V,T)$ relationships are combined with quantum computations of the specific heat as a function of temperature to predict the thermodynamic properties of high explosives that are needed in order to perform numerical solutions of compressible flow. There properties include the $E(P,V)$ surface and the Grüneisen coefficient.

2. Ab Initio Quantum Mechanics of RDX and HMX Decomposition

   Density functional methods are being used to compute the electronic structure of transition states and product molecules that occur in the decomposition of HMX and RDX molecules. The HONO elimination pathway is found to dominate concerted ring breaking.

3. Reaction Networks for RDX and HMX

   Reaction rate constants were computed for selected decomposition steps using the transition state theory. These reactions and rates were combined with existing reaction mechanisms for nitramine propellants to produce a comprehensive reaction mechanism for nitromethane (NM), RDX and HMX in the gas phase. The NM mechanism was validated against shock tube data available from the literature.

4. Binder Equation of State

   Equations of state of polymeric binders were computed by using classical molecular dynamics with force fields based on extensive quantum mechanical computations. Quantum computations were performed on representative oligomers to obtain charges and optimized force field parameters. An in-house chain packing algorithm was used to generate model amorphous polymer representations. Computations of the cohesive energy density were used to validate the polymer models.

5. Visco–elastic Modeling of Binders

   Molecular dynamics simulations of shear relaxation were used to determine the time dependent shear relaxation modulus for a visco-elastic model of estane.

3.4 Engineering Models of Explosives

Plastic-bonded high explosives usually consist of explosive and a small amount of plastic binder. The explosive is in the form of granulated material which is coated with an elastomer binder and pressed into a cohesive mass. At the level of an engineering model, the details of grains and binder are not resolved and the material is treated as homogeneous. The limiting case is when the binder is omitted completely and granular explosive is directly pressed into a charge. We used parameters from a particular case of this solvent-pressed HMX (HMX_sp) in the discussion below.

3.4.1 Equation Framework

The present model treats the explosive as a hydrodynamic material that can be modeled by the inviscid, reacting flow equations that are often referred to as the Euler equations. These equations are appropriate for modeling the propagation phase of detonations in which the detonation is preceded by a strong shock phase with a pressure level much higher than the elastic limit of the material.

The reacting explosive is treated as a single fluid that consists of a homogeneous mixture of reactants and products. The governing equations are:

$$\begin{aligned} \frac{\partial \rho}{\partial t} + \nabla \cdot (\rho \mathbf{u}) &= 0 \\ \frac{\partial}{\partial t}(\lambda \rho) + \nabla \cdot (\lambda \rho \mathbf{u}) &= \rho R \\ \frac{\partial}{\partial t}(\rho \mathbf{u}) + \nabla \cdot (\rho \mathbf{u}\,\mathbf{u} + \mathbf{I}P) &= 0 \\ \frac{\partial}{\partial t}(\rho E) + \nabla \cdot \left[\rho \mathbf{u}\left(E + \frac{P}{\rho}\right)\right] &= 0 \end{aligned}, \tag{3.1}$$

where ρ is the overall density of the fluid, λ the product mass fraction, R the reaction rate, $\mathbf{u}$ the velocity vector, P the pressure, e the specific internal energy, and $E = e + 1/2\,\|\mathbf{u}\|^2$ the specific total energy. For simplicity, the modifier "specific" is usually omitted when referring to properties such as e as the "energy".

The Euler equations are numerically solved in the conservative form:

$$\mathbf{U}_t + \nabla \cdot \mathbf{F}(\mathbf{U}) = \Omega(\mathbf{U})\,, \tag{3.2}$$

where $\mathbf{U} = (\rho, \lambda\,\rho, \rho\mathbf{u}, \rho E)^T$ is the vector of the conservative variables.

The chemistry is based on a simple one-step irreversible reaction $R \rightarrow P$, where the high explosive is initially composed only of reactants R. For simplicity, we prescribe a pressure-dependent depletion rate:

$$R(\lambda, P) = K\left(\frac{P}{P_{VN}}\right)^5 (1-\lambda)^{1/2}\,, \tag{3.3}$$

where $K = 2$ is a rate multiplier and P_{VN} is the von Neumann pressure.

3.4.2 Mixture Equilibrium Conditions

In order to complete the equation set and perform numerical solutions of the Euler equations, an equation of state (EOS) for a mixture of reactants and products is required. We use the model [48] of Johnson, Tang, and Forest (JTF), which assumes thermal and mechanical equilibrium between products and reactants. This model requires individual equations of state for the reactants and products. We use the Mie-Grüneisen (MG) model for the reactants and the Jones-Wilkins-Lee (JWL) model for the products. The mixture rules for computing energy and volume and the conditions of mechanical and thermal equilibrium are used to determine the common temperature and pressure of the reactants and products. This requires solving the following system of equations:

$$\begin{pmatrix} (1-\lambda)v_R + \lambda v_P - v \\ (1-\lambda)e_R + \lambda e_P - e \\ P^{MG}(v_R, e_R) - P^{JWL}(v_P, e_P) \\ T^{MG}(v_R, e_R) - T^{JWL}(v_P, e_P) \end{pmatrix} = \mathbf{0}, \tag{3.4}$$

where v is the total specific volume, e the total internal energy, and λ the mass-fraction of the products.

3.4.3 Mie-Grüneisen Equation of State

Experiments on solids provide a relation between the shock speed U_s and particle velocity u_p behind the shock. A first approximation consists of a linear relation (generally true for strong shocks):

$$U_s = c_0 + s\, u_p. \tag{3.5}$$

For HMX_sp, the following quantities are experimentally determined: $\rho_0 = 1/v_0 = 1.891\,\mathrm{g/cc}$, $c_0 = 3.07\,\mathrm{km/s}$ and $s = 1.79$.

From the linear relation above and the shock jump conditions, we can extract closed-form expressions for the pressure $P_{\mathcal{H}}$ and the internal energy $e_{\mathcal{H}}$ on the Hugoniot. Then, using the definition of the Grüneisen parameter, we obtain the Hugoniot-based expression for pressure, given below in Mie-Grüneisen form:

$$P(e,v) \sim \mathcal{G}\frac{e - e_{\mathcal{H}}(v)}{v} + P_{\mathcal{H}}(v) = \mathcal{G}\frac{e}{v} + f(v), \tag{3.6}$$

where the Grüneisen parameter $\mathcal{G}$ is chosen equal to 0.7.

Combining thermodynamic relationships and the jump relations yields an ordinary differential equation for the temperature on the shock Hugoniot:

$$\frac{dT_{\mathcal{H}}}{dv} = -\mathcal{G}\frac{T_{\mathcal{H}}}{v} + \frac{1}{2C_v(T_{\mathcal{H}})}\left[(v_0 - v)\left(\frac{\partial P}{\partial v}\right)_{\mathcal{H}} + P_{\mathcal{H}} - P_0\right] \tag{3.7}$$

Using the definition of the heat-capacity

$$C_v(T) = \left(\frac{\partial e}{\partial T}\right)_v, \tag{3.8}$$

we are able to compute the temperature at points off the Hugoniot:

$$T^{MG}(e,v) = T \approx \frac{e - e_{\mathcal{H}}(v)}{C_v(T)} + T_{\mathcal{H}}(v)\,. \tag{3.9}$$

The Material Properties group carried out quantum chemistry computations on HMX and computed the heat capacity C_v, which was fit to a quotient of polynomial functions.

3.4.4 JWL Equation of State

Cylinder-test experiments provide measurements of the isentropic pressure for the expanding products [39]. The data are usually analyzed by doing hydrodynamic simulations to optimize a parametric fit to the equation of state. A commonly used parametric form is the Jones-Wilkins-Lee (JWL) model

$$P_s(v) = Ae^{-R_1 v/v_0} + Be^{-R_2 v/v_0} + C(v/v_o)^{-\omega-1}, \tag{3.10}$$

where the various constants [24] are substance dependent. The experimentally measured detonation velocity for HMX is 9.11 km/s. Numerical experiments showed that the constants given in [24] actually correspond to a detonation velocity of 8.92 km/s; therefore, we changed the values of the constants, based on

$A = 5.99142\,\text{GPa}$	$R_1 = 3.70729$
$B = 10.6342\,\text{GPa}$	$R_2 = 0.946232$
$C = 10.7244\,\text{GPa}$	$\omega = 3.02716$

Table 3.1: JWL parameters for HMX, optimized for $U_{CJ} = 9.117$ km/s and $\rho_o = 1.891$ g/cm^3.

the velocity of 9.11 km/s and data from a thermo-chemical calculation (TIGER) using the JCZ3 equation of state. Our modified values are given in Table 3.1. In order to determine the pressure off the isentrope, we first need the energy on the isentrope. This is determined by using the first law of thermodynamics

$$P_s(v) = -\left(\frac{\partial e}{\partial v}\right)_s \tag{3.11}$$

and integrating to obtain

$$e_s(v) = e_{CJ} - \int_{v_{CJ}}^{v} P_s(v)dv. \tag{3.12}$$

The constant e_{CJ} is determined by finding the mathematical CJ condition, where the slope of the isentrope and Rayleigh line are equal. The definition of the Grüneisen parameter

$$\mathcal{G} = v\left(\frac{\partial P}{\partial e}\right)_v \tag{3.13}$$

provides an approximate expression for the pressure at points off the isentrope:

$$P^{JWL}(e, v) \approx \mathcal{G}\frac{e - e_s(v)}{v} + P_s(v) \tag{3.14}$$

and the thermodynamic identity

$$\left(\frac{\partial T}{\partial v}\right)_s = -\mathcal{G}\frac{T}{v} \tag{3.15}$$

can be used to find the temperature at points off the isentrope:

$$T_s(v) \approx T_{CJ}\left(\frac{v}{v_{CJ}}\right)^{-\mathcal{G}}. \tag{3.16}$$

The values of T_{CJ} and $\mathcal{G} = 0.77$ were found by fitting the results of the TIGER computation of the isentrope. The definition of the heat-capacity

$$C_v(T) = \left(\frac{\partial e}{\partial T}\right)_v \tag{3.17}$$

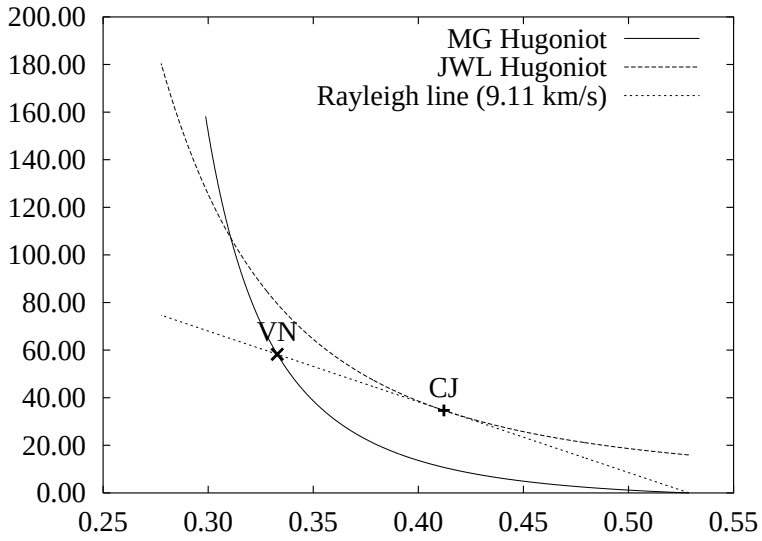

Figure 3.1: HMX_sp shock and detonation Hugoniots using $\rho_o = 1.891$ g/cm^3 and $U_{CJ} = 9.117$ km/s.

is used now to obtain the expression of the temperature at points off the isentrope:

$$T^{JWL}(e, v) \approx T \sim \frac{e - e_s(v)}{C_v(T)} + T_s(v). \tag{3.18}$$

We assume here that HMX_sp detonation products consist of only major species:

$$C_4H_8N_8O_8 \longrightarrow 4CO + 4H_2O + 4N_2. \tag{3.19}$$

The heat-capacity C_v for the resulting gas-mixture is given by

$$C_v = Y_{CO}\, C_v^{CO} + Y_{H_2O}\, C_v^{H_2O} + Y_{N_2}\, C_v^{N_2}, \tag{3.20}$$

where Y denotes the mass-fraction of each species. Furthermore, for each species i, $C_v^i = C_p^i - \tilde{R}/\tilde{M}_i$ where $\tilde{R} = 8.314\,\mathrm{Jg^{-1}K^{-1}}$. Between $2000\,K$ and $4000\,K$, we used the limiting high temperature values of heat capacities of each species $C_p^{CO} = 37.0\,\mathrm{Jmol^{-1}K^{-1}}$, $C_p^{H_2O} = 55.0\,\mathrm{Jmol^{-1}K^{-1}}$ and $C_p^{N_2} = 36.5\,\mathrm{Jmol^{-1}K^{-1}}$.

In Figure 3.1, we depict the Hugoniots of the reactants and products along with the Rayleigh line. This enables us to compute the von Neumann state. Chapman-Jouguet and von Neumann parameters are gathered in Table 3.2.

3.4.5 Computing the ZND Reaction Zone

In order to properly initialize a detonation wave, we must compute the ZND reaction zone [30]. It is achieved by solving a system of ODEs. This system

	CJ	VN
v [cc/g]	0.41	0.33
e [kJ/g]	1.91	5.70
P [GPa]	33.75	58.25
T [K]	3643	2328

Table 3.2: HMX_sp CJ and VN states using $\rho_o = 1.891$ g/cm^3 and $U_{CJ} = 9.11$ km/s.

of ODEs is obtained through manipulation of the Euler equations assuming a steady flow ($\partial_t(.) = 0$) and rewriting the equations in a Lagrangian frame.

$$\frac{\mathrm{d}}{\mathrm{dt}}W = \frac{\mathrm{d}}{\mathrm{dt}}\begin{pmatrix} v \\ e \\ w \\ \lambda \end{pmatrix} = Y(t,W) = R(P,\lambda)\begin{pmatrix} v\sigma/\eta \\ -Pv\sigma/\eta \\ u\sigma/\eta \\ 1 \end{pmatrix}, \tag{3.21}$$

where $w = u - U_s$, $\sigma = P_\lambda v/c^2$ is the thermicity and $\eta = 1 - w^2/c^2$ is the sonic parameter. Note that at the CJ point $w^2 = c^2$, therefore $\eta = 0$. In order to obtain a finite solution at this point, the thermicity must also vanish, $\sigma = 0$; which occurs when $\lambda = 1$. For a single-step, irreversible reaction, this is ensured by using the correct CJ velocity to compute the post-shock conditions, as discussed in Fickett and Davis [30].

We solve system (3.21) with a second-order accurate predictor-corrector technique and results are shown in Figure 3.2 where circles represent the reactants and solid lines the products.

3.4.6 Numerical Experiments

In order to integrate the reactive equations (3.1), we use the time-splitting technique proposed by Strang in [114]. Briefly, the operator splitting procedures are defined from the solutions of the homogeneous equations:

$$\mathbf{U}_t + \nabla \cdot \mathbf{F}(\mathbf{U}) = \mathbf{0} \tag{3.22}$$

and the system of ODEs:

$$\mathbf{U}_t = \Omega(\mathbf{U}). \tag{3.23}$$

If we call the advection operator $\mathcal{L}_A$ and the "chemistry" ODE operator $\mathcal{L}_C$, then Strang's splitting takes the form:

$$\mathbf{U}^{(n+1)} = \mathcal{L}_C\left(\frac{\Delta t}{2}\right)\mathcal{L}_A\left(\Delta t\right)\mathcal{L}_C\left(\frac{\Delta t}{2}\right)\mathbf{U}^{(n)}. \tag{3.24}$$

We choose to discretize equations (3.22) through a finite volume formulation on a Cartesian grid:

$$\frac{\partial}{\partial t}\int_{\mathcal{C}_i}\mathbf{U}\,\mathrm{d}\mathbf{x} + \int_{\partial\mathcal{C}_i}\mathbf{F}(\mathbf{U})\cdot\mathbf{n}\,\mathrm{dl} = 0, \tag{3.25}$$

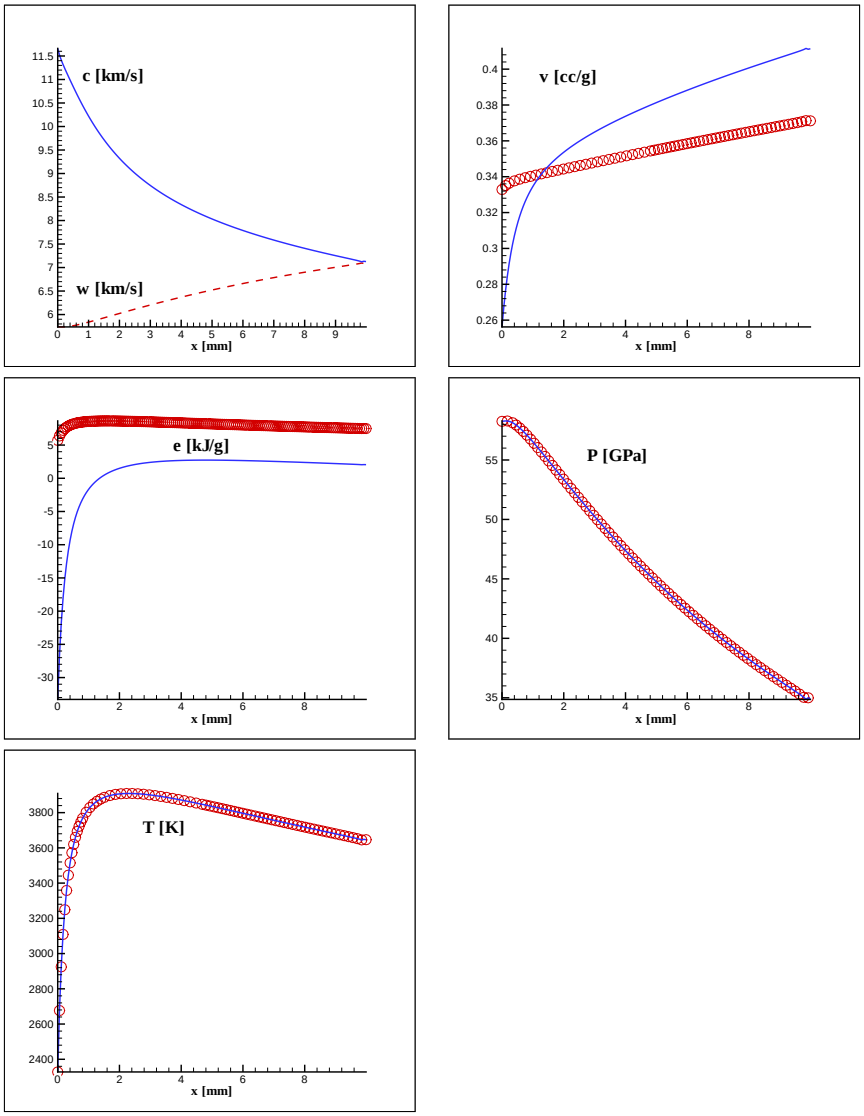

Figure 3.2: HMX_sp ZND reaction zone model with model parameters as discussed in the text.

where $\mathcal{C}_i$ represents the control volume over which we integrate, $\partial\mathcal{C}_i$ its boundary, d$\mathbf{x}$ the element of volume, and $\mathbf{n}$ the outward normal unit vector to $\mathcal{C}_i$. The integration of the convective fluxes at a cell interface is achieved *via* Roe's upwind numerical flux, extended by Glaister [35] to more general EoS. We implement this solver with Harten's entropy correction [38] on all waves. Time marching is explicit, and the time step Δt is chosen on the basis of the CFL

stability condition.

The chemistry part (3.23) of the equations reduces to the integration of the following ODE:

$$\frac{d}{dt}\lambda = R(\lambda, P)\,. \tag{3.26}$$

Since P varies as a function of λ, we should integrate (3.26) by using a technique such as Runge-Kutta. However, in Figure 3.2, we can see that the pressure varies very smoothly within the reaction zone. Therefore, we approximate the pressure as constant within a time-step ($\Delta t << 1$). This simplification enables us to use the following approximation, which saves considerable computational time:

$$\lambda^{(n+1)} \sim \lambda^{(n)} + 2\,\Delta t \left(\frac{P}{P_{VN}}\right)^5 \sqrt{1-\lambda^{(n)}} - \left(\Delta t \left(\frac{P}{P_{VN}}\right)^5\right)^2 . \tag{3.27}$$

In order to minimize further the computational time, we use a look-up table to compute the Mie-Grüneisen temperature (3.9). The temperature is precomputed for a range of volumes and energies and stored in a file. When needed, the temperature is computed from the table using bilinear interpolation. Figure 3.3 depicts the isocontours of the pressure of a detonation wave diffracting around a corner. In these figures, we can see the physical boundary represented by a solid line that separates the actual flow region from the ghost region where reflective boundary conditions are applied. First, the code is initialized with the ZND reaction zone (darkest region) computed earlier. To the left of the reaction zone, the solution lies at the CJ state (enforced as Dirichlet boundary condition as well) while to the right, the substance is at rest (the rightmost boundary is an outflow boundary condition). When the wave diffracts around the corner, we can see that the pressure drops substantially below the leading shock front and, as a result, the reaction subsides while it is sustained in the upper portion of the wave that is unaffected by the diffraction. The diffracted shock wave then reflects at the bottom of the domain and re-initiates a detonation. All the computations above were performed using the serial version of the Virtual Test Facility.

3.5 Reduced Reaction Modeling

In FY99, work in the field of reduced reaction modeling has continued from the previous year. The goal has remained to identify and implement a mechanism reduction technique for HE detonation simulations that suitably approximates the chemistry obtained from a detailed reaction mechanism while being sufficiently inexpensive to use in a 3-dimensional hydrocode on the fastest present day parallel computers. For operator-split computations of inviscid, compressible reacting flow with stiff chemistry source terms, the reaction step is by far the slowest to compute, and the computational cost scales at least with the square of the number of species. A typical detailed mechanism for HMX might contain close to 100 species (see Section 3.3). This highlights the need for re-

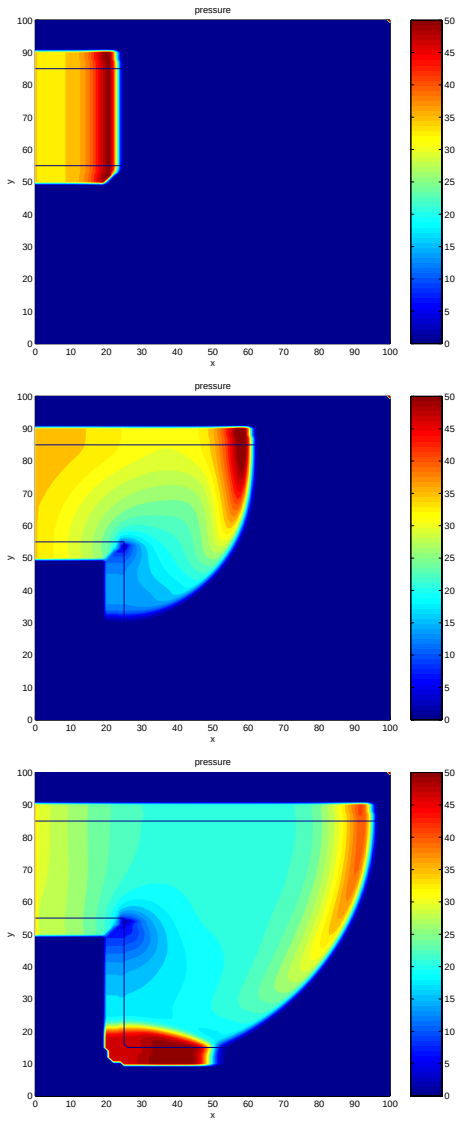

Figure 3.3: Detonation wave diffracting around a corner.

duced reaction models where the description of the chemistry must be reduced to no more than a handful of variables.

The reduction technique examined in FY98 was the Quasi Steady-State Approximation (QSSA). This year, the QSSA method was implemented in a 1-dimensional unsteady hydrocode and several example computations were run to simulate stable and unstable detonations in gaseous H_2–O_2. These results were compared with similar computations using a detailed reaction mechanism

and the QSSA reduced mechanism was optimized for a given parameter range of interest. The method was found to give moderate agreement with detailed chemistry and a satisfactory increase in computational performance. However, given the difficulty in automating this method for the reduction of large chemical systems and only moderate accuracy of the reduced schemes, it was decided that a more advanced method was preferable. The new method chosen was that of Intrinsic Low-Dimensional Manifolds (ILDM). A preliminary implementation of this method was performed and used to study H_2–O_2 and HMX reaction mechanisms.

3.5.1 QSSA Reduced Reaction Models

The Quasi Steady–State Approximation (QSSA) reduction technique is a classical method that was formalized for combustion systems by Peters [89]. It involves making steady–state assumptions about certain species and possibly partial equilibrium assumptions about certain reactions. This reduces the number of degrees of freedom in the chemical system and removes much of the stiffness in the problem. It is a simple analytical method, although it requires considerable insight to know which species can be approximated as steady–state.

All the codes are written in a modular fashion using CHEMKIN-II [52], where a new CHEMKIN reaction mechanism can simply be inserted at any time. A simple H_2–O_2 example was chosen for development purposes, where a more complex reaction mechanism could easily be used once the code is deemed satisfactory. In FY98, a preliminary reduced mechanism was proposed for the H_2–O_2 system. The detailed mechanism involved 8 species and 19 elementary, reversible reactions. After placing 3 of the species in steady–state, the resultant reduced mechanism contained 5 species and 3 reaction steps. This mechanism was partially validated against the detailed mechanism by steady 1-dimensional (ZND) detonation calculations.

In FY99, the QSSA form of the reduced mechanism was implemented into an unsteady 1-dimensional hydrocode. The code was validated by checking that it correctly reproduced the steady detonation solution for a sufficiently overdriven detonation simulation. The results of this validation are shown in Figure 3.4 for a stoichiometric H_2–O_2 detonation with an overdrive factor (square of the ratio of detonation speed D to Chapman–Jouget speed D_{CJ}) of 1.4. For the detailed mechanism in Figure 3.4(a), after an initial perturbation due to the startup error, the post-shock pressure P_{shock} soon settles down to a constant value almost exactly equal to the von Neumann pressure P_{vN}, the post-shock pressure in the steady ZND solution. This indicates that the detonation is sufficiently overdriven to be hydrodynamically stable. For the reduced mechanism in Figure 3.4(b), the steady detonation solution is again correctly captured, demonstrating that the code is valid. The main difference is that the reduced mechanism pressure profile takes longer to settle down to the steady solution which suggests it is closer to the stability limit.

Following this validation, the code was used to study unstable detonations. Decreasing the overdrive factor to 1.3, Figure 3.5(a) shows that the detailed

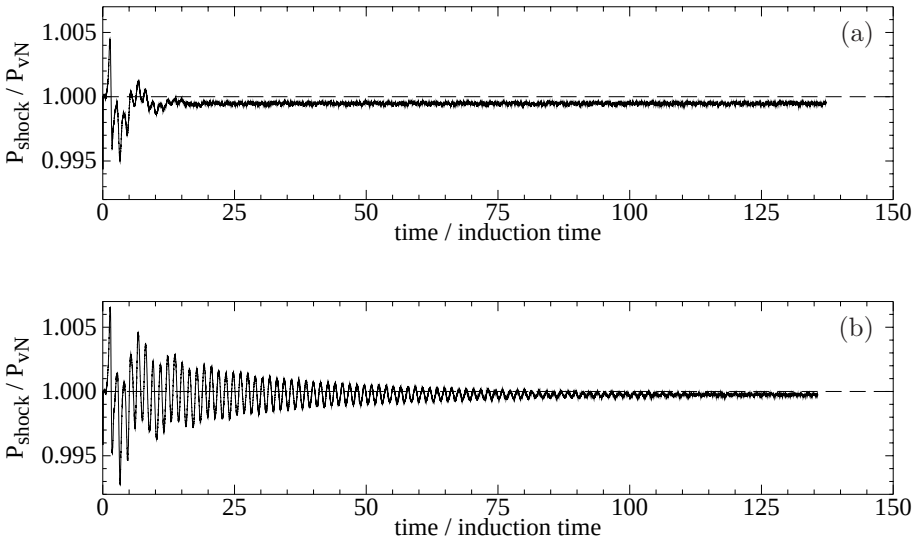

Figure 3.4: Stable 1-dimensional detonation in stoichiometric H_2–O_2, initially at $P_0 = 1$ atm and $T_0 = 300$ K, with $(D/D_{CJ})^2 = 1.4$; 100 mesh cells in induction zone. (a) Detailed mechanism; (b) 3–step reduced mechanism.

mechanism flow develops a longitudinal instability and the shock pressure eventually reaches a periodic solution. This is classically referred to as a "pulsating" or "galloping" detonation [30]. The reduced mechanism in Figure 3.5(b) also produces a galloping detonation. The period of oscillation appears to be quite similar, but the growth rate of the instability is too fast and the magnitude of the final oscillation is too large.

If the overdrive factor is further decreased, this time to 1.2, Figure 3.6(a) shows that the detailed mechanism flow develops a second longitudinal instability of longer period and greater final strength. This is to be expected from experiments where typically several unstable modes are witnessed together. The reduced mechanism flow in Figure 3.6(b) also develops a second unstable mode with close to the correct period. As before, there is some discrepancy in the instability growth rate and the final oscillation magnitude. In addition, the second unstable mode appears to completely damp out the first mode, in contrast to the detailed mechanism where both are present together.

To quantify the discrepancies between the detailed mechanism and reduced mechanism, the most important quantities were extracted from plots such as those presented in Figs. 3.4 to 3.6. The final periodic solution is generally of more interest than the startup flow, so the oscillation period and peak were examined in more detail. Figure 3.7 shows these two quantities for the single unstable mode case with overdrive factor of 1.3. The computational runs were repeated using a variety of reaction zone resolutions at the finest level of

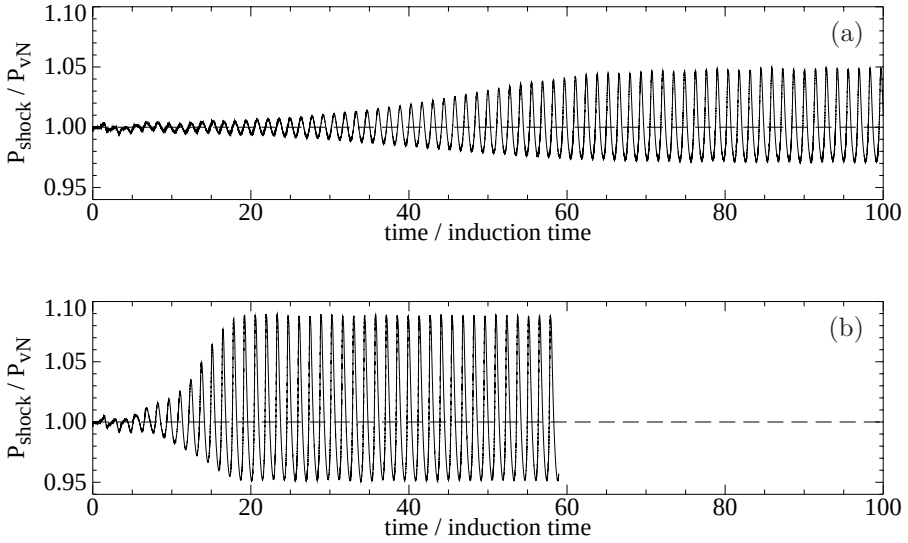

Figure 3.5: Pulsating 1-dimensional detonation in stoichiometric H_2–O_2, initially at $P_0 = 1$ atm and $T_0 = 300$ K, with $(D/D_{CJ})^2 = 1.3$; 200 mesh cells in induction zone. (a) Detailed mechanism; (b) 3–step reduced mechanism.

Step	Detailed mechanism	3–step reduced mechanism
Advection	11	5
Chemistry	89	23
Total	100	28

Table 3.3: Relative computational times for stable 1-dimensional detonation in stoichiometric H_2–O_2, initially at $P_0 = 1$ atm and $T_0 = 300$ K, with $(D/D_{CJ})^2 = 1.4$; 20 mesh cells in induction zone, fixed grid (no Adaptive Mesh Refinement).

the Adaptive Mesh Refinement (AMR). This permits a simultaneous grid convergence study for both the detailed and reduced mechanisms. For the grid converged solutions, the period of oscillation for the reduced mechanism agrees very well with that for the detailed mechanism, but the peak pressure is overpredicted by almost a factor of 2. However the reduced mechanism reaches a converged solution at a lower grid resolution, demonstrating a further computational time saving. This is to be expected because much of the stiffness is removed from the equations.

Finally, Table 3.3 shows the relative computational times for a test problem with the detailed and reduced mechanisms. The total computational times are

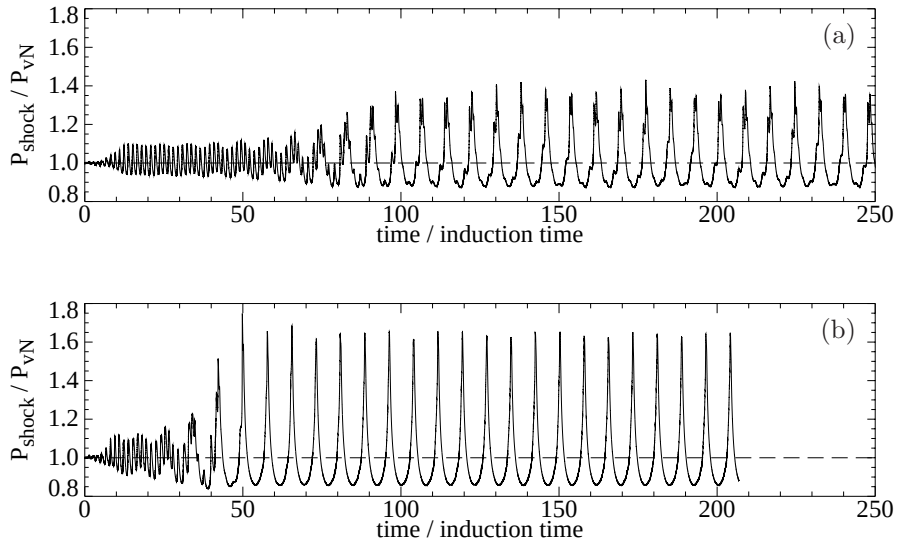

Figure 3.6: Pulsating 1-dimensional detonation in stoichiometric H_2–O_2, initially at $P_0 = 1$ atm and $T_0 = 300$ K, with $(D/D_{CJ})^2 = 1.2$; 200 mesh cells in induction zone. (a) Detailed mechanism; (b) 3–step reduced mechanism.

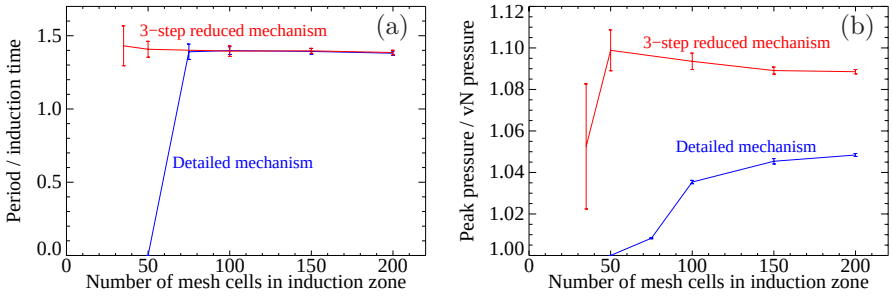

Figure 3.7: Pulsating 1-dimensional detonation in stoichiometric H_2–O_2, initially at $P_0 = 1$ atm and $T_0 = 300$ K, with $(D/D_{CJ})^2 = 1.3$. (a) Period of oscillation; (b) Peak pressure of oscillation.

subdivided into the times spent in the advection and chemistry steps of the operator-split scheme. The majority of time in the detailed mechanism is spent integrating the stiff ODEs of the chemistry step. This amount of time is reduced by almost a factor of 4 in the reduced mechanism. There is also a small saving in the fluid advection step due to the reduced number of variables in the solution vector. The overall saving in computational time is about a factor of 3.6. It

should be noted that the example presented here is quite a small system, where the number of degrees of freedom (the number of species minus the number of atomistic constraints) was only reduced from 6 to 3. For a more complex system such as HMX, this reduction would be far greater and the computational saving would be much more pronounced.

In summary, the QSSA technique produces reduced mechanisms that give reasonable agreement with detailed mechanisms for detonation simulations and result in a substantial saving of computational time. The detonation stability characteristics are correctly captured and the quantitative agreement in the periodic unsteady solutions are within a factor of 2.

However, this error is greater than desirable and, given the difficulty in applying this reduction technique for a large, less well understood chemical system, it was decided that a more sophisticated and systematic reduction technique should be investigated as an alternative. After attending the "Reduced Mechanisms Workshop" at Argonne National Laboratory in June, it was decided that Intrinsic Low-Dimensional Manifolds (ILDM) would be the best option.

3.5.2 Intrinsic Low-Dimensional Manifolds

The method of Intrinsic Low-Dimensional Manifolds (ILDM) was developed recently by Maas and Pope [70, 69, 71, 68]. It is based upon the empirical observation that chemical reaction systems tend towards low-dimensional manifolds in the reaction state space. Fast chemical processes relax towards the manifold and slow chemical processes represent movements along the manifold. If the fast processes occur on time scales much shorter than the other relevant time scales in the flow, then they can be decoupled and the chemical system approximated by just the slow processes on the manifold. No expert understanding of a detailed reaction mechanism is required to apply the ILDM method to it. The only required user input is the number of degrees of freedom, or dimension, of the ILDM. Implementation of the method involves identifying the ILDM and a suitable parameterization for it, storing the results in a lookup table for subsequent use in a hydrocode, and finally, projecting the reacting flow equations onto the manifold and solving them in a hydrocode.

To demonstrate the feasibility of this method for large reaction mechanisms of interest to ASCI, an eigen-analysis was performed on the HMX reaction mechanism currently being developed by the Material Properties group (see Section 3.3). At the time, this mechanism contained 72 species and 445 elementary reactions. An eigen-analysis of the governing ODEs' Jacobian was performed at various points in time for a constant volume explosion calculation. The results are shown in Figure 3.8. The inverse of the eigenvalues are the time scales of the chemical processes associated with the corresponding eigenvectors. Negative eigenvalues represent processes that relax onto the manifold, while positive eigenvalues represent non-relaxing processes. Typically, for chemical systems, almost all eigenvalues are negative. Ignoring the data at the early time 10^{-11} s, since this would not be resolved in an unsteady flow simulation, the other eigenvalue sets all demonstrate a good separation of time scales between the many

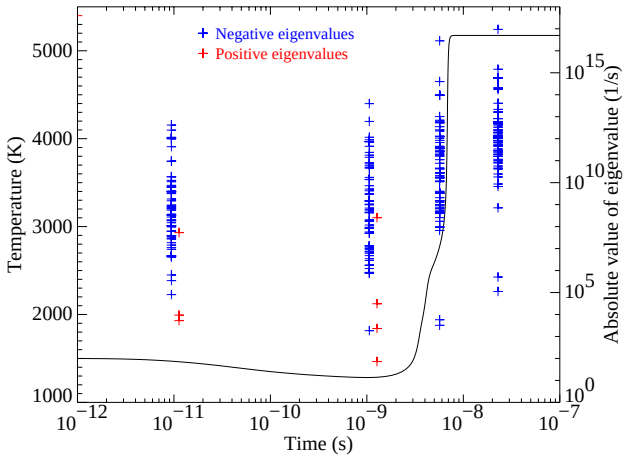

Figure 3.8: Eigen-analysis of reaction system ODEs' Jacobian, for an adiabatic constant volume explosion in HMX, initially at $P_0 = 1000$ atm and $T_0 = 1500$ K.

fast relaxing time scales and the few slow relaxing or non-relaxing time scales. This is precisely the property required to make the ILDM method successful. The number of slow time scales also gives an indication of the required ILDM dimension, in this case about 3 or 4. This is a substantial reduction from the initial 67 degrees of freedom and hence this method should result in enormous computational savings.

No publicly available ILDM code exists at this date so it was necessary to write our own. In FY99, work commenced on the creation of such a code and reached the point where a 1-dimensional ILDM could be solved for an arbitrary reaction mechanism. The results of this code are shown in Figure 3.9 for a simple H_2–O_2 example. The ordinates are specific mole numbers, which are the mass fractions divided by the species molecular weights, and are proportional to the mole fractions. Also shown are some sample reaction trajectories all having the same elemental composition, density and energy (and hence the same equilibrium point) but different initial molecular compositions. As the figure demonstrates, the trajectories all collapse onto a 1-dimensional ILDM before reaching the equilibrium point, which is a 0-dimensional ILDM. The 1-dimensional ILDM is very well captured by the ILDM code. Admittedly, these plots show a narrow range of composition, but this merely indicates that a higher dimension ILDM (2 or 3) would be needed in practice to represent the chemistry over a more useful range. These initial results indicate the feasibility of applying the ILDM technique to the problem of interest and show that we have successfully implemented the first stage of an ILDM code.

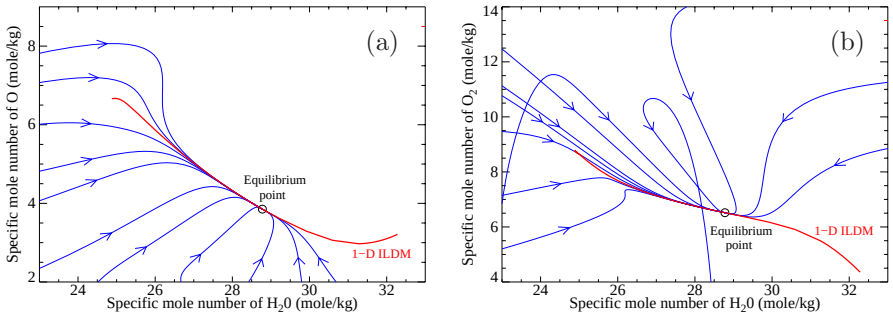

Figure 3.9: One-dimensional ILDM (red) and sample reaction trajectories (blue) for an adiabatic constant volume explosion in a mixture with H:O = 3:2 (equivalence ratio 0.75), $\rho = 3.18$ kg/m^3 and $e = 2.27$ MJ/kg. (a) Projection onto H_2O–O plane; (b) Projection onto H_2O–O_2 plane.

3.6 Models of Visco-elastic Binder Response

The problem of high rate shear deformations of an elastomer under varying pressure is studied in the context of understanding the role of binder deformation on the detonation sensitivity of plastically bonded explosives by taking into account dilatation-sensitive mechanical shear relaxation. Following the observation that pressurization prolongs the relaxation and retardation times of a visco-elastic elastomer, the implications of this phenomenon are considered for a thin layer of Hypalon-40 – as a model elastomer – sheared between two blocks of HMX under deformation rates typical in detonation scenarios. The consequences on heat generation are examined using small deformation as well as finite deformation analyses. While dilatation-insensitive visco-elastic behavior generates significant temperature increases, the effects of pressure-augmented dissipation clearly results in the possibility of "hot-spot" generation with a potential temperature rise on the order of 1000 C, thus leading potentially to the initiation of detonation in the adjacent explosive grains.

It is generally understood that during shock loading of high explosives the initiation of detonation occurs in localized, small regions within the explosive (referred to as *hot-spots*) where the local temperatures are sufficiently high to initiate the chemical reactions. Several mechanisms have been proposed to explain the origin of these hot-spots. These mechanisms include adiabatic heating of trapped gases in cavities, local viscous heating due to void collapse, frictional rubbing between adjacent explosive grains, and fracture of and shear-banding in the explosive crystals, etc. Experimental evidence exists for almost all of these mechanisms and in any given situation involving the detonation of an explosive by impact, one or more of these mechanisms may be dominant at various times during the initiation to detonation transition. However, one other mechanism that is particularly relevant to the class of high explosives referred to as Plastic

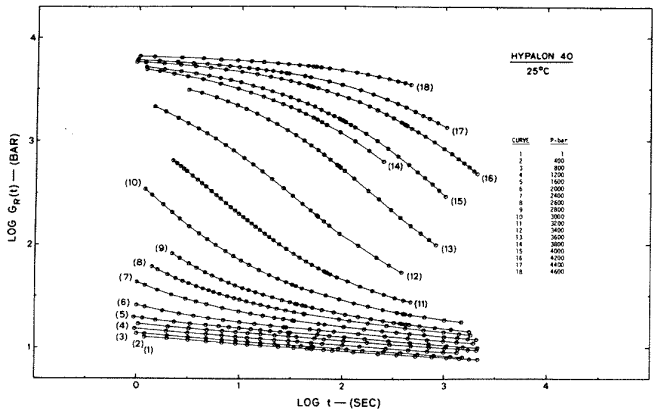

Figure 3.10: Pressure Stiffening of an Elastomer, from Fillers and Tschoegl [31].

Bonded Explosives (PBX) has not been studied in any great detail. Plastic bonded explosives are composed of explosive crystals typically 20–200 μm in dimension, held together in an elastomeric matrix that is typically a 2–5 μm thick layer around the explosive crystals. In this study we explore the possibility that the shear-induced heating of this thin binder layer can cause sufficiently high temperatures in the adjacent explosive grains to cause initiation of detonation in the energetic material.

At atmospheric pressures, elastomeric binders used in high explosives typically display rubbery behavior at room temperature and above and hence, possess the low moduli associated with such materials. However, it is known that elastomers undergo tremendous stiffening under imposed pressure (see Figure 3.10). Under shock wave loading, the thin binder layer in an explosive is subjected to large pressure and shear loads. Under these condition, the stiffening of the rubbery binder would lead to higher shear stress levels and correspondingly higher levels of inelastic dissipation in the binder. This inelastic deformation and consequent heating of the binder can cause local hot-spots to ignite in the adjacent explosive crystals. Increasing time and temperatures, however, will cause the binder to soften and lower the stress levels. The combined effect of pressure, time and temperature is represented through a master curve at a reference temperature and pressure (T_0, P_0) combined with a pressure and temperature dependent shift function $a_{T,P}(T, P)$ (see Figure 3.11) that represents the effect of pressure-induced stiffening and temperature-induced softening. It is the objective of this study to examine these competing effects and the implications for the initiation of detonations in plastic explosives. The form of the

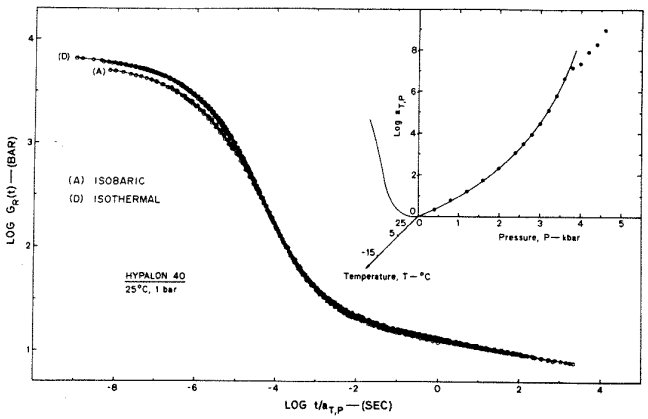

Figure 3.11: Master Relaxation Curve and Shift Function, from Fillers and Tschoegl [31].

shift function $a_{T,P}(T,P)$ suggested by Fillers and Tschoegl [31] is given as

$$\log a_{T,P} = -\frac{c_1[T - T_0 - \theta(P)]}{c_2 + T - T_0 - \theta(P)}, \tag{3.28}$$

where

$$\theta(P) = c_3 \ln[\frac{1 + c_4 P}{1 + c_4 P_0}] - c_5 \ln[\frac{1 + c_6 P}{1 + c_6 P_0}]\,. \tag{3.29}$$

In the interest of brevity, the values of the various parameters are not reproduced here.

3.6.1 Shearing of Binder Under Imposed Pressure

We now examine the problem of a thin layer of elastomeric binder being sheared under imposed pressure between two hard (semi-infinite) grains of explosive. A simple small deformation analysis is first presented that, nevertheless, demonstrates all the main features of the behavior that we seek to examine. A more detailed finite deformation analysis is then presented in a preliminary form.

Small Deformation Analysis

Consider a thin layer of visco-elastic binder sandwiched between two relatively large grains of explosive and undergoing shear deformation. Our objective is to evaluate the dynamic stress-deformation behavior of this binder material under these conditions. Our interest is also to evaluate the temperature increase in the binder as a result of visco-elastic dissipation and the resulting maximum temperatures in the adjacent explosive grains. If these temperatures are sufficiently high, they may lead to initiation of chemical reactions and explosion in

the explosive grain. The binder generally forms a thin layer of 2–10 μm between explosive crystals and is loaded by stress-waves traveling through the explosive. The transit time of these waves through the binder layer is on the order of a few nanoseconds whereas the time scales leading to detonation are of the order of tens of microseconds. Hence, it is convenient, and advantageous, to study the homogeneous shear deformation behavior of the binder.

Let the time-dependent behavior of the visco-elastic binder at the reference temperature and pressure (T_o, P_o) be characterized by a relaxation modulus function $G(t)$ represented by a prony series of the form

$$G(t) = \sum_{i=1}^{N} G_i \exp(-t/\tau_i^0). \tag{3.30}$$

Here τ_i^0 are the individual relaxation times at the reference temperature and pressure (T_0, P_0) and G_i are the corresponding moduli. The material may have, in fact, a very large number of individual relaxation mechanisms and corresponding relaxation times but, for computational purposes, only a finite number are chosen that still adequately model the overall relaxation behavior over the entire time-scale of the relaxation process. Furthermore, for a thermo- and piezo-rheologically simple material, the relaxation times at some other temperature and pressure (T, P) are given by

$$\tau_i(T, P) = \tau_i^0 a_{T,P} \tag{3.31}$$

where $a_{T,P} = a_{T,P}(T, P)$ is the shift function discussed in the previous section. The representation of Equation 3.31 corresponds to a shifting of the $\log[G(t)]$-$\log[t]$ curve by $\log(a_{TP})$ along the $\log[t]$ direction.

Consider, now, a Maxwell-Wiechert model as shown in Figure 3.12 consisting of N parallel elements each consisting of a spring and dash pot in series. Let G_i represent the individual spring moduli and η_i^0 the individual dash pot viscosities. If we define

$$\tau_i^0 = \eta_i^0 / G_i, \tag{3.32}$$

then the overall relaxation modulus in shear of the model is given by Equation 3.30. Hence, we take this Maxwell-Wiechert model as the mechanical spring-dash pot analog of the binder. This representation is necessary in order to calculate the rate of visco-elastic dissipation in the binder during deformation.

Since the individual spring-dash pot elements are in parallel, each such element undergoes the same straining. The individual dash pot viscosities, however, change during the deformation according to

$$\eta_i(t) = \eta_i^0 a_{T,P}(t) \tag{3.33}$$

which is equivalent to the representation in Equation 3.31.

In the following analysis, shear stresses are represented by σ instead of τ in order to avoid confusion with relaxation times which are written as τ_i. Correspondingly, shear strains are represented by ϵ. Let the overall rate of straining

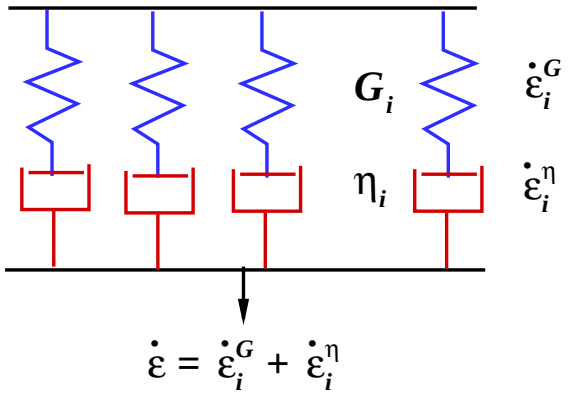

Figure 3.12: Maxwell-Wiechert model.

of the assembly at any instant be $\dot{\epsilon}(t)$. Then, for each spring-dash pot element i we may write

$$\dot{\epsilon}(t) = \dot{\epsilon}_i^G(t) + \dot{\epsilon}_i^\eta(t) \tag{3.34}$$

where $\dot{\epsilon}_i^G$ and $\dot{\epsilon}_i^\eta$ represent the rate of straining of the spring and dash pot elements respectively.

If σ_i represents the stress in this element, then

$$\dot{\epsilon}_i^G(t) = \frac{\dot{\sigma}_i(t)}{G_i} \tag{3.35}$$

and

$$\dot{\epsilon}_i^\eta(t) = \frac{\sigma_i(t)}{\eta_i^0 a_{T,P}(t)} = \frac{\sigma_i(t)}{G_i \tau_i^0 a_{T,P}(t)}\,. \tag{3.36}$$

Hence, we get

$$\dot{\epsilon}(t) = \frac{\dot{\sigma}_i(t)}{G_i} + \frac{\sigma_i(t)}{G_i \tau_i^0 a_{T,P}(t)}\,. \tag{3.37}$$

This can be rewritten as

$$\dot{\sigma}_i(t) = G_i \dot{\epsilon}(t) - \frac{\sigma_i(t)}{\tau_i^0 a_{T,P}(t)}\,. \tag{3.38}$$

Equation 3.38 can be integrated numerically to give $\sigma_i(t)$. The rate of viscoelastic dissipation in element i is then given by

$$\dot{D}_i(t) = \sigma_i(t)\dot{\epsilon}_i^\eta(t) = \frac{(\sigma_i(t))^2}{G_i \tau_i^0 a_{T,P}(t)} \tag{3.39}$$

and the total stress and dissipation rate in the material are given by

$$\sigma(t) = \sum_{i=0}^{N} \sigma_i(t) \tag{3.40}$$

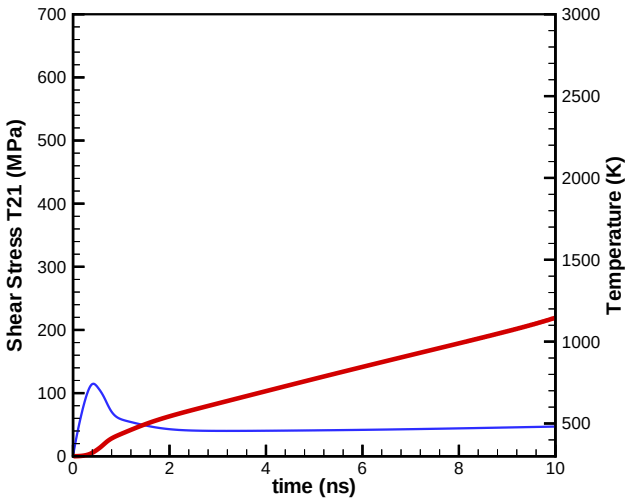

Figure 3.13: Small deformation analysis without pressure sensitivity.

and

$$\dot{D}(t) = \sum_{i=0}^{N} \dot{D}_i(t) = \sum_{i=0}^{N} \frac{(\sigma_i(t))^2}{G_i \tau_i^0 a_{T,P}(t)} \,. \tag{3.41}$$

Considering, as a point of departure, adiabatic heating of the specimen due to visco-elastic dissipative heating, the rate of temperature rise of the binder is given by

$$\dot{T}(t) = \frac{\dot{D}(t)}{\rho C} \tag{3.42}$$

where ρ and C are the density and specific heat capacity, respectively, of the binder. Accounting for heat conduction to the adjacent explosive grains as well as chemical heat generation in the explosive grains using simple Arrhenius kinetics, the temperature history $T_g(t)$ of the explosive grains is given by

$$(\rho C)_g T_{g,t} = k_g T_{g,xx} + \rho_g \Delta H \nu \exp\left(-\frac{\Delta G}{k T_g}\right) \tag{3.43}$$

where ΔH is the heat of detonation and ΔG is the activation energy of the chemical reaction.

A prony series representation of the form of Equation 3.30 is evaluated for the master relaxation curve $G(t)$ in Figure 3.11 by choosing 13 relaxation times spaced approximately one decade apart.

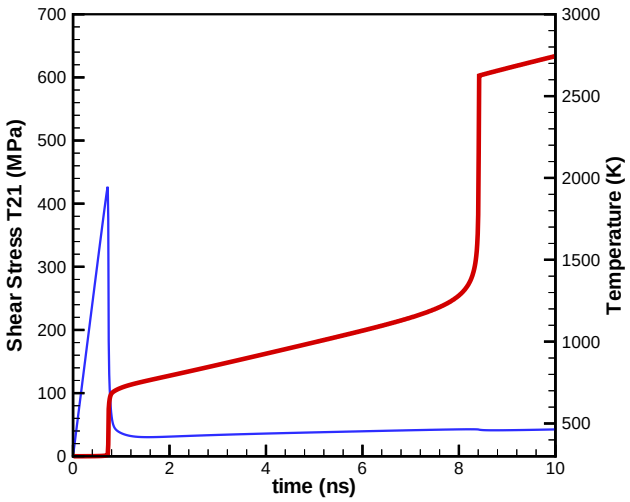

Figure 3.14: Small deformation analysis with pressure sensitivity.

3.6.2 Computational Results and Discussions

Equations 3.38-3.43 are converted to a finite-difference form for numerical implementation. A time step of 1 ns is used throughout the analysis and a total deformation time of 10 μs is considered. Typically, detonations in explosives initiate at time scales of the order of microseconds.

Figures 3.13 and 3.14 show the results for a constant strain rate deformation of 10^6 s^{-1} under an imposed pressure of 0.3 GPa. The two plots shown demonstrate the effect of taking into account the stiffening of the binder under the imposed pressure. Each plot shows the shear stress (thinner line) and temperature history at the interface between the explosive and the binder (thicker line) during the course of the deformation. When pressure-induced stiffening is not considered (Figure 3.13), the temperature near the interface increases uniformly with time but does not appear to have initiated any significant chemical decomposition of the explosive in the time scale of 10 μs. When pressure-induced stiffening is taken into account (Figure 3.14), a much higher shear stress is initially sustained by the binder with only very little dissipation and temperature rise. However, at around 1 μs, the binder appears to soften catastrophically leading to a significant instantaneous heating arising from the inelastic dissipation of the stored elastic energy in the binder. This temperature increase to about 700 K is apparently sufficient to cause the chemical energetics of the explosive to lead to a "thermal explosion" at around 8 μs.

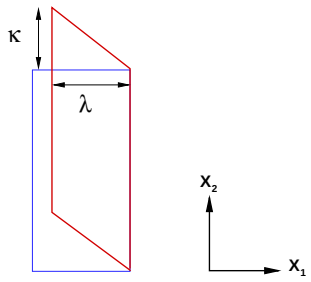

Figure 3.15: Finite deformation configuration.

3.6.3 Finite Deformation Analysis of Binder Deformation

The small deformation analysis presented in the previous sections allows us to understand the main characteristics of the shear response of the visco-elastic binder under the combined pressure and shear loading. However, in view of the large deformations experienced by the binder under these loading conditions, it is necessary to study the response with finite deformation considerations.

Again, we consider the case of one-dimensional homogeneous shear deformation of the binder between two hard explosive grains. As shown in Figure 3.15, if we let λ and κ represent the stretch and shear of the binder at any time during the deformation, the deformation gradient tensor can be written as

$$\mathbf{F} = \begin{pmatrix} \lambda(t) & 0 & 0 \\ -\kappa(t) & 1 & 0 \\ 0 & 0 & 1 \end{pmatrix} . \tag{3.44}$$

However, instead of simply considering the case of prescribed constant shear strain rate, we will include wave loading effects by prescribing the initial deformation rates $\dot{\lambda}_0$ and $\dot{\kappa}_0$ and appropriate elastic wave boundary conditions.

From the deformation gradient tensor the spatial velocity gradient is obtained by the relation

$$\mathbf{L} = \dot{\mathbf{F}}\mathbf{F}^{-1} . \tag{3.45}$$

The spatial velocity gradient can now be decomposed into a symmetric and a skew-symmetric as

$$\mathbf{L} = \mathbf{D} + \mathbf{W} \tag{3.46}$$

where $\mathbf{D}$ is the rate of deformation tensor and $\mathbf{W}$ is the spin rate tensor.

We now make the assumption that the deformation gradient tensor has a multiplicative decomposition of the form

$$\mathbf{F} = \mathbf{F}_i = \mathbf{F}_i^e \mathbf{F}_i^v \tag{3.47}$$

where $\mathbf{F}^e$ and $\mathbf{F}^v$ represent elastic and viscous components and the subscript i represents the assumption that several relaxation mechanisms are active concurrently in the material, each subjected to the same overall deformation. This gives

$$\mathbf{D} = \mathbf{D}_i = \mathbf{D}_i^e + \mathbf{D}_i^v \,. \tag{3.48}$$

Assume, in general, Neo-Hookean hyperelastic response with compressibility:

$$\sigma_i = \alpha^0 \mathbf{I} + \alpha^1 \mathbf{F}_i^e (\mathbf{F}_i^e)^T \,. \tag{3.49}$$

Write the viscous flow rule as

$$\mathbf{D}_i^v = \frac{\mathbf{S_i}}{(G_i \tau_i)} = \frac{\dot{\gamma}_i^p}{2\tau_i^{eff}} \mathbf{S}_i \,. \tag{3.50}$$

where $\mathbf{S}_i$ is the deviatoric part of the Cauchy stress tensor, σ_i, τ_i^{eff} are the effective stress in the elements,

$$\dot{\gamma}_i^p = \frac{2\tau_i^{eff}}{(G_i \tau_i)} \tag{3.51}$$

is the effective inelastic strain rate in element i and $\tau_i(t) = \tau_i^0 a_{T,P}$ are relaxation times, as before.

The resulting rate equations for the components of the first PK stress tensor $\mathbf{T}_i$ are of the form

$$\dot{T}_i^{\alpha\beta} = A_i^{\alpha\beta} \dot{\lambda} + B_i^{\alpha\beta} \dot{\kappa} - R_i^{\alpha\beta} \dot{\gamma}_i^p \tag{3.52}$$

where

$$A_i^{\alpha\beta} = A_i^{\alpha\beta}(\mathbf{T}_i, \lambda, \kappa) \tag{3.53}$$

etc.

The overall stress is given as

$$\mathbf{T} = \sum_{i=0}^{N} \mathbf{T}_i \tag{3.54}$$

and temperatures are calculated as before by summing the dissipation rates from each element.

3.7 Computational Results and Conclusions

Computational results with finite deformation considerations are shown in Figures 3.16 and 3.17 and indicate qualitatively similar behavior to that seen with the small deformation analysis. For this computation, the binder elasticity is taken to be linear, the initial shear strain rate represented by $\dot{\kappa}_0$ is taken to be 10^6 s^{-1} as before and $\dot{\lambda}_0$ is taken to be -0.3×10^6 s^{-1}.

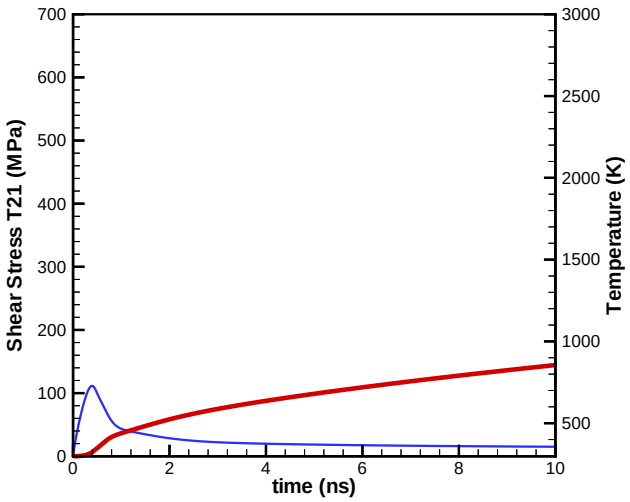

Figure 3.16: No Pressure Sensitivity (FD Analysis).

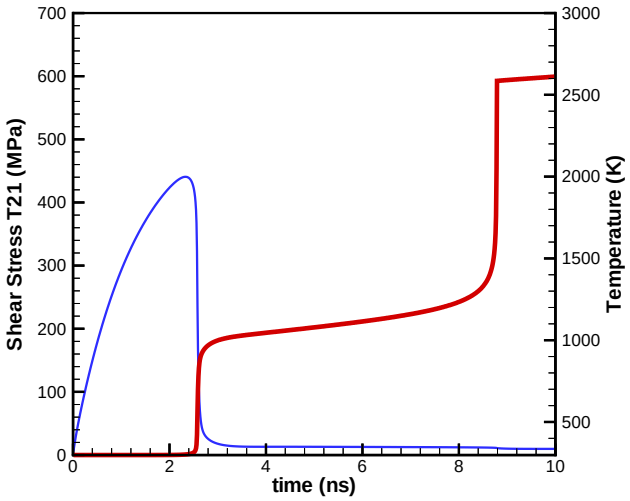

Figure 3.17: Effect of Pressure Sensitivity (FD Analysis).

3.7.1 Conclusions

The investigations conducted so far appear to indicate that if pressure-induced stiffening of the visco-elastic binder is accounted for, the mechanism of shear-induced inelastic dissipation in the explosive binder can cause the explosive to be heated locally to temperatures that are sufficient to lead to detonation in tens of microseconds and is thus a valid "hot-spot" mechanism.

3.8 FY 00 objectives

3.8.1 Material Properties

The force fields will be refined and improved EoS will be computed with molecular dynamics. Detailed reaction modeling of nitramines will continue and the development of corrections for dense fluid effects such as solvation will be explored. Molecular dynamics simulations of HE-binder interfaces will be carried out. Quantum mechanical molecular dynamics of reaction initiated by shock waves will be investigated with more realistic ensembles of molecules.

3.8.2 Engineering Models of Explosives

In FY00, the multi-reaction version of the JTF model will be used to compute reaction rates. This model and the current EoS description will be incorporated into the 3-dimensional version of the VTF. Improved versions of the reaction rate model will be explored and tested against available experimental data.

3.8.3 Reduced Reaction Modeling

In FY00, it is planned to complete the writing of the ILDM manifold solver and develop a table lookup algorithm. The method will then be implemented in a 0-dimensional combustion code and a 1-dimensional unsteady hydrocode. Validation will be performed against detailed mechanisms for H_2–O_2, small hydrocarbons, and gaseous nitramines such as nitromethane, RDX, and HMX. The ILDM hydrocode will finally be extended to a 2-dimensional, parallel code. Cellular detonation simulations will be performed and compared with experimental results.

If this proves to be successful, then work proposed for FY01 will include investigating the extension of this method to high pressures and the solid phase, with subsequent integration into the Virtual Test Facility (VTF).

3.8.4 Models of Visco-elastic Binder Response

During the early part of FY00, the analyses (finite deformation, in particular) will be refined. Further investigations will focus on development of physically-based constitutive laws of evolution and growth of generic hot-spots in high explosives with the ultimate aim of developing engineering models of detonation for use in integrated codes for the Virtual Test Facility.

Chapter 4

Solid Dynamics

4.1 Overview of FY 99 Accomplishments

1. Development of damage and crack modeling.

   (a) Spall: in progress. In FY99 we started to formulate a model of spall which contemplates three different scales. At the smallest scale, the model estimates the density of vacancies generated by the dragging of jogs formed as a result of dislocation intersections and double cross slip. The super-saturated distribution of vacancies eventually collapses to form voids. Following this nucleation phase, the voids grow by the accumulation of vacancies migrating by pipe diffusion. Once the void attains a size comparable to the mean distance between dislocations, growth occurs primarily by single-crystal plasticity. A finite element model of a single void cavitating in a plastically deforming crystal under the action of a high hydrostatic tensile pressure and at high strain rates is under development. This fundamental calculation will provide an irreversible equation of state which can be incorporated into the single-crystal plasticity models to predict ductile rupture.

   (b) Fracture and fragmentation: completed. Present capability includes finite-deformation irreversible cohesive elements to simulate fracture and fragmentation within a finite-element framework. The capability has been extensively verified and validated.

2. Mixed atomistic-continuum modeling in 2D with defects: We have completed extensive mixed continuum/atomistic calculations of defect-mediated material properties and unit processes, including: dislocation-junction strength; dislocation energies in fcc and bcc crystals as a function of orientation; and pipe diffusivities for vacancy migration. A 3D mixed

continuum/atomistic capability has also been completed. The capability is presently being applied to problems of nanoindentation in ductile single crystals.

3. 2D and 3D prototype of the integrated VTF: fully lagrangian capability in progress. We have completed prototypes of the fully lagrangian 2D and 3D VTF including engineering models of HE materials and metals. We have completed verification problems in 2D, with validation runs to begin soon. We have completed preliminary test runs in 3D and further runs are in progress, including the use of mesh adaption. MPI versions of the explicit dynamics and the Taylor averaging polycrystal model have been developed and their scalability properties have been assessed. A main focal point of activity has been the parallelization of our 2D and 3D tetrahedral meshers. Parallel versions of both meshers are presently in existence. The good scalability of the 2D mesher on the ASCI platforms has been established. A similar effort to appraise the scalability properties of the 3D mesher is presently underway.

4. Other activities: Other activities developed during the year which exceed the scope of the milestones include: the development and validation of a model of single crystal plasticity in Ta; the development of a mesh refinement/coarsening algorithm based on subdivision and edge collapse; models of subgrain dislocation structures in crystals.

4.2 Personnel

- Faculty:
  - Thomas J. Ahrens
  - Oscar P. Bruno
  - Alberto Cuitiño (Rutgers)
  - Michael Ortiz
  - Robert Phillips (Brown U.)
- Research fellows:
  - Raul Radovitzky
  - Eduardo Repetto
- Post-doctoral fellows:
  - Sylvie Aubrie
  - Jarek Knap
  - David Olmsted (Brown U.)
  - Dimitri Vaynblat
- Graduate students:

- Marisol Koslowski
- Adrian Lew
- Jean-Francois Molinari

4.3 Nanomechanics

We have developed a finite-element-based nodal dislocation dynamics model to simulate the structure and strength of dislocation junctions in FCC crystals. The model is based on anisotropic elasticity theory supplemented by the explicit inclusion of the separation of perfect dislocations into partial dislocations bounding a stacking fault. We have demonstrated that the model reproduces in precise detail the structure of the Lomer-Cottrell lock already obtained from atomistic simulations. In light of this success, we also have examined the strength of junctions culminating in a stress-strength diagram which is the locus of points in stress space corresponding to dissolution of the junction.

In FCC metals, a key mechanism limiting the movement of dislocations is the "forest intersection" mechanism, where segments of dislocations on a glide plane are rendered immobile as a result of intersection with dislocations on other glide planes. Such intersections can lead to complex *dislocation junction* structures since the cores of the dislocations in these metals are dissociated into partial dislocations separated by a stacking fault [42]. Furthermore, the structure of the junction also depends strongly on the geometric disposition (such as the line directions and Burgers vector) of the participating dislocations. A core level analysis of all the possible junction configurations is therefore important from a number of perspectives. Such core level calculations in conjunction with statistical averaging procedures can possibly provide key parameters that are used in models that predict the mechanical behavior of metallic crystals on a macro-scale. These models include single crystal plasticity models [8] and computational models that simulate the dynamics of a large collection of dislocations [119].

We have developed a mesoscopic dislocation dynamics model that can be used to simulate the structures and strength of dislocation junctions in FCC metals and may obviate the need for direct atomistic simulations of these junctions. For simple dislocation intersection geometries, the structure of dislocation junctions has been studied extensively using the theory of linear elasticity in a series of classic papers by Hirth and coworkers [40, 41, 49]. Analytical insights into more complicated intersection geometries have been gained by using the line tension approximation for the dislocation lines [101, 105]. While this approach provides a great deal of physical insight into the junction structure and strength, it ignores the extended core structure of the dislocations as well as the long range interaction between the dislocation segments. With rapid advances in computational power in recent years, it has become possible to perform atomistic simulations of dislocation intersections [13, 133, 98]. Typically these simulations [133, 98], are computationally demanding and raise serious questions concerning the role that boundary conditions play in dictating the results.

In the present study, we develop a mesoscopic method to study the structure and strength of dislocation junctions that includes the dissociation of the dislocation core into partial dislocations. The interaction between the dislocations are treated using the theory of anisotropic elasticity[4]. We find that our method reproduces, in precise detail, all the features of the dislocation junction structure obtained from a full atomistic treatment of the dislocation core. Our results demonstrate that the junction structure is almost entirely determined by elastic interaction between the partial dislocations, and the stacking fault energy.

In order to clearly demonstrate the role of the stacking fault in determining the junction structure, we consider dislocation junctions in two metals, namely, Al, with a high stacking fault energy (0.104 J/m^2) and Ag, with a low stacking fault energy(0.016 J/m^2). We limit our discussions to the Lomer-Cottrell lock[42]; a complete investigation of other junctions will be reported elsewhere.

The simulations are carried out through an adaptive finite element based nodal dislocation dynamics algorithm that is described in detail in [25, 107, 58]. We start our simulations with straight dislocation lines that are pinned at their end points. Simulations are carried out until the dislocations glide to their equilibrium configuration. Each dislocation line is allowed to split into partial dislocations by accounting for the energy cost of the stacking fault created in the process.

A time step of the dynamics process consists of moving the node connecting the segments with a velocity that is proportional to the nodal driving force. The computation of the nodal force requires the knowledge of the force per unit length at certain quadrature points on the dislocation segments that are attached to the node. The force per unit length at any point on a segment consists of a component arising from the stresses due to all the dislocation segments in the system including the segment itself. The Brown regularization procedure is adopted to guarantee that the self-stress contribution is well behaved [25, 107, 58]. When the interaction between the segments belonging to different dislocations is attractive, they approach each other in the process of forming a junction. However, the stress acting on one of the segments due to the other one diverges as their separation vanishes. To remove this difficulty, we treat the stresses as constant for distances less than a critical separation distance, r_c, with a value equal to that of the stress computed at r_c.

As a result, the segments are locked once they are closer than this critical distance; a junction has formed. From an elastic perspective, at distances larger than r_c, the stresses produced by the junction segments correspond to those produced by a dislocation whose Burgers vector is the vector sum of those of the two segments that make up the junction. Once the junction is formed, it can unzip if the external stresses cause the segments that form the junction to move away from each other. The calculations described here were carried out with $r_c = b$, although we have also considered the cases in which the cutoff was $b/2$ and $2b$, without noticeable change to the resulting junction structures. In addition to the stress from the dislocation segments, the force per unit length consists of a component arising from the stacking fault. This component is

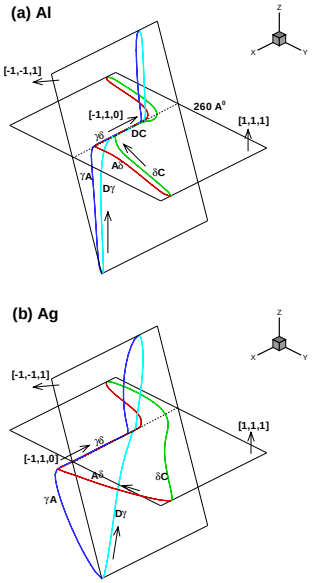

Figure 4.1: Structure of the Lomer-Cottrell Junction in Al and Ag. The line directions and the Burgers vectors of the dislocation segments are indicated in the figure. The junction forms along the dotted line, which is the line of intersection of the two slip planes.

normal to the dislocation segment and has a magnitude that equals the stacking fault energy and acts in a direction tending to shrink the stacking fault. In the simulations that we describe, we have ignored the frictional stress since we have found that its inclusion is unimportant. A key feature of our simulations is the adaptive positioning of the nodes, so that regions with large curvature have more nodes per unit length.

We demonstrate our results by first considering the equilibrium configuration of a Lomer-Cottrell lock as shown in Figure 4.1. This configuration has been chosen so as to make a direct comparison of our results with the atomistic simulations for Al reported in [98]. The pinning points are arranged such that in the starting configuration the dislocation line directions make an angle of 60^0 with the $[\bar{1}, 1, 0]$ direction. This direction coincides with the line of intersection of the slip planes of the dislocations that form the junction.

The line directions of each of the partial dislocations and their slip plane normals are given in the figure. We follow the notation described in [42] to label the Burgers vectors of the partial dislocations by referring to the Thompson tetrahedron. For example, the $a/2[0, 1, \bar{1}](111)$ dislocation splits into partial dislocations $A\delta$ and δC with Burgers vectors $a/6[\bar{1}, 2, \bar{1}]$ and $a/6[1, 1, \bar{2}]$ respectively. As is evident from the figure, the junction segment in the case of Al, has split into separate parts. A stair-rod segment with Burgers vector $\gamma\delta$ of the type $a/6\langle 110\rangle$ forms an extended node on the left side of the junction. The re-

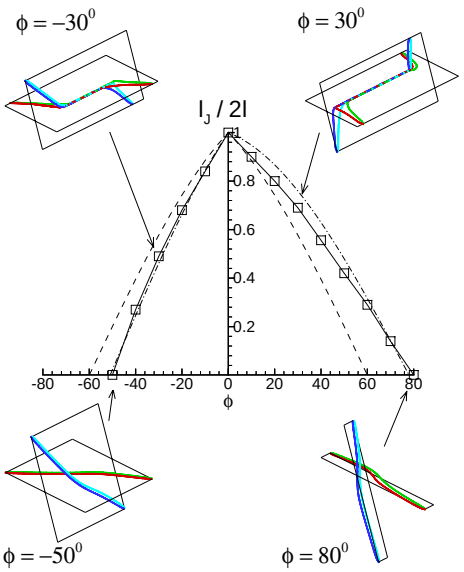

Figure 4.2: Junction length of the Lomer Cottrell lock in Al as a function of the line directions of the participating dislocations. The dashed and dashed-dot lines are the predictions of the direction dependent and independent line-tension models respectively and the "squares" are the results obtained using our mesoscopic model. We also show the evolution of the junction structure as the line directions are varied.

maining part of the junction is a sessile Lomer dislocation segment. The length of the stair-rod segment is 38Å, while the Lomer is 42Å, which is in excellent agreement with the atomistic results[98]. The dislocation dynamics model also agrees with the atomistic results in predicting the structure of the right hand node, which is point-like and is the meeting point of constricted dislocation segments.

As an extension of earlier results and to highlight the dependence of the junction structure on the stacking fault energy, we have also computed the geometry of the Lomer-Cottrell junction in Ag. The dislocation junction in Ag, for this configuration, has an entirely different structure. The junction segment is entirely composed of a stair-rod dislocation of length 180Å. The smaller stacking fault energy keeps the segments δC and $D\gamma$ from participating in the junction formation process.

We now consider the effect of altering the junction angle on the structure of the dislocation junction. We use ϕ to denote the angle between the dislocation line direction in the starting configuration and the $[\bar{1}, 1, 0]$ direction, l_J for the junction length and $2l$ for the distance between the pinning points. In Figure 4.2, we plot the junction length and structure as the orientation of the pinning points is altered. For comparison we also show the results obtained by

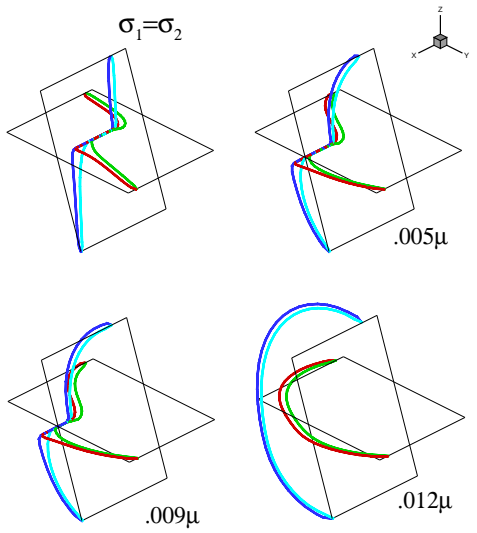

Figure 4.3: Evolution of the symmetric Lomer Cottrell lock in Figure 4.1, on applying an external stress. The resolved shear stress on the two junctions are the same.

using both the isotropic [101, 105] and anisotropic line-tension models within isotropic elasticity. We find that the results of our simulations are in very good agreement with the predictions of the anisotropic line-tension model [59]. For the positive angle junctions, the participating dislocations enter in mostly "edge" orientation, while in the case of negative angle junctions, they enter in the screw orientation. As a result, the energy gain in the former case is bigger than the latter by a factor $1/(1-\nu)$, where ν is the Poisson ratio. This has two immediate consequences that are borne out by our simulations: firstly, the "edge" like junctions are stabler to higher incidence angles and secondly, the "edge" locks are strong relative to "screw" locks for the same incidence angle. In fact, TEM studies of dislocation junctions [50, 54] reveal a preponderance of the "edge" like junctions over their "screw" counterparts. While one explanation for the instability of the "screw" junctions is the ability of the parent dislocations to cross-slip resulting in the transformation of the sessile lock to a glissile one, our simulations provide yet another explanation for the stability of the "edge" like junctions.

Far more interesting than the structure of junctions is their behavior under stress. Figure 4.3 shows the evolution of the dislocation junction in Figure 4.1 under the influence of an externally applied stress. The resolved shear stress on the dislocations in the $(1,1,1)$ and $(\bar{1},\bar{1},1)$ slip planes are labeled σ_1 and σ_2 respectively. We have chosen the orientation of the applied stress for this series of pictures such that $\sigma_1 = \sigma_2$. On increasing the stress, the length of the Lomer

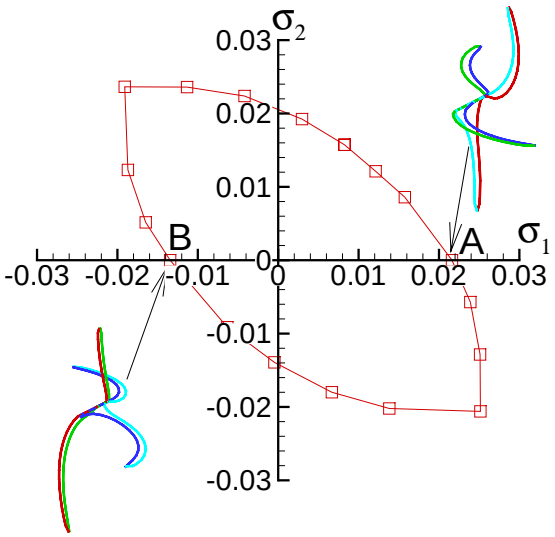

Figure 4.4: The "yield surface"for the symmetric Lomer-Cottrell lock in Figure 4.1. The stresses are in the units of shear modulus of Al. We also display the structure of the junctions prior to destruction for the points marked A and B.

segment initially increases on going from no applied stress to a stress of 0.006μ (μ is the shear modulus).

On increasing the stress further, the junction translates and undergoes an unzipping mechanism, whereby the length of the Lomer segment decreases. This behavior is evident for the stress level of $.009\mu$. The junction breaks at a stress level of about 0.012μ after which they continue to bow out. The configuration shown at stress of 0.012μ, is not in equilibrium, but a snap shot after the junction has been destroyed. We have carried out similar calculations for several values of resolved shear stress acting on the two dislocations. A "yield surface" for dislocation destruction is shown in Figure 4.4. This surface is symmetric about the line $\sigma_1 = \sigma_2$, but depends on the sign of σ_1 and σ_2. This symmetry breaking is readily understood by looking at the configurations of the dislocations under action of positive and negative σ_1 (denoted in Figure 4.4 by points A and B respectively) with $\sigma_2 = 0$. The presence of the stair-rod node makes it more difficult for the horizontal segment to bow out in case (A) compared to case (B) and requires a larger value of shear stress to break the junction.

It is interesting to compare the predictions of the line tension model and the atomistic simulations with the results obtained from our simulations. An important prediction of the line tension model is the scaling of the breaking stress of symmetric junctions with the distance between the pinning points, written as $2l$. The line tension model predicts the average critical resolved shear

stress to break the symmetric junctions to be $\approx 0.5\mu b/l$. We have simulated the breaking of symmetric junctions with lengths ranging from 300Åto $1\mu m$ by applying the external stress in different orientations. We have found that the critical breaking stress scales as $\sigma_c \sim \mu b/l$. For the cases $\sigma_1 = \sigma_2$ and $\sigma_1 = -\sigma_2$ the critical resolved shear stress behaves like $\sigma_c = 0.64\mu b/l$ and $\sigma_c = 1.24\mu b/l$, respectively. For the 300 Åjunction, for the case when $\sigma_1 = 1.3\sigma_2$, the atomistic simulations gave $\sigma_c = .017\mu = 0.8\mu b/l$, which is in good agreement with our results.

The features that are missed in our model and the effect they may have on the results discussed thus far should be carefully noted. In our simulations, the dislocations do not acquire a jog as they cross. While this does not affect the junction structure, it will alter the breaking stress, since the external stress should supply the energy required to create the jog. However, the jog contribution to the breaking stress is only a small fraction of the stress required to unzip the junctions [101, 105]. In order to examine the effect of the stress cut-off distance, r_c, we have also carried out all the above simulations by choosing r_c to equal $b/2$ and $2b$. The junction structure showed very little difference in the two calculations. Also, the breaking stress in all the cases was within 10% of the values reported here.

In conclusion, we have developed an efficient method to study dislocation interactions in FCC metals. We have illustrated that the method can provide "rules" like critical angle for junction formation and breaking stress criteria, which can be used in 3D dislocation dynamics models. The results from our simulations for junctions in different configurations, when appropriately averaged, can provide parameters related to junction strength in models for single crystal plasticity. Fits to these parameters from tension tests on single crystals have revealed a hierarchy of junction strengths in FCC crystals [32]. Work is in progress to verify the observed hierarchy on the basis of our simulations.

4.4 Micromechanics

We have completed the development and validation of a model of single-crystal plasticity for Ta based on the forest-dislocation theory of hardening, dislocation kinetics, notions of thermal activation, and full finite-deformation kinematics. A complete account of the model may be found in [113]. Highlights of the model and its validation are given next. In all cases, the parameters of the model have been determined either from atomistic calculations or by direct fitting to the experimental data of Mitchell and Spitzig [78].

The theoretical framework within which the model is developed is as follows. We adopt a conventional multiplicative kinematics of the form

$$\boldsymbol{F} = \boldsymbol{F}^{\mathrm{e}}\boldsymbol{F}^{\mathrm{p}} \tag{4.1}$$

where $\boldsymbol{F}$ is the deformation gradient, $\boldsymbol{F}^{\mathrm{e}}$ is the elastic lattice distortion and rotation, and $\boldsymbol{F}^{\mathrm{p}}$ is the plastic deformation, which represents the net effect of crystallographic slip and leaves the lattice undistorted and unrotated. In addition, the plastic deformation is volume preserving.

In materials such as metals, the elastic response is ostensibly independent of the internal processes and the free energy decomposes additively as

$$\phi = W^{\mathrm{e}}(\boldsymbol{F}^{\mathrm{e}}, T) + W^{\mathrm{p}}(T, \boldsymbol{F}^{\mathrm{p}}, \boldsymbol{Q}) \tag{4.2}$$

where T is the absolute temperature and $\boldsymbol{Q}$ is some suitable set of internal variables. The function W^{e} determines the elastic response of the metal, e. g., upon unloading, whereas the function W^{p} describes the hardening of the crystal. Physically, W^{p} represents the stored energy due to the plastic working of the material.

We further assume that the volumetric and deviatoric elastic responses as decoupled, i. e.,

$$W^{\mathrm{e}}(\boldsymbol{F}^{\mathrm{e}}, T) = W^{\mathrm{e,vol}}(J^{\mathrm{e}}, T) + W^{\mathrm{e,dev}}(\boldsymbol{F}^{\mathrm{e,dev}}, T) \tag{4.3}$$

where

$$J^{\mathrm{e}} = \det(\boldsymbol{F}^{\mathrm{e}}) \tag{4.4}$$

measures the volumetric elastic deformation, and

$$\boldsymbol{F}^{\mathrm{e,dev}} = J^{\mathrm{e}-1/3}\boldsymbol{F}^{\mathrm{e}} \tag{4.5}$$

is the deviatoric or unimodular elastic deformation. Without much loss of generality, we may assume that the deviatoric elastic deformations are small. Under these conditions, a simple form of the deviatoric part of the elastic energy density is:

$$W^{\mathrm{e,dev}} = \frac{1}{2}\boldsymbol{E}^{\mathrm{e,dev}} : \mathcal{C} : \boldsymbol{E}^{\mathrm{e,dev}} \tag{4.6}$$

where $\mathcal{C}$ is the elastic moduli tensor and

$$\boldsymbol{E}^{\mathrm{e,dev}} = \frac{1}{2}[(\boldsymbol{F}^{\mathrm{e,dev}})^{T}\boldsymbol{F}^{\mathrm{e,dev}} - \boldsymbol{I}] \tag{4.7}$$

is the deviatoric Lagragian elastic strain. The elastic properties of a cubic crystal are fully described by the three Voigt constants C_{11}, C_{12} and C_{44}. To a first approximation, the temperature dependence of the moduli may be taken to be linear, leading to the relation:

$$C_{ij}(T) = C^{0}_{ij} - T\, C^{1}_{ij} \tag{4.8}$$

This linear dependence of the elastic moduli on temperature is observed expreimentally, and can additionally be justified by recourse to statistical mechanics [127].

The volumetric strain energy density $W^{\mathrm{e,vol}}$ acts as a potential for the volumetric equation state, i. e.,

$$p = W^{\mathrm{e,vol}}_{,J}(J, T) \tag{4.9}$$

C_{11} (GPa)	C_{12} (GPa)	C_{44} (GPa)
$266.488 - 0.021T$	$156.248 - 0.006T$	$90.020 - 0.015T$

Table 4.1: Elastic moduli of Ta

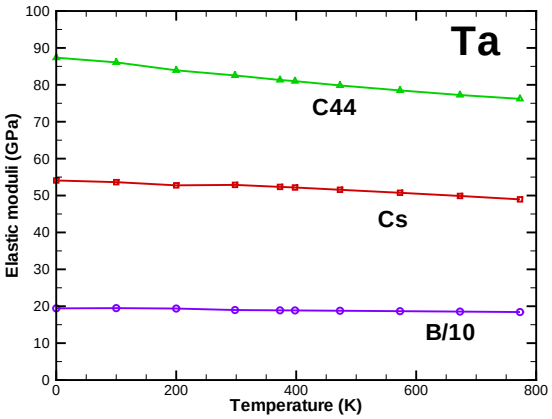

Figure 4.5: Dependence of elastic moduli on temperature (Simmons & Wang [110]), $C_s = (C_{11} - C_{12})/2$, $B = (C_{11} + 2C_{12})/3$.

where we have used the identity $J^{\mathrm{e}} = J = \det \boldsymbol{F}$ which results from the volume-preserving property of $\boldsymbol{F}^{\mathrm{p}}$. We adopt an equation of state of the Vinet form [121]

$$W^{\mathrm{e,vol}}(J,T) = \frac{9B_0}{\eta^2}\left\{1 - \left(1 - \eta(1 - J^{\frac{1}{3}})\right)\exp\left(\eta(1 - J^{\frac{1}{3}})\right)\right\} \tag{4.10}$$

where $\eta = \frac{3}{2}(B_0' - 1)$. The material parameters B_0 and B_0' are the bulk modulus and its pressure derivative at $J = 1$, respectively. These parameters depend on temperature only.

The temperature-dependent elastic moduli of Tantalum were obtained from tables collected by Simmons and Wang [110]. The values in those tables confirm a linear dependence on temperature, as illustrated in Figure 4.5. The exact numerical values are given in Table 4.1. Material parameters for the equation of state (4.10) have been fitted to results of molecular dynamics computations at different temperatures by Cohen *et al.* [17]. The resulting set of pressure vs. volume curves are illustrated in Figure 4.6.

Plastic deformations in single crystals are crystallographic in nature. The conventional flow rule in this case is of the form

$$\dot{\boldsymbol{F}}^{\mathrm{p}} = \left(\sum_{\alpha=1}^{N} \dot{\gamma}^{\alpha} \boldsymbol{s}^{\alpha} \otimes \boldsymbol{m}^{\alpha}\right) \boldsymbol{F}^{\mathrm{p}} \tag{4.11}$$

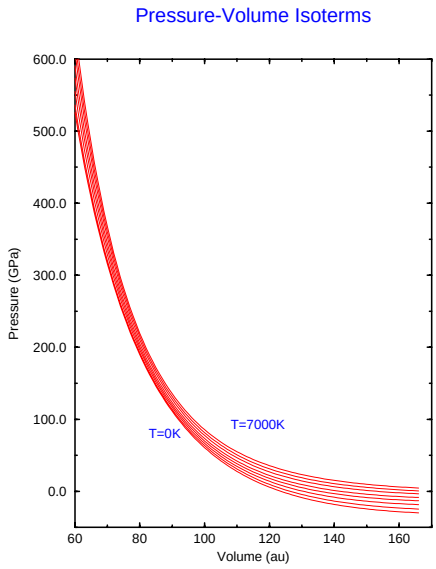

Figure 4.6: Equation of state (Cohen *et al.* [17])

where γ^α is the slip strain, and $\boldsymbol{s}^\alpha$, and $\boldsymbol{m}^\alpha$ are orthogonal unit vectors defining the slip direction and slip-plane normal corresponding to slip system α. The collection $\boldsymbol{\gamma}$ of slip strains is part of the internal variable set $\boldsymbol{Q}$. A zero value of a slip rate $\dot{\gamma}^\alpha$ signifies that the corresponding slip system α is inactive. The flow rule (4.11) allows for multiple slip, i. e., for simultaneous activity on more than one system over a region of the crystal. The vectors $\{\boldsymbol{s}^\alpha, \boldsymbol{m}^\alpha\}$ remain constant throughout the deformation and are determined by crystallography. For bcc crystals, we consider the 24 slip systems listed in Table 4.2 in the Schmid and Boas nomenclature.

Slip on the $\{112\}$ systems is known to be asymmetric: slip is easier when the applied stress is such that dislocations move in the twinning direction [45]. However, the experimental evidence [33] suggests that the extent of the twinning/anti-twinning asymmetry is relatively small. We account for this asymmetry simply by assigning different initial critical resolved shear stresses to the twinning and anti-twinning directions:

$$\tau_0^A > \tau_0^T = \tau_0^R \tag{4.12}$$

where the superscripts R, T and A refer to the $\{110\}$ systems, the $\{112\}$ systems with slip in the twinning direction and the $\{112\}$ systems with slip in the anti-twin direction, respectively. In calculations we simply assume the ratio $\tau_0^A = 1.05\tau_0^T$.

We have extended the statistical-mechanical treatment of the forest-dislocation mechanism of Cuitiño and Ortiz [84, 20] to account for obstacles of finite strength. We consider the motion of dislocations through a slip system α. The

Syst.	Direction	Plane	Syst.	Direction	Plane	Group
$A2$	$[\bar{1}11]$	$(0\bar{1}1)$	$A2'$	$[\bar{1}11]$	(211)	A
$A3$	$[\bar{1}11]$	(101)	$A3'$	$[\bar{1}11]$	$(12\bar{1})$	T
$A6$	$[\bar{1}11]$	(110)	$A6'$	$[\bar{1}11]$	$(1\bar{1}2)$	T
$B2$	$[111]$	$(0\bar{1}1)$	$B2''$	$[111]$	$(\bar{2}11)$	A
$B4$	$[111]$	$(\bar{1}01)$	$B4'$	$[111]$	$(1\bar{2}1)$	A
$B5$	$[111]$	$(\bar{1}10)$	$B5'$	$[111]$	$(11\bar{2})$	A
$C1$	$[11\bar{1}]$	$(0\bar{1}1)$	$C1'$	$[11\bar{1}]$	$(2\bar{1}1)$	T
$C3$	$[11\bar{1}]$	(101)	$C3''$	$[11\bar{1}]$	$(\bar{1}21)$	T
$C5$	$[11\bar{1}]$	$(\bar{1}10)$	$C5''$	$[11\bar{1}]$	(112)	A
$D1$	$[1\bar{1}1]$	$(0\bar{1}1)$	$D1''$	$[1\bar{1}1]$	$(21\bar{1})$	T
$D4$	$[1\bar{1}1]$	$(\bar{1}01)$	$D4''$	$[1\bar{1}1]$	(121)	A
$D6$	$[1\bar{1}1]$	(110)	$D6''$	$[1\bar{1}1]$	$(\bar{1}12)$	T

Table 4.2: Slip systems of bcc crystals

co-planar	glissile	weak sessile	strong sessile
1	1	1	2

Table 4.3: Relative junction strengths in Ta

motion of the dislocations is hindered by forest dislocations from secondary systems β threading the slip plane α. Forest dislocations react with primary dislocation to form point junctions. From a macroscopic point of view, the junction may be regarded as point obstacles. Pairs of such point obstacles arrest the primary dislocations, which require a certain threshold resolved shear stress s to overcome the barrier. The strength of the barrier is determined by line tension and by the strength of the point obstacles themselves.

The strength of the junctions depends on the type of dislocations forming the junction. Experimental estimates of junction strengths have been given by Franciosi and Zaoui [32] for the twelve slip systems belonging to the family of {111} planes and [110] directions in fcc crystals, and by Franciosi [33] for the twenty-four systems of types {211} [111] and {110} [111] in bcc crystals. For fcc crystals, they classify the interactions according to whether the dislocations belong to the same system, fail to form junctions, form Hirth locks, co-planar junctions, glissile junctions, or sessile Lomer-Cottrell locks, in order of increasing strength, while in bcc crystals, the Hirth lock does not exist and there are thus four categories of interactions. The strength of some of these obstacles has recently been computed by Baskes *et al.* [7] and Rodney and Shenoy [99] using atomistic models (see also Section 4.3 of this report). In our model we account four types of junctions: co-planar, glissile, weak sessile and strong sessile. Their assumed relative strengths are listed in Table 4.3.

The percolation-type motion of primary dislocations through the forest obstacles can be characterized analytically [84, 20, 113]. The resulting hardening

a_0	a_1	a_2
80×10^{-5}	$5.75a_0$	$7.5a_0$

Table 4.4: Tantalum interaction coefficients

relation is of the form:

$$\dot{g}^\alpha = h^\alpha \dot{\gamma}^\alpha \tag{4.13}$$

where g^α is the critical resolved shear stress on the primary system α due to the forest mechanism, and h^α is the corresponding self-hardening modulus, which is determined explicitly by the theory as a function of the obstacle densities. For instance, in the particular case of obstacles of the same strength one has:

$$h^\alpha = h_{\mathrm{c}}^\alpha \frac{g^{\alpha 3}}{\tau_{\mathrm{c}}^{\alpha 3}} \left[\cosh\left(\frac{\tau_{\mathrm{c}}^{\alpha 2}}{g^{\alpha 2}} \left(1 - \frac{g^{\alpha 2}}{s_{\max}^2} \right) \right) - 1 \right] \tag{4.14}$$

where

$$\tau_{\mathrm{c}}^\alpha = \frac{E^\alpha}{b} \sqrt{\pi n^\alpha} \quad \text{and} \quad h_{\mathrm{c}}^\alpha = \frac{\tau_{\mathrm{c}}^\alpha}{\gamma_{\mathrm{c}}^\alpha} \tag{4.15}$$

are a characteristic shear stress and plastic modulus, respectively, n^α is the obstacle density per unit area of the primary plane, E^α is the dislocation core energy per unit length and $s_{\max}$ is the obstacle strength. Equation (4.14) predicts an initial infinite hardening modulus at $\tau^\alpha = 0$. The hardening modulus subsequently decreases monotonically to zero as τ^α approaches $s_{\max}$.

The obstacle density on the primary plane is assumed to be related to the dislocation densities in all secondary systems by a geometrical relation of the form:

$$n^\alpha = \sum_\beta a^{\alpha\beta} \rho^\beta \tag{4.16}$$

where $a^{\alpha\beta}$ are interaction coefficients. Following Franciosi [33] we classify these interactions according to the colinearity of their slip direction, leading to the following values: a_0 for self-hardening, a_1 for colinear systems and a_2 for non-colinear systems. For Ta, numerical values for these parameters are collected in Table 4.4. Processes resulting in changes in dislocation density include production by fixed sources, such as Frank-Read sources, breeding by cross-glide and pair annihilation (see [57] for a review). The operation of fixed Franck-Read sources, however, usually stops after inducing a relatively small amount of plastic deformation. Consequently, production by fixed sources, while sometimes important during the early stages of plastic deformation, is quickly eclipsed by production due to cross-glide and can be safely neglected. Consideration of these multiplication mechanisms leads to a kinetic equation of the form:

$$\dot{\rho}^\alpha = \left(1 - \sqrt{\frac{\rho^\alpha}{\rho_{\mathrm{sat}}}} \right) \frac{\dot{\gamma}^\alpha}{\gamma_{\mathrm{sat}}} \tag{4.17}$$

where ρ_{sat} is a saturation density at which the rate of annihilation balances the rate of production, and γ_{sat} is a saturation shear strain. Eq. (4.17) defines a linear ordinary differential equation for ρ^α of solution

$$\rho^\alpha = \rho_{\text{sat}} \left[1 - \left(1 - \sqrt{\frac{\rho_0^\alpha}{\rho_{\text{sat}}}} \right) \exp\left(-\frac{\gamma^\alpha}{2\gamma_{\text{sat}}} \right) \right]^2 \tag{4.18}$$

where ρ_0^α is the initial dislocation density in system α, and we have assumed that $\gamma^\alpha(0) = 0$. In calculations we take $\rho_0 = 1{\times}10^{12}$ (m^{-2}) and $\rho_{\text{sat}} = 1{\times}10^{15}(\text{m}^{-2})$.

In addition to the forest obstacles, the crystal lattice itself offers some resistance to the movement of dislocation lines. The stress required to overcome the lattice resistance at $T = 0$ K is the Peierls stress τ_P. In bcc crystals, the $\langle 111 \rangle$ screw dislocation lines have a non-planar core, resulting in a relatively high Peierls stress compared to that of the edge dislocations. As a result, the dislocation population will consist primarily of long screw segments lying within Peierls valleys. At temperatures > 0 K, double-kinks may be nucleated by thermal activation, and slip may take place under a lower applied stress [45]. The kink-pair energy of formation cannot be reliably estimated from elasticity elasticity since is is composed mostly of core region. It can, however, be accurately computed from atomistic models [129]. For Mo at zero stress Xu and Moriarty [129] found formation energies $2E_k$ of the order of 1 eV for kinks separated by a distance greater than $L_k = 15b$. Standard arguments from critical state theory [113] lead to a rate-sensitivity relation of the form:

$$\tau^\alpha = g^\alpha(\gamma^\alpha) + \tau_P \frac{1}{\beta E_k} \text{asinh}\left[\frac{\dot{\gamma}^\alpha}{\dot{\gamma}_0} \exp(\beta E_k) \right] \tag{4.19}$$

Here, $\beta = 1/k_B T$ and, as before, g^α is the athermal flow stress due to the forest obstacles. Eq. 4.19 gives the temperature and strain rate dependence of the critical resolved shear stress, Fig. 4.7. The yield stress drops nearly linearly up to a critical temperature T_c, beyond which it rapidly tends to the athermal limit g^α. The critical temperature T_c increases with the strain rate. At very high strain-rates ($\dot{\gamma} > 10^4\ s^{-1}$) we additionally take electron and phonon drag into account, as these mechanisms become rate-limiting in that regime.

We additionally account for the temperature and strain-rate dependence of: the initial yield stress g_0, the dislocation line tension, the reference obstacle strength s_0 and the saturation slip strain γ_{sat}. We have found that consideration of these dependencies is required in order to match the experimental data. We have found empirically that all these dependencies can be described in a unified manner, in much the same way as the treatment given to the temperature and rate-dependency of the resolved shear stress discussed in the foregoing. In particular, in our model the effect of increasing (decreasing) the strain rate has the same identical effect to decreasing (increasing) the temperature, and viceversa, as argued by Tang *et al.* [115]. Details of the model may be found in [113]

Figs. 4.8 and 4.9 show the predicted stress-strain curves for a [213] Ta crystal and the their dependence on temperature and strain rate. It is evident from

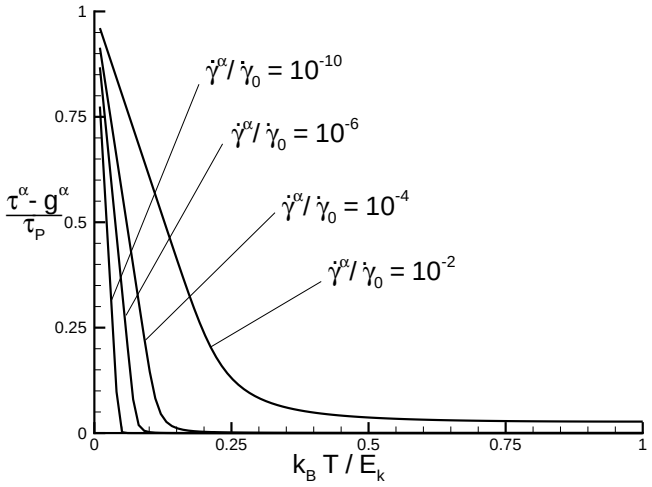

Figure 4.7: Temperature dependence of the yield stress for various strain rates. Note that the typical order of magnitude of $\dot{\gamma}_0 = 10^6\ s^{-1}$.

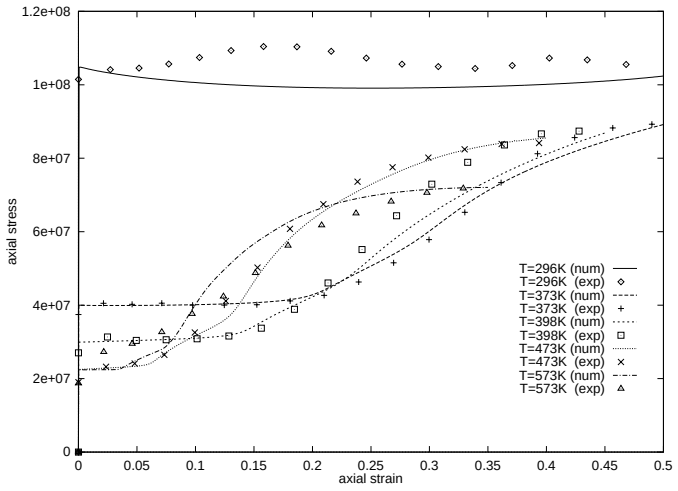

Figure 4.8: Temperature dependence of stress-strain curves for [213] single crystal Ta: predictions of the model and experimental data of Mitchell & Spitzig [78].

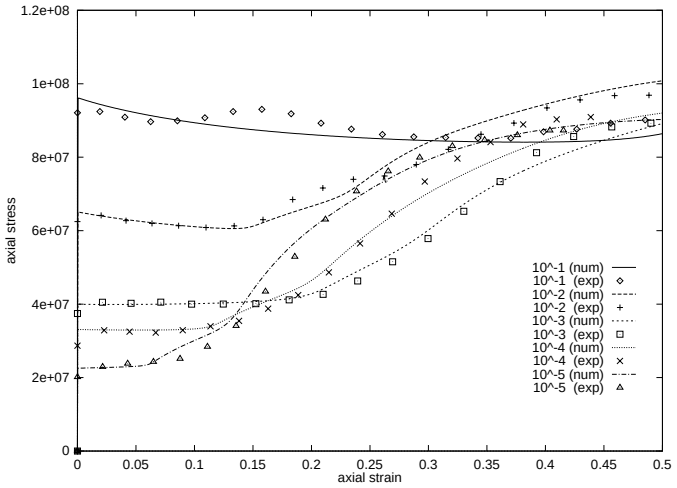

Figure 4.9: Temperature dependence of stress-strain curves for [213] single crystal Ta: predictions of the model and experimental data of Mitchell & Spitzig [78].

these figures that the model captures salient features of the behavior of Ta crystals such as: the dependence of the initial yield point on temperature and strain rate; the presence of a marked stage I of easy glide, specially at low temperature and high strain rates; the sharp onset of stage II hardening and its tendency to shift towards lower strains as the temperature increases; the initial parabolic hardening followed by saturation within the stage II of hardening; and the temperature and strain-rate dependence of the saturation stress.

4.5 Macromechanics

4.5.1 Verification of Lagrangian HE capability

We are in the process of evaluating several approaches for the integration of fluid and solid models: i) an Eulerian description for fluids coupled to a Lagrangian description of solids; ii) A fully Eulerian description of fluids and solids; and iii) a fully Lagrangian description of fluids and solids. The first approach combines the most conventional treatments of fluids (Eulerian) and solids (Lagrangian), but suffers from the difficulties inherent to the coupling of heterogeneous descriptions of mechanical and thermal behavior. The second and third approaches obviate this difficulty by giving all components of the model a unified treatment. Descriptions of solids within an Eulerian approach are compounded by the need to track material points, free surfaces, material interfaces, evaluate complex constitutive equations at fixed material points, and the need to account for elastic unloading and the development of residual stresses. Lagrangian descriptions of fluids are limited by deformation-induced mesh distortion and, consequently, their feasibility depends critically on the ability to continuously adapt the mesh.

The developments described elsewhere in this report, aimed at developing precisely one such adaptive-meshing capability, are ultimately what renders the fully Lagrangian approach viable.

The Lagrangian HE capability has been rather extensively verified over the past year, and highlights of this verification are reported next. The Lagrangian form of the governing field equations is:

$$\begin{aligned}
\rho_{0,t} &= 0, \text{ in } B_0 && (4.20)\\
\mathbf{F} &= \nabla_0 \boldsymbol{\varphi}, \text{ in } B_0 && (4.21)\\
\boldsymbol{\varphi} &= \bar{\boldsymbol{\varphi}}, \text{ on } \partial B_{01} && (4.22)\\
\rho_0 \boldsymbol{\varphi}_{,tt} &= \nabla_0 \cdot \mathbf{P}, \text{ in } B_0 && (4.23)\\
\mathbf{P} \cdot \mathbf{N} &= \bar{\mathbf{T}}, \text{ on } \partial B_{02} && (4.24)\\
\rho_0 E_{,t} &= \mathbf{P} \cdot \dot{\mathbf{F}} - \nabla_0 \cdot \mathbf{H}, \text{ in } B_0 && (4.25)
\end{aligned}$$

where $\boldsymbol{\varphi} : B_0 \times [t_1, t_2] \rightarrow \mathbb{R}^3$ is the deformation mapping defined over the fixed reference configuration B_0 of the continuum, ∇_0 is the material gradient over B_0, ρ_0 is the mass density per unit undeformed volume, $\mathbf{F}$ is the deformation gradient, $\bar{\boldsymbol{\varphi}}$ is the prescribed deformation mapping over the displacement boundary ∂B_{01}, $\mathbf{P}$ is the first Piola-Kirchhoff stress tensor, $\bar{\mathbf{T}}$ are the prescribed tractions over the traction boundary ∂B_{02}, $\mathbf{N}$ is the unit normal to ∂B_0, E is the internal energy per unit mass, and $\mathbf{H}$ is the heat flux field over B_0. All verification cases reported here are carried out assuming adiabatic conditions and, consequently, the heat flux field $\mathbf{H} = \mathbf{0}$ throughout. These field equations are closed by appending to them the following constitutive relations. We begin by assuming an additive decomposition of stress into equilibrium and viscous parts:

$$\mathbf{P} = \mathbf{P}^e + \mathbf{P}^v \tag{4.26}$$

The equilibrium response of the HE material is assumed to be Neo-Hookean in shear, which gives:

$$\mathbf{P}^e = -Jp\mathbf{F}^{-T} + (1 - \Lambda)\mu_0 \left(\mathbf{F} - \mathbf{F}^{-T}\right) \tag{4.27}$$

where $J = \det(\mathbf{F}) = \rho_0/\rho$ is the Jacobian of the deformation, p is the pressure, Λ is the undeformed volume fraction of unreacted material, and μ_0 is a shear modulus. Assuming Newtonian viscosity, the viscous stresses are of the form:

$$\begin{aligned}
\mathbf{P}^v &= J\boldsymbol{\sigma}^v\mathbf{F}^{-T} && (4.28)\\
\sigma^v &= 2\eta\mathbf{d}^{dev} && (4.29)\\
\mathbf{d}^{dev} &= sym\left(\dot{\mathbf{F}}\mathbf{F}^{-1}\right)^{dev} && (4.30)
\end{aligned}$$

where $\boldsymbol{\sigma}$ is the viscous part of the Cauchy stress tensor, η is the Newtonian viscosity, $\mathbf{d}$ is the rate-of-deformation tensor, and a superposed *dev* denotes the deviatoric part of the tensor. For purposes of verification we assume an equation of state of the Mie-Grüneisen form [80]:

$$p = \frac{\mathcal{G}\rho_0}{J}E + f(J, \Lambda) \tag{4.31}$$

where

$$f(J,\Lambda) = \mathcal{G}\Lambda Q\frac{\rho_0}{J} + \begin{cases} \rho_0 c_0^2 \frac{(1-J)}{[1-s(1-J)]^2}\left[1 - \frac{\mathcal{G}}{2J}(1-J)\right] & J \leq 1 \\ \rho_0 c_0^2\left(\frac{1}{J} - 1\right) & J > 1 \end{cases} \tag{4.32}$$

and a simple depletion law of the form:

$$\dot{\Lambda} = R(\Lambda, p) = \begin{cases} K\left(\frac{p}{p_{VN}}\right)^m (1-\Lambda)^{1/2} & p > \frac{p_{VN}}{3} \\ 0 & p \leq \frac{p_{VN}}{3} \end{cases} \tag{4.33}$$

where p_{VN} is the Von Neumann pressure. A set of independent unknown fields of the problem is $\{\boldsymbol{\varphi}(\mathbf{X},t), E(\mathbf{X},t), \Lambda(\mathbf{X},t)\}$, $\mathbf{X} \in B_0$, $t \in [t_1, t_2]$. In order to have a well-defined initial-value problem we need to append to the preceding equations initial conditions for all the independent fields, i. e.,

$$\boldsymbol{\varphi}(\mathbf{X},0) = \boldsymbol{\varphi}_0(\mathbf{X}), \quad \mathbf{X} \in B_0 \tag{4.34}$$

$$\boldsymbol{\varphi}_{,t}(\mathbf{X},0) = \mathbf{V}_0(\mathbf{X}), \quad \mathbf{X} \in B_0 \tag{4.35}$$

$$E(\mathbf{X},0) = E_0(\mathbf{X}), \quad \mathbf{X} \in B_0 \tag{4.36}$$

$$\Lambda(\mathbf{X},0) = 0, \quad \mathbf{X} \in B_0 \tag{4.37}$$

where $\boldsymbol{\varphi}_0$ is the initial deformation mapping, $\mathbf{V}_0$ is the initial velocity field, E_0 is the initial internal energy density field, and, for definiteness, we set the initial time $t_1 = 0$ and assume that the HE material is initially unreacted.

The time discretization of the problem is effected by recourse to Newmark explicit algorithm with $\beta = 0, \gamma = 1/2$. The domain is discretized into quadratic 6-node triangular elements in two dimensions, and into quadratic ten-node tetrahedral elements in three dimensions. The constitutive updates are carried out at the Gauss points of the elements by means of a Runge-Kutta-type method.

We have tested the Lagrangian HE capability just described in two and three-dimensional configurations. The domain of the two-dimensional test cases is a $10^{-4} \times 10^{-5}$ m^2 rectangular chamber. The walls of the chamber are assumed to be rigid. The detonation and subsequent flow of the reacted products is driven from the left by a piston traveling at speed $V_0 = 2176.932$ m/s, which matches the particle speed in a Chapman-Jouguet detonation. The piston comes in contact with the HE material at the speed V_0 at $t = 0$. All three dimensional test cases simulate a similar piston driven detonation and flow in a cylinder of radius 0.8×10^{-5} m and length 10^{-6} m. The values of the parameters used for in calculations are collected in Table 4.5. A converged one-dimensional solution was also computed with a very small grid size equal to 0.5×10^{-7} the length of the tube. This one-dimensional solution effectively stands in for the exact solution and is taken as a basis for assessing the accuracy of the multi-dimensional solutions.

The number of elements and nodes in each test case are shown in Table 4.6. A typical mesh used in the three-dimensional test cases in shown in Figure 4.10. All meshes are generated automatically with our own variant of the advancing

ρ_0	η	Q	μ_0	C	c_0	K	$\mathcal{G}$	s	m
1891	1	14.7×10^6	0	20	3070	3.5×10^9	0.7	1.79	0

Table 4.5: Values of the material parameters

Case	#elements	#nodes
1	212854	427905
2	52718	106533
3	253432	351341

Table 4.6: Mesh statistics for 2D and 3D test cases

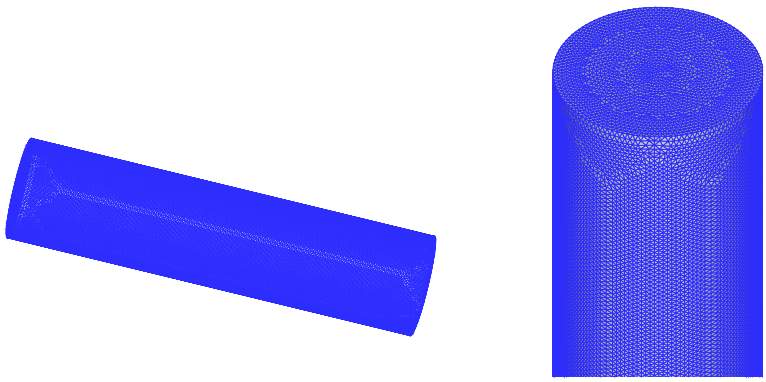

(a) (b)

Figure 4.10: Mesh used in test case 3. a) Overall view. b) Zoom.

front method [93]. The resulting two-dimensional meshes are nearly perfectly hexagonal, with an occasional irregular vertex. The resulting three-dimensional meshes are structured so that the nodal set defines a regular fcc lattice almost everywhere. The time step is set automatically to $0.05 - 0.1$ the stable time step for explicit integration.

Contours of pressure, fraction of unreacted material and particle velocity are shown in Figure 4.11 for the two dimensional test cases, and in 4.13 for the three-dimensional cases. Figure 4.12 depicts the time evolution of the pressure field in a two-dimensional test case.

As mentioned earlier, the results of the converged one-dimensional solution have been used as a basis for assessing the accuracy of the multidimensional calculations. Comparisons have been made both during the initial transient

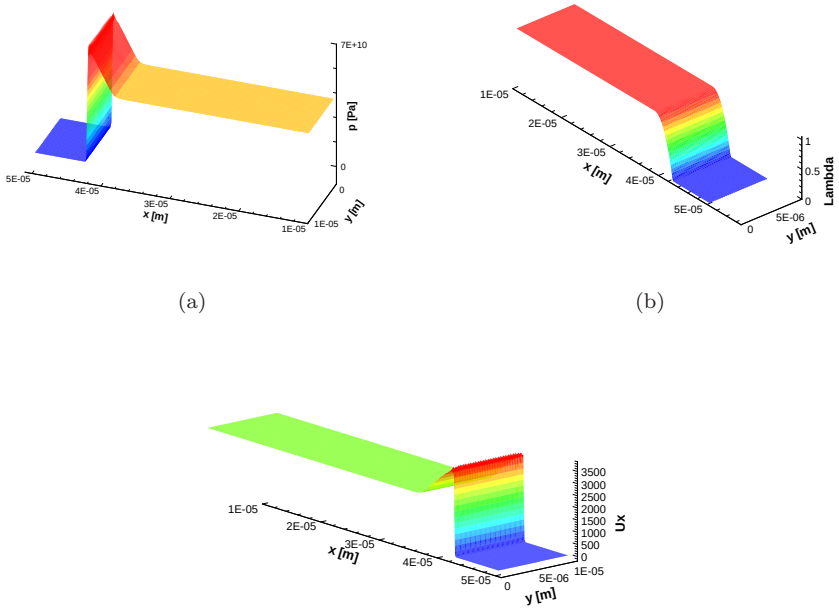

(a) (b)

(c)

Figure 4.11: Computed fields for the two-dimensional test case 3. a) Pressure. b) Fraction of unreacted HE material. c) Axial particle velocity.

regime and at later times following the development of an ostensibly steady profile. The transient two-dimensional solutions are shown in Figures 4.14 and 4.15, the latter being the most accurate of the two, whereas the steady two-dimensional solutions are shown in Figures 4.16 and 4.17. All profiles correspond to the centerline of the container. As may be seen from these figures, the accuracy of the finite-element solutions is excellent. The results collected in Table 4.7 also demonstrate how detonation parameters are well-captured by the finite-element solution, as well as the general trend towards convergence with regular mesh refinement.

A similar comparison has been carried out between the three-dimensional finite-element solutions and the converged one-dimensional solution in the transient regime. Solution profiles along the axis of the cylinder are shown in Figure 4.18. Here again, the good accuracy of the three-dimensional finite-element solution is evident in the figure.

As an application of the verified Lagrangian HE capability we have carried out a coupled solid/HE calculation in the VTF2D configuration. The calculation concerns the detonation of an HE material within a steel container. The material

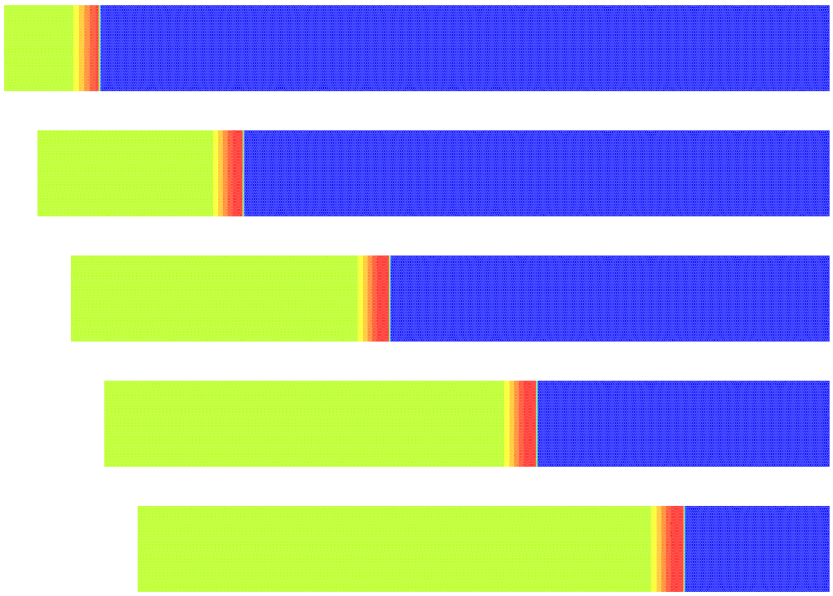

Figure 4.12: Time-evolution of pressure field at time intervals of 1.78^{-9} seconds

Case	p_{CJ} [GPa]	v_{CJ} [m^3/ton]	p_{VN} [GPa]	v_{VN} [m^3/ton]	D [m/s]
Theoretical	39.51	0.4089	66.17	0.3279	9596
4	39.56	0.4069	65.73	0.3300	9595
1	39.51	-	64.03	-	9512
2	39.61	-	64.73	-	9730

Table 4.7: Calculated detonation parameters

parameters adopted in the calculation are shown in Tables 4.8 and 4.9. The HE material is initially undetonated and at rest. A velocity $V_0 = 2176.932$ m/s is suddenly applied to the left end of the HE material at $t = 0$ and held constant thereon. Figure 4.19 shows the time evolution of the pressure field, as well as the deformation of the steel container. Figure 4.20 depicts a snapshot of the unreacted volume fraction Λ.

This calculation demonstrates the relative ease with which the Lagrangian treatment of the HE material permits its coupling to highly-deformable solids. Indeed, since both the HE and the solid components are represented in an identical manner, all compatibility conditions at material boundaries are trivially satisfied. The penalty to be paid is that, for the calculations to be possible, the

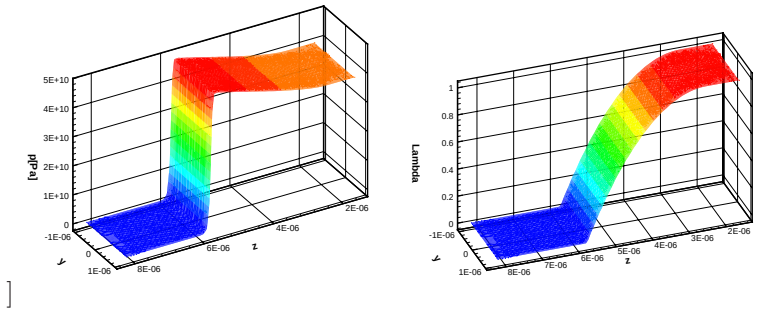

(b)

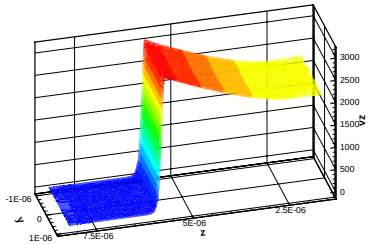

(c)

Figure 4.13: Longitudinal section of computed fields for the three-dimensional test case 3. a) Pressure. b) Fraction of unreacted HE material. c) Axial particle velocity.

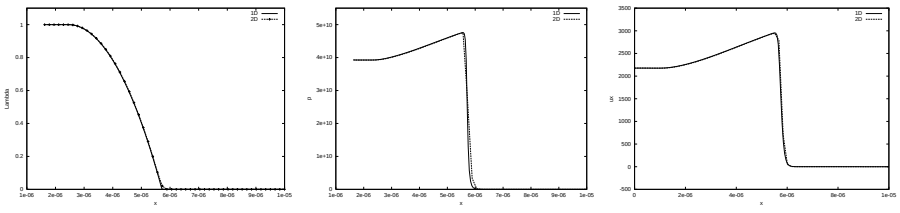

Figure 4.14: Converged one-dimensional solution *vs.* two-dimensional solution in the transient regime.

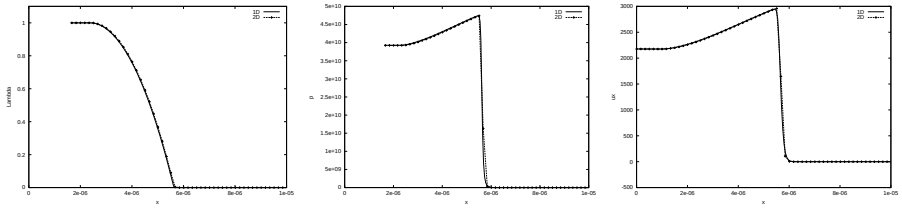

Figure 4.15: Converged one-dimensional solution *vs.* two-dimensional solution in the transient regime.

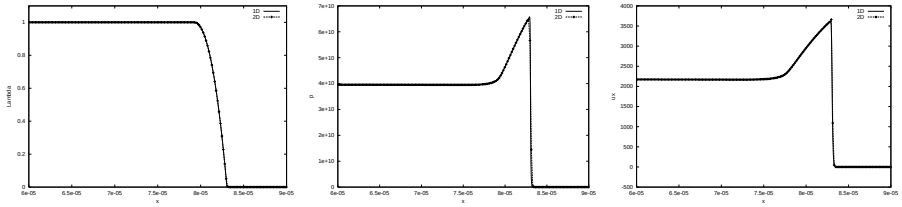

Figure 4.16: Converged one-dimensional solution *vs.* two-dimensional in the steady regime.

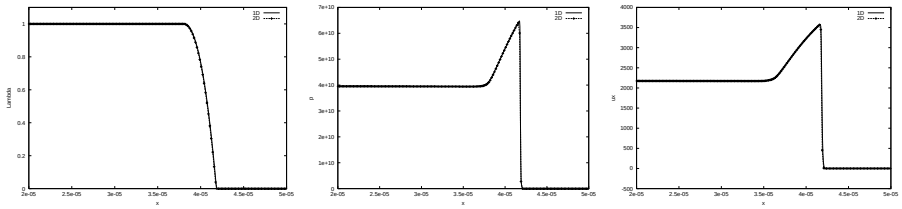

Figure 4.17: Converged one-dimensional solution *vs.* two-dimensional solution in the steady regime.

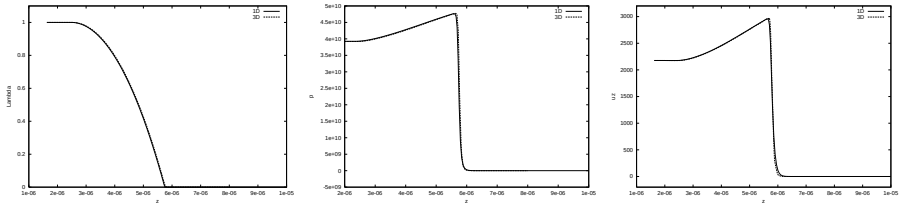

Figure 4.18: Converged one-dimensional solution *vs.* three-dimensional solution in the transient regime.

ρ_0	η	Q	μ_0	C	c_0	K
1891	1000	14.7 10^6	0	20	3070	2×10^6

$\mathcal{G}$	s	m	tolrel	tolabs	igf
0.7	1.79	0	10^{-9}	10^{-12}	.2

Table 4.8: HE material constants used in the VTF2D application.

	ρ_0	E	ν
Wall	7800	210×10^9	0.3

Table 4.9: Steel material constants used in the VTF2D application.

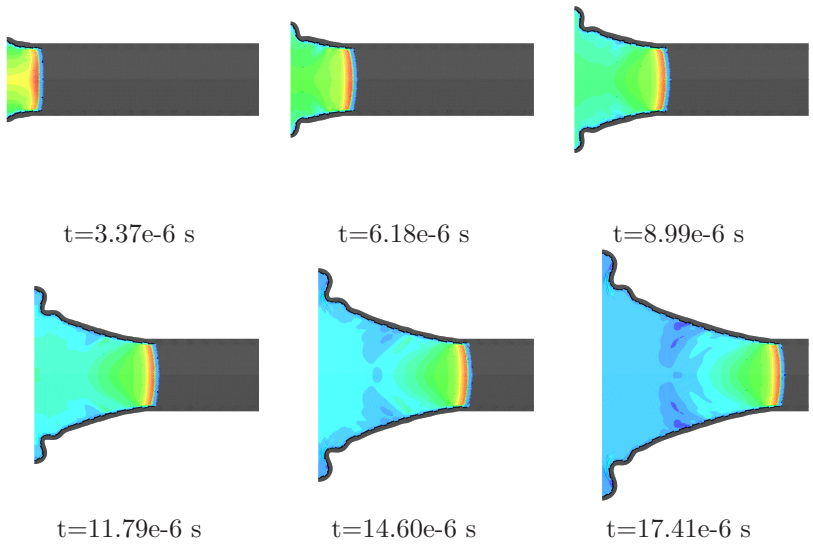

Figure 4.19: Pressure field evolution in the VTF2D application.

computational mesh must be continuously adapted. This issue is taken up in Section 4.5.2.

4.5.2 Development of adaptive mesh refinement and coarsening capability

One of the principal activities of this past year has been the development, verification and validation of an adaptive mesh refinement and coarsening capability. Mesh adaption is a critical aspect of the Lagrangian capability envisioned in the project, as it enables the simulation of unconstrained flows by eliminating the

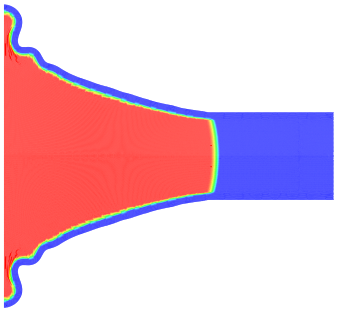

Figure 4.20: Unreacted volume fraction field in the VTF2D application.

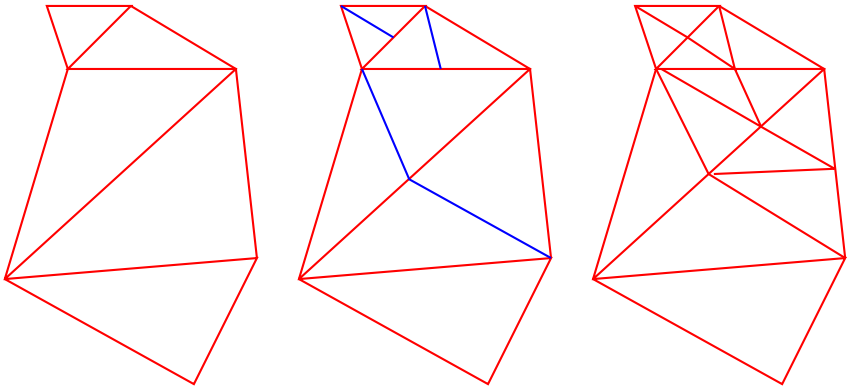

Figure 4.21: Illustration of Rivara's [97] longest-edge subdivision algorithm. Upper left triangle to be subdivided (left). Blue segments mark the longest edge propagation path (middle). Final subdivided mesh (right).

deformation-induced mesh distortion; it enables the resolution of fine features of the solution such as shear bands; when based on error estimation, it optimizes the accuracy of the solution and minimizes the computational expense. All calculations carried out to date are based on the method of *a posteriori* error estimation and remapping for strongly nonlinear dynamic problems developed by Radovitzky and Ortiz [92].

Of all the refinement strategies evaluated so far, those which are based on subdivision have been found to be the fastest and most robust. We have implemented Rivara's [97, 96] longest-edge bisection algorithm in two and three dimensions. Rivara's algorithm has the appealing feature that it guarantees as lower bound to the aspect ratio of the elements. This is particularly important in

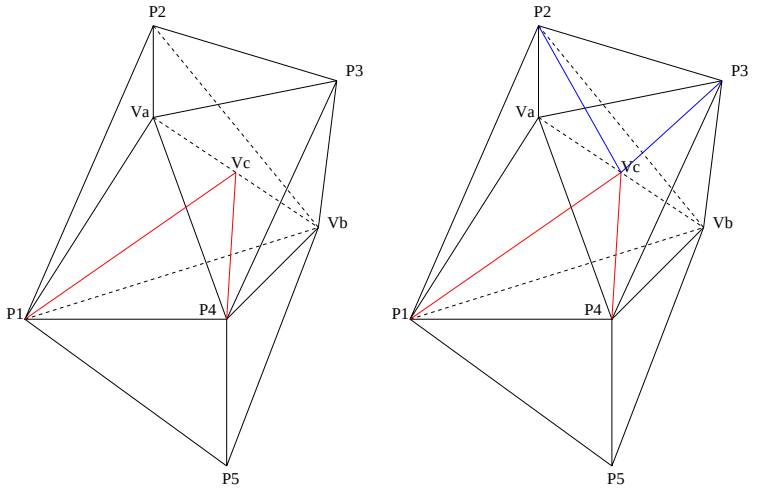

Figure 4.22: Illustration of three-dimensional longest-edge subdivision algorithm, interior edge. Segment (V_a, V_b) to be subdivided, new segments shown in red and blue.

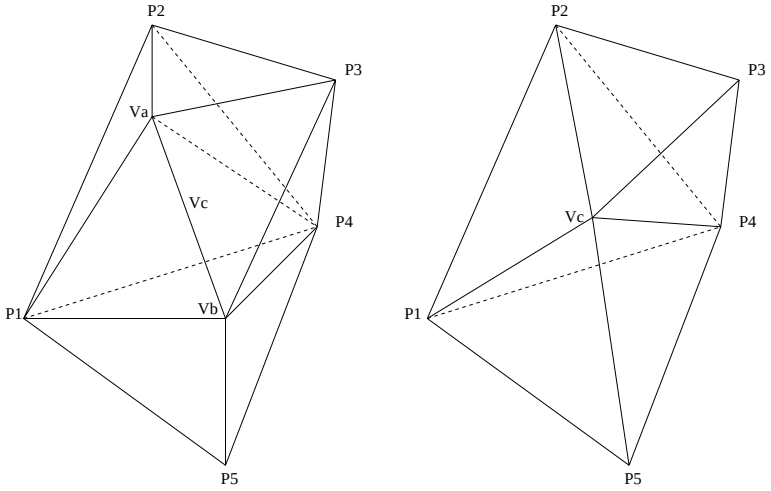

Figure 4.23: Illustration of three-dimensional edge-collapse mesh-coarsening algorithm, interior edge. Nodes V_a and V_b are collapsed onto node V_c.

explicit dynamics, since bad elements may have the deleterious effect of greatly reducing the critical time step for explicit integration. Rivara's algorithm is shown schematically in Figure 4.21. In collaboration with Peter Schröder of CS, we have developed an approach to mesh coarsening based on edge collapse, a technique first developed in the field of computer graphics [112, 44, 53, 106].

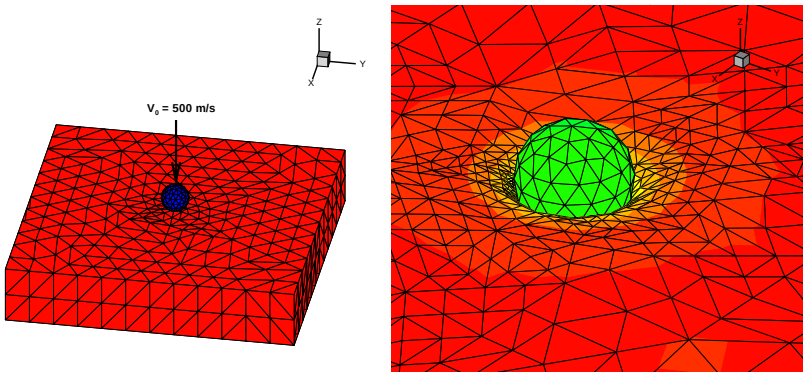

(a) (b)

Figure 4.24: Steel sphere impacting an elastomeric plate at normal incidence. a) Test conditions. b) Adapted mesh at point of maximum penetration.

Figs. 4.22 and 4.23 depict some of the basic operations involved in the three-dimensional implementation of bisection. Special rules need to be adopted when bisecting and collapsing edges which are contained within, or are incident to, surfaces.

We have validated the Lagrangian capability in a number of experimental configurations. Figure 4.5.2 shows one snapshot of a simulation of the erosive wear tests of Hutchings [47, 46, 117, 118] for the particular case of elastomers subjected to normal or glancing impact by small hard particles. Good agreement has been found between the predictions of the model and the experimental measurements. The variation of erosion rate with impact velocity, impact angle, particle size, elastic modulus of the material, coefficient of friction and fatigue properties are all accounted for. This simulation showcases the contact/friction algorithm and the adaptive remeshing algorithm in the presence of inertia effects and large deformations.

We have also simulated the Ta cylinder implosion tests of Nesterenko [16, 82] as a means of further validating the Lagrangian capability. In these tests, Tantalum was subjected to high plastic strains (global effective strains between 0 and 3) at high strain rates (in excess of 10^4 s^{-1}). Tubular specimens, embedded in thick-walled cylinders made of copper, were collapsed quasi-uniformly by placing a explosive charge co-axially with the thick-walled cylinder. Microstructural features observed included subgrain dislocation structures such as modeled within the group [85]. Grain-scale localization produced by anisotropic plastic flow and localized recovery and recrystallization was observed at the higher plastic strains. Residual tensile 'hoop' stresses are generated near the central hole region upon unloading; this resulted in ductile fracturing along shear lo-

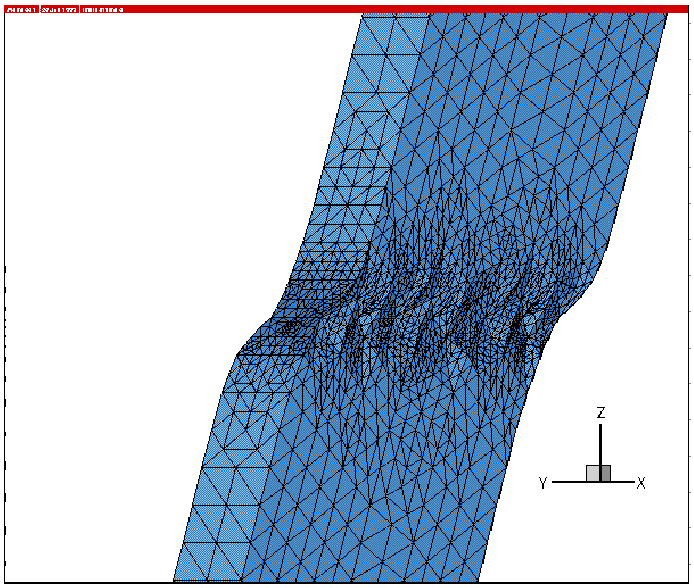

Figure 4.25: Three-dimensional simulation of adiabatic shear banding in Ta.

calization bands. Figure 4.5.2 shows a simulation of adiabatic shear banding in Ta under conditions closely matching those of Nesterenko's experiments. The simulation showcases the ability of the adaptive meshing capability to resolve the three-dimensional shear band structure under dynamic conditions and large plastic deformations. The microshear bands which form within the main band are also noteworthy.

Finally, a detail of the detonating HE charge in a preliminary full Lagrangian simulation of the VTF3D is shown in Figure 4.26. The calculation exercises a complete three-dimensional model of the VTF3D, including a copper canister, a detonator, Ta and Al test materials, and a HE charge. The simulation makes use of the verified Lagrangian HE capability presented in Section 4.5.1. The simulation showcases our present three-dimensional mesh-adaption capability. Thus, as my be seen from the figure, the initial coarse mesh, Figure 4.26a, undergoes several levels of refinement as the detonation front passes by, and is subsequently coarsened behind the front, Figure 4.26b.

4.6 FY 00 objectives

Tasks to be completed by the end of FY00:

- Unstructured meshing in 2D and 3D:
  - Adaptive meshing using subdivision and edge-collapse.
  - Parallel implementation of 2D and 3D meshing algorithms.

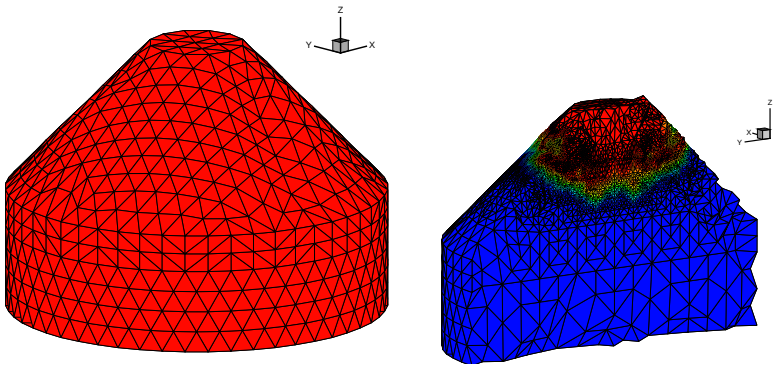

Figure 4.26: Detail of the HE charge in a Lagrangian simulation of the VTF3D showcasing three-dimensional mesh-adaption capability. Level contours depict the volume fraction of unreacted product.

  - Further algorithmic developments related to the VTF3D.

- Mixed atomistic-continuum modeling:
  - Development of 3D dynamic atomistic-continuum models with defects.
- Constitutive modeling:
  - Integration of fragmentation and non-smooth contact.
  - Improvement of single-crystal plasticity models.
  - Integration of subgrain structure models.
  - Validation of Lagrangian HE models.
- Equations of state for polymorphic materials:
  - Development of models for mixed-phase release isentropes.
- Software integration:
  - Integrated 3D simulation with Eulerian fluid solver.
- Integrated fully lagrangian simulations:
  - Integrated 2D simulation with verified HE models.
  - Integrated 3D simulation with verified HE models

Chapter 5

Materials Properties

5.1 Overview of FY 99 Accomplishments

5.1.1 High Explosives

- Binder and grain interactions for Kel-F and Estane;
- Equations of state for HMX and TATB;
- Reaction dynamics and molecular processes;
- Reaction networks for RDX and HMX.

5.1.2 Solid Dynamics

- Equations of state for Ta, Fe, Oxides, and Ceramics;
- Phase transition studies of Ta, Carbon, and Ceramics;
- Constitutive equations describing:
    1. Elastic properties of metals, alloys, and ceramics;
    2. Thermodynamic properties;
    3. Plasticity and behavior under large strain rates.

5.1.3 Software Integration

- Integration of MP code with HE;
- Self-integration of MP code.

5.2 Personnel

5.2.1 Senior Researchers

- William A. Goddard, III (Caltech MSC)
- Tahir Cagin (Caltech MSC)
- Ronald Cohen (Carnegie Institute, Washington)
- Siddharth Dasgupta (Caltech MSC)
- Richard P. Muller (Caltech MSC)

5.2.2 Postdoctoral Fellows

- Gregg Caldwell (Caltech MSC)
- Debashis Chakraborty (Caltech MSC)
- Jianwei Che (Caltech MSC)
- Oguz Gulseren (Carnegie Institute, Washington)
- Daniel Mainz (Caltech MSC)
- S. Mukherjee (Carnegie Institute, Washington)
- Enrique Pifarre (Caltech MSC)
- Alejandro Strachan (Caltech MSC)
- Yanhua Zhou (Caltech MSC)

5.2.3 Graduate Students

- Weiqiao Deng (Caltech MSC)
- Michael Feldmann (Caltech MSC)
- Hao Li (Caltech MSC)
- Ryan Martin (Caltech MSC)
- Yue Qi (Caltech MSC)
- Guofeng Wang (Caltech MSC)
- Georgios Zamanakos (Caltech MSC)

5.2.4 Undergraduate Students

- Wren Montgomery (Caltech MSC)

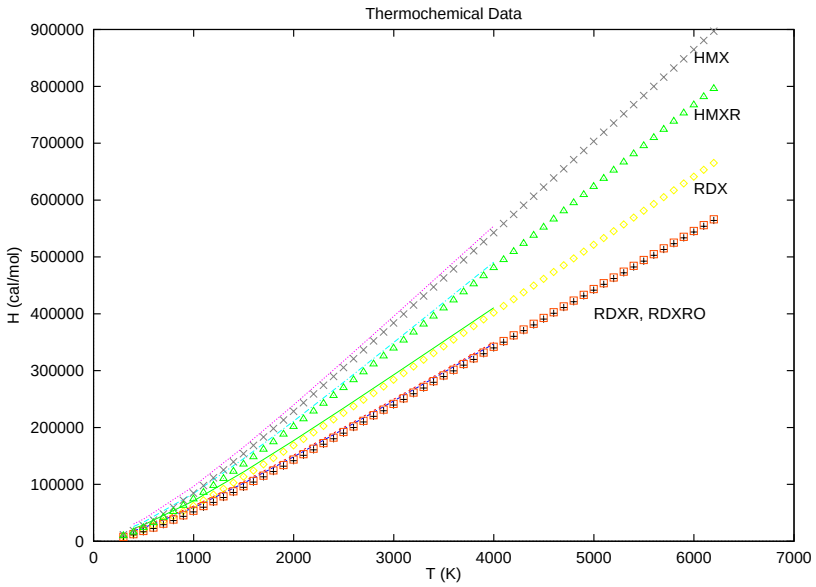

Figure 5.1: Quantum chemical data (points) and fit to NASA thermochemical form (lines) for the enthalpy of the additional species required in the reaction network model.

5.2.5 Professional Staff

- Darryl Willick (Caltech MSC)

5.3 Materials properties for high explosives

5.3.1 Reaction Network Model for RDX and HMX

During the past year we have developed a detailed reaction network model for nitramine detonation. We first took existing models for nitromethane and RDX detonation and added additional species so that the mechanisms could also describe HMX detonation. This extension required the quantum chemical calculation of additional thermochemical data, and the fit of these data to the NASA standard form. Both the data and the fit are shown in Figures 5.1–5.3.

Figures 5.4 and 5.5 show the application of this model to RDX and HMX combustion, respectively. Validation of this model is particularly difficult, as little experimental data exists for HMX and RDX. We have compared the results of simulations on nitromethane to the shock tube data generated by Guirguis [36]. This comparison is shown in Figure 5.6.

5.3.2 Unimolecular decomposition of RDX

During this year we have also undertaken a detailed study of the initial decomposition steps in RDX and HMX. The nitramines, hexahydro-1,3,5-trinitro-1,3,5-

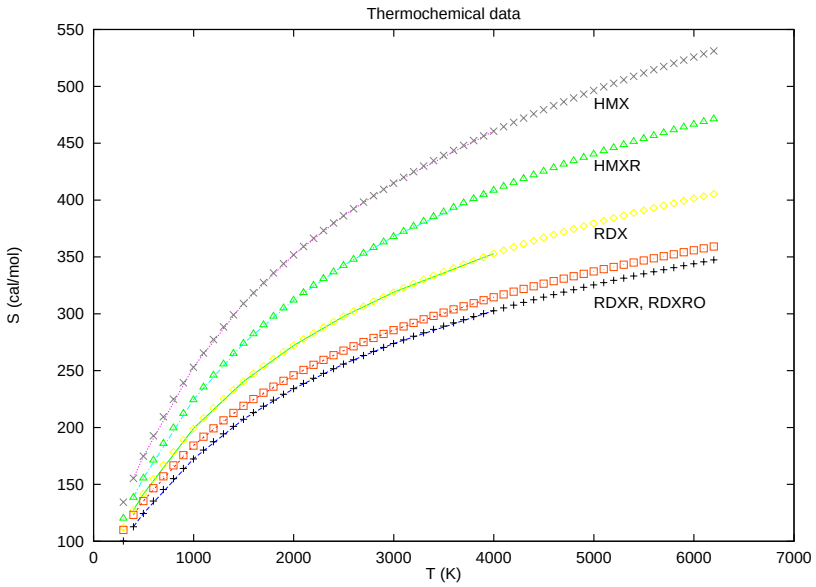

Figure 5.2: Quantum chemical data (points) and fit to NASA thermochemical form (lines) for the entropy of the additional species required in the reaction network model.

triazine (RDX), and octahydro-1,3,5,7- tetranitro-1,3,5,7-tetrazocine (HMX), are important energetic ingredients, used in applications ranging from automobile air bags to rocket propellants and explosives, since they release a large amount of energy in bulk decomposition. Thermal decomposition of these energetic materials has been observed to form very simple final product molecules, such as, HCN, NO, N2O, NO2, CO, CO2, H2O, H2CO, etc. Understanding the underlying complex chemical processes is essential to obtain to an improved model for combustion or detonation of these energetic materials.

A number of experimental studies have been directed toward elucidating the mechanistic details of the thermal decomposition of RDX, and HMX and various plausible reaction pathways have been proposed. Most of these experiments dealt with bulk phase materials, including decomposition in the condensed phase (solid or liquid) and the gas phase flame structure near the burning surface. In order to determine the initial steps of decomposition for these condensed phase studies, we focused on the gas phase pyrolysis. Mechanistic details of unimolecular decomposition of these energetic materials in gas phase have been examined here using first principles quantum mechanics (ab initio density functional theory (DFT) with a modest 6-31G(d) basis set).

For the unimolecular decomposition of RDX, we find three pathways:

1. Concerted decomposition of the ring to form three CH_2NNO_2 ($M = 74$) molecules (Figure 5.7).

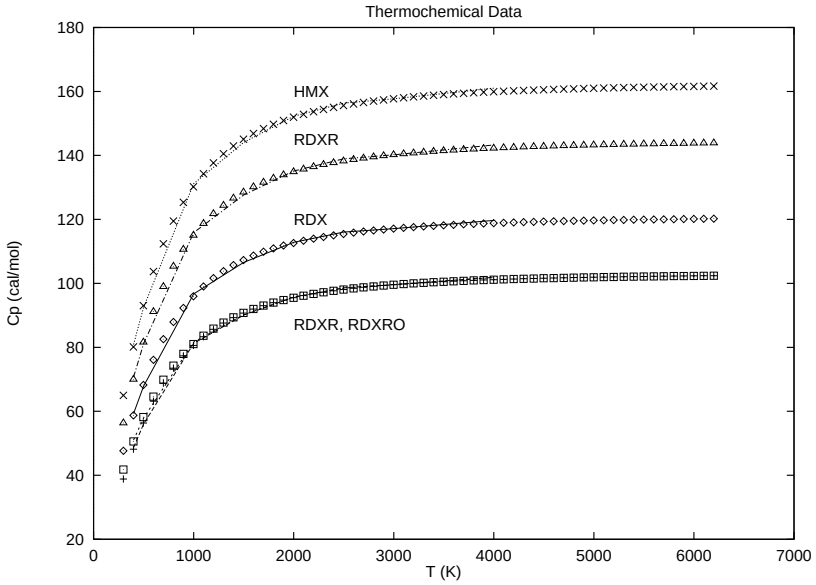

Figure 5.3: Quantum chemical data (points) and fit to NASA thermochemical form (lines) for the heat capacity of the additional species required in the reaction network model.

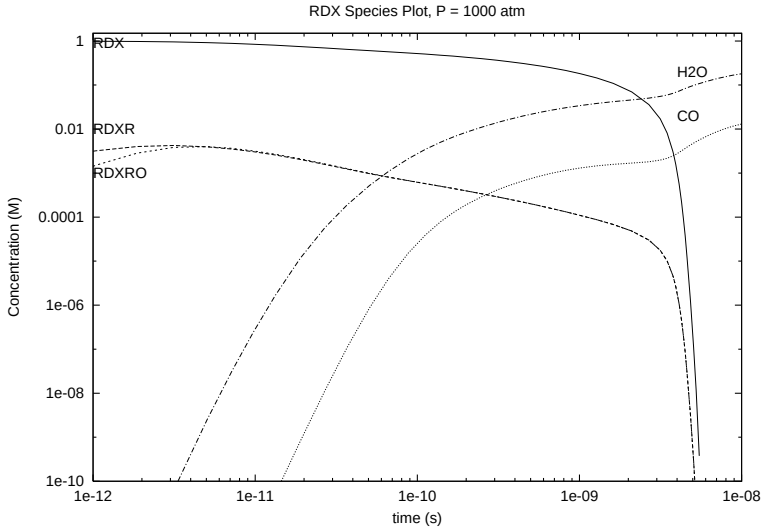

Figure 5.4: Major species profile for RDX detonation. The initial conditions are T=1500 K and P=1000 atm.

2. Homolytic cleavage of an NN bond to form NO_2 ($M = 46$) plus RDR ($M = 176$) which subsequently decomposes to form various products (Figure

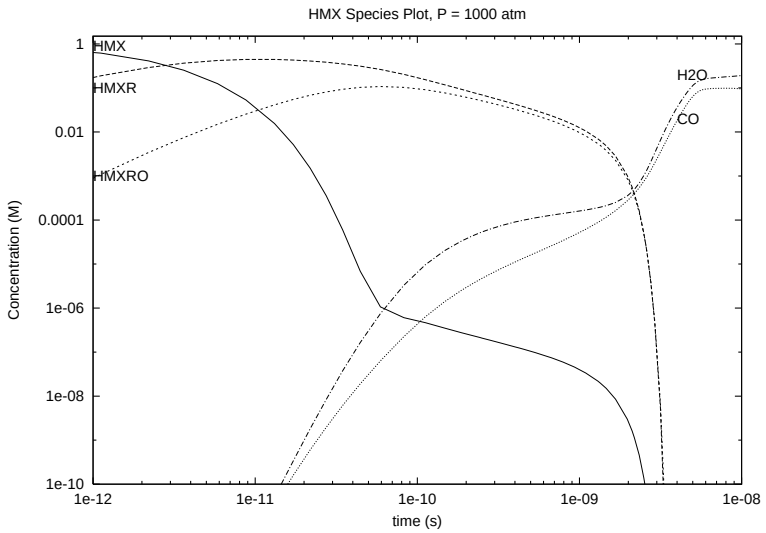

Figure 5.5: Major species profile for HMX detonation. The initial conditions are T=1500 K and P=1000 atm.

5.8). This pathway had been considered to be one of the most important decomposition pathways for RDX, both experimentally and theoretically.

3. Successive HONO elimination to form 3 HONO ($M = 47$) plus stable 1,3,5-triazine (TAZ) ($M = 81$) with subsequent decomposition of HONO to HO ($M = 17$) and NO ($M = 30$) and at higher energies of TAZ into three HCN ($M = 27$) (Figure 5.9).

These predictions (energetics and mechanisms) are roughly consistent with previous gas phase experimental results of RDX decomposition.

Similarly, two distinct decomposition pathways have been identified for the unimolecular decomposition of HMX. Our theoretical calculations reveal that the concerted decomposition of HMX molecule to four MN molecular fragments is not a favorable pathway:

1. Homolytic cleavage of N-N bond to form NO2 ($M = 46$) plus HMXR ($M = 250$) which subsequently decomposes to form various products (Figure 5.10). This is one of the two major global reactions considered in the condensed phase decomposition of HMX.

2. Successive HONO elimination to form 4 HONO ($M = 47$) plus stable intermediate (INT108) with subsequent decomposition of HONO to HO (M=17) and NO (M=30) and at higher energies of INT108 into four HCN (M=27) (Figure 5.11).

Our calculation clearly shows that for both RDX and HMX successive HONO elimination leading to the formation of TAZ (81) and INT108 respectively is

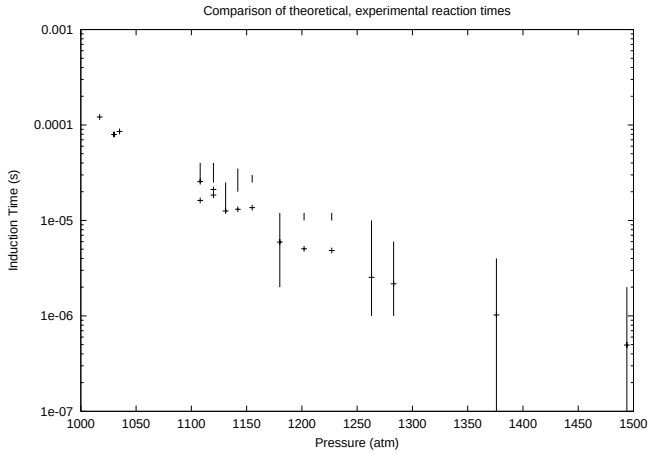

Figure 5.6: Validation of the results of our model (points) with Guirguis' shock tube data (bars).

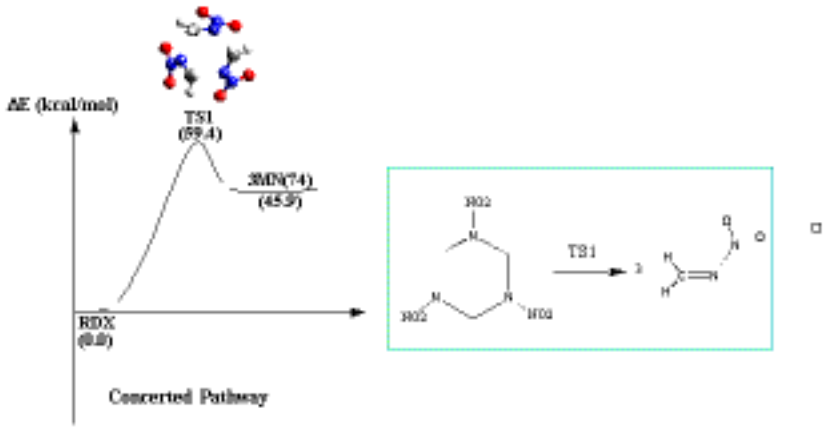

Figure 5.7: Concerted reaction pathway for RDX

the most exothermic decomposition pathway. N-N homolysis is also an energetically favorable initiation process but the associated endothermicity for further decomposition makes this channel less favorable than the HONO elimination pathway. Furthermore, the present scheme could account for majority of the observed mass fragments in condensed phase decomposition of RDX and HMX.

Thermochemical quantities (Cv, H, S etc.) of all the reactants, intermediates and products were then computed at the same B3LYP/6-31G(d) level of theory and fit to the 14 term NASA form. Rate constants for each of the unimolecular decomposition pathways were then computed. Detailed reaction kinetics for early stage gas phase reactions related to RDX and HMX combustion

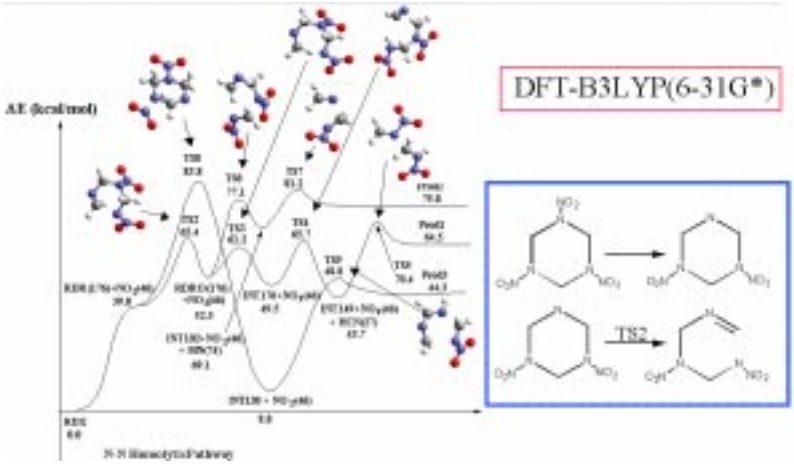

Figure 5.8: Homolytic NN cleavage in RDX

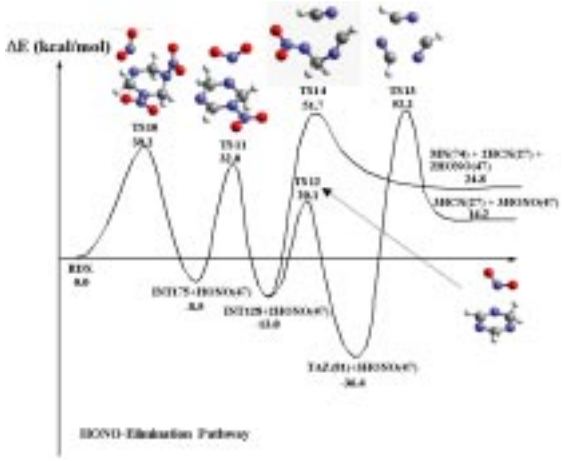

Figure 5.9: HONO Elimination Pathway for RDX

- CH_2N reactions with NO_x, N_2O, OH, etc.
- decomposition of CH_2NNO_2, CH_2NNO, etc.

were also incorporated in the reaction mechanism. The final mechanism, based collectively on the GRI nitromethane mechanism, Melius nitromethane mechanism, Yetter RDX mechanism and the new decomposition scheme for RDX and HMX, consists of 85 species and 461 reactions. This was used in detailed modeling of HE detonation. The species profile of the HMX detonation model is shown below (Figure 5.5).

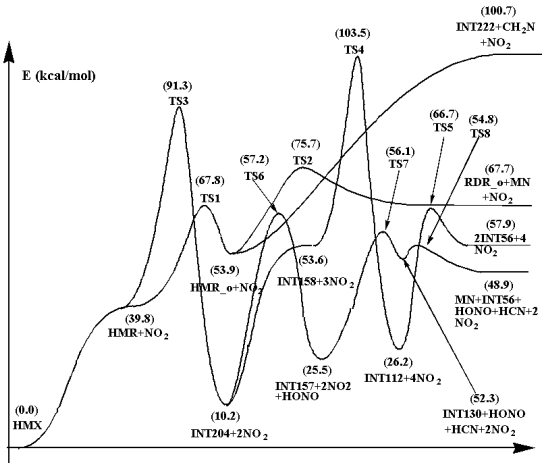

Figure 5.10: Homolytic NN cleavage in HMX

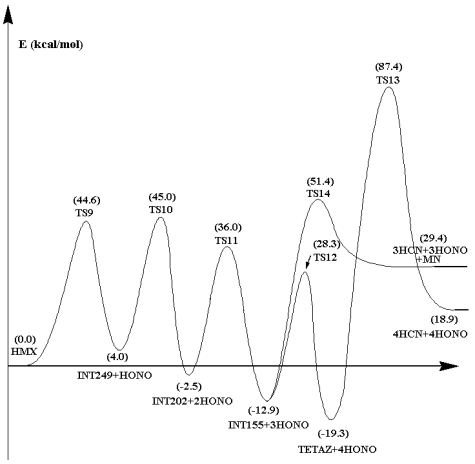

Figure 5.11: HONO Elimination Pathway in HMX

5.3.3 Modeling Pure HEDM materials

In order to provide first principles materials properties of different high energy density materials (TATB, HMX, RDX) as well as polymeric binders used in primary explosives, we have undertaken ab initio and molecular dynamics simulations of these materials. The following section summarizes the progress made in the 2nd year of this project.

TATB

To calculate the intra- and inter-molecular potential for TATB in the condensed phase, we need to develop a vibrationally accurate force field. To model the

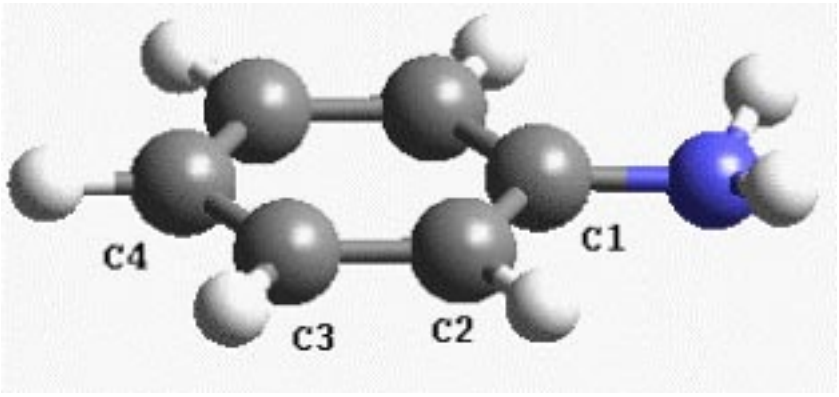

	Inversion	NH	NC	C1-C2	C2-C3	C3-C4	HNH	C6C1C2	C1C2C3	C2C3C4	C3C4C5
MW Expt.	39.4	1.001	1.402	1.397	1.394	1.396	113.9	119.4	120.1	120.7	118.9
DFT	39.1	1.011	1.406	1.399	1.393	1.396	111.6	118.6	120.5	120.7	119

Figure 5.12: Comparison between calculated and gas phase geometries for aniline.

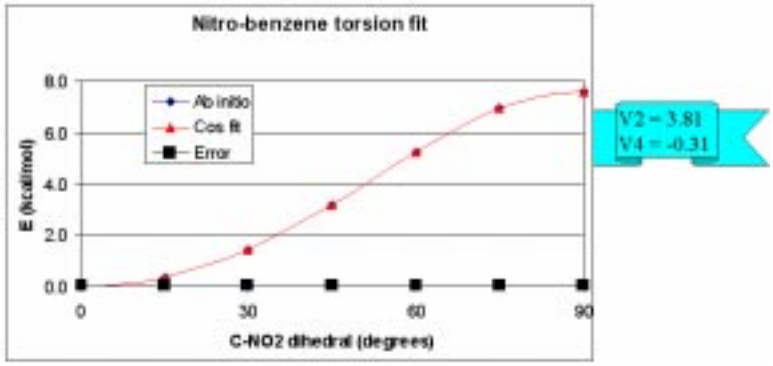

Figure 5.13: Nitrobenzene torsional potential.

strong inter-molecular H-bond between adjacent TATB molecules, we need to calculate the Potential Energy Surface (PES) for this interaction, using model compounds. Towards this goal, we have used DFT (B3LYP/6-31G**) calculations to compute the geometry of aniline ($C_6H_5 = NH_2$) and nitro-benzene ($C_6H_5NO_2$). The calculated geometry is in good agreement with the microwave determined gas phase structures (Figure 5.12). We have used the DFT calculations to parameterize the torsional potential around the CN bonds in the aniline and nitrobenzene molecules (Figures 5.13–5.14). The ab initio potential energy surface was fit to the molecular H::O van der Waals parameter to parameterize the H-bond (Figure 5.15).

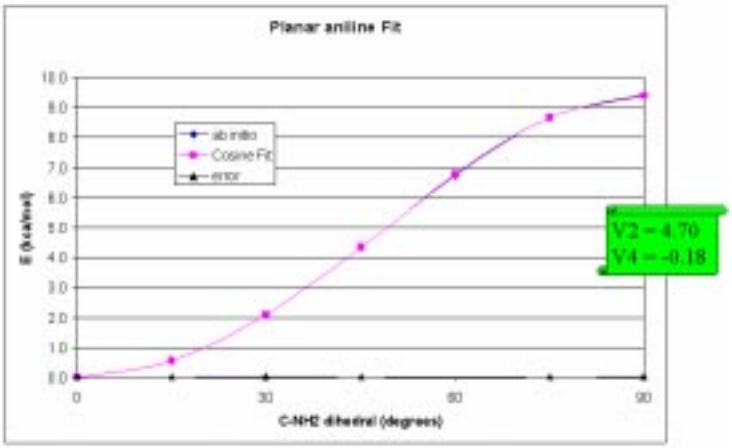

Figure 5.14: Aniline torsional potential.

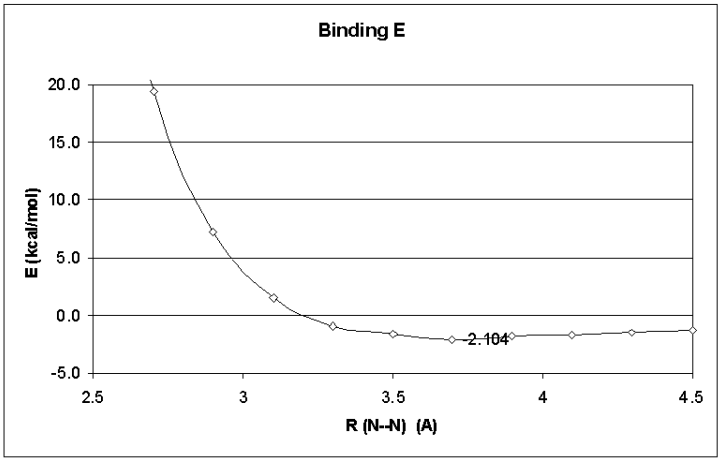

Figure 5.15: Ab initio Potential Energy Surface for inter-molecular H-bond.

HMX

We have been using the Dreiding II force field for initial validation of our method of calculating Equation of State (EOS) for the unreacted HE material. While the Dreiding II force field was not developed for accurately predicting vibrational frequencies (which are important in considering energy transfer from the lattice modes to the internal modes), the force field predicts structures quite well as was demonstrated in the previous annual report. We have now tested the bulk mechanical properties (elastic constants) since we can now compare them with experimental values from inelastic neutron scattering experiments (Figure 5.16). The majority of the elastic constants calculated by Dreiding II are in good

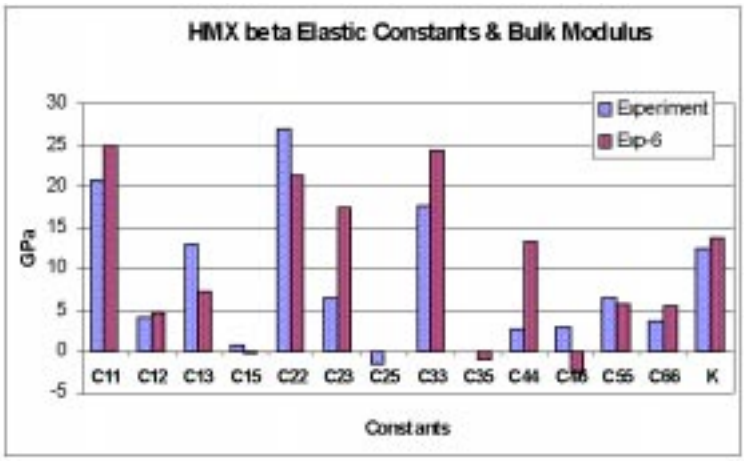

Figure 5.16: Comparison of elastic constants for HMX using the level 0 Dreiding II force field.

agreement with the experimental values.

Molecular dynamics treats the atoms as classical entities following Newton's force laws. While this treatment yields correct behavior at high temperatures, at the lower temperatures quantum effects are significant. The highest frequency modes in organic molecules (such as HMX, RDX, and TATB) are the C-H and N-O stretching modes and at lower temperatures, quantum mechanically these are not well populated. MD simulations assume equi-partition of energy in all vibrational modes, and yields the classical limit of the specific heat ($= 3NKT$). In order to calculate the correct specific heat at low temperatures, one needs the proper partition function based on the vibrational density of states. We use the velocity autocorrelation function to calculate the density of states, and from that we calculate the proper ensemble averages of a variety of thermodynamic properties (internal energy, specific heat, entropy etc.) (Figure 5.17).

5.3.4 Modeling Polymeric binders

Many polymers are used as binders in a variety of High Explosive systems. Our efforts have concentrated on Kel F-800, Estane (a thermoplastic polyurethane) and Poly(methyl methacrylate), PMMA. We are using atomistic modeling tools to calculate properties such as equation of state, moduli, glass transition, viscosities, and shear hardening in order to predict the performance properties of the material.

Kel F-800:

Kel F-800 (Figure 5.18 is used as the binder for the TATB explosive in the PBX-9502 system, where it makes up 5formulation. The polymer is a random copolymer of chlorotrifluoroethylene and vinylidene fluoride monomer units in

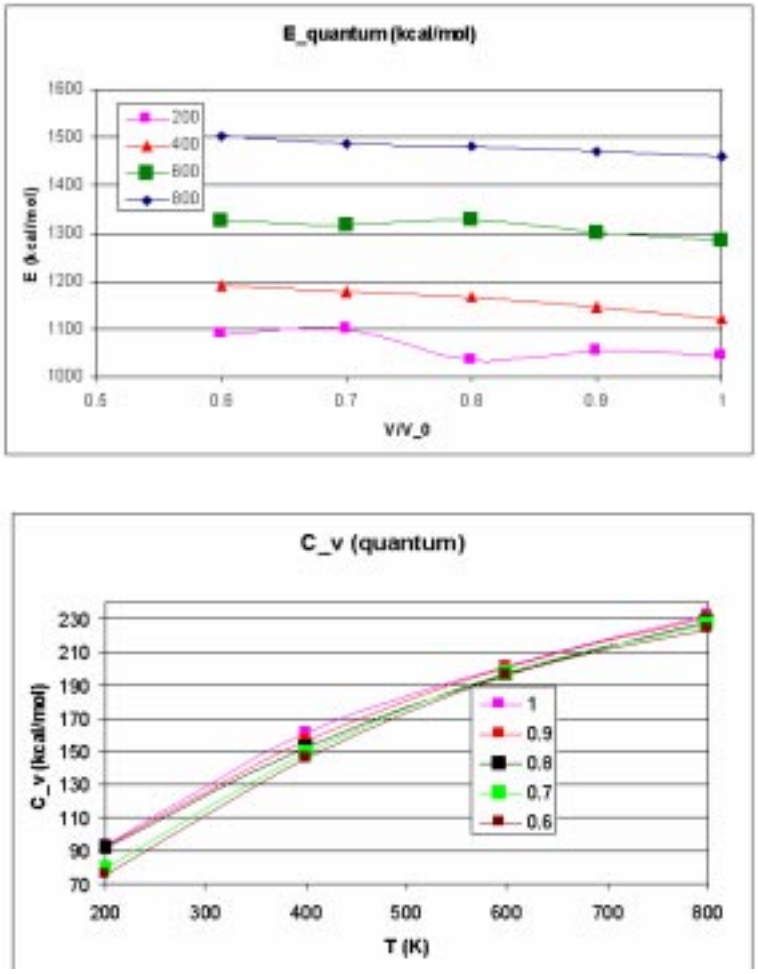

Figure 5.17: Calculation of internal energy and specific heat (Cv) from velocity autocorrelation to correct for quantum mechanical effects.

a 3:1 ratio. The presence of the vinylidene fluoride disrupts the crystallinity of the chlorotrifluoroethylene to form an essentially amorphous polymer. Although amorphous, the polymer is very dense due to the presence of the chlorine and fluorine atoms.

Equation of State from atomistic simulations:

The choice of force field is critical for these systems. Dreiding-EXP6 force field was chosen for the first set of calculations because it has valence and van der Waals parameters well suited for calculating molecular structures. The charges

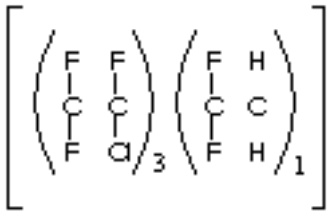

Figure 5.18: The Kel F-800 monomer.

on the halogen atoms are not well represented by default charge equilibration (QEq) scheme. We have instead used the more reliable electrostatic potential derived quantum mechanical charges, which were calculated from a set of small molecule analogs. Various oligomers of CTFE and VDF were built and their Hartree-Fock geometry optimized with the 6-31G** basis set.

To best represent the amorphous polymer, the packing of the chains has to be optimized. We have used in-house developed algorithms for this purpose and tested by comparing with experimental Cohesive Energy Density for a variety of polymers. The chains were built from the monomers with the QM charges. Various ensembles were generated using different number of chains per unit cell. In each case, 1500 NVT dynamics steps were done to get the best possible packing and equilibrium state.

In an effort to mimic the real system more accurately, poly-dispersity was introduced into the model. The model consisted of 24 individual polymer chains of differing chain lengths.

There is very little experimental data available for Kel F-800. In order to validate our model, the solubility parameter was calculated using the CED code. A range of polymers has been studied and their solubility parameters/(values compared to experiment. For the very similar PCTFE polymer where this data is available, the calculated (is well within the experimental range, as also for PVC and PMMA polymers. This lends confidence that the model and force field selected for the Kel F simulations is reasonable and the calculated (value should compare well with experimental values.

The equation of state represents pressure as a function of volume and temperature, or alternatively as a function of volume and internal energy. The Mie-Grüneisen equation of state has been widely used for unreacted solids to model their material behavior. In this form the pressure and energy at arbitrary states are related to conditions along a reference path of known thermodynamic characteristics:

$$P(e,V) = G(V)\frac{E - E_c(V)}{V} + P_c(V) \tag{5.1}$$

We use the cold compression values as our reference state (denoted by subscript c). For this purpose the cold compression curves were calculated and fit

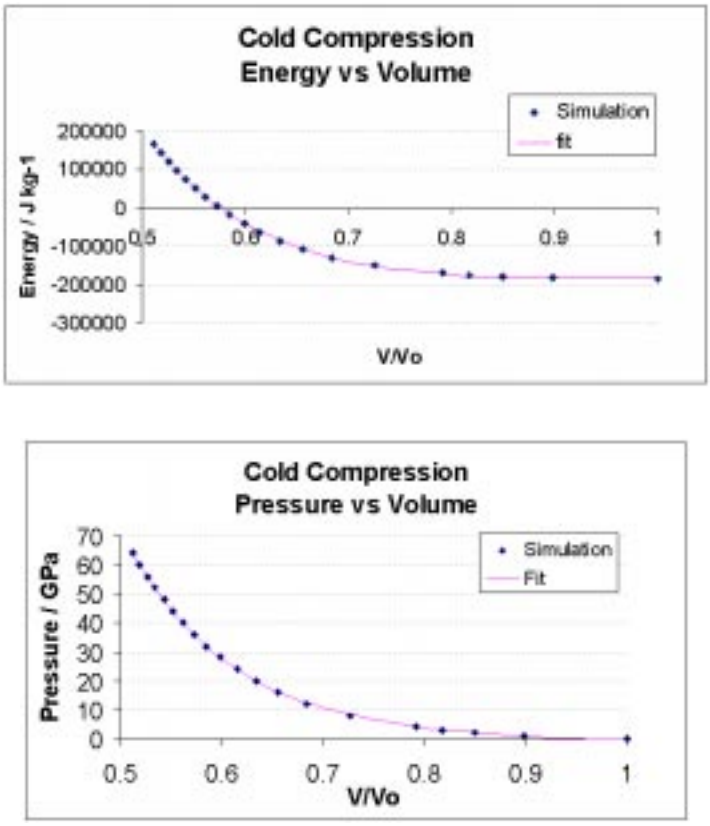

Figure 5.19: Cold compression curves (Specific Internal Energy and Pressure vs. Volume compression ratio) for Kel F-800.

to a Birch-Murnaghan form. (Figure 5.19). The Grüneisen parameter, G, in equation 5.1 is defined as:

$$G = V\left(\frac{\partial P}{\partial E}\right)_V = V\left(\frac{\left(\frac{\partial P}{\partial T}\right)_V}{\left(\frac{\partial P}{\partial T}\right)_V}\right) \tag{5.2}$$

In order to get the temperature dependence of the internal energy and pressure, constant volume dynamics calculations were performed. The thermodynamic properties were derived from the vibrational density of states obtained from the velocity auto-correlation of molecular dynamics trajectories (Figure 5.20). The equation for the Grüneisen parameter, calculated using this data (Figure 5.21) is $G = 0.4584 - 0.3852 * (V/V_0)$. The Grüneisen parameter and EoS for Estane and PMMA are currently being calculated in the same way.

5.4 Materials Properties for Solid Dynamics

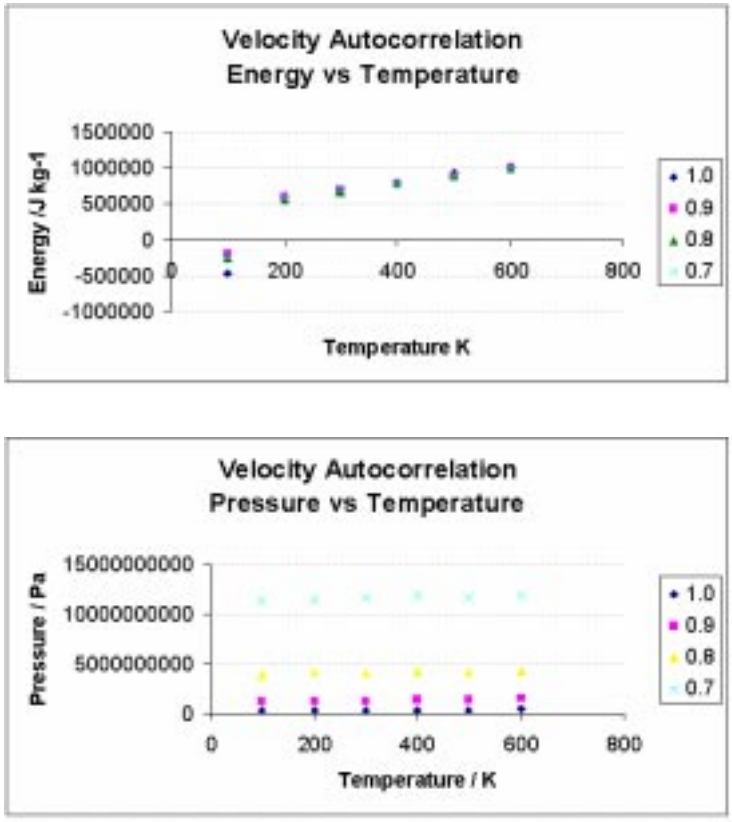

Figure 5.20: Energy and Pressure vs Temperature at various fixed volumes from NVT dynamics

5.4.1 Tantalum Force Field from First Principles

Theoretical understanding and calculation of mechanical properties of materials such as equations of state, dislocation motion and interaction, brittle and ductile fracture, spall strength etc, requires accurate description of processes which occur at very different time and space scales, ranging from ps and nm to sec. and meters. Consequently there has been a growing interest in *multiscale modeling*.

The most fundamental and accurate, quantum mechanical (QM), description of interatomic interactions, being computationally expensive, is restricted to relatively small systems and short time-scales. On the other hand, the description of the atomic interactions via classical force fields (FF) and the use of molecular dynamics (MD) allows the simulation of millions of atoms for longer times (∼ns). The drawback is that some accuracy is lost.

In this report we propose a strategy to bridge QM and FF modeling for BCC metal tantalum. We use a very accurate QM, LAPW GGA method to calculate different mechanical properties of Ta which require small number of atoms,

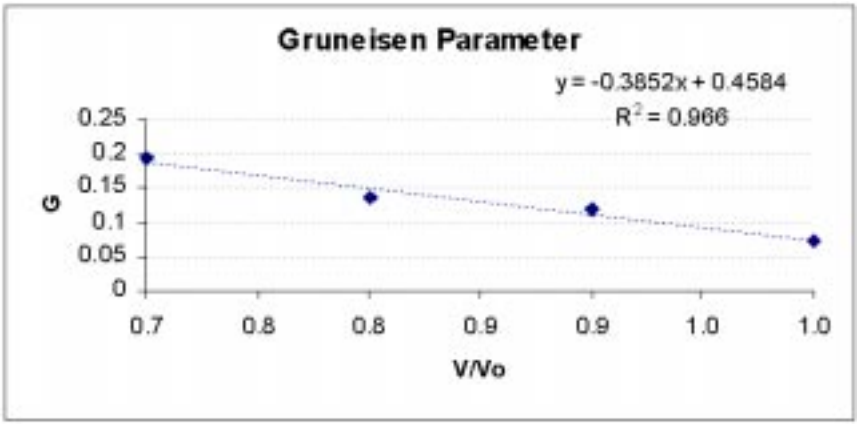

Figure 5.21: Gruneisen parameter for Kel F.

namely zero temperature equation of state for BCC FCC and HPC crystalline phases, elastic constants, and vacancy formation energy. This data, obtained from first principles, is used to fit a many body classical Embedded Atom Model FF (qEAM FF).

We then use this qEAM FF using MD simulations to study different properties which require larger simulation cells and longer times. In particular in this report we calculate the melting curve of Ta up to pressures of $\sim 500GPa$.

5.4.2 qEAM force field

In order to predict mechanical properties of materials and processes like phase diagram, dislocations structures and mobility, mechanical failure, etc. it is important to have accurate classical force fields to describe the atomic interactions. With MD simulations is then possible to study large systems (millions of atoms) for relatively long times (ns).

One of the most popular many-body force fields for metals is the Embedded Atom Model (EAM), proposed by Daw and Baskes in 1984 [23]. This approach is computationally efficient and has been used successfully for numerous applications, like thermodynamic functions, liquid metals, defects, grain boundary structure, fracture, etc.

The EAM implementation that we have used is based on the one proposed by Chantaririwan and Milstein, [14]. The energy of a given atomic configuration with atom positions $\{r_i\}$ is given by:

$$U\{r_i\} = \sum_{i}^{N} F(\rho_i) + \sum_{i<j} \phi(r_{ij}), \tag{5.3}$$

with

$$\rho_i = \sum_{j \neq i} f(r_{ij}) \tag{5.4}$$

where $F(\rho)$ is the embedding energy, ρ_i is the total electron on the atomic site i, $f(r)$ is the electron density function, $\phi(r)$ is a two-body term and $r_{ij} = |r_i - r_j|$.

Following [14] we took the two-body term as:

$$\phi(r) = (r - r_m)^4 \sum_{i=0}^{7} b_i r^i. \tag{5.5}$$

The electron density is:

$$f(r) = \frac{1 + a_1 \cos(\frac{\alpha r}{V^{1/3}}) + a_2 \sin(\frac{\alpha r}{V^{1/3}})}{r^\beta}, \tag{5.6}$$

where V is the volume per atom of the system. This electron density is volume dependent, but structure independent. Finally the embedding energy is defined from:

$$F(\rho) = U_{Rose}(V) - \sum_{i<j} \phi(r_{ij}), \tag{5.7}$$

where $U_{Rose}(V)$ is the Rose's universal equation of state and the sum is made in the reference (BCC) structure. We developed a classical EAM force field for Ta purely based on first principles theoretical results, with no use of experimental data. In fitting the EAM FF parameters we used the following first principles data:

- Zero temperature energy-volume and pressure-volume curves for different crystal structures (BCC, FCC and A15) in a wide pressure range, from ~ -10 GPa to ~ 500 GPa. For the BCC and FCC structures the data from Cohen was used, while for A15 we used the data calculated by Soderlind and Moriarty [111].
- Zero temperature elastic coefficients, shown in Section 5.4.3.
- Unrelaxed vacancy formation energy at zero pressure, shown in Section 5.4.4.
- Energetic of homogeneously sheared BCC crystal, from Ref. [111].
- Unrelaxed (100) surface energy from [122]

Ta is a BCC metal and no pressure-induced phase transition to other solid structure has been found experimentally or theoretically. Nevertheless, using QM it is possible to calculate, with high accuracy, the equation of state (EOS) for different crystal structures (see section I) although they may not be thermodynamically stable. Including the EOS of different phases in the FF development leads to correct classical description of the atomic interactions even when the environment of an atom is not that of the stable phase, this is very important to study defects and non-equilibrium processes. We fit the parameters entering the qEAM FF energy expression to QM data using an optimization algorithm based on simulated annealing. A comparison between the qEAM FF and QM results is shown in the following subsections.

	$V_0(A^3)$	K_T(GPa)	K'_T	c_{11} (GPa)	c_{12} (GPa)	c_{44} (GPa)
	Theory (0 K)					
This work	18.36	183	4.13	265	146	61
LAPW [1]	18.33	188.27	4.08	245.18	159.8	67.58
LMTO [2]	17.68	203	-	281	163	93
	Theory (300 K)					
This work	18.4	176	4.9	-	-	-
	Experiment (300 K)					
DAC [3]	18.04	194.7±4.8	3.4	264	159.7	82.2

Table 5.1: EOS parameters for BCC Tantalum.

5.4.3 Equation of state

In Figure 5.22 we show energy (top) and pressure (bottom) as a function of volume for BCC Ta at $T = 0°$ K. The circles denote QM results and the lines the qEAM. Figures 5.23 and 5.24 show the same results for FCC and A15 Ta. It is clear that the qEAM FF reproduces the zero temperature EOS for the three different phases very well.

Table 5.1 shows zero pressure volume (V_0), bulk modulus (K_0), its derivative with respect to pressure (K'_0) and the elastic constants obtained using the qEAM FF together with the QM values from Section I and the ones reported in [111].

We calculated the T= 300 K EOS using isothermal-isobaric MD with a Hoover [43] thermostat and Rahman-Parrinello barostat [88]. In Table 5.1 we show the T=300 K zero pressure volume (V_0), bulk modulus (K_T) and its first derivative with respect to volume; we also show recent experimental data at $T = 300$ K. It is clear from this table that the qEAM FF, reproduces the EOS very well.

5.4.4 Vacancy formation energy

The zero pressure vacancy formation energy from Section II was used to fit the qEAM FF. The unrelaxed vacancy formation free energy obtained using the qEAM FF is 3.1 eV, in very good agreement with QM results. In Figure 5.25 we show unrelaxed vacancy formation energy as a function of pressure; the thick solid line shows qEAM results and circles denote QM results.

In order to calculate vacancy formation energy as finite temperatures as a function of pressure we performed NPT MD simulations using cell containing $N = 1458$ atoms with periodic boundary conditions. In Figure 5.26 we show vacancy formation energy (top) and enthalpy (bottom) as a function of pressure for $T = 300$ K and $T = 1000$ K.

[1] O. Gulseren and R. Cohen
[2] P. Soderlind and J. A. Moriarty, [111].
[3] H. Cynn and C. Yoo, [21].

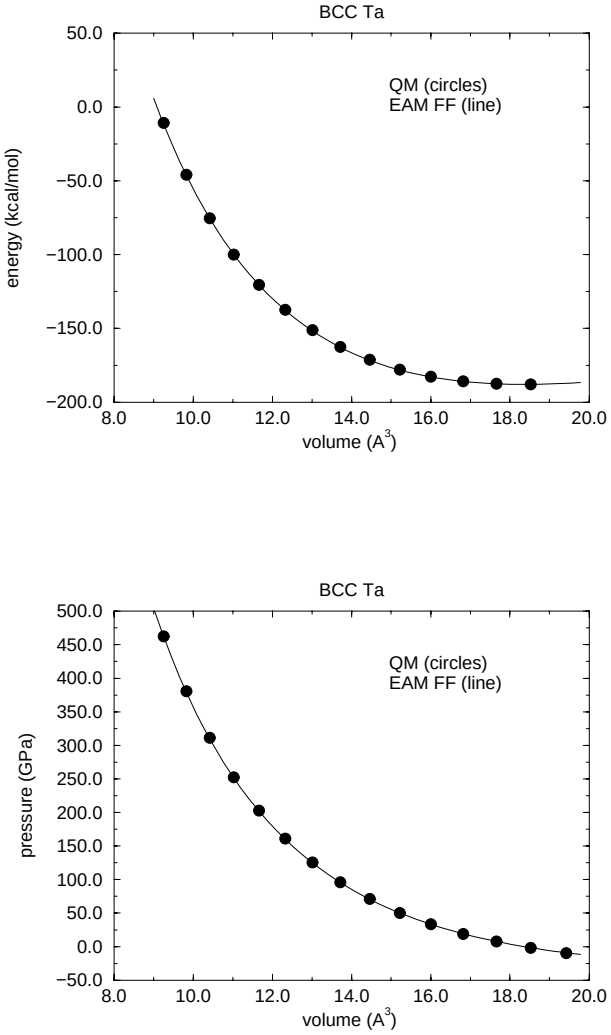

Figure 5.22: Zero temperature BCC Ta energy (a) and pressure (b) as a function of volume. Circles denote LAWP GGA results, section I, and lines show qEAM FF results.

5.4.5 Surface energy

The unrelaxed (100) surface energy using the qEAM FF is 2000 J/m^2, lower than the first principles value of 2800 J/m^2. Low surface energy is a common

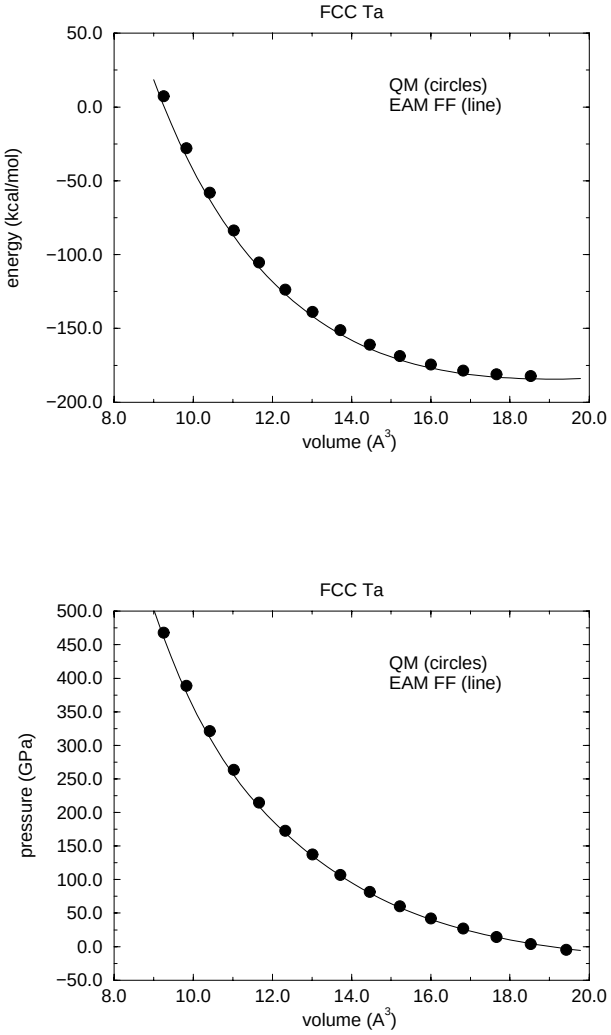

Figure 5.23: Zero temperature FCC Ta energy (a) and pressure (b) as a function of volume. Circles denote LAWP GGA results, section I, and lines show qEAM FF results.

problem in EAM-like force fields.

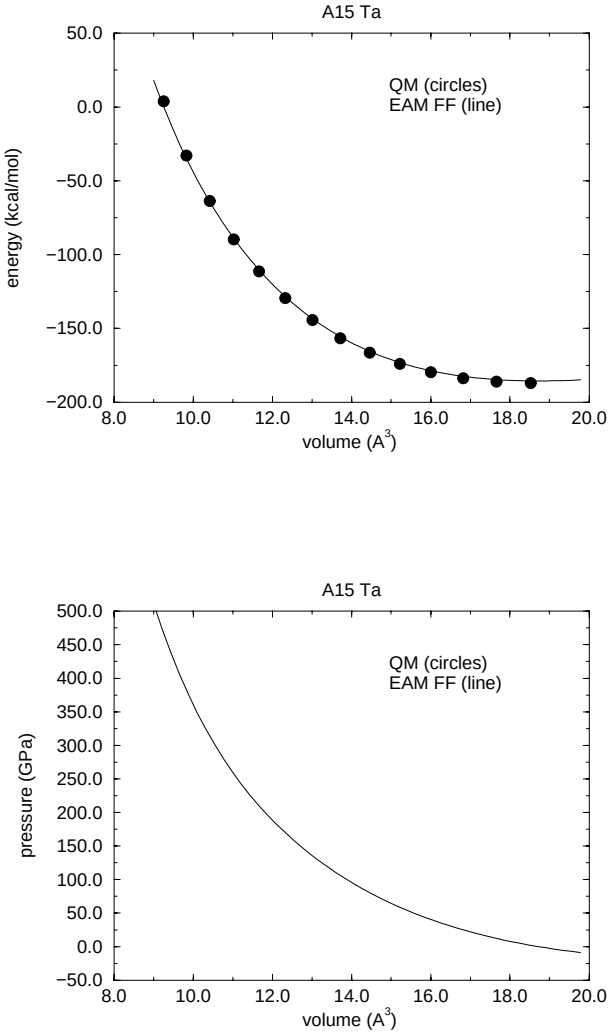

Figure 5.24: Zero temperature A15 Ta energy (a) and pressure (b) as a function of volume. Circles denote LAWP GGA results Ref. [111], and lines show qEAM FF results.

5.4.6 Melting curve of Ta

The study of phase transitions with MD is difficult. The simulations usually treat the solid as an infinite periodic system, and hence lack the surface sites

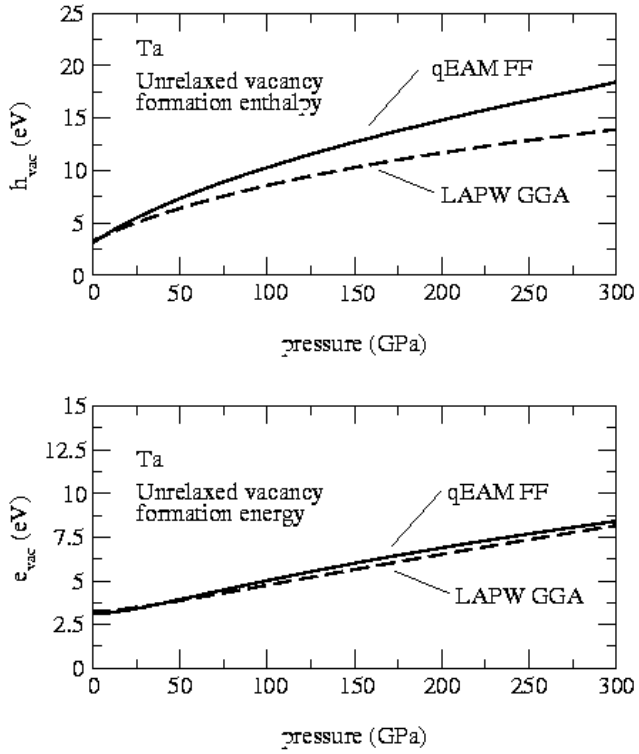

Figure 5.25: Unrelaxed vacancy formation enthalpy (a) and energy (b) as function of pressure. Dashed lines represent QM results of section I and full lines show qEAM results.

that normally nucleate a new phase. The most direct way of studying melting via MD is: (a) start with the perfect crystal at low temperature, and heat the system (at constant pressure) at a given rate until it melts; (b) cool the liquid system until re-crystallization. However, the small system size (nm) and short time scales (ns) in MD, limit the fluctuations and defect concentration which trigger the phase transition; this leads to superheating of the solid and undercooling of the liquid which makes an accurate calculation of the melting temperature impossible. We illustrate this problem in Figure 5.27, where we show the results of zero pressure heating and cooling, with a rate of 100 K per 25 ps, of a 1024 atom system with periodic boundary conditions. In Figure 5.27 we plot enthalpy (top) and volume (bottom) as a function of temperature. In order to overcome some of these problems we calculate the melting temperature using the "two phase technique". It consists of introducing an interface at the beginning of the simulation, i.e. place a pre-simulated liquid and a pre-simulated solid in the computational cell. Once this initial configuration is built we perform TPN MD (using Hoover thermostat and Rahman-Parinello

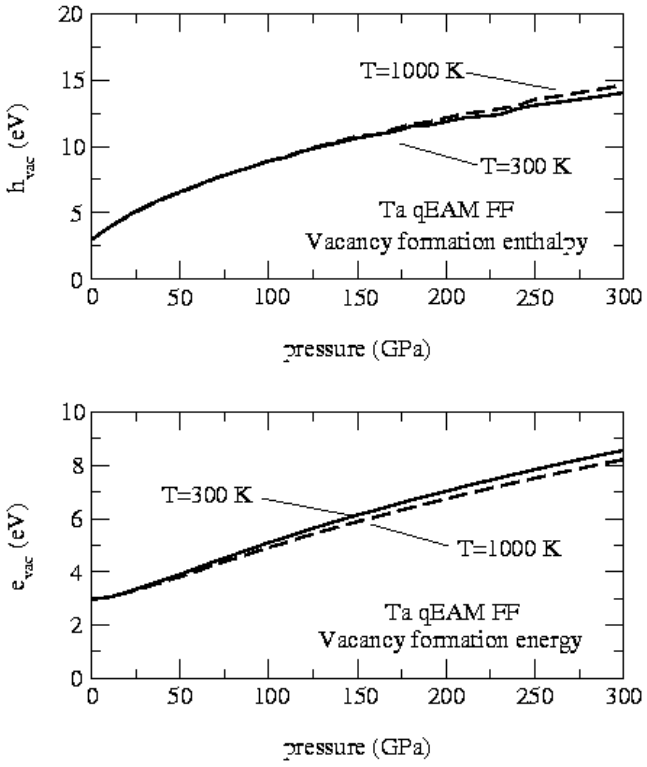

Figure 5.26: Vacancy formation enthalpy (a) and energy (b) as function of pressure for T=300 K (solid lines) and T=1000 K (dashed lines).

barostat) simulation and observe which phase grows. If the temperature T is lower than $T_{melt}(P)$ the liquid will start crystallizing, on the other hand the solid will melt if $T > T_{melt}(P)$.

Given that liquid-solid phase transition is first order, i.e. the energy of the solid and liquid in equilibrium differ by a finite amount, it is very easy to know whether the system is crystallizing or melting by analyzing the time evolution of the total potential energy during the MD run. In Figure 5.28 we show potential energy as a function of time for zero pressure two-phase simulations at different temperatures. We can see that at T=3100 K the potential decreases with time; this means that the solid phase is growing and $T_{melt} > 3100$ K. On the other hand, for $T = 3200$ K the energy grows, the system is, then, melting and $T_{melt} < 3300$ K. At T = 3150 K the energy is rather constant and the both phases are in equilibrium. This value for the zero pressure melting is in very good agreement with experimental results, which find $T_{melt}3290 \pm 100$ K. This is a very important validation of the FF, taking into account that only zero temperature data was used in its development.

The slope of the melting curve is given by the Clausius Clapeyron equation:

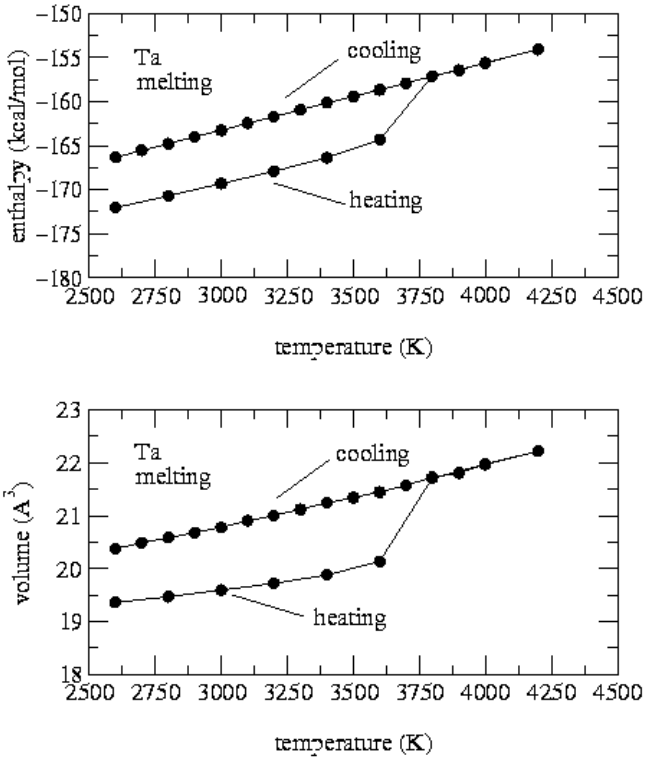

Figure 5.27: Melting. Enthalpy (a) and volume (b) as a function of temperature, during heating of BCC Ta (lower branches) and cooling of liquid Ta (higher branches).

$$\left[\frac{dP}{dT}\right] = \frac{1}{T}\frac{\Delta H}{\Delta V}, \tag{5.8}$$

where ΔH and ΔV are the enthalpy and volume difference between the liquid and solid in equilibrium respectively. From our MD runs, see Figure 5.27, the slope of the melting curve at zero pressure is $\left[\frac{dT}{dP}\right] \sim 80$ K/GPa, the experimental value is $\left[\frac{dT}{dP}\right]$ 60 ± 10 [21]. Using the procedure described below we calculated the melting temperature for for different pressures, up to 500 GPa. In Figure 5.29 we show the melting curve for Ta.

5.4.7 Discussion

We have presented here a multiscale strategy in which accurate QM calculations are used the develop a fully first principles force field. In this way the computer expensive QM calculations need to be done in small systems. We have calculated EOS for different structures, elastic coefficients and vacancy formation energy.

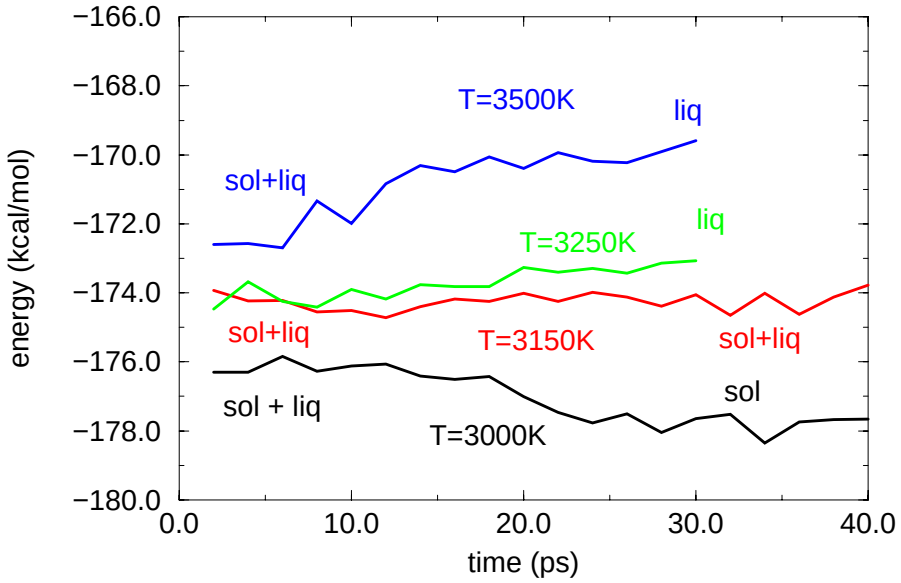

Figure 5.28: Two phase simulations. Time evolution of the potential energy in TPN MD at zero pressure for different temperatures. For T=3100 K (dashed line) the potential energy decreases with time, i.e. the system is crystallizing; for T=3200 K the potential energy grows denoting melting. For $T = 3150 \sim T_{melt}(P = 0)$ the potential energy remains constant.

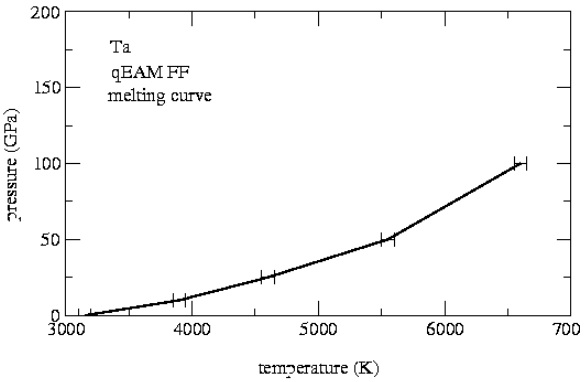

Figure 5.29: Melting curve for Ta up to P= 500 GPa. Resulting from two phase simulation technique.

This results are in very good agreement with experiment and recent ab initio calculations.

The QM data is then used to develop a classical force field, capable of describing with very accuracy the atomic interactions in Ta. We used the qEAM

FF with MD to calculate the melting curve for Ta. The zero pressure melting temperature obtained from our simulations $T_{melt} = 3150 \pm 50$ K is in very good agreement with the experimental result of 3290 ± 100 K.

5.4.8 Crack propagation in Ta slabs

Using first principles based qEAM potentials for Ta we studied crack propagation via MD with expanding periodic boundary conditions. The sample we used is constructed in such a way that the sides of the system, are far away from the crack. They are thermostated, while the rest of the system follows the Newton's equations. To investigate the effect of temperature and strain rate on brittle and ductile behavior, we studied the same model system at T = 300 K and T = 600 K and at various strain rates. The strain rates are maintained by moving the boundaries at constant velocity, 80 m/s, 40 m/s and 20 m/s.

We define a local temperature of the expanding system from the velocity fluctuations over the mean collective velocity. In practice we divide the system in small regions and calculate, for each region, its mean velocity and fluctuations.

Figure 5.30, 5.31, and 5.32 illustrate simulations of crack tips in Ta. We found that the crack tip temperature grows as the crack propagates it reaches a maximum when the system is plastically deforming and then decreases while the system relaxes back to the BCC structure. This process can happen several times.

5.5 Materials properties methodology development

The previous sections have detailed prediction of materials properties using existing methods. It has also been necessary to spend some time investigating how current methodology might be improved, either by more intelligent use of parallelization, or by the application of new techniques to yield more accurate solutions.

5.5.1 Quantum Mechanical Methodology

Typical parallel speedups of quantum mechanical programs are shown in Figure 5.33. Although this performance is often adequate to achieve materials properties for small molecules, there are still many systems that cannot be computed in reasonable amount of time with this level of performance. Moreover, in many cases accurate materials properties may *not* by computing using small models. We have begun to investigate approaches that will take us the next step. These "divide-and-conquer" techniques separate a large problem into a series of smaller problems. This division linearizes the problem (i.e. makes it solvable in time that is a linear function (rather than a quadratic or cubic function) of the system size). More significantly, it also supplies a trivial parallelization of the problem. Figure 5.34 shows the results of simple and buffered divide and conquer schemes compared to the full Hamiltonian (i.e. the standard) approach. We anticipate more progress on these techniques in subsequent years.

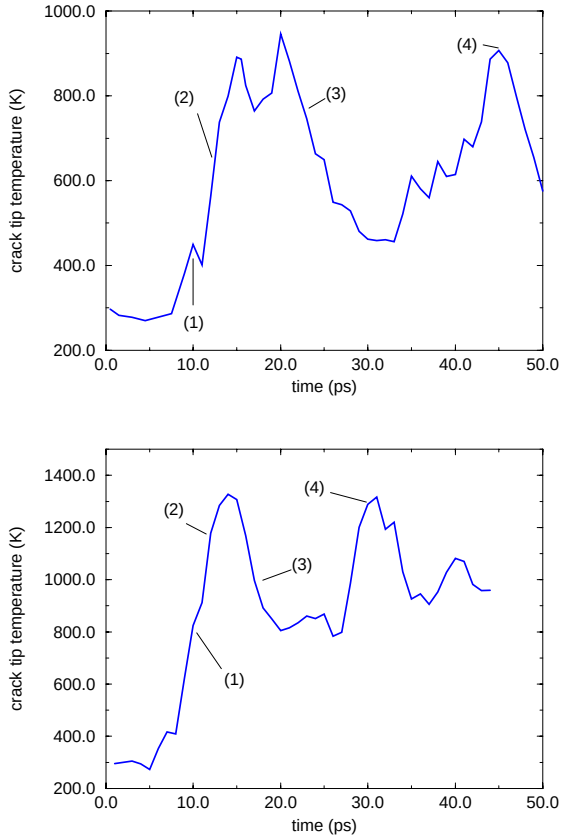

Figure 5.30: Top: Temperature of the crack tip as a function of time for v = 40 m/s and T=300K. Bottom: Temperature of the crack tip as a function of time, T=300K, v = 80 m/s

5.5.2 Thermal Conductivity of Diamond and Related Materials from Molecular Dynamics Simulations

There are two major approaches to theoretical studies of the thermal conductivities of materials:

1. The most fundamental approach is to base the calculations on first principles atomistic simulations. This allows the properties for new materials to be predicted in advance of experiment. This is particularly useful for nanoscale devices where the experiments are quite difficult. Atomistic simulations have been employed to determine diffusion coefficients, viscosities, and thermal conductivities for fluids. Both equilibrium and non-equilibrium dynamic simulations[27, 72, 22] have been reported for various systems. The calculated results are often in reasonable agreement with experimental measurements.

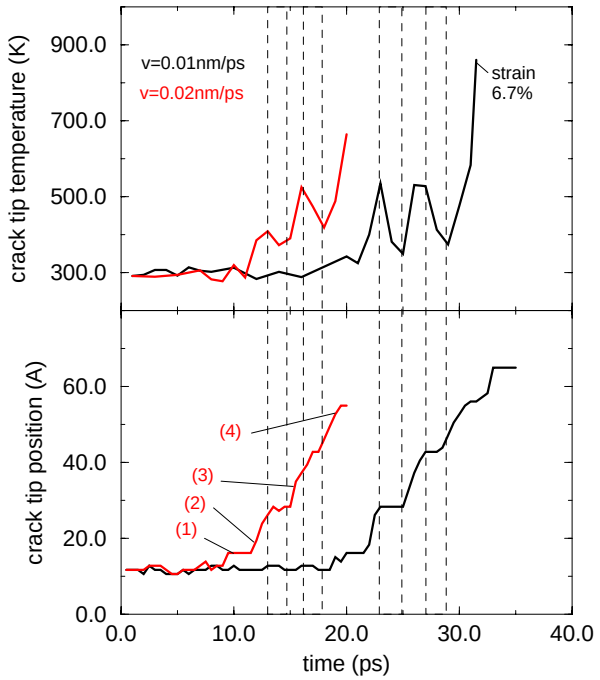

Figure 5.31: Temperature and position of the crack tip as a function of time. For v = 10 m/s and v = 20 m/s and T=300K.

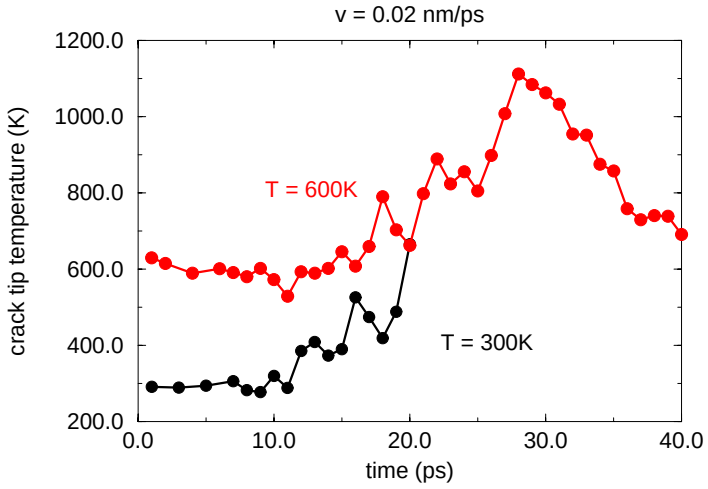

Figure 5.32: Temperature of the crack tip as a function of time. For v = 20 m/s, T=300K and T=600K

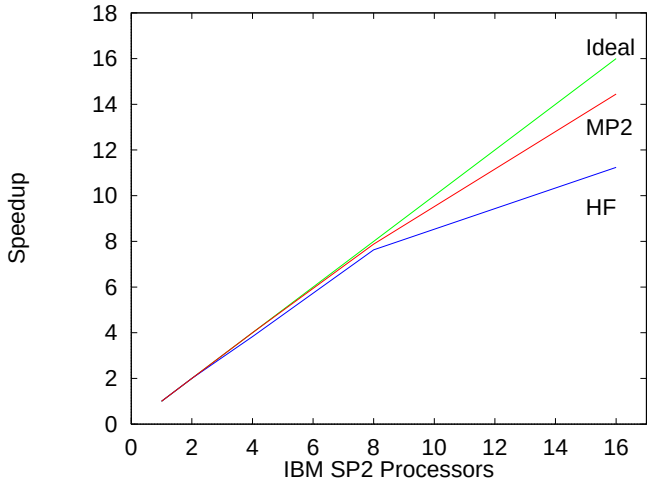

Figure 5.33: Parallelization of Jaguar quantum chemistry package on the IBM SP2 platform.

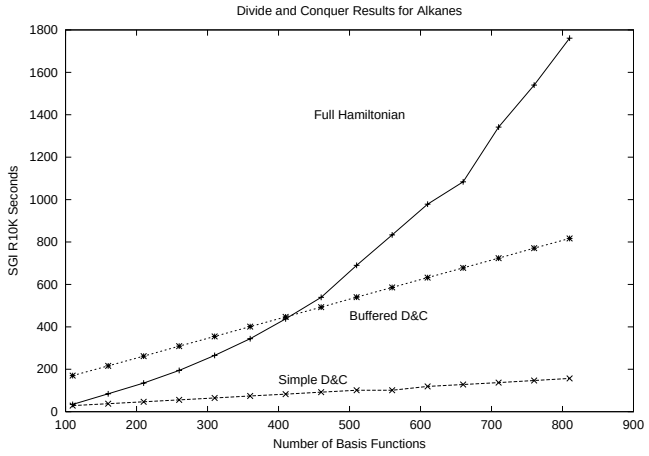

Figure 5.34: Comparison of simple and buffered divide and conquer schemes to the full Hamiltonian (normal) technique

2. More commonly, thermal conductivity has been studied using continuum models and kinetic theories such as the Boltzmann transport equation. For example, Walkauskas et. al. [125] calculated the lattice thermal conductivity of GaAs wires; Balandin et. al. [5] calculated the thermal conductivity reduction in the Si quantum well; Gurevich [37] discussed in detail the use of general principles of physical kinetics to describe phonon transport theory. These approaches must assume the fundamental constitutive equation and parameters.

The advantage of using the Boltzmann equation (BE) is that large systems can be studied reasonably quickly. However, certain parameters such as phonon relaxation time $\tau(\omega)$ and phonon density of states (DOS) must be obtained either from experiments or other theoretical estimates. In addition, solving the integro-differential BE for general cases is nontrivial. Moreover, for nanoscale electronic devices, it is very difficult to measure directly phonon properties required to predict the thermal conductivity.

Thus, it is of great interest to develop methods for using first principles atomistic simulations to predict the thermal properties. In particular, recent advances in characterizing the interactions between atoms using classical force fields (FF) based on high level quantum mechanical calculations provides the opportunity to make first principles predictions on interesting organic and inorganic materials without additional data from experiment. This also allows the effect of microscopic structure (interfaces and surface reconstruction) to be studied quantitatively. In addition, such atomistic simulations can provide the input data (the DOS and relaxation times) to the BE approach. Thus, it can bridge between atomistic dynamics and continuum kinetics.

One can generally partition the thermal conductivity of a material into:

- the electronic thermal conductivity which depends on the electronic band structure, electron scattering, and electron-phonon interaction, and
- the lattice conductivity which depends mainly on the phonons (nuclear vibrations) and phonon scattering.

Here, we only consider the lattice thermal conductivity (as derived from the FF). This is appropriate for the systems considered here since they have large band gaps leading to small electronic contributions to thermal conduction. Because the phonon main free path in crystalline solids is much longer than that in liquids and amorphous solids, it is particularly challenging to calculate thermal conductivity for solid phase crystalline systems. Thus, to simulate the total phonon transport properties, one might expect that the periodic cell for the molecular dynamics (MD) simulations should be larger than the phonon mean free path, which can be on the order of hundreds nanometers. Moreover, calculating the phonon-phonon interactions responsible for limiting the thermal conductivity is one of the most complicated problems in solid physics. Indeed, there have been few attempts to achieve this objective (Gillan[34] reviewed calculation of ionic solids by MD, Paolini[87] calculated the thermal conductivity of defective ionic crystals, Murashov[81] calculated the thermal conductivity of model zeolites via MD).

We examine herein how to use MD simulations to provide some understanding of the various processes related to thermal conductivity and discuss the limitations in such approaches. We use the Green-Kubo (GK) relation derived from linear response theory to extract the thermal conductivity from energy current correlation functions. We find that the accuracy of thermal conductivity is sensitive to the size of the periodic unit cell in the MD simulation (which limits the phonon wavelength). However, we find that it is possible to extract the

an accurate thermal conductivity from periodic cells 60 times smaller than the actual phonon mean free path. The reason is that the energy current correlation time is much shorter than energy relaxation time. We illustrate this by using equilibrium MD simulations to calculate thermal conductivity of bulk crystalline diamond, including the effect on vacancies, isotopes, mass, and nanostructures. Since diamond is well-known as an exceedingly good thermal conductor, these calculations on diamond crystal provide a rigorous test of our methods.

Fourier's Law and the Green-Kubo Relation

The macroscopic thermal conductivity is defined from Fourier's law for heat flow under nonuniform temperature distribution. The steady state heat flow $\vec{J}_q$ is obtained by keeping the system and reservoirs in contact,

$$\vec{J}_q = -\Lambda \cdot \nabla T, \tag{5.9}$$

where Λ is the thermal conductivity tensor and $\vec{J}_q$ is the heat current produced by the temperature gradient ∇T. Fourier's law of heat flow, Equation 5.9, can be derived from linear response theory[56]. For isotropic or cubic systems we obtain

$$\Lambda_{ij} = \lambda \delta_{ij} \tag{5.10}$$

where λ is denoted as the (scalar) thermal conductivity.

From energy conservation, the energy current $\vec{J}_E$ must satisfy

$$\frac{\partial H}{\partial t} + \nabla \cdot \vec{J}_E = 0, \tag{5.11}$$

where H is the total Hamiltonian. Here the total energy current $\vec{J}_E$ includes both the heat current $\vec{J}_q$ plus the convection contribution, μJ, where $\vec{J}$ is the particle current, and μ is the chemical potential. The relation between energy current and heat current is given by[73]

$$\vec{J}_q = \vec{J}_E - \mu \vec{J}, \tag{5.12}$$

We will consider solids, where diffusion is negligible, so that $\vec{J}_E$ can be replaced by $\vec{J}_q$ in 5.11.

The formal operator solution for energy current can be written as[73]

$$\vec{J}_q \approx \vec{J}_E = \frac{1}{2} \int d^3 r \left[\vec{r} \frac{\partial h}{\partial t} + \frac{\partial h}{\partial t} \vec{r} \right], \tag{5.13}$$

where h is the Hamiltonian density at $\vec{r}$. In the classical limit, the energy density $h(\vec{r})$ reduces to the site energy of each particle. Therefore, in classical MD simulations, heat currents can be expressed in terms of local classical properties

of each particle

$$\Re = \sum_i \vec{r}_i h_i, \tag{5.14}$$

$$H = \sum_i h_i, \tag{5.15}$$

$$\vec{J}_q = \frac{d}{dt}\Re. \tag{5.16}$$

One approach to the simulation would be to put the system in contact with two different reservoirs with temperature T_1 and T_2. The heat current would be calculated when the system arrives at the steady state. However, with 10^6 atoms in a unit cell, the system will only have dimensions of ∼25 nm on a side. Thus, even a small temperature difference of 10K across this system would have a thermal gradient of 4×10^8 K/m, an unrealistically huge thermal loading for a macroscopic system. It is unlikely that linear response theory will still hold under such extreme thermal loading. Moreover, even this temperature gradient may be smaller than the thermal fluctuations in the system, making it difficult to obtain converged results in reasonable simulation times.

Instead, we use the fluctuation-dissipation theorem from linear response theory to provide the connection between the energy dissipation in irreversible processes and the thermal fluctuations in equilibrium[56]. In this case, the thermal conductivity tensor can be expressed in terms of heat current correlation functions[56, 73],

$$\Lambda^q = \frac{1}{k_B T^2 V} \int_0^\infty dt\, C_J^q(t), \tag{5.17}$$

$$C_J^q(t) = \langle \vec{J}_q(t); \vec{J}_q(0) \rangle, \tag{5.18}$$

where C_J^q is the *quantum canonical correlation function*, defined as,

$$\langle a; b \rangle = \frac{1}{\beta} \int_0^\beta d\xi\, \mathrm{Tr}\left[\rho \exp(\xi H)\, a \exp(-\xi H) b\right] \tag{5.19}$$

where ρ is the density matrix of the system at equilibrium, $\beta = \frac{1}{k_B T}$, and a, b are dynamic operators.

The Force Field for Carbon

We use the Brenner bond-order dependent FF for representing interactions between carbon atoms. [12]

The Heat Flux

As indicated earlier the interaction potential is formally pairwise, allowing the site energy h_i in 5.14 to be defined as

$$h_i = \frac{p_i^2}{2m_i} + \frac{1}{2} \sum_j V_{ij} \tag{5.20}$$

Therefore, the heat current can be calculated through 5.16. Because V_{ij} is in fact a many-body potential [20], the calculation of heat current $\vec{J}_q(t)$ is much more complicated than for a truly pairwise FF. After some algebra steps, $\vec{J}_q$ is given by

$$\vec{J}_q(t) = \sum_i \vec{v}_i h_i + \frac{1}{2} \sum_{i,j} \sum_{k,l} \vec{r}_{ik} \vec{F}_{ij}^{kl} \cdot \vec{v}_i, \tag{5.21}$$

with

$$\vec{F}_{ij}^{kl} = -\frac{\partial V_{kl}}{\partial \vec{r}_{ij}}. \tag{5.22}$$

In deriving above equations, we implicitly imposed the condition that there is no net momentum for the system. For a truly pairwise FF, 5.21 recasts to the familiar form [56, 74],

$$\vec{J}_q(t) = \sum_i \vec{v}_i h_i + \frac{1}{2} \sum_{i,j} \vec{r}_{ij} \vec{F}_{ij} \cdot \vec{v}_i. \tag{5.23}$$

Model Systems

A 1 fs time step was employed in all MD simulations. For each system, we initially equilibrated the system using Gaussian thermostat MD (300 K) for 40 psec. After equilibration, we carried out 400 ps of constant energy (NVE) MD, calculating the heat current for every time step.

All simulations on diamond started with a cubic unit cell constant of 3.556 Å. This unit cell was extended to build large super-cells for the MD simulations (thus, an $8 \times 8 \times 8$ cell leads to 4096 atoms). Periodic boundary conditions were applied to the super cell in all three directions.

Bulk Diamond, Isotopically Pure

To test the convergence of MD simulations on thermal conductivity, we carried out simulations for cubic diamond, described with super cells containing 512 ($4 \times 4 \times 4$), 1000 ($5 \times 5 \times 5$), 1728 ($6 \times 6 \times 6$), 2744 ($7 \times 7 \times 7$), 4096 ($8 \times 8 \times 8$), and 8000 ($10 \times 10 \times 10$) atoms. Since diamond is isotopic, we used 5.10 to calculate the scalar thermal conductivity (which reduces the uncertainty in the theoretical values). As discussed in previous sections, the phonon mean free path is the limiting factor to obtaining accurate results. For too small a simulation cell, the time for phonon to travel through the simulation cell is much shorter than the decay time of the current correlation function. This causes the phonons to be scattered more frequently than they would be in the infinite system. In this case, only the short time correlation function is accurate.

Even so we can estimate the thermal conductivity from simulations using periodic cells smaller than the mean free path. Thus, based on the macroscopic law of relaxation and Onsager's postulate for microscopic thermal fluctuation, we expect that the asymptotic decay of the heat correlation function will be exponential. Since the kinetic coefficients depend mostly on long time decay rate

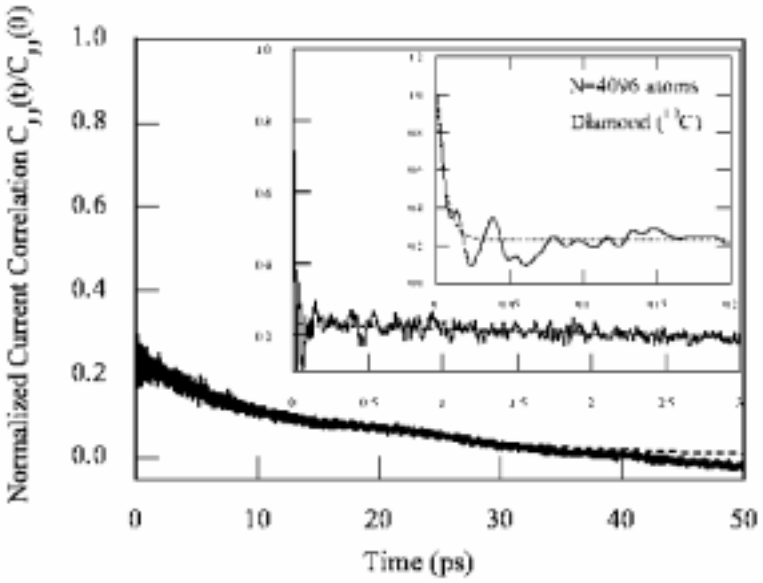

Figure 5.35: The heat current correlation function and the double exponential fitting for the $N = 4096$ atom simulation of ^{12}C diamond (T=300K, t_{run}=400 ps). The insets show the short time region at different scales. The parameters for the fitted double exponential function (dashed lines) are given in Table 5.2.

behavior and since an exponential-decay behavior is exhibited in a microscopic time scale, we expect that a medium sized simulation cell can be used to extract the decay rate of the heat dissipation.

Figure 5.35 shows the heat current correlation functions at short times for a cubic diamond crystal with 4096 atoms. We see a rapid initial decay (∼50 fs) followed by a long time exponential decay of the correlation function. Probably the initial fast decay is due to high frequency optical modes in the crystal, which do not significantly contribute to thermal conductivities (either conceptually and computationally), because they couple only weakly to the low frequency acoustic modes and they are little populated at room temperature.

To fit the correlation function we used a double exponential function

$$C_J^c(t) = A_o \exp(-t/\tau_o) + A_a \exp(-t/\tau_a), \qquad t \geq 0, \tag{5.24}$$

where the subscripts o and a denote fast optical modes and slow acoustic modes, respectively. The thermal conductivity is then given by

$$\lambda = \frac{1}{k_B T^2 V} \left(A_o \tau_o + A_a \tau_a \right). \tag{5.25}$$

The parameters A_o, τ_o, A_a, and τ_a, are derived from the first 3 ps using non-linear least square methods (Marquardt-Levenberg). This leads to the results

Atoms	A_o/V	τ_o (ps)	A_a/V	τ_a (ps)
512	822.0	0.00575	138.9	10.605
1000	805.3	0.00592	147.2	10.608
1728	813.6	0.00577	198.0	16.393
2744	814.7	0.00575	181.8	14.719
4096	811.0	0.00571	233.9	16.527
8000	808.1	0.00582	176.3	16.656
∞	810.5	0.0058	189.6	16.66

Table 5.2: Parameters for the double exponential fitting of the heat current correlation functions for ^{12}C diamond based on 5.24. $A_o/V = 810.5$ (kcal/mol)^2/(Å·ps^2) and $A_a/V = 189.6$ (kcal/mol)^2/(Å·ps^2).

in Table 5.2, where we see that high frequency optical modes contribute only 0.1% to the thermal conductivity. Note that the current correlation function at very short time ($\leq$ 20 fs) is not exponential in the strict sense, since only Markovian processes have an exponential decay correlation function. In most physical processes, non-exponential decay of the correlation function near $t = 0$ is quite common. However, for the cases studied here, this does not make a significant difference in the final calculated thermal conductivity. Therefore, it is satisfactory to use an exponential function to fit the initial trend. (This is the cause of the fitting function over-shooting the value at the origin.)

Figure 5.36 shows the dependence of the calculated thermal conductivities on the size of the simulation cell. The uncertainties shown here are estimated by $\sqrt{2\tau/t_{run}}$ where t_{run} is the simulation length. When the simulation cell is too small, the particles in the simulation cell do not have sufficient time to lose their previous dynamic information before a periodically equivalent phonon travels to the same place. As a result the longer correlation functions (τ_a) are contaminated from memory effects. Thus, for very small simulation cells, only the very short time correlation function resembles the real system behavior. This is shown in Table 5.2 where τ_a is independent of size. From Figure 5.36 and Table 5.2, we see that a cell of $\sim$28.44Å ($N = 4096$ atoms) is required to obtain a converged thermal conductivity .

In kinetic theory, the thermal conductivity is given by,[135]

$$\lambda \approx \frac{1}{3} C v L, \tag{5.26}$$

where C is the specific heat, and v is the speed of sound, and L is the phonon mean free path. Our simulations (based on the Brenner FF) lead to $\rho = 3.5$ g/cm^3, $C_v = 0.12$ cal/g/K (calculated from quantum corrected velocity correlation functions[9]), a compressibility of $\beta_T = 0.0020$ GPa^{-1} and hence a speed of sound of $v = 1/\sqrt{\rho\beta_T} = 12.0$ km/s. Using $\lambda = 12.2$ w/cm/K, 5.26 leads to a mean free path for acoustic phonons of $L = 174$ nm. The experimental values[18, 3] are $\rho = 3.5$ g/cm^3, $C_p = 0.11$ cal/g/K, $\beta_T = 0.0022$ GPa^{-1} and

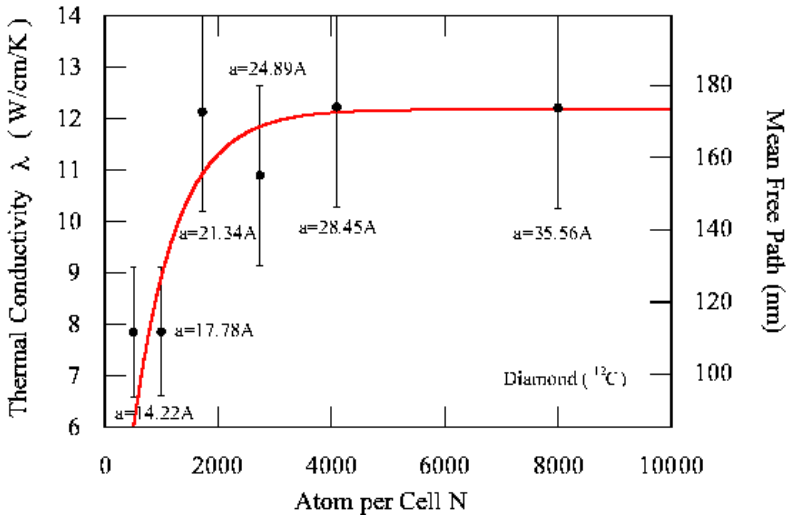

Figure 5.36: The thermal conductivity of isotopically pure ^{12}C diamond as a function of simulation cell size. The size of cubic diamond supercells are indicated in the figure. The error bar is estimated from $(2\tau_o/t_{run})^{1/2}$ with t_{run}=400 ps. The right Y coordinate indicates the length of average phonon mean free path $L = 3\lambda/C_v v$ where C_v (the constant volume heat capacity) is calculated from quantum corrected velocity correlation function[9], which gives $C_v = 0.12$ cal/g/K and the velocity of sound, v, is obtained from $v = 1/\sqrt{\rho\beta_T} =$ 12 km/s.

v = 11.4 km/s. Using the experimental value of λ = 33 w/cm/K, leads to $L = 494$ nm.

The comparison of the values for ρ, C_v, β_T, and v from theory using the Brenner potential are within 10% of experimental values. Thus it is surprising that the calculated λ is 60% smaller than the experimental results. As discussed in Section IV. B. 1, the calculated thermal expansion is 3.4 times higher than experimental value, suggesting that the Brenner potential is too anharmonic. This will lead to much smaller values for λ, as observed.

Although the phonon mean free path $L \sim 1740$Å is much larger than the cell length, we still obtain a converged value for λ of $a = 28.44$ ÅThis is because we need not seek a completely converged correlation function, which would require a cell of $N = 5.9 \times 10^8$ atoms. Instead, we need only to extract the τ_a decay constant from the initial correlation function. Table 5.2 lists the exponential decay constants of the correlation functions for systems of different sizes. The weighting factors A_o and A_a are normalized by the volume and the values for various N are averaged over all N to reduce the error. The fitted relaxation times are $\tau_o = 0.0058$ ps and $\tau_a = 16.6$ ps.

Defects

The above calculations assumed a perfect crystal, where the thermal scattering is due solely to anharmonic vibrations of the atoms. However, real materials have many defects. We consider here the effect of isotopic variations, vacancies, and mass variations for composite systems.

Isotopic Substitutions

The natural abundance of ^{13}C is 1.1%. Since the phonon frequency depends on mass this leads to local fluctuations in the natural frequency which can lead to increased phonon scattering. Thus, natural diamond crystals always contain a significant number of scattering centers. The decreased phonon mean free path due to increased scattering makes it easier to calculate λ since the correlation function convergences faster, allowing a smaller super cell to be used in the MD simulations.

Indeed, experiments by Anthony et al.[3] found that the thermal conductivity of diamond at room temperature increased by 50% when the concentration of isotope ^{13}C was reduced by a factor of 15! Their remarkable discovery led to a patent [2] and stimulated a number of studies to understand the sensitive behavior of diamond thermal conductivity to the isotopic purity. Theoretical investigations and further experiments concluded the main effect of isotopic substitution on the thermal conductivity is due to normal (N) processes of the phonon scattering in diamond crystals[10, 6, 126, 83], which conserves the total wave vector of scattering phonons. The Umklapp (U) processes of phonon scattering, in which the total wave vector changes by a reciprocal latter vector, also contribute. Our MD simulations contain no presumptions about the importance of U-process versus N-processes. Indeed, we were concerned whether a purely classical calculation would capture the substance of isotopic scattering. In principle, the classical dynamics should include such contributions, and hence, an important and effective test of our classical methods is to verify the remarkable isotope effect on diamond thermal conductivity.

Figure 5.37a shows the calculated thermal conductivities of diamond containing the 1.1% natural abundance of ^{13}C. We chose the sites randomly. The results are clear from Figure 5.37. First, the calculated thermal conductivity for diamond with natural abundance ^{13}C is much lower than for pure ^{12}C. Indeed, we calculate that

$$\frac{\lambda\left(^{12}C\right)}{\lambda(nat.abund.)} = 1.45 \pm 0.16 \tag{5.27}$$

which compares well with the experimental values[3, 83] of 1.50 ± 0.05 and 1.4. The ratio of increasing in thermal conductivity in pure diamond is depicted in Figure 5.37b. This result confirms the conclusion[10, 6, 126, 83] that no additional defects are necessary to explain the large isotope effect in natural diamond. Thus, the MD calculations explain the surprisingly high sensitivity to isotopic substitution.

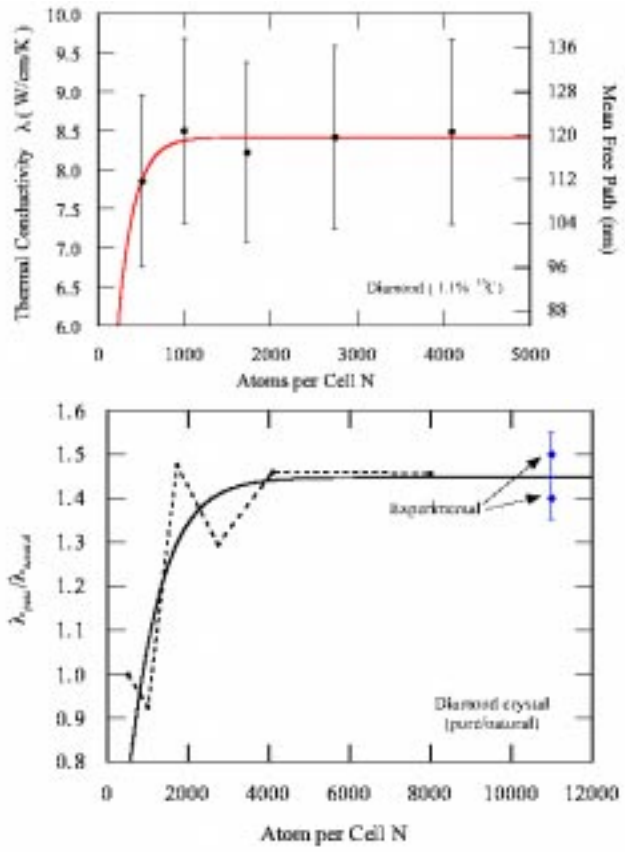

Figure 5.37: (a) The thermal conductivities for the perfect diamond structure with 1.1% natural abundance of ^{13}C (T=300 K). The right Y coordinate indicates the average phonon mean free path. The error bar is estimated from $(2\tau/t_{run})^{1/2}$ with $t_{run} = 400$ ps. (b) Ratio of thermal conductivity for pure ^{12}C diamond with respect to that for 1.1% ^{12}C. The experimental values are from references by Anthony[3] and Olson[83].

Comparing Figure 5.37a and Figure 5.36, it is clear that including isotopic variations leads to much faster convergence with the simulation cell in the calculation of thermal conductivity than the pure ^{12}C crystal. This is due to the decreased phonon mean free path.

We used the Brenner FF in our calculations. This FF was not optimized for describing the crystal properties of diamond important for phonons (e.g., elastic constants, thermal expansion constant, phonon dispersion relations, etc.). It leads to (i) a compressibility of 0.0020 GPa^{-1} compared to the experimental value of 0.0022 GPa^{-1} and (ii) a phonon frequency at the Γ point of 1288 cm^{-1} compared with the experimental value of 1333.9 cm^{-1}. These calculated

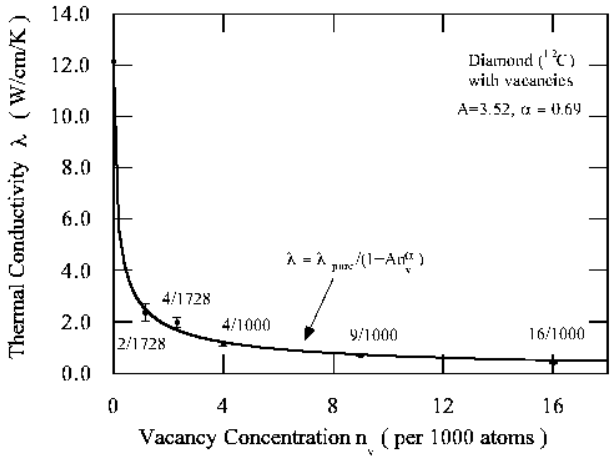

Figure 5.38: The thermal conductivities of ^{12}C diamond containing random distributions of vacancies. The solid curve is the fitting to the function 5.30, where $\alpha = 0.69$, and $A = 3.52$, see details in text.

properties (including heat capacity) agree reasonably well with experimental values. This is not surprising since the Brenner FF parameters were optimized to fit properties at low temperature. However, this FF fails to accurately describe the diamond crystal anharmonicity vital to the thermal conductivity. Thus as shown in section IV.A, the Brenner FF predicts the linear thermal expansion coefficient at room temperature to be $\beta = 4.16 \times 10^{-6}\ \ K^{-1}$, much larger than experimental value[19] $\beta = 1.18 \times 10^{-6}\ \ K^{-1}$. This indicates that the Brenner FF is too anharmonic. Since the thermal conductivity decreases dramatically with increasing thermal expansion coefficient[134], we believe that the large anharmonicity of the Brenner potential is responsible for the calculated thermal conductivity for natural diamond ($\lambda = 8.4$ w/cm/K at 300 K) being significantly lower than the experimental value, $\lambda = 21.9$ w/cm/K at 298 K.

We expect that a FF with a more accurate description of the anharmonicity would lead to better agreement with the experimental magnitude for the thermal conductivity of diamond. Thus, our earlier calculations[15] on C_{60} crystals, which used a very accurate FF, led to $\lambda = 4 \times 10^{-3} W/cm/K$ in good agreement with the experimental value of $\lambda = 0.4 W/m/K$. Although the calculated thermal conductivity λ for diamond differs substantially from experiment, we expect that relative changes in the thermal conductivity due to defects are valid. This view is supported by the accurate prediction of the isotope effect.

Vacancies

As a second application, we studied the effects of vacancies on the thermal conductivity. Here we considered a cell with $N = 1000$ or 1728 atoms and included

a random distribution of vacancies, leading to the results in Figure 5.38, which shows that the thermal conductivity decreases rapidly with vacancy concentration, n_v. Assuming that vacancy scattering is independent of the acoustic scattering dominant in the pure perfect crystal, we expect the total phonon scattering length (L) to be,

$$L_{tot}^{-1} \approx L_{pure}^{-1} + L_{vac}^{-1}, \tag{5.28}$$

where L_{pure} denotes the scattering length in perfect crystal and L_{vac} denotes the scattering length induced by vacancies. Assuming that the sound velocity and heat capacity are not affected by the vacancies, 5.28 leads to

$$\lambda_{tot}(n_v) = \frac{\lambda_{pure}\lambda_{vac}}{\lambda_{pure} + \lambda_{vac}} = \frac{\lambda_{pure}}{1 + \lambda_{pure}/\lambda_{vac}}. \tag{5.29}$$

Figure 5.38 shows the results for n_v up to 1.6% which are accurately fitted by 5.29i, with

$$\lambda_{tot}(n_v) = \frac{\lambda_{pure}}{1 + An_v^{\alpha}}. \tag{5.30}$$

where $A = 413.6(\pm 10.8\%)$ and $\alpha = 0.69(\pm 0.11)$.

The fit in 5.30 suggests that the vacancy contribution to thermal conductivity leads to a scaling law of

$$\lambda_{vac} \propto n_v^{-\alpha}, \tag{5.31}$$

where $\alpha \sim 0.7$. This result agrees with the phenomenological theory,[37] which estimates the exponent to be 1/2 to 3/4.

Our calculations indicate that with vacancies (as for the pure systems) the fast decay in the heat current correlation function integrates to a very small contribution to the overall thermal conductivity. This indicates that optical phonons have little effect on the values of the thermal conductivity (see the $A_o\tau_o$ value in Table 5.2). Figure 5.39 depicts the heat current correlation function for the case of 4 vacancies per 1000 atoms. Since the heat current correlation function is well converged, both direct integration and exponential fitting give same results for the thermal conductivity. This justifies the use of exponential fitting in the previous calculations, since only the portion of converged correlation functions were used to carry out the fitting.

Mass Dependence of Thermal Conductivity

In the classical limit, the thermal conductivity is expected to depend inversely on the square-root on atomic mass. This is because velocity of sound scales as $1/\sqrt{M}$ whereas the mean free path and specific heat do not change appreciably with mass in the classical limit. Figure 5.40 shows that the calculated thermal conductivity as a function of the atomic mass does behave as $1/\sqrt{M}$.

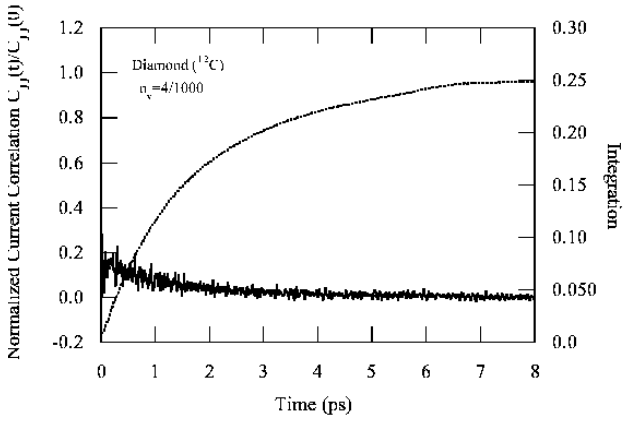

Figure 5.39: The heat current correlation function for the system with a concentration $n_v = 0.004$ vacancy. The exponential fit to the data is shown by dashed line (almost invisible under the heat correlation function). The time integrated curve is shown by dotted line.

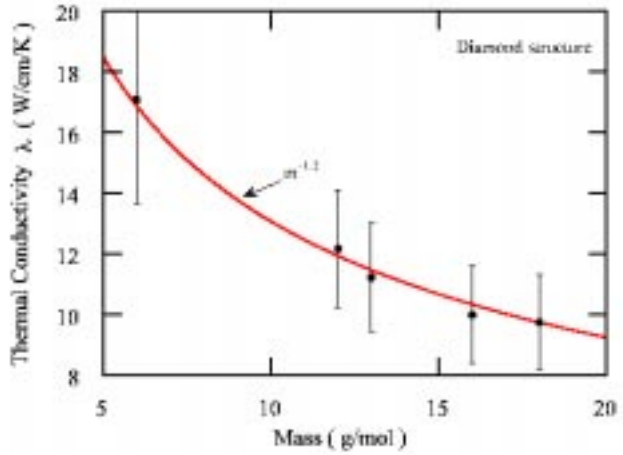

Figure 5.40: The dependence of the calculated thermal conductivities (pure systems) on atomic mass. The solid line is the fit to the phenomenological relation of $A/\sqrt{M}$.

Binary Alloys

A primary motivation in developing techniques to use MD simulations for calculating thermal conductivity is to predict the thermal properties of electronic devices based of thin films of heterostructures (e.g. the GaN/AlN/SiC/Si struc-

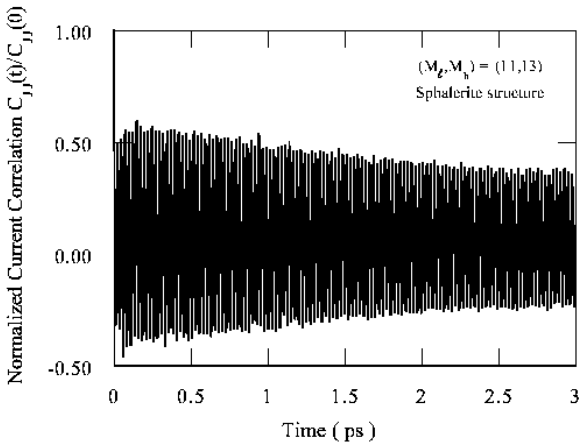

Figure 5.41: The heat current correlation function for $(M_l, M_h) = (11,13)$ sphalerite.

ture for high quality GaN films). To study the effects on thermal conductivity of mass mismatches in these systems, we chose to use the diamond FF but to consider equal numbers of atoms with light and heavy masses M_l and M_h. We kept $M_l + M_h = 24$ amu so that the macroscopic density remains constant, leading to the same velocity of sound (using the same FF leads to the same elastic constants). In the classical limit the specific heat will also remain constant in 5.26. In this case, the variation of thermal conductivities should depend mainly on the variation of phonon mean free path.

The $M_l M_h$ Sphalerite (B3 Cubic) System

First we consider the case in which the M_l and M_h alternate as in the cubic sphalerite or zinc blend structure (B3). The heat current correlation function at short times for $M_l/M_h = 11/13$ is shown in Figure 5.41. A striking feature here is that the heat current correlation function has a regular high frequency oscillation absent in the single component systems. This is due to the relative oscillation between bonded atoms with different mass. The lighter mass atoms move with a higher average velocity than the heavier mass atoms, giving a high amplitude heat current oscillation. When the two masses are same,the heat current due to this (optical) oscillation tends to cancel, so that no such heat current oscillations are observed in single component systems (see discussion in Section IV.B).

The Fourier Transformation of the correlation function, Figure 5.43, shows a strong peak at 1342 cm^{-1} that represents this oscillation frequency. Figure 5.44 shows how this frequency depends on the reduced mass. $\mu = M_l M_h/(M_l + M_h)$.

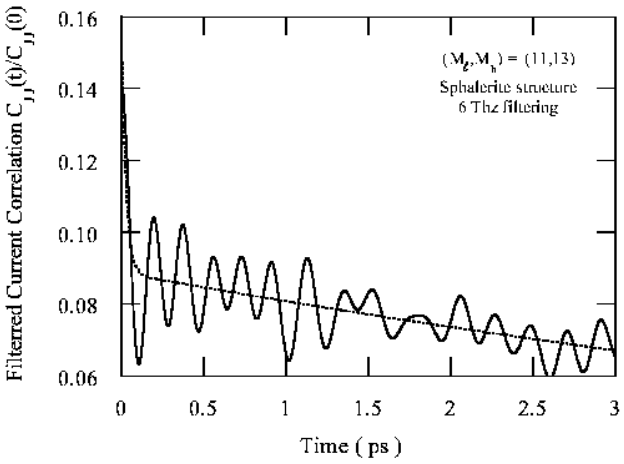

Figure 5.42: The heat current correlation function from above after Fourier low pass filtering using $\nu_{max} = 6$ (THz). The dotted line is the fitted double exponential fitting.

We see that

$$\omega(\mu) = A\sqrt{\frac{1}{\mu}}. \tag{5.32}$$

where $A = 3353.3$ cm^{-1}(g/mol)$^{1/2}$. This compares to a calculated frequency[9] for Γ_{15} of 1288 cm^{-1}.

The oscillation in the original correlation function Figure 5.41 makes it difficult to do either a direct integration or an exponential fitting. Therefore, to extract the underlying behavior of the correlation function, we used a square low pass Fourier filter to remove the oscillations above 6 Thz (200 cm^{-1}), since such modes do not contribute to the thermal conductivity. This leads to the correlation function in Figure 5.42, which was fitted to the double exponential functions. The validity was checked by the same procedure as for the single component system. The thermal conductivity was calculated using 5.25, leading to the thermal conductivities as a function of the reduced mass depicted in Figure 5.45.

Figure 5.45 shows that the thermal conductivity drops sharply when the single component system is changed into a binary system. Thus, λ drops by 37.1% when the single component ^{12}C system is changed to the 11/13 binary system. This drop implies a significant increase in the phonon scattering for the binary system as compared to a single component system. The result is not so surprising when we consider that just 1.1% of ^{13}C in the natural diamond leads to a thermal conductivity 31% lower than for pure ^{12}C diamond crystal.

Figure 5.45 shows two regions. Below $\mu = 5.625(M_l/M_h = 9/15)$ the λ is

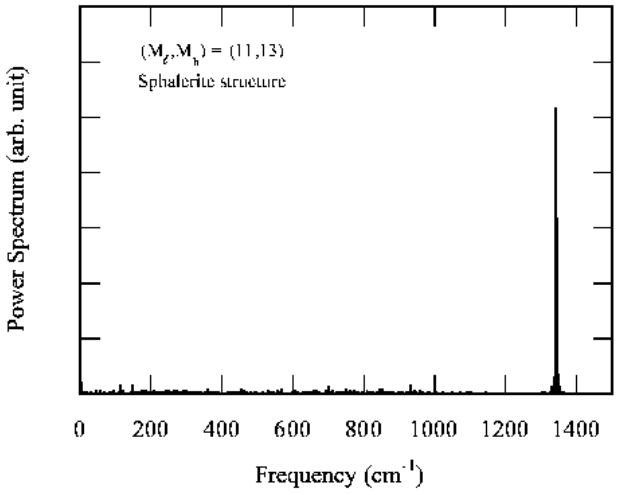

Figure 5.43: Power spectrum of Figure 5.41. The peak at 1342 cm^{-1} is interpreted as the optimal vibrational mode (Γ_{15}).

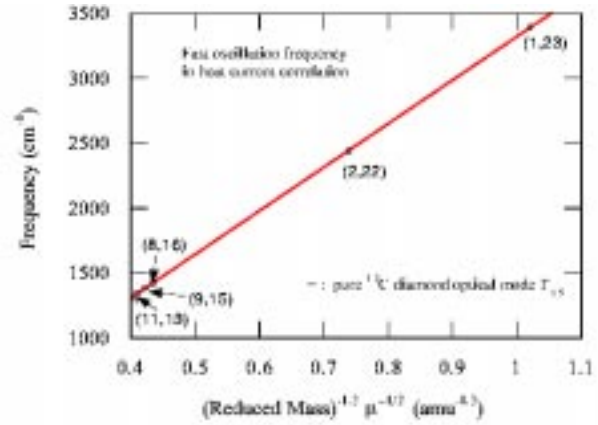

Figure 5.44: The characteristic frequencies of (M_l, M_h) sphalerite extracted from the Fourier transform of the heat current correlation function. The composition of (M_l,M_h) is labeled in the figure. The solid line is the linear fit [with $A = 3353.3$ $\mathrm{cm}^{-1}/(\mathrm{amu})^{1/2}$]. The plus symbol indicates the frequency of the Γ_{15} vibration in pure ^{12}C diamond.

linear in μ, leading to $\lambda = \lambda(o) + A\mu$ with A =0.72. Whereas for μ above 5.958 ($M_l/M_h = 11/13$) λ is linear in μ with $\lambda = \lambda(o) + B\mu$ where $B = 117.5$. We do

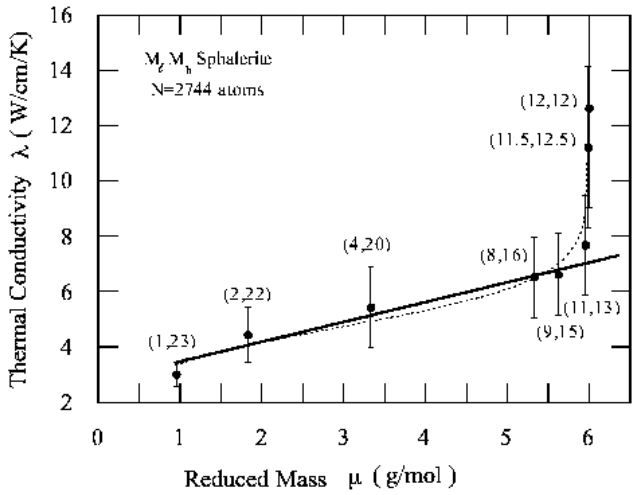

Figure 5.45: The thermal conductivity of (M_l, M_h) sphalerite as a function of reduced mass, $\mu = M_l M_h/(M_l + M_h)$. The solid line is the linear fit where the dashed line is a smooth function fit.

not have an explanation for this sharp transition.

Layered Alloys of Diamond

It is of interest to understand how the thermal conductivity depends on thin layers with different masses and force constants (e.g. GaN/AlN/SiC/Si). Here size confinement and interface effects can lead to thermal conductivities for thin layer structures quite different from the uniform bulk systems. The phonon mean free path of a thin layer structure is limited by the scattering on the interfaces. To study such systems, we formed layered structures using two masses (M_l and M_h). We considered $M_l/M_h = 4/20$ to match the mass ratio in a GaN semiconductor. In the limit of an alternating the mass for each atomic layer, we obtain exactly the sphalerite crystal structure. As indicated in Figure 5.45, the (4,20) case leads to λ =5.42 W/cm/K compared to λ = 12.2 W/cm/K for pure ^{12}C.

Increasing the thickness of each layer while keeping the total number of M_l and M_h atoms fixed leads to variation in the thermal conductivity. From mass dependence studies of perfect crystals (see Section IV.B.3), we expect that

$$\lambda_l = \frac{\sqrt{M_c}\lambda_c}{\sqrt{M_l}}, \tag{5.33}$$

$$\lambda_h = \frac{\sqrt{M_c}\lambda_c}{\sqrt{M_h}}. \tag{5.34}$$

For a macroscopic system, we obtain,

$$\lambda_{\perp}^{-1} = \frac{1}{2}(\lambda_l^{-1} + \lambda_h^{-1}), \quad \text{and} \quad \lambda_{\parallel} = \frac{1}{2}(\lambda_l + \lambda_h). \tag{5.35}$$

Combining 5.35, 5.33, and 5.34, and ignoring the effects of interfaces, we would expect that the thermal conductivity of layered structure to be,

$$F_{\parallel} = \frac{\lambda_{\parallel}}{\lambda_c} = \frac{\sqrt{M_c}(\sqrt{M_l} + \sqrt{M_h})}{2\sqrt{M_l M_h}}, \tag{5.36}$$

$$F_{\perp} = \frac{\lambda_{\perp}}{\lambda_c} = \frac{2\sqrt{M_c}}{\sqrt{M_l} + \sqrt{M_h}}. \tag{5.37}$$

Taking $M_l = 4$, $M_h = 20$, and $M_c = 12$, we obtain $F_{\parallel} = 1.45$ and $F_{\perp} = 1.07$ for the thermal conductivity of layered structure in the continuum limit. These results differ dramatically from simulation results which leads to $F_{\parallel} = 0.42$ and $F_{\perp} = 0.0034$ for the $l^{12}h^{12}$ case. This disagreements shows that there are clear size effects. Such size effects can be explained with the phonon mean free path is larger than the layer dimensions, making the impedance mismatch at the interfaces important. Such size effects in the thermal conductivity for nanoscale dimensions may have significant impact on the design of nanoscale devices (where energy must be rapidly dissipated).

To provide a relationship between the microscopic and continuum description, we introduce a boundary scattering process with a scattering length $D^{\perp,\parallel}$ proportional to the layer thickness l,

$$D_{\perp,\parallel} = l/\alpha^{\perp,\parallel}, \tag{5.38}$$

where $\alpha^{\perp,\parallel}$ is the scale constant that accounts for the effects in scattering in the perpendicular or parallel direction due to the level of interface mismatch. The symbols $\perp, \parallel$ denote the directionality respect to layer orientation. We expect that $\alpha^{\perp} \leq 1$. But that $\alpha^{\perp} \to 1$ for very distinct materials due to increasing of boundary scattering of phonons. We expect that $\alpha^{\parallel}$ is very small since the layered structure should have little effect on the parallel direction.

In the independent scattering approximation, we write the total phonon mean free path L_{tot} as,

$$L_{tot}^{-1} = (1-s)\left(L^{-1} + D_l^{-1} + D_h^{-1}\right) + sL_{lh}^{-1}. \tag{5.39}$$

Here L is the effective scattering length for pure systems and L_{lh} is the value for the sphalerite light-heavy systems. D_l and D_h are the characteristic scattering lengths for the light and heavy portions of the system. Our simulations have l as half of the periodicity for the perpendicular direction (i.e. actual layer thickness). s is an order parameter indicating how much the system differs from a pure sphalerite structure: for pure sphalerite structure $s = 1$, and for completely layered structure $s = 0$. Using 5.39, we can write the thermal conductivity for layered systems as,

$$\lambda_{\perp} = \lambda_c L^{-1}\left[sL_{lh}^{-1} + (1-s)\left(L^{-1} + D_{l,\perp}^{-1} + D_{h,\perp}^{-1}\right)\right]^{-1}, \tag{5.40}$$

$$\lambda_{\parallel} = \lambda_c L^{-1}\left[sL_{lh}^{-1} + (1-s)\left(L^{-1} + D_{l,\parallel}^{-1} + D_{h,\parallel}^{-1}\right)\right]^{-1}. \tag{5.41}$$

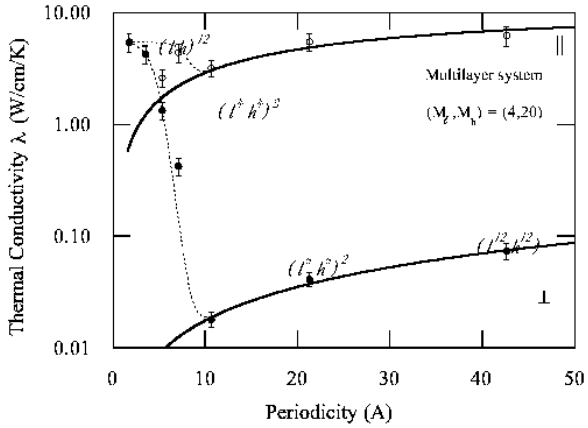

Figure 5.46: The thermal conductivity for M_l/M_h layered systems (the distribution of atoms in the layers is shown). The filled circles indicate the thermal conductivity in the direction perpendicular to the layers, and the open circles are for the ones parallel to the layers. The solid lines are calculated from 5.40 and 5.41 with $s = 0$ and $\alpha^{\perp,\parallel} = 1$. The dashed lines are calculated also from 5.40 and 5.41 but with $s \neq 0$ (taken s in the form of 5.44).

Note that above equations are valid for systems with same density, in other words, with same heat capacity and velocity of sound in the classical limit. In pure light or heavy systems, λ_c will have to be modified accordingly. At the sphalerite limit, 5.40 and 5.41 lead to the thermal conductivity of the binary composite,

$$\lambda = \lambda_\perp = \lambda_\parallel = \lambda_c L^{-1} L_{lh} = \lambda_{lh}, \tag{5.42}$$

In a previous section, we have obtained $L = 174$ nm. Thus, w can easily deduce the phonon mean free path L_{lh} from the above equation,

$$L_{lh} = 77\text{nm}. \tag{5.43}$$

The case of $s = 0$ in 5.40 and 5.41 (a system far from the sphalerite limit) leads to the solid line in Figure 5.46, which uses $\alpha^\perp = 1$ and $\alpha^\parallel = 0.004$. This suggests that the phonon scattering at a perpendicular interfaces is ~ 250 times larger than for a parallel interfaces. The filled circles show the simulated conductivities calculated from the simulations in the direction perpendicular to the layers. We see that for layer thicknesses above 6 atomic layers (~ 10 Å), the thermal conductivities agree well with the continuum theory. This suggests that for this system $s = 0$ for layers thicker than 10 Å. For layers thinner than 10 Å, the thermal conductivity jumps back to a value ~ 100 times larger, approaching the sphalerite value at the limit of $s = 1$.

Temperature (K)	0	247.7	297.3	346.8	396.2	495.1
Volume (Å^3)	15446.2	15494.8	15505.6	15515.1	15524.5	15543.0

Table 5.3: The volumes of simulation cell of 2744 atoms at various temperatures. The experimental lattice constant at 298 K is 3.56688 Å, which gives the volume of the cell 15565.4 Å^3.

This behavior suggests that increasing thicknesses of 10 Åin nanoscale composites can have very dramatic decreasing in the thermal conductivity. 5.40 and 5.41 in the simulation results leads to $s_1 = 1.0$, $s_2 = 0.9997$, $s_3 = 0.9941$, $s_4 = 0.9733$, and $s_6 = 0$, where the subscripts indicate the number of layers. We then described this order parameter in an approximating fitted form to the,

$$s = \frac{1 + \cos[0.01138(x - 1.778)]}{2\left[1 + \exp\left(\frac{x-8.505}{0.5896}\right)\right]}, \tag{5.44}$$

where x is the periodic length. In terms of layer numbers, 5.44 becomes

$$s = \frac{1 + \cos[0.01280(n_\perp - 2)]}{2\left[1 + \exp\left(\frac{n_\perp - 9.567}{0.6632}\right)\right]}. \tag{5.45}$$

where $n_\perp$ is the number of continuous atomic layers having the same mass.

5.6 FY 00 objectives

5.6.1 High Explosives

- Extend reaction networks to HMX;
- Develop an equation of state for HMX using a vibrationally accurate force field;
- Implement a reactive force-field description for HMX, RDX, and TATB;
- Complete the equations of state for the Kel-F and Estane binders;
- Perform molecular dynamics simulations of energetic material crystallites in a polymer blender.

5.6.2 Solid Dynamics

- Develop an equation of state for Ta based fully on quantum mechanical calculations;
- Atomistic simulation of shock wave propagation in Ta;
- Completion of Ta force fields capable of describing spall and dislocations;
- Compute a quantum mechanical equation of state for Fe including FCC, BCC, HCP and A15 phases.

5.6.3 Methodology

- Perform hybrid DFT/QMC calculations on potential energy surfaces;
- Develop new density functionals for metals;
- Perform QM-MD simulations on metals;
- Implement improved diagonalization techniques in QM programs;
- Extend MP Software Integration.

Chapter 6

Compressible Turbulence

6.1 Overview of FY 99 Accomplishments

In this chapter we describe the accomplishments to date of our research program in compressible turbulence. The origin of compressible turbulence in the virtual facility lies in the fact that under the appropriate loading conditions strong shocks can propagate and interact with solid targets consisting of layers of distinct materials with the result that material strength is no longer relevant. Such interactions also arise in this facility if the target materials are already in the fluid or gaseous state and consist of density stratified layers of material with superposed perturbations. An example of such a configuration is shown in Figure 6.1. Upon interaction with the shock, the material interfaces are impulsively accelerated and the resulting baroclinic generation of vorticity due to the misalignment of pressure and density gradients gives rise to the well-known Richtmyer-Meshkov instability and ultimately produces turbulent mixing that can contaminate or dilute the materials bordering the interfaces. The modeling and simulation of these Richtmyer-Meshkov instabilities and the resulting inhomogeneous anisotropic turbulence is a major thrust of the center's research program. The instability process as well as the modeling of the resulting turbulence lies at the heart of many ASCI applications. An understanding of compressible turbulence and mixing is essential, for example, in important ASCI applications in which shock-driven implosion is a key step. In order to develop an understanding of the relevant phenomena and a modeling capability the compressible turbulence effort has concentrated on the following objectives:

- Direct numerical simulation (DNS) of strong shock Richtmyer-Meshkov instability. The ultimate objective here is to develop an LES model which can coexist with shock capturing schemes and thus provide reliable turbulence modeling in the presence of shock waves.
- Development of a DNS database for decaying and driven compressible

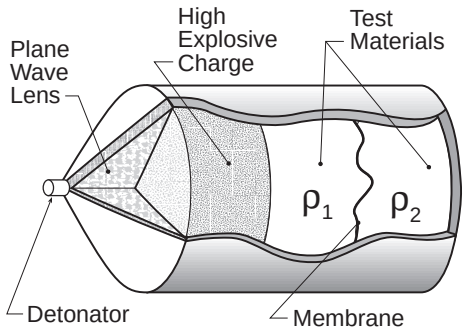

Figure 6.1: A caricature of the proposed facility which gives rise to compressible turbulence. In the configuration shown above, the materials (in the gaseous or fluid state) are exposed directly to the loading arising from the point detonation of the high explosive.

turbulence. The objective is to have a basis of comparison to verify our turbulence modeling efforts. The specific flows under consideration are

- Decaying compressible turbulence
- Richtmyer-Meshkov instability initiated by weak shocks
- Rayleigh-Taylor instabilities

These flows, while involving only relatively weak compressibility effects are typical of the turbulent states to be found even in compressible turbulence driven by strong shocks.

- Development of sub-grid scale (SGS) models for large eddy simulation (LES) of compressible turbulence.
- Detailed comparison with existing and new experimental measurements of Richtmyer-Meshkov and Rayleigh-Taylor instabilities
- Integrated simulations of HE driven turbulence in the VTF with a full LES capability.

Our accomplishments to date are itemized briefly below:

Simulations of 3-D Richtmyer-Meshkov instability

This work is ongoing. We have performed several large runs of shock-contact interaction resulting in R-M instability including the effects of reshock. To date resolutions of $2048 \times 256 \times 256$ have been achieved on the LANL Blue Mountain platform. Scalability assessments have been performed and have shown that our unigrid CFD capability is very scalable. High resolution visualization of this data via the Responsive Workbench are currently in progress.

High resolution 3-D DNS of decaying turbulence

This work is now complete. We have produced a database of highly accurate fully resolved decaying compressible turbulent flows for comparison with simulations utilizing SGS schemes. Achievements to date include the development of two parallel codes, one a fully compressible multi-species DNS code with full physical viscosity utilizing Padé-base methods and the other a high order incompressible spectral element solver. Both codes have been implemented on the ASCI platforms.

Sub-grid modeling for LES of compressible turbulence

Two SGS models have been developed and comparisons have been carried out with DNS simulations of decaying turbulence with encouraging results. The first is a model based on the stretched subgrid vortex model of Saffman and Pullin. The second is based on the nonlinear model of Kosovic.

Development of 3-D AMR solver

This work is ongoing. We have successfully developed a 2-D solver for compressible flow utilizing adaptive mesh refinement under the GrACE computational framework. Extensions to 3-D are underway with the objective of high resolution simulations of Richtmyer-Meshkov simulations with reshock.

High resolution 3-D DNS of R-M and R-T flows

This work is ongoing. Achievements to date include the development of two parallel codes, one a fully compressible multi-species DNS code with full physical viscosity utilizing Padé-base methods and the other a high order incompressible spectral element solver. Both codes have been implemented on the ASCI platforms.

6.2 Personnel

The FY 99 personnel participating in the Compressible Turbulence research activity are listed below.

- Faculty and Senior Researchers
  - Dan Meiron (PI)
  - Dale Pullin
  - Paul Dimotakis
  - Brad Sturtevant
  - Tony Leonard
  - Ravi Samtaney
  - Ron Henderson
- Postdoctoral Scholars

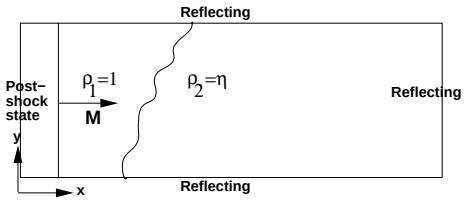

Figure 6.2: Schematic of the shock contact-discontinuity interaction.

  - Branko Kosovic
  - Stefan Deusch

- Research Staff
  - Santiago Lombeyda
  - James Patton

- Graduate Students
  - Tobias Voelkl
  - Gerard O'Reilly
  - Jimmy Fung
  - Piet Moeleker

6.3 Simulations of strong shock R-M instability

The Richtmyer-Meshkov instability arises at an interface separating two gases subjected to an impulsive acceleration [94]. In his original paper, Richtmyer used a shock-wave to provide the impulsive acceleration to an interface (contact discontinuity) with long wavelength perturbations, and performed a linear stability analysis. Subsequently, analysis, numerical simulation and experimental studies of the interactions of shock-waves with contact-discontinuities have become associated with the domain of RM instability. The principal interaction parameters are the Mach number of the shock, M_s, the Atwood number across the contact defined as $At = (\rho_2 - \rho_1)/(\rho_2 + \rho_1)$, and the geometry of the interface. Typically, the interface is perturbed with a single or multiple harmonic perturbations, or random white noise perturbations. A shock-wave (called the incident shock) is initialized on the left of an interface and moves from left to right (similar to the situation depicted in Figure 6.1). The incident shock refracts at the interface and bifurcates into a reflected wave (which may be a shock or an expansion fan) and a transmitted shock. The current effort has focussed on interactions of strong shock waves ($M_s \geq 10$) with single harmonic or randomly perturbed interfaces in three dimensions and is an extension of work by Samtaney and Meiron [102]. The main emphasis in RM flows is on the quantification of the so-called "mixing width" and its growth rate. The

primary subject of investigation is an examination of the effects of "reshock" on the growth of the mixing width. By reshock we mean the following: the transmitted shock reflects off the right boundary and this reflected wave interacts with the interface.

6.3.1 Run Parameters

We simulate the compressible Euler equations using the Equilibrium Flux Method [90]. The physical domain, $[-0.8, 12] \times [0, 1.6] \times [0, 1.6]$, was discretized by a uniform mesh of $1024 \times 128 \times 128$ cells. For all the results presented the shock Mach number was fixed at $M_s = 10$. The interface geometry was either a single mode perturbation or a white noise random perturbation. The single mode interface is given by $A = 0.35 \cos ky \cos kz$ where $k = 2\pi/\lambda$ and $\lambda = 3.2$. Two different Atwood numbers were investigated: $At = 0.5$ and $At = -0.33$. Note that a positive (resp. negative) Atwood number corresponds to the fast-slow (resp. slow-fast) case which means that the transmitted shock speed is slower (resp. faster) than the incident shock speed. Time was scaled such that it takes a unit time for an acoustic wave in the unshocked incident gas to travel one wavelength λ.

6.3.2 Results

Single Mode Perturbations

Images of volume-rendered density field at different times are shown in Figures 6.3 and 6.4, for $At = 0.5$ and $At = -0.33$, respectively. In both cases the incident shock initially compresses the interface which reduces the mixing width rapidly. After the passage of the incident shock, W increases due to the instability for the positive Atwood ratio interface. For the positive Atwood number interface, reshock causes a phase reversal of the interface. On the other hand, for the negative Atwood number interface, the interface undergoes a phase reversal early during the interaction after which the mixing width grows. After reshock there is no phase reversal and the interface mixing width continues to grow. The mixing width as a function of time is plotted in Figure 6.5. For the positive Atwood number interface, the growth rate after reshock is comparable to that before reshock. For the negative Atwood ratio interface, the growth rate is significantly enhanced after reshock. Since the transmitted shock moves significantly faster in the negative Atwood number case, the entire process occurs rapidly for $At = -0.33$ when compared with the $At = 0.5$ case in our normalized time units.

Random Perturbations

The evolution of the mixing width for a randomly perturbed interface is shown in Figure 6.6. As before, the incident shock first compresses the perturbations which is seen as a reduction in mixing width. The instability then leads to a slow growth of the mixing width. However, for the positive Atwood number case ($At = 0.5$), the growth of the mixing width is so slow, that even at $t \approx 0.75$,

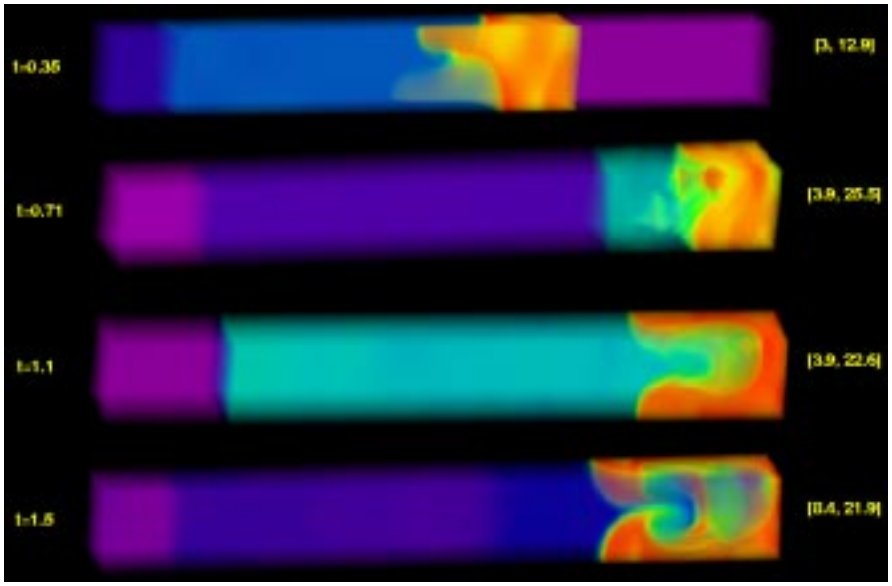

Figure 6.3: Images of volume-rendered density field at various times. The Atwood ratio $At = 0.5$. The color-map is varies from purple-blue to red with increasing density. The minimum and maximum density values for the color-scale are shown in parentheses on right of each image. The ratio of the initial perturbation amplitude to wavelength is 0.109. The shock Mach number is $M_s = 10$.

$W(t)$ is less than its initial value $W(0)$. At $t \approx 0.8$, the interface is reshocked which causes a significant increase in the growth rate. A similar observation was made by Vetter and Sturtevant [120] in shock-tube experiments. It is interesting to note that the growth rate of the $At = -0.33$ case is larger than the $At = 0.5$ case.

Results at higher resolution

We have performed high resolution simulations of the R-M instability on the LANL ASCI Blue Pacific platform. The resolution of these runs is $2048 \times 256 \times 256$. Shown in Figure 6.7 are some early time results. At the top of the figure we show the full simulation domain and the early time interaction of the shock with the density stratification. The parameters for the run are similar to those described above. At the bottom of the figure we show a detail of the mixing zone after the shock has passed. These high resolution runs will be essential to verify the large scale features of the R-M instability. They are particularly essential in simulating the effect of reshock. Indeed, we anticipate that such simulations will eventually require the 3-D AMR capability under development.

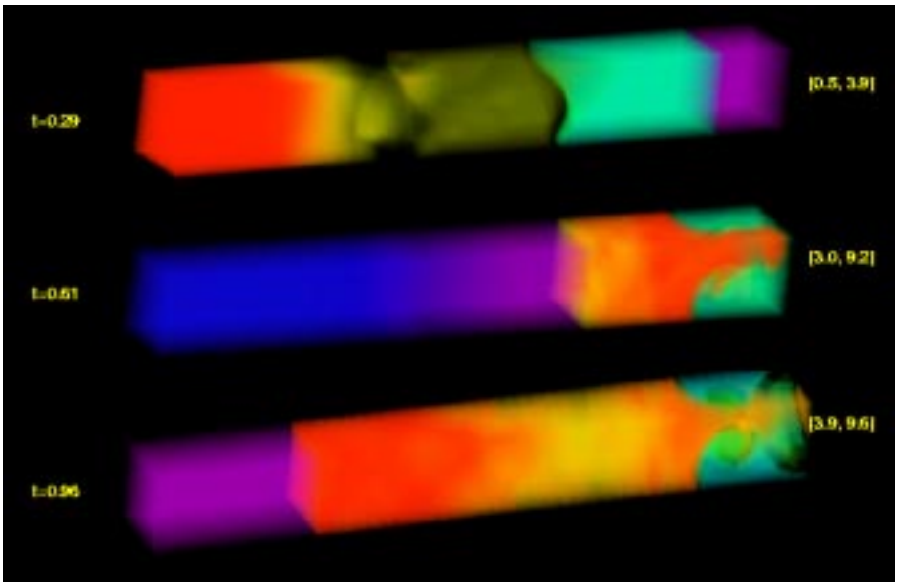

Figure 6.4: Images of volume-rendered density field at various times. The Atwood ratio $At = -0.33$. The color-map is varies from purple-blue to red with increasing density. The minimum and maximum density values for the color-scale are shown in parentheses on right of each image. The ratio of the initial perturbation amplitude to wavelength is 0.109. The shock Mach number is $M_s = 10$.

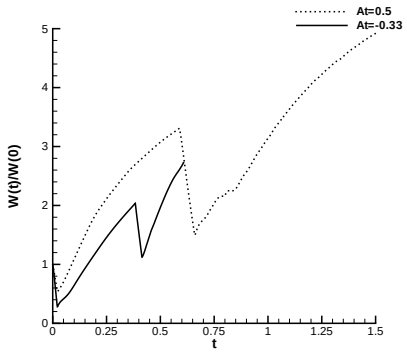

Figure 6.5: Time history of mixing width for a single harmonic perturbation. The mixing width is scaled by the mixing width at $t = 0$. The ratio of the initial perturbation amplitude to wavelength is 0.109. The shock Mach number is $M_s = 10$.

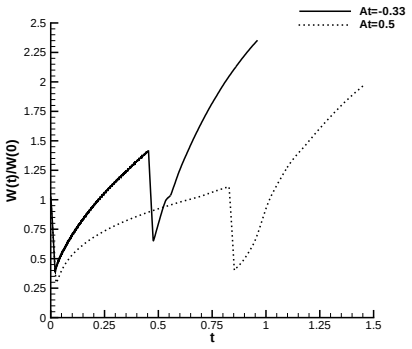

Figure 6.6: Time history of mixing width of a randomly perturbed interface. The mixing width is scaled by the mixing width at $t = 0$. The shock Mach number is $M_s = 10$.

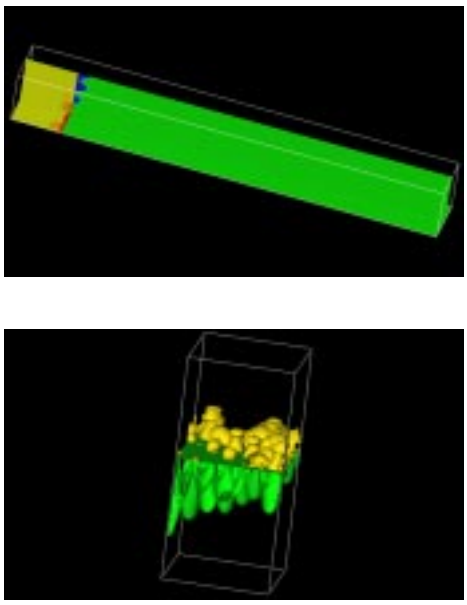

Figure 6.7: Top: Vertical and horizontal slices of the density for the early interaction of a Mach 10 shock at high resolution ($2048 \times 256 \times 256$) with a perturbed density interface. Bottom: isosurface of the density after the shock has propagated away from the interface.

6.4 Turbulence modeling

In this section we describe our efforts in developing a turbulence model suitable for compressible turbulent flows. Our ultimate objective is to develop a model

which can be used to perform LES simulations of the strong shock Richtmyer-Meshkov instability with particular emphasis on the compressible turbulence caused by shock-vorticity interactions (reshock).

6.4.1 Favre-filtered Navier-Stokes Equations

For the purposes of large-eddy simulation, we begin with the Favre-filtered Navier-Stokes equations, where the Favre average $\widetilde{Q}$ of Q is $\widetilde{Q} = \rho\bar{Q}/\bar{Q}$ and $\bar{Q}$ is the filtered quantity. The Favre filtered continuity, momentum and energy equations are respectively, in conservative form

$$\frac{\partial\bar{\rho}}{\partial t} + \frac{\partial\bar{\rho}\widetilde{u}_i}{\partial x_i} = 0, \tag{6.1}$$

$$\frac{\partial\bar{\rho}\widetilde{u}_i}{\partial t} + \frac{\partial(\bar{\rho}\widetilde{u}_i\widetilde{u}_j + \bar{p}/\gamma M^2\delta_{ij})}{\partial x_j} = \frac{1}{Re}\frac{\partial\widetilde{\sigma}_{ij}}{\partial x_j} - \frac{\partial\tau_{ij}}{\partial x_j}, \tag{6.2}$$

$$\begin{aligned}\frac{\partial\bar{E}}{\partial t} + \frac{\partial(\bar{E} + \bar{p}/\gamma M^2)\widetilde{u}_i}{\partial x_i} = \\ \frac{1}{\alpha}\frac{\partial}{\partial x_i}\left(k\frac{\partial\widetilde{T}}{\partial x_i}\right) + \frac{1}{Re}\frac{\partial(\widetilde{\sigma}_{ij}\widetilde{u}_j)}{\partial x_i} - \frac{1}{(\gamma-1)M^2}\frac{\partial(\bar{\rho}q_i)}{\partial x_i} \\ -\frac{1}{2}\frac{\partial[\bar{\rho}(\widetilde{u_j u_j u_i} - \widetilde{u_j u_j}\widetilde{u}_i)]}{\partial x_i} + \frac{1}{Re}\frac{\partial(\widetilde{\sigma_{ij}u_j} - \widetilde{\sigma}_{ij}\widetilde{u}_j)}{\partial x_i},\end{aligned} \tag{6.3}$$

where

$$\tau_{ij} = \bar{\rho}(\widetilde{u_i u_j} - \widetilde{u}_i\widetilde{u}_j),$$

and

$$\bar{E} = \frac{\bar{p}}{(\gamma-1)\gamma M^2} + \frac{1}{2}\bar{\rho}(\widetilde{u}_j\widetilde{u}_j) + \frac{1}{2}\bar{\rho}(\widetilde{u_j u_j} - \widetilde{u}_j\widetilde{u}_j),$$

and the subgrid heat flux, q_i is

$$q_i = \widetilde{Tu_i} - \widetilde{T}\widetilde{u}_i.$$

The filtered equation of state is

$$\bar{p} = \bar{\rho}\widetilde{T}. \tag{6.4}$$

For LES, the terms which must be modeled are τ_{ij}, the turbulent heat flux q_i, the triple correlation $\widetilde{u_j u_j u_i} - \widetilde{u_j u_j}\widetilde{u}_i$ and the subgrid viscous work $\widetilde{\sigma_{ij}u_j} - \widetilde{\sigma}_{ij}\widetilde{u}_j$. A brief description of the two subgrid models used for the present LES calculations follows.

6.4.2 The stretched-vortex sgs-model

The stretched vortex model for LES of incompressible flows [76, 77] can, with some modifications, be extended to subgrid modeling for compressible flow. In this model it is assumed that subgrid motion is that produced by straight, nearly axisymmetric vortices [91]. The resulting subgrid stresses are

$$\tau_{ij} = \bar{\rho} K \left(\delta_{ij} - \mathrm{e}_i^v \, \mathrm{e}_j^v\right), \qquad K = \int_{k_c}^{\infty} E(k)\, dk, \tag{6.5}$$

where K is the subgrid energy and e_i^v, $i = 1, 2, 3$ are the direction cosines of the subgrid vortex axis. The subgrid energy is estimated by assuming a Kolmogorov form of $E(k)$ for the subgrid motion

$$\begin{aligned} E(k) &= \mathcal{K}_0 \, \epsilon^{2/3} \, k^{-5/3}, \; k_c < k < J\eta^{-1}, \\ &= 0, \qquad\qquad\qquad k > J\eta^{-1}, \end{aligned} \tag{6.6}$$

where $\mathcal{K}_0$ is the Kolmogorov prefactor, $\eta = (\nu^3/\epsilon)^{\frac{1}{4}}$ is the local Kolmogorov length. The e_i^v are fixed in the model by the assumption that the subgrid vortices align locally (i.e. within each cell) with the principal eigenvectors of the resolved rate-of-strain tensor, $\widetilde{S}_{ij} = (\partial \tilde{u}_i/\partial x_j + \partial \tilde{u}_j/\partial x_i)/2$ [76]. We estimate the product $\mathcal{K}_0 \, \epsilon^{2/3}$ in (6.6) by utilizing an estimate of the local second-order velocity structure functions obtained from the six-point stencil surrounding each cell [75, 123]. We assume that both the SGS triple correlation and the viscous subgrid work terms are small and can be neglected compared to other retained terms. The subgrid heat flux term may not be small [79] and must be modeled. Presently we model q_i by subgrid convection of a passive scalar taken as the temperature $\tilde{T}$. We solve the passive-scalar convection equation in the frame of reference of the subgrid vortex and then calculate subgrid heat flux analytically. Using a random phase approximation to average fluxes over SGS fluctuating temperature we can obtain the tensor-diffusivity model [123]

$$q_i = \frac{1}{2} \Delta \, K^{1/2} \left(\delta_{ij} - \mathrm{e}_i^v \, \mathrm{e}_j^v\right) \frac{\partial \widetilde{T}}{\partial x_j}, \tag{6.7}$$

where Δ is the local mesh size. Because K and e_i^v are already available from the SGS model, the calculation of q_i only requires the additional evaluation of temperature gradients. The model contains as parameters the cell-size Δx and the spectral cutoff $J = O(1)$ in the energy spectrum.

At $t/\tau = 1.5$, a time at which the turbulence may be considered to be fully developed, we truncated the 256^3 DNS data to 32^3 and performed an LES with the SGS model proposed in this section. A comparison of decay of turbulent kinetic energy between LES and DNS is shown in Figure 6.8 for the stretched-vortex model. The LES was performed at several different orders of accuracy. The agreement with DNS is good for tenth and sixth-order accurate schemes and fair for the fourth-order scheme. The second order accurate scheme did not complete as negative temperatures developed.

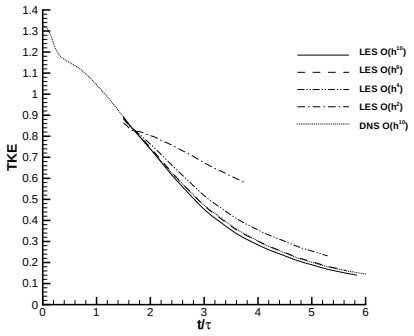

Figure 6.8: Comparison of decay of turbulent kinetic energy between DNS (tenth-order accurate) with LES, using the stretched vortex SGS, at different orders of accuracy.

6.4.3 A Nonlinear Subgrid Model

A nonlinear subgrid-scale model [55] was developed for LES of incompressible, high Reynolds number flows. This model was designed to account for the backscatter of turbulent kinetic energy and the normal stress effects in shear-driven flows. We have modified the model to account for the effects of compressibility, and to provide the correct behavior in the limit of the filter length scale approaching the Kolmogorov length scale. The anisotropic component of the subgrid stress tensor is modeled as

$$\begin{aligned} \tau_{ij} = \quad & - \quad \bar{\rho}(C_s\Delta)^2 \left\{ 2(2\widetilde{S}_{mn}\widetilde{S}_{mn})^{\frac{1}{2}} \left(\widetilde{S}_{ij} - \widetilde{S}_{kk}\delta_{ij} \right) \right. \\ & + \quad C_1 \left(\widetilde{S}_{ik}\widetilde{S}_{kj} + \frac{1}{3}\, C_r^{\frac{1}{2}}\, \widetilde{S}_{mn}\widetilde{S}_{mn}\, \delta_{ij} \right) \\ & + \quad \left. C_2 \left(\widetilde{S}_{ik}\, \widetilde{\Omega}_{kj} - \widetilde{\Omega}_{ik}\, \widetilde{S}_{kj} \right) \right\}, \end{aligned} \tag{6.8}$$

where $\tilde{\Omega}_{ij}$ is the rotation rate tensor. A natural extension of the nonlinear subgrid model to compressible flows included modeling the isotropic component of the subgrid stress tensor using the model developed by Yoshizawa [130] where we accounted for the limit $\Delta \to \eta$. The parameter C_r is defined as the ratio of resolved and total dissipation rate. Under the assumption of isotropy this parameter can be estimated as

$$C_r = 15\frac{\mu}{Re}\left(\frac{15}{2\widetilde{S}_{mn}\widetilde{S}_{mn}}\right)^{\frac{1}{2}}\left(\frac{1}{10}\mathcal{K}_0\right)^{\frac{3}{2}}\left(\frac{\pi}{\Delta}\right)^2. \tag{6.9}$$

Notice that the parameter C_r can be related to the ratio of the filter length scale, Δ, and Kolmogorov length scale, η, so that $C_r = (\eta/\Delta)^{4/3}$. Model parameters

can be determined considering homogeneous turbulent flows. The Smagorinsky parameter, C_s, and the nonlinear model parameter, C_1, were determined so that the model provides correct inertial transfer of energy including the backscatter of energy in isotropic turbulent flows

$$C_s = \left[\frac{(1 - C_r)\ (1 + C_b)}{\left(\frac{3}{2}\mathcal{K}_0\right)^{\frac{3}{2}}\ \pi^2} \right]^{\frac{1}{2}}, \tag{6.10}$$

$$C_1 = \frac{\sqrt{960}\ C_b}{7\ (1 + C_b)(1 - C_r)\ \mathcal{S}(k_c)}. \tag{6.11}$$

Here, C_b is the backscatter parameter, defined as the ratio of the rate of backscatter of energy and the dissipation rate [62], and $\mathcal{S}(k_c)$ is the skewness of the resolved stream-wise velocity derivative. The backscatter parameter is the only free parameter in the model. The nonlinear model parameter C_2 was determined so that the model captures the normal stress effects observed in homogeneous sheared flows. The values of normal turbulent stresses measured in homogeneous turbulence subjected to the simple shear were used [55] to find that

$$C_2 \approx C_1 \tag{6.12}$$

To model subgrid heat flux q_i we used a simple gradient diffusion model

$$q_i = -2\frac{(C_s\Delta)^2}{Pr_t}\ (2\widetilde{S}_{mn}\widetilde{S}_{mn})^{\frac{1}{2}}\frac{\partial\widetilde{T}}{\partial x_i}, \tag{6.13}$$

where Pr_t is the subgrid turbulent Prandtl number. The nonlinear model was used in LES of compressible decaying isotropic turbulence. In these simulations the backscatter parameter was set to $C_b = 0.15$. Again the LES uses compact differencing schemes with different orders of accuracy. We also attempted to use an explicit second order centered differencing scheme. The decay of total turbulent kinetic energy given by the nonlinear SGS model compared to the DNS results is given in Figure 6.9. We point out that only when the highest order scheme was used was LES completed successfully. Simulations with lower order schemes terminated prematurely due to development of negative pressures or temperatures. We remark that neither of the two SGS models tested presently contains explicit recognition of shocks or of shocklets.

6.5 DNS of compressible turbulence

In this section we describe direct numerical simulations of decaying isotropic, compressible turbulence in a periodic domain. Comparisons with LES are shown in the previous section. The present DNS was performed using a 10-th-order compact Páde scheme [61]. High order methods with near-spectral accuracy are limited to turbulent Mach numbers $M_t^2 =< u_i u_i > / < c >^2$ (<> indicates average over the periodic domain) such that only weak shocklets appear.

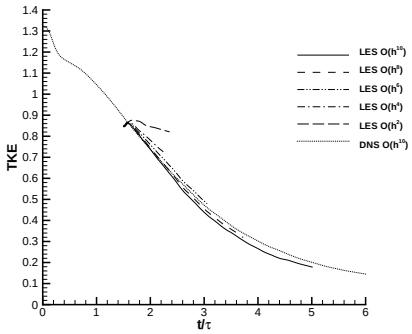

Figure 6.9: Comparison of decay of turbulent kinetic energy between DNS (tenth-order accurate) with LES, using the nonlinear SGS model, at different orders of accuracy.

An extensive discussion of decaying isotropic compressible turbulence was given by Blaisdell *et al.* [11]. He described 96^3 pseudo-spectral simulations for which the initial root-mean-square Mach number, M_{rms} varied from 0.05-0.7, and the initial Taylor microscale Reynolds number Re_λ was $O(50)$. Note that M_{rms} is defined differently from M_t but usually the difference in their numerical values is small. Blaisdell describes several simulations for which spectra for the solenoidal and the dilatational velocity components, pressure and density fluctuations are specified. The existence of eddy shocklets in DNS of decaying isotropic turbulence was demonstrated by Lee *et al.* [60]. They reported results from 64^3 and 128^3 simulations with their largest $Re_\lambda = 50$ and largest turbulent Mach number $M_t = 0.612$. Their initial conditions were limited to purely solenoidal velocity fields with no fluctuations of any thermodynamic fields. The spatial derivatives were calculated with a sixth order compact finite difference scheme.

Erlebacher *et al.* [26] performed a DNS of decaying isotropic turbulence with a split numerical method and a Fourier collocation method to evaluate the spatial derivatives and using 64^3, 96^3 and 128^3 points. Their peak $Re_\lambda \approx 39$ and peak $M_t \approx 0.6$. The initial density field was uniform while the pressure fluctuations were obtained by solving a Poisson equation for the pressure fluctuations. They observed that if the dimensionless root-mean-square of the density and temperatures were smaller than the turbulent Mach number, that is, $\rho_{rms}, T_{rms} << M_t$ initially, then the turbulence statistics are effectively quasi-incompressible. The DNS of decaying isotropic turbulence by Zang *et al.* [132] focused in a parameter regime where no eddy shocklets were observed. Their initial density was uniform, but pressure and temperature fluctuations were imposed by specifying the spectrum for the temperature. The initial divergence field was not zero in several of their simulations. Their largest simulation involved 96^3 points, with the peak $Re_\lambda = 27$ and peak $M_t = 0.4$.

With the exception of Blaisdell *et al.* [11], all of the above-cited simulations employed a non-conservative formulation of the energy equation. Presently, we explicitly time-march the total energy per unit volume E, and use a conservative form for the energy equation. We find, consistent with observations by Blaisdell *et al.* [11], that a skew-symmetric form of the nonlinear term in the momentum equation gives more stable simulations than a uniformly conservative method.

6.5.1 Equations and Numerical Method

The compressible Navier-Stokes equations in dimensionless form are given below.

$$\frac{\partial \rho}{\partial t} + \frac{\partial \rho u_i}{\partial x_i} = 0, \tag{6.14}$$

$$\frac{\partial \rho u_i}{\partial t} + \frac{\partial (\rho u_i u_j + p/\gamma M^2 \delta_{ij})}{\partial x_j} = \frac{1}{Re} \frac{\partial \sigma_{ij}}{\partial x_j}, \tag{6.15}$$

where

$$\sigma_{ij} = \mu \left(\frac{\partial u_i}{\partial x_j} + \frac{\partial u_j}{\partial x_i} \right) - \frac{2}{3} \mu \frac{\partial u_k}{\partial x_k} \delta_{ij},$$

and μ is the non-dimensional viscosity, which has a power law dependence on temperature as $\mu = T^{0.76}$,

$$\frac{\partial E}{\partial t} + \frac{\partial (E + p/\gamma M^2) u_i}{\partial x_i} = \frac{1}{\alpha} \frac{\partial}{\partial x_i} \left(k \frac{\partial T}{\partial x_i} \right) + \frac{1}{Re} \frac{\partial \sigma_{ij} u_j}{\partial x_i}, \tag{6.16}$$

where $\alpha = PrRe(\gamma - 1)M^2$, k is the dimensionless thermal conductivity and γ is the adiabatic exponent of the gas. The system is closed with an equation of state for a perfect gas,

$$p = \rho T, \quad i.e., \quad E = \frac{p}{(\gamma - 1)\gamma M^2} + \frac{1}{2} \rho (u_j u_j).$$

In the above equations, the length scale is L, the velocity scale is U and the time scale is L/U. The reference density and sound speed are respectively ρ_0 and c_0. The total energy is then scaled by $\rho_0 U^2$, and the pressure scale is $p_0 = \rho_0 c_0^2/\gamma$. The reference viscosity and conductivity are μ_0 and k_0 respectively. The non-dimensional parameters are a reference Reynolds number $Re = \rho_0 UL/\mu_0$, a reference Mach number $M = U/c_0$ and a Prandtl number $Pr = \mu_0 c_p/k_0$, where c_p is the specific heat of the gas at constant pressure. Note that we have written the equations in the strong conservation form.

The above equations were solved numerically with a high order compact finite difference scheme [61]. A FORTRAN-90 code was implemented on different parallel architectures (CRAY T3E and SGI Origin 2000), and the scalability of the code with increasing the number of processors was good (See Figure 6.10). The order of the spatial discretization was kept flexible and could be varied from

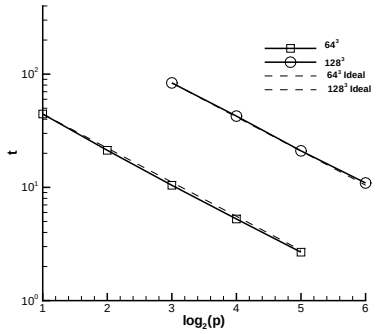

Figure 6.10: Time taken for one time step of the DNS code versus number of processors used for two different problem sizes. The dashed curves indicate ideal scalability. Note that the abscissa is the logarithm to base two of the number of processors.

a second-order explicit central differencing to tenth-order compact finite differencing. The maximum order of accuracy was limited to ten because, for periodic boundary conditions, this leads to a pentadiagonal system of linear equations with corner terms, and can be solved in an efficient manner with linear complexity of the solution algorithm [128]. No explicit filtering or de-aliasing of the nonlinear terms in the governing equations is performed. The code conserves mass and total energy to machine precision. The time marching is an explicit low-storage third order Runge-Kutta technique.

6.5.2 Initial and Boundary Conditions

The simulation domain has extent $[0, 2\pi] \times [0, 2\pi] \times [0, 2\pi]$, and the boundary conditions were periodic in all three Cartesian directions for all the flow variables. We start with a specified spectrum for velocity which is divergence free initially and given by

$$E(k) = Ak^4 \exp(-k^2/k_0^2). \tag{6.17}$$

where k is the wave number, k_0 is the wave number at which the spectrum peaks, and A is a constant chosen to get a specified initial kinetic energy.

Attempts at DNS of decaying compressible turbulence using spectral or centered finite difference methods suffer from a start-up problem [11]. Before amplitude-phase correlations develop from the initial uncorrelated random field, the flow undergoes a fast transient during which the divergence of the velocity increases rapidly (depending upon the initialization procedure and the initial M_t), accompanied by a rapid decay in M_t and the Taylor microscale Reynolds number Re_λ, and large negative values of the velocity derivative skewness. By trial and error, using several different startup strategies described below, we found that negative temperatures would often develop in the initial transient

if both M_t and Re_λ are sufficiently large. These phenomena are probably associated with the appearance of shocklets with associated flow gradients larger than our uniform Páde scheme can resolve. Thus, our present DNS of isotropic compressible turbulence is limited by the initial start-up problem.

We discuss four different methods of initializing the flow field.

- *IC1*: Given the solenoidal velocity, one can calculate the pressure by taking the inner product of velocity with the momentum equations, and assuming the rate of change of divergence to be zero initially. No initial density fluctuations are assumed. The resulting pressure Poisson equation must be solved iteratively if the viscosity is temperature dependent. The initial flow field then has a fluctuating pressure and an identical fluctuating temperature field. This method however limits the turbulence Mach number M_t to approximately no more than 0.5.

- *IC2*: Given the solenoidal velocity, a small M_t expansion of the Navier-Stokes equations can be carried out [95]. This leads to a non-zero divergence velocity component initially. Furthermore, fluctuations of pressure, density and temperature fields are initially present. The first step in this procedure is the calculation of the "incompressible" pressure fluctuations. Therefore, as in the previous case, we are still limited to small M_t.

- *IC3*: If the initial field is assumed homentropic then a Poisson equation for temperature can be derived. This Poisson equation must be solved iteratively because it has a source term depending upon temperature itself. In this case, we have fluctuations in pressure and density while the entropy is the same everywhere. This initialization method allows for a slightly higher initial turbulent Mach number than the previous two methods.

- *IC4*: The simplest homentropic case is where we have no fluctuations of any thermodynamic quantity.

At the present time, a systematic study of dependence of initial conditions is in progress. For the remainder of the report, we present results which employ *IC4*.

6.5.3 Run Parameters

Several exploratory simulations at 64^3 and 128^3 resolutions were performed with different methods of initializing the flow variables. The code was verified at low Mach numbers by comparing the decay of turbulent kinetic energy from the compressible code against a DNS of incompressible isotropic turbulence [128]. The agreement was satisfactory.

In this report, we will focus on results of one simulation with formally tenth-order spatial accuracy. The spatial resolution was 256^3, the initial Taylor microscale Reynolds number was $Re_\lambda = 175$, the initial turbulent Mach number was $M_t = 0.488$. The values of (A, k_0) for the initial spectrum of the solenoidal velocity were chosen to be $(0.011, 4)$. Other parameters used were the reference

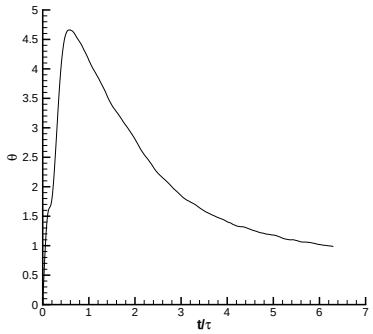

Figure 6.11: Time history of root-mean-square divergence θ. τ is the eddy turnover time at $t = 0$. $M_t = 0.488$, $Re_\lambda = 175$ at t=0.

Reynolds number $Re = 375$, the reference Mach number $M = 0.3$, Prandtl number $Pr = 0.7$, dimensionless conductivity $k = 1$, and ratio of specific heats $\gamma = 1.4$.

6.5.4 Results

In Figure 6.11 the root-mean-square of the divergence, denoted by θ, is plotted as a function of time. The evolution curve $\theta(t)$ is quite similar in shape to those observed by Ristorcelli [95] and Lee [60]. The rapid rise in θ is indicative of a strong initial transient in the present simulation. Note that the average divergence is zero. A time history of velocity derivative skewness is shown in Figure 6.13. For $t/\tau \geq 1.5$ we observe a value of skewness close to the generally accepted value of -0.5. In Figure 6.12, the turbulent kinetic energy (TKE), defined as $1/2 < \rho u_i u_i >$ is plotted as a function of time. At $t/\tau = 1.5$, a time at which the turbulence may be considered to be fully developed, we truncated the 256^3 DNS data to 32^3 and performed an under-resolved DNS with no subgrid stress model and with sixth-order Padè filtering. The TKE from the 32^3 under-resolved DNS is plotted in Figure 6.12 as a dotted curve. This comparison of the decay of turbulent kinetic energy for the 256^3 DNS data with the 32^3 under-resolved DNS is presented as a reference against which the performance of the SGS models can be judged. Time histories of the turbulent Mach number and Taylor microscale Reynolds number are shown in Figures 6.14 and 6.15, respectively. The value of $k_{max}\eta$ where k_{max} is the largest total wavenumber and η is the Kolmogorov length scale was 2.45 at $t = 0$, and attained a minimum value of 1.81 during the course of the simulation, indicating that the computation was converged in the sense of resolving the Kolmogorov scale. The compensated velocity spectrum at various times in the simulation is shown in Figure 6.16.

We now turn to the existence of eddy-shocklets in this simulation. A snapshot of the divergence field (volume-rendered) at $t/\tau = 0.75$ is shown in Fig-

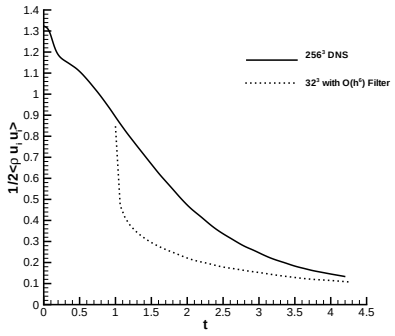

Figure 6.12: Time history of average kinetic energy. τ is the eddy turnover time at $t = 0$. $M_t = 0.488$, $Re_\lambda = 175$ at t=0. The dotted curve is the 32^3 under-resolved DNS with no SGS model and sixth-order Padè filtering.

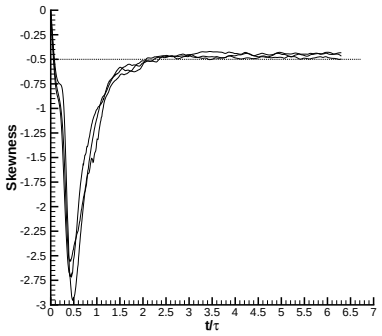

Figure 6.13: Time history of skewness of the velocity derivatives $\partial u_1/\partial x_1$, $\partial u_2/\partial x_2$, and $\partial u_3/\partial x_3$. τ is the eddy turnover time at $t = 0$. $M_t = 0.488$, $Re_\lambda = 175$ at t=0.

ure 6.17. Several regions of very high compression (negative divergence) are clearly observed. These regions are the eddy shocklets where the flow in a local frame of reference decelerates from supersonic to subsonic. Figure 6.18 reveals a broad-band divergence spectrum. While the simulation is well-resolved in the sense that $k_{max}\eta$ is larger than one, we have now the possibility, for compressible turbulence, of the existence of a physically relevant length scale smaller than the Kolmogorov length scale associated with shocklet formation. The dissipation rate due to divergence $\epsilon_c = 4/3\mu\theta^2$ is still small compared to the total dissipation rate even though M_t is moderate and there are several shocklets present (See Figure 6.19).

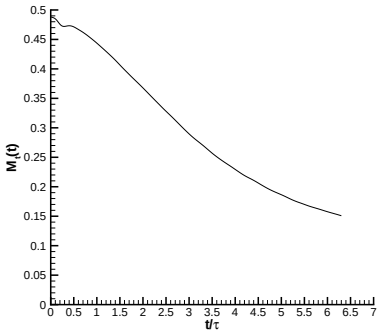

Figure 6.14: Time history of turbulent Mach number. τ is the eddy turnover time at $t = 0$. $M_t = 0.488$, $Re_\lambda = 175$ at t=0.

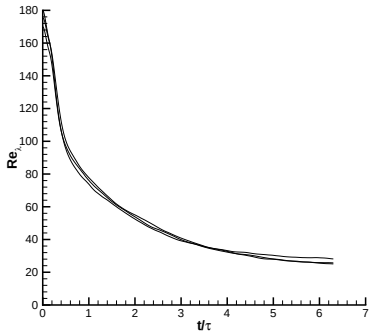

Figure 6.15: Time history of Taylor microscale Reynolds number. Re_λ is calculated using the diagonal components of the Taylor microscale. τ is the eddy turnover time at $t = 0$. $M_t = 0.488$, $Re_\lambda = 175$ at t=0.

6.6 DNS of Rayleigh-Taylor instabilities

In this section we describe our ongoing work on the simulation of Rayleigh-Taylor instability. The objective here is to produce fully resolved DNS of the Rayleigh-Taylor instability assuming either incompressible flow or weak compressibility but with the inclusion of interspecies diffusion effects. These effects are rarely considered in developments of compressible turbulence yet such phenomena affect the overall density profile of the flow and therefore must also affect growth rates as well as rates of mixing. The numerical simulations described below can be used to provide a database for theories of species mixing and test the ability of turbulence models to predict scalar transport under turbulent conditions; it is our intention to examine the models described above in

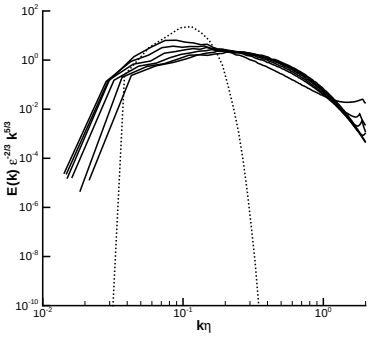

Figure 6.16: Compensated velocity spectrum at various times. The dotted curve is the velocity spectrum at $t = 0$. $M_t = 0.488$, $Re_\lambda = 175$ at t=0.

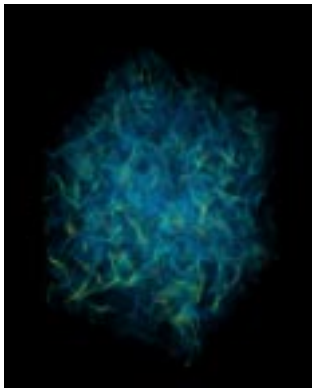

Figure 6.17: Volume-rendered snapshot of the velocity divergence field at $t/\tau = 0.75$. τ is the eddy turnover time at $t = 0$. $M_t = 0.488$, $Re_\lambda = 175$ at t=0.

this context.

6.6.1 Equations of motion and numerical method

Our starting point for these simulations is the compressible Navier-Stokes equations but including the effects of Fickian species diffusion. Thus in addition to the usual dimensionless parameters we must now also consider the effect of the Schmidt number (Sc) which measures the ratio of diffusivities of the miscible species. In this case we consider only two species. The density and species

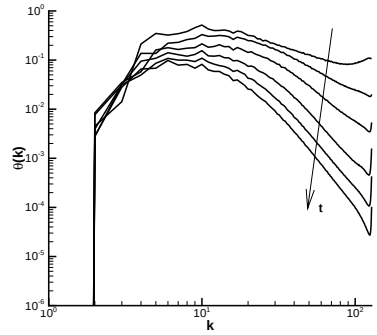

Figure 6.18: Spectrum of the velocity divergence at various times. $M_t = 0.488$, $Re_\lambda = 175$ at t=0.

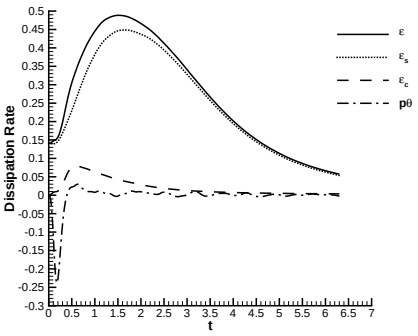

Figure 6.19: Time history of the dissipation rate. ϵ is the total dissipation rate, ϵ_c is the compressible dissipation rate, and ϵ_s is the dissipation rate due to the solenoidal component of velocity. $M_t = 0.488$, $Re_\lambda = 175$ at t=0.

concentration equations are given by

$$\frac{\partial \rho}{\partial t} + \frac{\partial \rho u_i}{\partial x_i} = 0 \tag{6.18}$$

$$\frac{\partial \rho c}{\partial t} + \frac{\partial \rho c u_i}{\partial x_i} = \frac{1}{ReSc}\frac{\partial I_i}{\partial x_i} \tag{6.19}$$

where

$$I_i = -\rho D\left[\frac{\partial c}{\partial x_i} + \frac{\kappa_T}{T}\frac{\partial T}{\partial x_i} + \frac{\kappa_p}{p}\frac{\partial p}{\partial x_i}\right]$$

We assume here that $\kappa_T = \kappa_p = 0$. The momentum equations are given by

$$\frac{\partial \rho u_i}{\partial t} + \frac{\partial(\rho u_i u_j + p/\gamma M^2 \delta_{ij})}{\partial x_j} = \frac{1}{Re}\left(\frac{\partial \sigma_{ij}}{\partial x_j}\right) - \frac{\rho u_2 \delta_{i2}}{Fr} \tag{6.20}$$

where

$$\sigma_{ij} = \mu \left(\frac{\partial u_i}{\partial x_j} + \frac{\partial u_j}{\partial x_i} \right) - \frac{2}{3} \mu \frac{\partial u_k}{\partial x_k} \delta_{ij}$$

and the energy equation is given by

$$\frac{\partial E}{\partial t} + \frac{\partial (E + p/\gamma M^2) u_i}{\partial x_i} = -\frac{1}{\alpha} \frac{1}{Pr} \frac{\partial q_i}{\partial x_i} + \frac{1}{Re} \frac{\partial \sigma_{ij} u_j}{\partial x_i} \tag{6.21}$$

with

$$\begin{aligned} q_i &= \left[\kappa_T \left(\frac{\partial \mu}{\partial c} \right)_{p,T} - T \left(\frac{\partial \mu}{\partial T} \right)_{p,c} + \mu \right] I_i - \left(k \frac{\partial T}{\partial x_i} \right) \\ \alpha &= PrRe(\gamma - 1) M^2 \\ p &= \rho T \left[c + (1 - c)/\eta \right] \end{aligned}$$

Note that one interesting feature of these equations is that even if incompressibility is assumed the divergence of the flow can still be nonzero due to mass diffusion effects.

For the simulations described below we consider a cubic domain defined by $0 \leq x \leq 2\pi$, $-4\pi \leq y \leq 4\pi$, and $0 \leq z \leq 2\pi$. We assume no slip boundary conditions on the top and bottom walls ($u_i(x, \pm 4\pi, z) = 0$), that the walls are isothermal and that the concentrations at the top and bottom walls are fixed. This latter condition is reasonable since the late-time aspects of the simulation where the flow has reached the top and bottom boundaries are already affected by the no-slip conditions and thus would not be relevant to our observations of the instability at intermediate times. Thus we use the boundary conditions $c(x, 4\pi, z) = 0$, $c(x, -4\pi, z) = 1$.

The flow is initialized via the density field which is taken to be

$$\rho(x, y, z) = \frac{\rho_1 + \rho_2}{2} \left[1 + At \tanh(y - \epsilon f(x)) \right] \tag{6.22}$$

where

$$f(x) = \sum_k^N \exp(-\sigma k^2)(\alpha_k \cos x + \beta_k \sin x)(\gamma_k \cos z + \delta_k \sin z)$$

where At is the Atwood ratio. For the simulations described here we take $N = 120$, $\sigma = 0.01$, $At = 0.5$, $\epsilon = 0.5$. The coefficients $\alpha_k, \beta_k, \gamma_k, \delta_k$ are chosen from a uniform distribution.

The numerical method employed here is the same compact finite difference method described above with tenth order accuracy in the interior but with a fourth order boundary scheme. A parallel application was written in FORTRAN-90 with MPI used for message passing. A notable feature of this approach is that it requires an all-to-all communication pattern due to the nonlocal high order Padé methods. The code can perform simulations in both two or three dimensions.

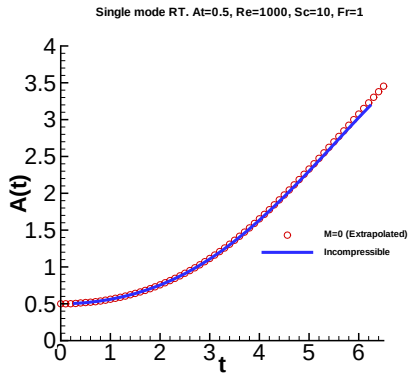

Figure 6.20: Comparison of the evolution of the amplitude of a compressible Rayleigh-Taylor unstable layer at low Mach number with the evolution as computed via an incompressible spectral element code.

In order to assess the growth of the stratified layer we define the amplitude of the mixing layer by the expression

$$A(t) = \frac{1}{2}[\max(\bar{\rho}) - \min(\bar{\rho})] \quad \text{where} \tag{6.23}$$

$$\bar{\rho}(x,z,t) = \frac{H\rho_2 - \int \rho dy}{\rho_2 - \rho_1} - \frac{H}{2}$$

This provides an appropriate generalization for continuous stratified fluid layers but also has the advantage that it reduces to the classical definition for discrete layers. We describe the results of these simulations below.

6.6.2 Results

2-D single mode simulations

In order to verify our calculations we display in Figure 6.20 the amplitude as calculated from a highly accurate spectral element code. As our solver is unable to simulate purely incompressible flow we have approached the incompressible limit by performing a series of runs with decreasing Mach number and then extrapolating to the zero Mach number limit. The encouraging comparison between the two results indicates that the compressible solver performs correctly in the low Mach number limit. We have studied R-T growth in 2-D using single mode initial conditions and the following choice of parameters: $M = 0.05, At = 0.5, Re = 1000, Sc = 10, Fr = 1$. In Figure 6.21 we plot the density field along with the velocity associated with the density field. Note the thickening of the density layer particularly in the roll-up region. It is this feature which will affect strongly the late time dynamics of the bubbles and spikes when miscible fluids are considered.

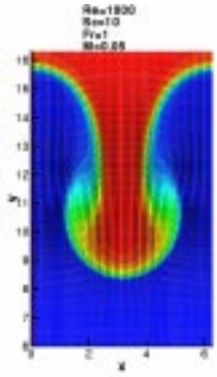

Figure 6.21: A zoom of the density field at an intermediate time in a simulation of Rayleigh-Taylor instability with species diffusion present. The parameters for this run were $M = 0.05, At = 0.5, Re = 1000, Sc = 10, Fr = 1$

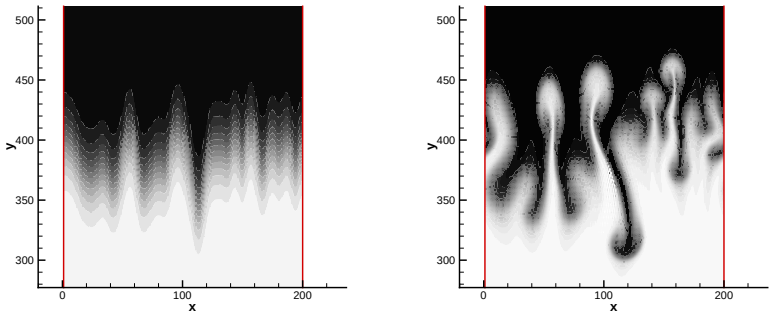

Figure 6.22: Simulation of the growth of an R-T unstable layer seeded with multi-mode perturbations. Left: Gray scale image of initial condition of the density field. Right: Results at intermediate time. The parameters for this run were $M = 0.1, At = 0.5, Re = 1000, Sc = 10, Fr = 1$

2-D multi-mode simulations

In Figure 6.22 we consider the growth of the layer seeded with multi-mode perturbations. Shown in the left half of the figure are the initial conditions. In the right half are results at intermediate time. The parameters for this run were $M = 0.1, At = 0.5, Re = 1000, Sc = 10, Fr = 1$ In Figure 6.23 we display the evolution of the amplitude as a function of time at two Mach numbers: $M = 0.05$ and $M = 0.1$.

In the future we will utilize this capability to simulate three dimensional R-T instabilities with species diffusion and focus on the effects of weak compressibility. We will also continue an ongoing collaboration with Dr. A. Cook

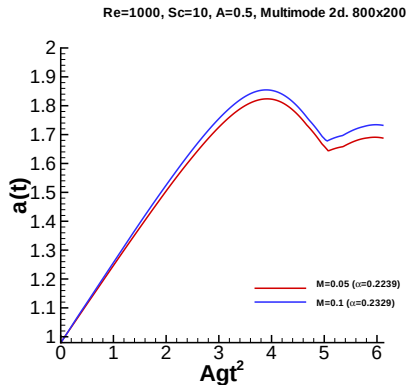

Figure 6.23: The evolution of the amplitude of the multi-mode R-T instability shown in Figure 6.22 for two Mach numbers:$M = 0.05$ and $M = 0.1$.

of LLNL to assess the effects of mixing on R-T growth rates. Finally we will extend our LES modeling to include scalar mixing and validate our LES models via detailed comparison with high resolution DNS.

6.7 FY 00 objectives

Development of 3-D AMR solver

We plan to continue to develop a 3-D solver with AMR capability in order to perform simulations of strong shock Richtmyer-Meshkov instability. This work is already quite far along and utilizes the GrACE distributed array environment due to Manish Parashar. We will evaluate the performance and scalability of this solver in collaboration with the Computational Science group. One important application will be the simulation of reshock phenomena.

Simulations of strong shock R-M instability

We plan to continue our high resolution studies of Richtmyer-Meshkov instability using both a unigrid and AMR capability on the ASCI platforms. We will implement a high order shock capturing solver using the ENO/WENO approach of Osher et al. This will allow us to study shock turbulence interaction and to evaluate the performance of our compressible turbulence models. The resolution of these runs will also be increased upwards of 2048^3. We will initially target the ASCI Blue Pacific and Blue Mountain platforms.

Turbulence modeling

Our work on turbulence modeling will shift into an evaluation phase as we assess the ability of our models to cope with shock waves as well the strong anisotropy of the turbulence in Richtmyer-Meshkov flows. We will apply the high order ENO/WENO solvers described above to the R-M instability and assess the

performance of both the stretched vortex subgrid model as well as the nonlinear model.

DNS of Rayleigh-Taylor instabilities

We will extend our numerical simulations of Rayleigh-Taylor instabilities to three dimensions and examine the effects of interspecies diffusion on the growth of the mixing layer. This will serve as an important database in order to assess the ability of the turbulence models we have developed to model the transport and diffusion of the density field.

Chapter 7

Computational Science

7.1 Overview of FY 99 Accomplishments

1. Pyre: we have defined the architecture of the overarching application and we have made significant progress towards the full implementation of our problem solving environment. For an overview of the environment see Section 2.5.

2. Scalability: we have conducted extensive studies of the scalability properties of the codes that were used to achieve our goals for FY 99. These studies are discussed in detail in Section 7.3.

3. Visualization: the primary focus of our visualization activities was the construction of custom modules for the IRIS Explorer visualization environment in order to support the current needs of the Center. In addition, we have identified a small set of candidate visualization engines for integration into Pyre. This effort is discussed in detail in Section 7.4

4. Distributed computing: We completed an investigation of the Globus facilities necessary for the various aspect of remote staging and remote data access. Prototype modules that employ them have been constructed and an effort is well underway for a complete integration of the relevant Globus facilities in Pyre.

5. Scalable I/O: we have performed performance studies of the various layers of the Scalable I/O infrastructure that were made available to us during this year. Detail can be found in Section 7.5

7.2 Personnel

The FY 99 personnel participating in the Computational Science research activity are listed below.

- Faculty and Senior Researchers
  - Jim Pool (PI)
  - Michael Aivazis
  - Peter Schroder
  - Carl Kesselman
  - Dan Reed
  - Randy Bramley
  - Bob Ward
  - Manish Parashar
- Postdoctoral Scholars
  - Maciej Brodowicz
  - Mathieu Desbrun
- Research Staff
  - Sharon Brunett
  - Santiago Lombeyda
  - James Patton
- Graduate Students
  - Sean Mauch

7.3 Scalability

Assessing the scalability characteristics of the Center's various applications atop a variety of ASCI platforms is an important component of the project's goals. If applications fail to scale well for problem sizes of interest, inhibitors need to be identified and resolutions tested. The following sections discuss various scalability studies for components of the solid dynamics and compressible turbulence applications on the ASCI massively-parallel supercomputers.

7.3.1 Solid Dynamics

Scalable Unstructured Meshing

As part of the Center's scalability effort, the Center's Lagrangian engine, *Adlib*, was profiled with the intent to identify and prioritize performance bottlenecks. Initial profiling was done on both the ASCI Blue-Mountain and ASCI Blue-Pacific, resulting in the same high level conclusions. The overwhelming majority of time execution time was being consumed by integrating the equations of dynamics. Parallelizing the dynamics loop was the obvious first step for improving the performance and scalability in *Adlib*. The implementation was based on distributing the computation of the finite element constitutive updates among

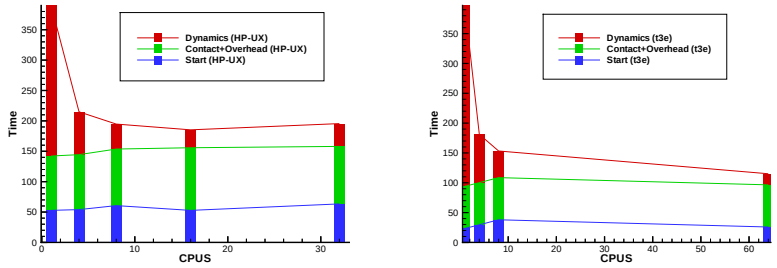

Figure 7.1: Profile and scalability properties of parallel dynamics in *Adlib*: Execution times discriminated by task vs. number of CPUs on Caltech's Hewlett Packard Exemplar and PSC's Cray T3E

the pool of allocated processors, assembling the requisite internal forces on a per processor basis. Each processor's residual was communicated in an all to all fashion via MPI calls. Figure 7.1 shows that the approach effectively reduces the execution time spent in the integration of the dynamics up to the point where other sequential bottlenecks take over. Of course, this simple approach to parallelizing the dynamics loop falls short of providing the sought scalability because the finite element data is not distributed, and therefore the storage available per processor poses a severe limitation on the problem size attainable.

Our attention next focused on scaled speedup, such that increased problem size and resources available to *Adlib* would yield satisfactory time to solution. The first issue which addressed increased problem size was the concurrent generation and storage of the finite element mesh used in the problem's discretization. To this end, we adopted a strategy based on applying the sequential mesh generation algorithm to subproblems. A natural avenue for creation of subproblems was provided by domain decomposition. Domain decomposition possesses some advantages. Specifically of interest for scalability is the fact that a byproduct of the parallel meshing operation results in the data being distributed and readily available for parallel finite element analysis.

The parallel meshing implementation comprises two phases, sequential initialization phase and the concurrent volume meshing phase. Figure 7.2 depicts the parallel meshing phases. During initialization, a coarse mesh is first generated sequentially from the original boundary representation (BRep). This mesh is partitioned into P parts using a popular graph partitioning library called Metis [51]. Then, each partitions simplified BRep is reconstructed from the partition mesh. Finally, this BRep is re-meshed to accommodate the specified mesh density. It bears emphasis that the initialization step is done sequentially in order to guarantee that the partition meshes will remain conforming upon parallel volume meshing. The second step, concurrent application of the se-

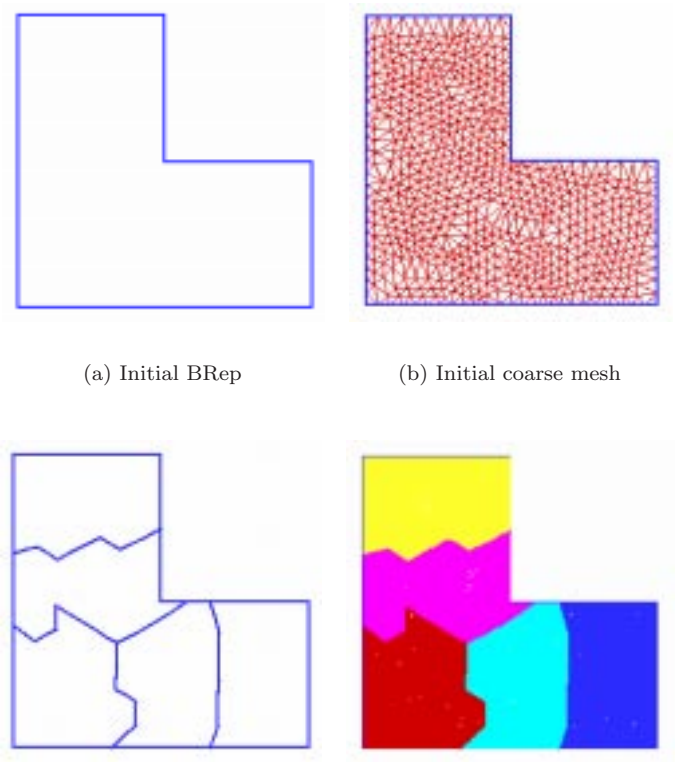

(a) Initial BRep (b) Initial coarse mesh

(c) Partition boundaries (d) Partition meshes

Figure 7.2: Explanation of the proposed parallel meshing algorithm

quential volume meshing algorithm to the distributed partitions, proceeds with literally *no* communications.

We have implemented the proposed approach in two and three dimensions and assessed its scalability properties (in two dimensions only) on two ASCI platforms (Blue Mountain and Blue Pacific) and on the Center's 256 processor Hewlett Packard Exemplar XClass.

Figures 7.3 and 7.4 show the results of the scalability study conducted on ASCI Blue-Mountain. Figure7.3 represents the execution time of a given experiment vs. the number of processors upon which it was executed. The different curves correspond to different problem sizes. It can be observed that, for any given problem size, the curve exhibits an initial steep negative slope, which gradually decreases as the number of processors increases. A stage is reached in which the workload per processor is so small that the overall timings are swamped by initialization. The observed downgrades are not related to appli-

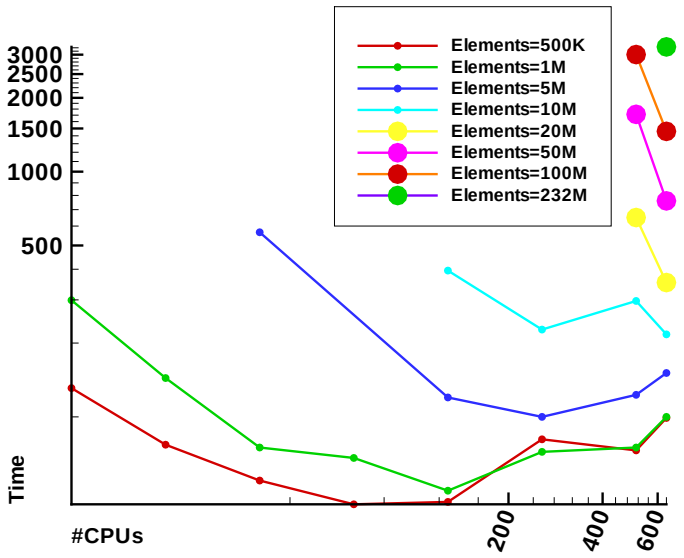

Figure 7.3: Parallel meshing speedup curves on ASCI Blue Mountain

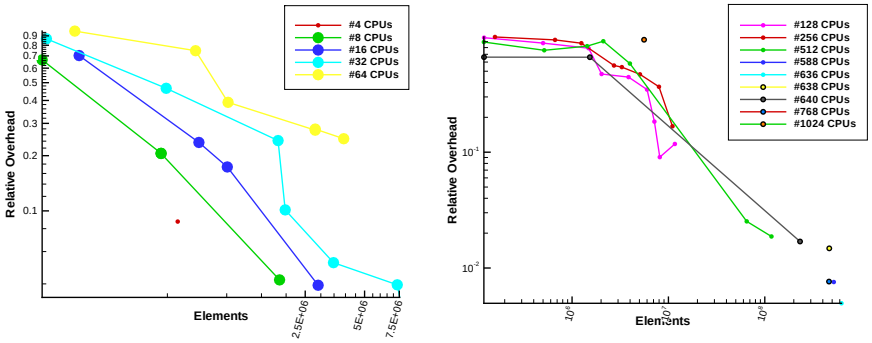

Figure 7.4: Parallel meshing relative overheads on ASCI Blue Mountain

cation communication overhead, since such communications are nonexistent.

The parallel speedup curve plots can guide production run design. Optimal processor count for a given problem size, along with runtime duration on a given platform, can be determined by examining the speedup curves of prior runs. Figure 7.4 shows the overhead time associated with the initialization step. The plots show relative overhead expressed as $(T_{tot} - T_{mesh})/T_{tot}$, where T_{tot} is the total execution time and T_{mesh} is the time spent on parallel meshing vs. resulting mesh elements. The different curves correspond to different number of processors. Consistently, it is observed that for small problem sizes the overhead

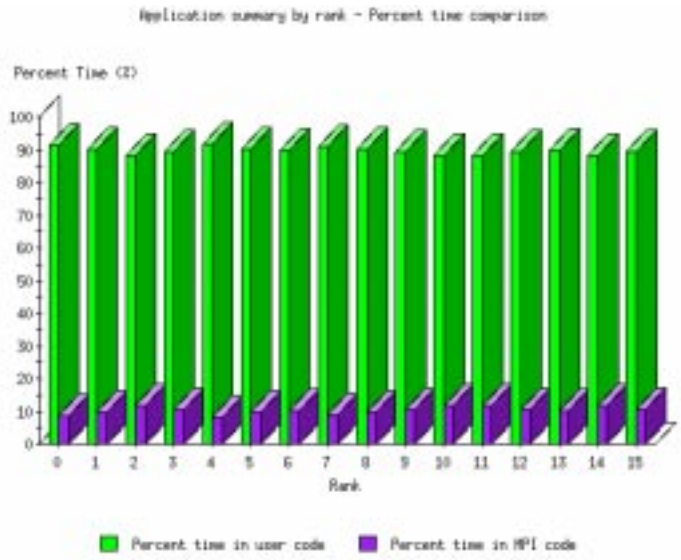

Figure 7.5: MPI communication overhead for multi-physics polycrystal model atop the Hewlett Packard XClass

is relatively large. However, in the range of interest, which is when the problem grows arbitrarily large, the overhead becomes negligible. The algorithm has been able to produce meshes of 0.8 billion elements generated on 1024 processors.

Polycrystal Model Scalability

The Center's solid dynamics group has a polycrystal model simulation for which scalability can be achieved through more complex multiphysics. Taylor averaging is used to calculate crystal responses for the selected polycrystal model. Multiple replicas of the solid are created for each processor, assigning each replica a unique polycrystalline orientation. Taylor averaging calculations proceed independently and concurrently on all processors, until strain information is communicated via an MPI_All_Reduce to all solid replicas. Figure 7.5 shows the MPI communication overhead for strain messages on Hewlett Packard XClass.

7.3.2 Compressible Turbulence Scalability

Prism Scalability

The Center's turbulence simulation application, *Prism* , requires the use of methods with high-order accuracy to minimize the effects of numerical dissipation. The communications kernel utilized by *Prism* is a matrix transpose, requiring all-to-all communications. Good scalability is, of course, hard to ob-

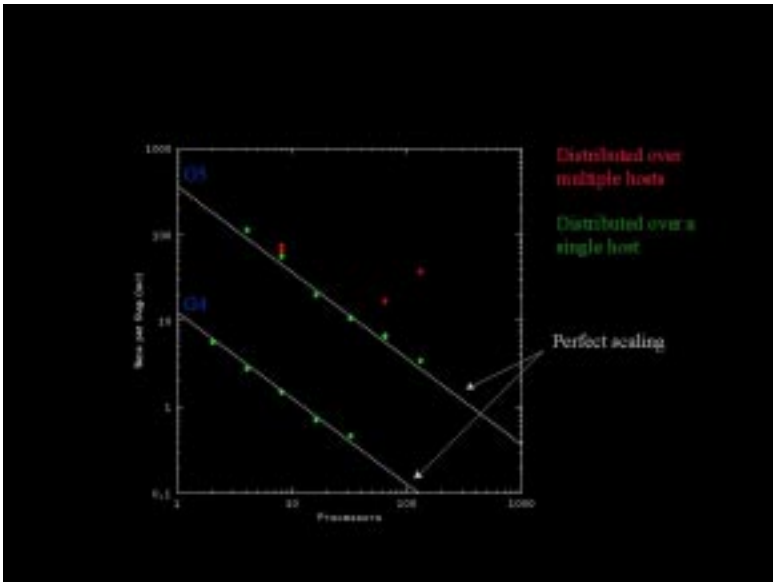

Figure 7.6: Prism scalability for single and multiple hosts on ASCI Blue Mountain

tain when increasingly large processor counts are involved in frequent all-to-all communications.

Scalability runs were conducted on ASCI Blue Mountain for two problem sizes of interest. Figure 7.6 shows speedup curves for turbulent channel flow at high and low resolution. Nearly perfect scaling is observed on up to 128 processors. Of particular interest is the poor performance when communications occurs outside a single 128 CPU host. All-to-all message traffic distributed over multiple hosts is indeed the dominant factor in *Prism* communication scaling problems observed on ASCI Blue Mountain. All-to-all communication performance involving multiple hosts must be addressed before serious production runs involving hundreds of processors with significant all-to-all communication demands are practical.

DNS Scalability

The Center's Direct Numerical Simulation code was studied for scaling behavior with 2D and 3D test cases. In the 3D case, the ratio of communications to calculation is very small, producing nearly perfect scaling for $64 \times 64 \times 64$ and $128 \times 128 \times 128$ problem sizes. The 2D problem does not scale as well, due to all-to-all communications overwhelming computation demands for matrix transposes every 15 time steps. Figure 7.7 shows the scaling properties of 3D and 2D DNS on the PSC T3E and ASCI Blue Mountain.

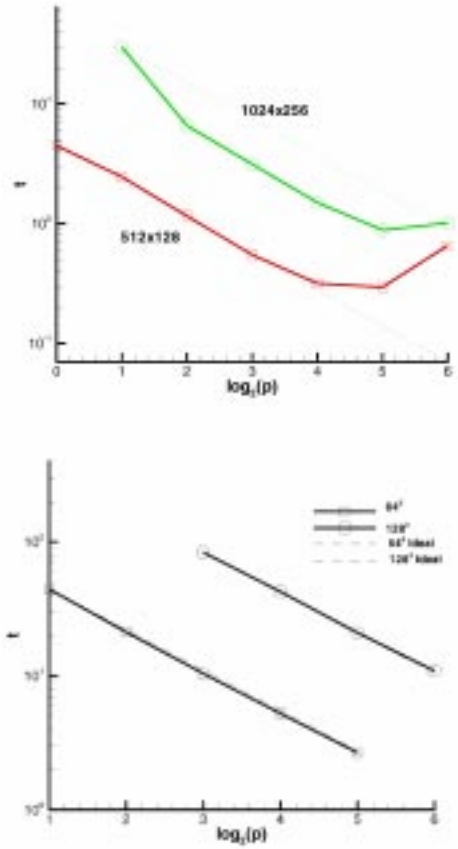

Figure 7.7: 3D and 2D DNS scalability on PSC T3E and ASCI Blue Mountain

RM3D Scalability

The modeling and simulation of Richtmyer-Meshkov instabilities is at the heart of the Center's compressible turbulence work. The *RM3D* application simulates Euler equations of motion for compressible fluid in three dimensions. Understanding and enhancing the scalability properties of *RM3D* involve testing small to large problem sizes, and adjusting the problem domain decomposition across processors. Best performance and scaling is achieved when each processor is assigned a cube of data, thus minimizing surface to area to volume. The volume of data transferred between processors is correspondingly reduced, and the work in ghost cells is minimized. Figures 7.8 and 7.9 shows speedup curves for $1024 \times 128 \times 128$ and $2048 \times 256 \times 256$ grid sizes runs on ASCI Blue Mountain and on the PSC Cray T3E

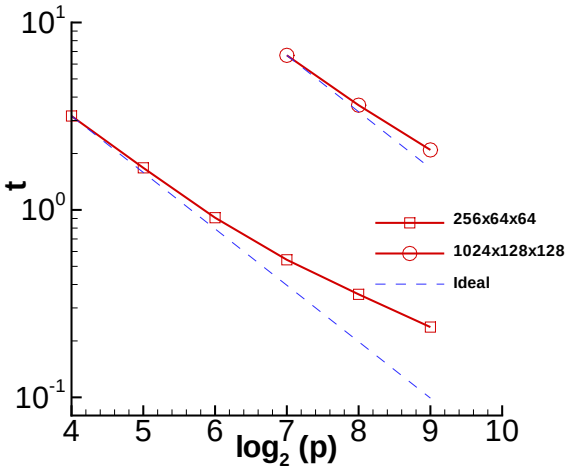

Figure 7.8: CPU time for one time step of the CFD engine RM3d on the CRAY-T3E.

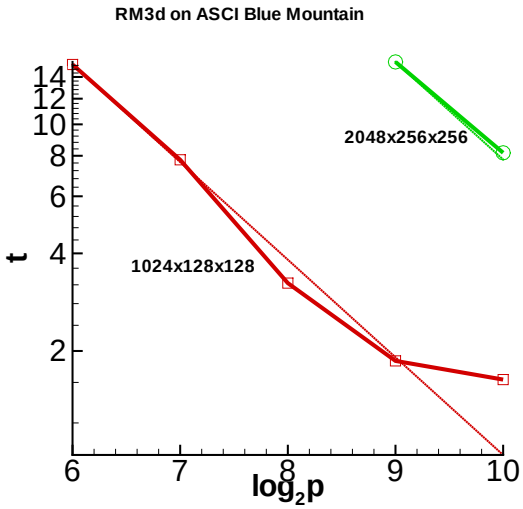

Figure 7.9: CPU time for one time of the CFD engine RM3d on ASCI Blue Mountain.

7.3.3 Virtual Test Facility Pseudo Solid Solver Scalability

A Virtual Test Facility beam solver was constructed, which tied the VTF driver to a CFD engine solving Euler equations, and a solid beam solver. Best scalability is achieved when the fluid solver's problem domain is decomposed into

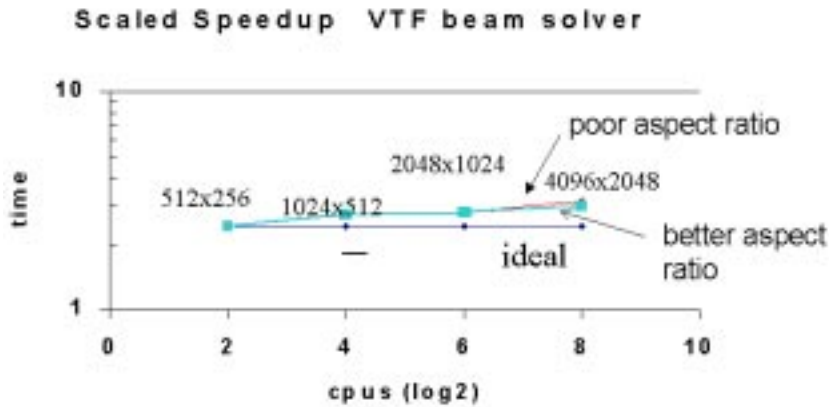

Figure 7.10: Scalability for VTF beam solver on ASCI Blue Mountain

uniform rectangular patches. Similarly, when the subdomain is distributed to processors in thin slices, poor performance result.

Every time step, explicit coupling is dominated by nearest neighbor communications. Thus, attention minimizing the volume of data communicated among neighboring processors is important for good scaling and performance. Another important performance problem to recognize is the sequential bottleneck imposed by the sequential solid solver. Runs with larger processor counts certainly suffer performance degradation from the sequential solver, which was not yet parallelized at the time of the VTF Pseudo Solid Solver scaling studies. Figure 7.10 shows VTF beam solver scaling runs for well distributed subdomains across 512 processors on ASCI Blue Mountain. Figure 7.11 shows scalability results for the VTF application using the adlib solid solver. The adlib solver runs in each processor and therefore acts as a serial bottleneck as the number of processors are increased. In future versions of the VTF the solid solver will be made fully parallel and will this difficulty will be avoided. Nevertheless it is interesting to note that even with the solid solver as a serial bottleneck it is still possible to obtain reasonable results when one considers scaled speedup. A clear trend which emerges from examining the above plots is that the scalability improves as one reduces the surface communication to the volume ratio.

7.4 Visualization

Throughout 1999 the Visualization Effort took shape in the form of biweekly meetings throughout the latter half of the year [64]. Meetings brought together the different sciences involved in the center to engage on visualization matters. Meetings covered topics ranging from tutorials on tools for visualization (IRIS Explorer, Open Inventor, the Visualization ToolKit, VRML, etc.), to discussions

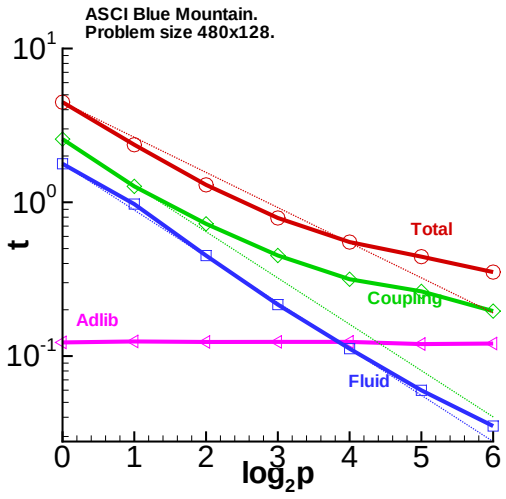

Figure 7.11: VTF with Adlib on ASCI Blue Mountain

on integration as part of the larger framework, as well as a sharing of knowledge, needs, results, and accomplishments.

As a result of these discussions it was resolved to adopt a high level graphics language for individuals visualization needs, as well as for the larger framework. The resolution take was to acquire TGS' version of Open Inventor which has been ported to most Unix platforms as well as to Windows NT. On November 1999 TGS' Open Inventor was purchased for LINUX, IRIX, HP-UX, and NT platforms.

The visualization effort also led to the creation of a central repository of visualization tools which took the form of modules for IRIS explorer and stand alone Open Inventor filters [63, 66]. A sampling of the work done using such modules includes the visualizations of the 2D axis-symmetric shock in 3D presented at the October review.

As for the individual sciences' perspective, collaborations took place for the visualization of simulations in solid mechanics, fluid mechanics, and material properties. Results can be found by consulting the web page [65].

Finally in October 1999 Caltech was awarded an NSF grant for "Multiresolution Visualization Tools for the Interactive Exploration and Analysis of Large-Scale Multidimensional Experimental and Simulated Data" (see [67]). Research being done under such though orthogonal to the efforts being done as part of the ASCI/ASAP grant, is complementary of the needs of the scientists and the center itself. It is expected that work resulting from this project will be directly applicable to large data sets resulting from fluid and solid mechanics simulations.

7.5 Scalable I/O

During the year, we continued development work on HDF5 instrumentation and analysis software as part of the ASCI DMF I/O characterization and optimization effort. At the request of the HDF developers, we extended our HDF instrumentation to track the number of bytes requested for dynamic memory allocation (malloc) operations. Code was added to the first stage of the HDF post-processing software to produce histograms showing the number of byte requests in certain ranges for read, write and malloc operations.

The HDF developers also requested that we make the I/O characterization reports more succinct. In response, we added options that allow the user to specify which HDF routines are to be instrumented and what data should be reported (e.g., one can specify that only activity occurring within a call to a certain routine should be recorded, or that one should analyze activity only on a particular processor). The HDF instrumentation was also modified to allow the same library to run with or without MPI.

During the development of HDF 5, new entry points are frequently added to support new features. To reduce the frequency of I/O characterization library modifications and to ease integration by the HDF development team, we created a set of macros to extract the names of the HDF entry points from the HDF source code during the build process for the Pablo-instrumented HDF library.

7.5.1 Installation and Ports

Along with the development work on HDF 5, we ported and tested the Pablo I/O software a variety of platforms each time a new version of HDF was released. This testing included the Pablo I/O measurement library with the Unix I/O and MPI-I/O extensions, as well as SDDF analysis programs.

We ported the Pablo tools to the IBM SP at LLNL, the ASCI Red at SNL, and the Origin at LANL. In addition, we ported the tools to the HP Exemplar and SGI Origin at Caltech. This included the Pablo I/O library with Unix I/O, MPI I/O and HDF extensions, the SDDF analysis package and the I/O, MPI I/O and HDF analysis software. Finally, we packaged the source code and binary versions for SUN, SGI, HP Exemplar, and IBM SP platforms, along with documentation, and make these available via the Pablo web site: http://www-pablo.cs.uiuc.edu

We also worked with the HDF 5 developers to help optimize HDF 5 performance. Working with the HDF 5 quality assurance team, we identified areas where targeted library modifications could improve performance.

7.5.2 I/O Characterization

During the summer, we acquired and analyzed substantial amounts of I/O data from the ARES and ALE3D codes on the LLNL IBM SP. ARES and ALE3D measurements were conducted using two versions of MPI and on both the GPFS and PIOFS file systems.

We summarized our analyses of ARES and ALE3D LLNL IBM SP perfor-

mance, as well as experiments conducted with the LANL EULER using the NCSA SGI Origin, in a series of reports.1 We also used the Pablo Virtue visualization system to create "time tunnel" renderings and videotapes. Finally, sanitized descriptions of the ARES, ALE3D and EULER codes, along with the I/O traces, were placed on the Pablo web site. In accordance with LLNL requests, neither the codes nor the data identify their origin.

Use of the EULER code on the NCSA Origin suggested possible I/O configuration problems at NCSA. SGI representatives used benchmarks that mimicked the EULER I/O patterns to assess possible remediation. Based on this, the I/O system on the NCSA Origin was later reconfigured and performance improved significantly.

Finally, we presented the of our ASCI code analyses at the ASCI meeting in May at Caltech. In response queries from Steve Lewis, we repeated some of the experiments to determine quantify performance improvements with the latest release of GPFS.

7.5.3 New Developments

With additional support from NSF via the NSF CADRE program, we completed design and began development of a new, thread-safe Performance Capture Facility (PCF). The goal of this work is to increase interoperability with Globus, one of the standard substrates for distributed computation, and to create a thread-safe version of the I/O instrumentation system.

The current Pablo I/O library was originally developed to support analysis of SPMD-style applications with only one thread per process. This is suitable for analyzing performance of parallel applications run using MPI but produces unpredictable results when used with threaded applications or libraries, including with Globus applications.

The new PCF is designed to be thread safe and to operate in both file-based and Autopilot modes. The first mode will generate SDDF performance files, much like the current Pablo instrumentation library. The second mode relies on our Autopilot sensor/actuator toolkit, which is built atop Globus, to export performance data via distributed sensors. This enables I/O characterization of networked, distributed applications.

7.6 FY 00 objectives

7.6.1 Pyre

The major objective for our problem solving environment is the seamless integration of the work of the Material Properties group. In particular, there are two areas that will be receiving special attention. The first such area is the proper archiving of the large number of simulations necessary to infer the material properties of interest. This includes both the results of such simulations but also the large number of input parameters and versions of the programs used in the studies. This will permit the relatively effortless reproduction of any given set of results and will enable meaningful comparisons between simulations. The

other area of focus is the automated migration of the MP simulation results in the material properties database employed by Pyre for use by the Center's solvers.

In addition, we will continue to integrate the capabilities provided by the focused subgroups on visualization, distributed computing and scalable I/O, as described in the following subsections.

7.6.2 Visualization

The visualization group will continue to support the visualization needs of the Center by providing custom solutions and modules for use within the IRIS Explorer environment. We intend to improve the Center's capabilities to visualize three-dimensional adaptive hierarchical Cartesian and tetrahedral meshes and in particular we will continue to investigate how to best capture visually the presence of string shocks in such meshes.

In addition to the post-processing visualization capabilities, we intend to improve our on-line status monitoring and visualization capabilities by incorporating in Pyre the capabilities of advanced three-dimensional rendering toolkits such as OpenInventor. The goal is to enable the application developers to better monitor the simulation status and provide advanced debugging tools so that software defects can be diagnosed more easily. Finally, we will continue to develop algorithms and implement tools for advanced parallel visualization.

7.6.3 Scalable I/O

During FY00 we plan to complete the development of the thread-safe Performance Capture Facility. The facility will support performance analysis of Unix I/O, MPI I/O, MPI and HDF operations, reusing large sections of I/O characterization code developed for the older Pablo instrumentation library.

In addition, we will embark on an analysis of the I/O characteristics of the Center's codes. The new Performance Capture Facility will be used for this characterization and will be integrated with the Caltech/ISI Globus effort.

Finally, we will continue our joint effort with the HDF5 development team and begin analysis of the DMF layer. We will extend the Performance Capture Facility to support the analysis of DMF. We also intend to conduct additional experiments with the ARES and ALE3D applications to track improvements in their performance over time and with use of DMF. We intend to begin analysis of applications from LANL and Sandia. This trace data is taken from codes that use an existing serial I/O library. Developers analyzed this library and determined it to be unsuitable to take to a parallel environment. Subsequent analysis with Pablo also demonstrates some of the same problems (as seen in the trace data that follows). Developers of the replacement I/O library expect a very different pattern of I/O once the new library is integrated into the codes.

Bibliography

[1] J. D. Anderson. *Hypersonic and High Temperature Gas Dynamics*. McGraw Hill, 1989.

[2] T. R. Anthony, W. F. Banholzer, and J. F. Fleischer. Single-crystal diamond of very high thermal conductivity. *US Patent Office*, US 5310447, 1994.

[3] T. R. Anthony, W. F. Banholzer, J. F. Fleischer, L. Wei, P. K. Kuo, R. L. Thomas, and R. W. Pryor. *Phys. Rev. B*, 42:1104, 1990.

[4] D. J. Bacon, D. M .Barnett, and R. O. Scattergood. *Progress in Materials Science*, 23:51, 1979.

[5] A. Balandin and K. Wang. *Phys. Rev. B*, 58:1544, 1998.

[6] W. F. Banholzer and T. R. Anthony. *Thin solid films*, 212:1, 1992.

[7] M.I. Baskes, R.G. Hoagland, and T. Tsuji. An atomistic study of the strength of an extended-dislocation barrier. *Modelling and Simulation in Materials Science and Engineering*, 6(1):9–18, 1998.

[8] J. L. Bassani. *Advances in Applied Mechanics*, 30:191, 1994.

[9] P. H. Berens, D. H. J. Mackay, G. M. White, and K. R. Wilson. *J. Chem. Phys.*, 79:2375, 1993.

[10] R. Berman. *Phys. Rev. B*, 45:5726, 1992.

[11] G. A. Blaidell, N. N. Mansour, and W. C. Reynolds. *Compressibility effects on the growth and structure of homogeneous turbulent shear flow. Report No. TF50.* Stanford University, Stanford, CA, 1991.

[12] D. W. Brenner. *Phys. Rev. B*, 42:9458, 1990.

[13] V. Bulatov, F. Abraham, L. Kubin, B. Devincre, and S. Yip. *Nature*, 391:669, 1998.

[14] Somchart Chantasiriwan and Frederick Milstein. *Phys. Rev. B*, 53:14080, 1996.

[15] J. Che, T. Cagin, and W. A. Goddard III. *Nanotechnology*, 10:263, 1999.

[16] Y.J. Chen, J.C. LaSalvia, V.F. Nesterenko, M.A. Meyers, M.P. Bondar, and Y.L. Lukyanov. High-strain, high-strain rate deformation, shear localization and recrystallization in tantalum. *Journal de Physique IV*, 7(C3):435–440, 1997.

[17] R. Cohen, 1999. private communication.

[18] CRC. *CRC Handbook of Chemistry and Physics*. CRC Press, Boca Raton, Florida, 71 edition, 1990.

[19] CRC. *CRC Handbook of Chemistry and Physics*. CRC Press, Boca Raton, Florida, 76 edition, 1995.

[20] A. M. Cuitiño and M. Ortiz. Computational modelling of single crystals. *Modelling and Simulation in Materials Science and Engineering*, 1:255–263, 1992.

[21] Hyunchae Cynn and Choong-Shik Yoo. *Phys. Rev. B*, 59:8526, 1999.

[22] P. J. Davis and D. J. Evans. *J. Chem. Phys.*, 103:4261, 1995.

[23] M. S. Daw and M. I. Baskes. *Phys. Rev. B*, 29:6443, 1984.

[24] B.M. Dobratz. LLNL Explosives Handbook - Properties of Chemical Explosives and Explosive Simulants. *LLNL Report UCRL-52997*, 1981.

[25] M. S. Duesbery, N. P. Louat, and K. Sadananda. *Philosophical Magazine A*, 65:311, 1995.

[26] G. Erlebacher, M. Y. Hussaini, C. G. Speziale, and T. A. Zang. Toward the large-eddy simulation of compressible turbulent flows. *Journal of Fluid Mech.*, 238:155–185, 1992.

[27] D. J. Evans. *Phys. Lett. A.*, 91:457, 1982.

[28] R.P. Fedkiw, T. Aslam, B. Merriman, and S. Osher. A non-oscillatory Eulerian approach to interfaces in multimaterial flows. *UCLA-CAM Report 98-17*, 1998.

[29] R.P. Fedkiw, T. Aslam, B. Merriman, and S. Osher. A non-oscillatory eulerian approach to interfaces in multimaterial flows (the ghost fluid method). *Journal of Computational Physics*, 152(2):457–492, 1999.

[30] W. Fickett and W. C. Davis. *Detonation*. University of California Press, 1979.

[31] R. W. Fillers and N. W. Tschoegl. The effect of pressure on the mechanical properties of polymers. *Trans. Soc. Rheology*, 21(1):51–100, 1977.

[32] P. Franciosi and A. Zaoui. Multislip in f.c.c. crystals: A theoretical approach compared with experimental data. *Acta Metallurgica*, 30:1627, 1982.

[33] P. Franciosi and A. Zaoui. Glide mechanisms in b.c.c. crystals: an investigation of the case of α-iron through multislip and latent hardening tests. *Acta Metallurgica*, 31:1331, 1983.

[34] M. J. Gillan. *Phys. Scripta*, T39:362, 1991.

[35] P. Glaister. An Approximate Linearised Riemann Solver for the Euler Equations for Real Gases. *Journal of Computational Physics*, 74:382–408, 1988.

[36] R. Guirguis, D. Hsu, D. Bogan, and E. Oran. A mechanism for ignition of high-temperature gaseous nitromethane : The key role of the nitro group in chemical explosives. *Combustion and Flame*, 61:51–62, 1985.

[37] V. L. Gurevich. Transport in phonon systems. 1986.

[38] A. Harten. High resolution schemes for hyperbolic conservation laws. *Journal of Computational Physics*, 49:357–393, 1983.

[39] L.G. Hill. Detonation product equation-of-state directly from the cylinder test. In *21st International Symposium on Shock Waves, Great Keppel Island, Australia, July 20-25, 1997*, 1997.

[40] J. P. Hirth. *Journal of Applied Physics*, 32:700, 1961.

[41] J. P. Hirth. *Journal of Applied Physics*, 33:2286, 1962.

[42] J. P. Hirth and J. Lothe. *Theory of Dislocations*. Kreiger, Malabar, Florida, 1992.

[43] W. G. Hoover. *Phys. Rev. A*, 31:1695, 1985.

[44] H. Hoppe. Efficient implementation of progressive meshes. *Computer and Graphics*, 22(1):27–36, 1998.

[45] D. Hull and D. J. Bacon. *Introduction to Dislocations*, volume 37 of *International Series on Materials Science and Technology*. Elsevier Science Inc., 3rd edition, 1984.

[46] I.M. Hutchings. Wear by particulates. *Chemical Engineering Science*, 42(4):869–878, 1987.

[47] I.M. Hutchings, D.W.T. Deuchar, and A.H. Muhr. Erosion of unfilled elastomers by solid particle impact. *Journal of Materials Science*, 22(11):4071–4076, 1987.

[48] J.N. Johnson, P.K. Tang, and C.A. Forest. Shock-wave initiation of heterogeneous reactive solids. *Journal of Applied Physics*, 57:4323–4334, 1985.

[49] T. Jossang, J. P. Hirth, and C. S. Hartley. *Journal of Applied Physics*, 36:2400, 1965.

[50] H. P. Karnthaler. *Philosophical Magazine A*, page 141, 1978.

[51] G. Karypis. *Metis, A Family of Multilevel partitioning algorithms*. University of Minnesota, http://www-users.cs.umn.edu/karypis/metis/main.-shtml.

[52] R. J. Kee, F. M. Rupley, and J. A. Miller. Chemkin-II: A Fortran chemical kinetics package for the analysis of gas-phase chemical kinetics. Technical Report SAND89-8009, Sandia National Laboratories, 1989.

[53] L. Kobbelt and P. Schroder. A multiresolution framework fo variational subdivision. Technical Report CS-TR-97-05, Computer Graphics Research Group, Computer Science Department, California Institute of Technology, 1997.

[54] A. Korner and H. P. Karnthaler. *Philosophical Magazine A*, page 275, 1981.

[55] B. Kosovic. Subgrid-scale modelling for the large-eddy simulation of high-Reynolds-number boundary layers. *J. Fluid Mech.*, 336:151–182, 1997.

[56] R. Kubo, M. Toda, and N. Hashitsume. *Statistical Physics II*. Springer-Verlag, Berlin, 1985.

[57] D. Kuhlmann-Wilsdorf. Theory of plastic deformation: properties of low energy dislocation structures. *Materials Science and Engineering*, A113:1, 1989.

[58] R. V. Kukta. PhD thesis, Brown University, Brown University, 1998.

[59] K. W. Schwarz L. K. Wickham and J. S. Stolken. *Physics Review Letters*, 83:4574, 1999.

[60] S. Lee, S. K. Lele, and P. Moin. Eddy shocklets in decaying compressible turbulence. *Phys. Fluids*, 3(4):657–664, 1991.

[61] S. K. Lele. Compact Finite Difference Schemes with Spectral-like Resolution. *Journal of Comput. Phys.*, 102:16–42, 1992.

[62] D.C. Leslie and G.L. Quarini. The application of turbulence theory to the formulation of subgrid modelling procedures. *J. Fluid Mech.*, 91:65–91, 1979.

[63] S. Lombeyda. www.cacr.caltech.-edu/˜ slombey/asci/repository. 1999.

[64] S. Lombeyda. www.cacr.caltech.edu/˜ slombey/asci. 1999.

[65] S. Lombeyda. www.cacr.caltech.edu/˜ slombey/asci/ascigallery.html. 1999.

[66] S. Lombeyda. www.cacr.caltech.edu/˜ slombey/nag/explorer/repository. 1999.

[67] S. Lombeyda. www.cacr.caltech.edu/projects/ldviz/. 1999.

[68] U. Maas. Efficient calculation of intrinsic low-dimensional manifolds for the simplification of chemical kinetics. *Computing and Visualization in Science*, 1:69–81, 1998.

[69] U. Maas and S. B. Pope. Implementation of simplified chemical kinetics based on intrinsic low-dimensional manifolds. In *24th Symp. (Intl) on Combustion*, pages 103–112, Pittsburgh, 1992. The Combustion Institute.

[70] U. Maas and S. B. Pope. Simplifying chemical kinetics: Intrinsic low-dimensional manifolds in composition space. *Combust. Flame*, 88:239–264, 1992.

[71] U. Maas and S. B. Pope. Laminar flame calculations using simplified chemical kinetics based on intrinsic low-dimensional manifolds. In *25th Symp. (Intl) on Combustion*, pages 1349–1356, Pittsburgh, 1994. The Combustion Institute.

[72] D. Macgowan and D. J. Evans. *Phys. Lett. A*, 117:414, 1986.

[73] G. D. Mahan. *Many-Particle Physics*. Plenum Press, New York and London, 1993.

[74] D. A. McQuarrie. *Statistical Mechanics*. Harper & Row Publishers, 1976.

[75] O. Métais and M. Lesieur. Spectral large-eddy simulations of isotropic and stably stratified turbulence. *J. Fluid Mech.*, 239:157–194, 1992.

[76] A. Misra and D. I. Pullin. A vortex-based subgrid model for large-eddy simulation. *Phys. Fluids*, 9:2243–2454, 1997.

[77] A. Misra, D. I. Pullin, and D. C. Chan. Large-eddy simulation using the stretched-vortex SGS model. In Chaoqun Liu and Zhining Liu, editors, *Advances in DNS/LES. Proceedings of the First AFOSR International Conference on DNS /LES*, pages 385–392. Greyden Press (Columbus), 1997.

[78] T.E. Mitchell and W.A. Spitzig. Three-stage hardening in tantalum single crystals. *Acta Metallurgica*, 13:1169–1179, 1965.

[79] P. Moin, K. Squires, W. Cabot, and S. Lee. A dynamic subgrid-scale model for compressible turbulence and scalar transport. *Phys. Fluids*, 3(11):2746–2757, 1991.

[80] E. Morano, M. Arienti, and J. Shepherd. Nonreactive euler flows with mie-grüneisen equation of state for high explosives. Technical Report Caltech Explosion Dynamics Laboratory Report FM99-8, California Institute of Technology, Galcit, Pasadena, CA, 1999.

[81] V. V. Murashov. *J. Phys.: Condens. Matter*, 11:1261, 1999.

[82] V.F. Nesterenko, M.A. Meyers, J.C. LaSalvia, M.P. Bondar, Y.J. Chen, and Y.L. Lukyanov. Shear localization and recrystallization in high-strain, high-strain-rate deformation of tantalum. *Materials Science and Engineering A-Structural Materials Properties Microstructure and Processing*, 229(1-2):23–41, 1997.

[83] J. R. Olson, R. O. Pohl, J. W. Vandersande, A. Zoltan, T. R. Anthony, and W. F. Banholzer. *Phys. Rev. B*, 47:14850, 1993.

[84] M. Ortiz and E. P. Popov. A statistical theory of polycrystalline plasticity. *Proceedings of the Royal Society of London*, A379:439–458, 1982.

[85] M. Ortiz, E. A. Repetto, and L. Stainier. A theory of subgrain dislocation structures. *Journal of the Mechanics and Physics of Solids*, 2000. to appear.

[86] Stanley Osher and Chi-Wang Shu. Efficient implementation of Essentially Non-Oscillatory shock-capturing schemes, II. *J. Comput. Phys.*, 83 (1):32–78, 1989.

[87] G. V. Paolini, P. J. Lindan, and J. H. Harding. *J. Chem. Phys.*, 106:3681, 1997.

[88] M. Parinello and A. Rahman. *J. Appl. Phys.*, 52:7182, 1981.

[89] N. Peters. Systematic reduction of flame kinetics: Principles and details. *Prog. Astronaut. Aeronaut.*, 113:67–86, 1988.

[90] D. I. Pullin. Direct simulation methods for compressible ideal gas flow. *J. Comput. Phys.*, 34:231–244, 1980.

[91] D. I. Pullin and P. G. Saffman. Reynolds stresses and one-dimensional spectra for vortex models of homogeneous anisotropic turbulence. *Phys. Fluids*, 6:1787–1796, 1994.

[92] R. Radovitzky and M. Ortiz. Error estimation and adaptive meshing in strongly nonlinear dynamic problems. *Computer Methods in Applied Mechanics and Engineering*, 172(1-4):203–240, 1999.

[93] R. Radovitzky and M. Ortiz. Tetrahedral mesh generation based on node insertion in crystal lattice arrangements and advancing-front-Delaunay triangulation. *Computer Methods in Applied Mechanics and Engineering*, 2000. in press.

[94] R. D. Richtmyer. Taylor instability in shock acceleration of compressible fluids. *Comm. Pure and Appl. Math.*, XIII:297–319, 1960.

[95] J. R. Ristorcelli and G. A. Blaisdell. Consistent initial conditions for the DNS of compressible turbulence. *Phys. Fluids*, 9(1):4–6, 1997.

[96] M.C. Rivara. New mathematical tools and techniques for the refinement and/or improvement of unstructured triangulations. In *Proceedings of the 5th. international meshing roundtable*, pages 77–86, Pittsburgh, Pennsylvania, 1996. Sandia National Laboratories.

[97] M.C. Rivara and C. Levin. A 3d refinement algorithm suitable for adaptive and multi-grid techniques. *Communications in applied numerical methods*, 8:281–290, 1992.

[98] D. Rodney and R. Phillips. *Physics Review Letters*, 82:1704, 1999.

[99] D. Rodney and R. Phillips. Structure and strength of dislocation junctions: An atomic level analysis. *Physical Review Letters*, 82(8):1704–1707, 1999.

[100] Fedkiw R.P., Aslam T., Merriman B., and Osher S. A non-oscillatory eulerian approach to interfaces in multimaterial flows (the ghost fluid method). *J. Comput. Phys.*, 152(2):457–492, 1999.

[101] G. Saada. *Acta Metallurgica*, 8:841, 1960.

[102] R. Samtaney and D. I. Meiron. Hypervelocity Richtmyer-Meshkov instability. *Phys. Fluids*, 9(6):1783–1803, 1997.

[103] R. Samtaney and D. I. Pullin. On initial-value and self-similar solutions of the compressible Euler equations. *Phys. Fluids.*, 8(10):2650–2655, 1996.

[104] R. Samtaney and N. J. Zabusky. Circulation deposition on shock-accelerated planar and curved density-stratified interfaces: models and scaling laws. *J. Fluid Mech.*, 269:45–78, 1994.

[105] G. Schoeck and R. Frydnam. *Physics Status Solidi*, 53:661, 1972.

[106] P. Schroder et al. Maps: Multiresolution adaptive parameterization of surfaces. In *Proceedings of SIGGRAPH 98*, 1998.

[107] K. W. Schwarz. *Journal of Applied Physics*, 85:108, 1999.

[108] J. A. Sethian. *Level Set Methods: Evolving Interfaces in Geometry, Fluid Mechanics, Computer Vision, and Materials Science*. Cambridge Monographs on Applied and Computational Mathematics. Cambridge University Press, 1996.

[109] C.W. Shu and S. Osher. Efficient implementation of essentially non-oscillatory shock-capturing schemes. *Journal of Computational Physics*, 77:439–471, 1988.

[110] G. Simmons and H. Wang. *Single crystal elastic constants and calculated aggregate properties: A handbook*. M.I.T. Press, Cambridge, Massachusetts, 1971.

[111] Per Söderlind and John A. Moriarty. *Phys. Rev. B*, 57:10340, 1998.

[112] O.G. Staadt and M.H. Gross. Avoiding errors in progressive tetrahedralizations. Technical Report TR-287, Computer Graphics Research Group, Institute of Scinetific Computing, Computer Science Department, ETH Zurich, 1998.

[113] L. Stainier and M. Ortiz. A constitutive theory for bcc single crystals with application to tantalum. to be submitted.

[114] G. Strang. On the construction and comparison of difference schemes. *SIAM J. Numer. Anal.*, 5:506:517, 1968.

[115] M. Tang, B. Devincre, and L.P. Kubin. Simulation and modelling of forest hardening in body centre cubic crystals at low temperature. *Modelling and Simulation in Materials Science and Engineering*, 7(5):893–908, 1999.

[116] P.A. Thompson. *Compressible fluid dynamics*. McGraw-Hill Book Company, 1972.

[117] S.P. Timothy and I.M. Hutchings. The impact of a soft metal sphere on a hard metal target .1. deformation of the sphere. *Philosophical Magazine A-Physics of Condensed Matter Structure Defects and Mechanical Properties*, 54(1):93–102, 1986.

[118] S.P. Timothy and I.M. Hutchings. The impact of a soft metal sphere on a hard metal target .2. deformation of the target. *Philosophical Magazine A-Physics of Condensed Matter Structure Defects and Mechanical Properties*, 54(1):103–113, 1986.

[119] M. Verdier, M. Fivel, and I. Groma. *Modeling and Simulation in Materials Science and Engineering*, 6:755, 1998.

[120] M. Vetter and B. Sturtevant. Experiments on the richtmyer-meshkov instability of an air/sf6 interface. *Shock Waves*, 4(5):247–252, 1995.

[121] P. Vinet, J.H. Rose, J. Ferrante, and J.R. Smith. Universal features of the equation of state of solids. *Journal of the Physics of Condensed Matter*, 1:1941–1963, 1989.

[122] L. Vitos, A. V. Ruban, H. L. Skriver, and J. Kollár. *Surf. Sci.*, 441:186, 1998.

[123] T. Voelkl, D. I. Pullin, and R. D. Henderson. The stretched-vortex SGS model in physical space. In *Presented at the Second AFOSR International Conference on DNS /LES.* Rutgers University, June 7-10, 1999.

[124] J. von Neumann and R.D. Richtmyer. A method for the numerical calculation of hydrodynamic shocks. *J. Appl. Phys.*, 21:232–237, 1950.

[125] S. Walkauskas, D. Broido, K. Kempa, and T. Reinecke. *J. Appl. Phys.*, 85:2579, 1999.

[126] L. Wei, P. K. Kuo, R. L. Thomas, T. R. Anthony, and W. F. Banholzer. *Phys. Rev. Lett.*, 70:3764, 1993.

[127] J. H. Weiner. *Statistical Mechanics of Elasticity.* John Wiley & Sons, New York, 1983.

[128] A. Wray. Private communication. *NASA Ames Research Center.*, 1998.

[129] W. Xu and J. A. Moriarty. Accurate atomistic simulations of the peierls barrier and kink-pair formation energy for ¡111¿ screw dislocations in bcc Mo. *Computational Materials Science*, 9:348–356, 1998.

[130] A. Yoshizawa. Statistical theory for compressible turbulent shear flows, with the application to subgrid modeling. *Phys. Fluids*, 29:2152–2164, 1986.

[131] W.C. Young. *Roark's Formulas for Stress and Strain.* McGraw Hil, 1989.

[132] T. A. Zang, R. B. Dahlburg, and J. P. Dahlburg. Direct and large-eddy simulations of three dimensional Navier-Stokes turbulence. *Phys. Fluids*, 4(1):127–140, 1992.

[133] S. J. Zhou, P. S. Lomdahl D. L. .Preston, and D. M. Beazley. *Science*, 279:1525, 1998.

[134] J. M. Ziman. *Electrons and Phonons.* The Clarendon Press, Oxford, 1967.

[135] J. M. Ziman. *Principles of the Theory of Solids.* Cambridge University Press, Cambridge, 1972.